A review of the dense *Z*-pinch

TOPICAL REVIEW

A review of the dense Z-pinch

M G Haines

Blackett Laboratory, Imperial College, London SW7 2BW, UK

Abstract

The Z-pinch, perhaps the oldest subject in plasma physics, has achieved a remarkable renaissance in recent years, following a few decades of neglect due to its basically unstable MHD character. Using wire arrays, a significant transition at high wire number led to a great improvement in both compression and uniformity of the Z-pinch. Resulting from this the Z-accelerator at Sandia at 20 MA in 100 ns has produced a powerful, short pulse, soft x-ray source >230 TW for 4.5 ns) at a high efficiency of ~15%. This has applications to inertial confinement fusion. Several hohlraum designs have been tested. The vacuum hohlraum has demonstrated the control of symmetry of irradiation on a capsule, while the dynamic hohlraum at a higher radiation temperature of 230 eV has compressed a capsule from 2 mm to 0.8 mm diameter with a neutron yield $>3 \times 10^{11}$ thermal DD neutrons, a record for any capsule implosion. World record ion temperatures of >200 keV have recently been measured in a stainless-steel plasma designed for Kα emission at stagnation, due, it was predicted, to ion-viscous heating associated with the dissipation of fast-growing short wavelength nonlinear MHD instabilities. Direct fusion experiments using deuterium gas-puffs have yielded 3.9×10^{13} neutrons with only 5% asymmetry, suggesting for the first time a mainly thermal source. The physics of wire-array implosions is a dominant theme. It is concerned with the transformation of wires to liquid-vapour expanding cores; then the generation of a surrounding plasma corona which carries most of the current, with inward flowing low magnetic Reynolds number jets correlated with axial instabilities on each wire; later an almost constant velocity, snowplough-like implosion occurs during which gaps appear in the cores, leading to stagnation on the axis, and the production of the main soft-x-ray pulse. These studies have been pursued also with smaller facilities in other laboratories around the world. At Imperial College, conical and radial wire arrays have led to highly collimated tungsten plasma jets with a Mach number of >20, allowing laboratory astrophysics experiments to be undertaken. These highlights will be underpinned in this review with the basic physics of Z-pinches including stability, kinetic effects, and finally its applications.

(Some figures in this article are in colour only in the electronic version)

Contents

1. Introduction

This review is being written at a time of intense and growing interest in the dense Z-pinch. This recent growth has been spearheaded by the use of the large pulsed-power facilities at the Sandia National Laboratory in Albuquerque for the subject of Z-pinches. It led over the last few years to quite dramatic results in the form of high yields of soft x-rays (1–2 MJ) with peak powers greater than 200 TW in a pulse of 4.5 ns duration [1–3]. These results were obtained by the implosion under the action of the pinch force on wire arrays made of tungsten carrying a current rising to 20 MA over 100 ns. The wall-plug efficiency of conversion to x-rays has the remarkably high value of 15%, allowing the possibility of creating high volume hohlraums already at a radiation temperature of over 150 eV, for radiation driven hydrodynamic experiments, with application to astrophysics as well as to inertial confinement fusion. Wire-array implosions are among the highlights of recent annual meetings of the Plasma Physics

Division of the American Physical Society as well as the series of International Conferences on Dense Z-pinches, and represent a marked shift of interest back to perhaps the oldest topic in plasma physics. At the 2005 European Physical Society Conference on Plasma Physics, the opening Alfvén Prize lecture and the following plenary lecture were devoted to the remarkable achievements of wire-array Z-pinches.

The new growth in Z-pinch research was already occurring from 1975 from smaller and pioneering research at Imperial College, Ecole Polytechnique, the universities of Düsseldorf and Stuttgart in Europe, Los Alamos National Laboratory, the Naval Research Laboratory at Washington, the Air Force Research Laboratory at Albuquerque, Physics International and Maxwell Laboratories in the US, and the Russian laboratories at Troitzk and Tomsk, plus many other smaller groups.

One stimulus for this growth was the technological development of pulsed power at AWE (Aldermaston) pioneered by Martin and his team [6], and further developed in the national laboratories in the US and USSR in the 1970s. This would allow the coupling of 1–100 TW of power in typically a 100 ns pulse to a Z-pinch load.

Whilst a major purpose of such experiments in the US national laboratories was the development of an intense pulsed x-ray source, the availability of megampère and megavolt power sources led the more academic scientific world to study also the subjects of radiative collapse and high power-density controlled fusion, together with the possibility of stabilizing by finite ion Larmor radius and sheared flow. This was the main original motivation behind the DZP project at Imperial College which led to the construction of the MAGPIE (Mega Ampère Generator for Plasma Implosion Experiments) facility (2.4 MV, 2 MA, 150 ns) in 1989 [7]. It was opened formally in April 1993 at the 3rd International DZP Conference in London by J C Martin and by Drs R S Pease and S I Braginskii, the two independent discoverers in 1957 of a so-called limiting current (known as the Pease–Braginskii current), when bremsstrahlung losses balance Joule heating [8, 9].

In addition to the availability of technology was the theoretical realization that under the conditions for fusion or for radiative collapse [10], the ion Larmor radius would be a significant fraction of the pinch radius, and enhanced stability might occur [11–13]; this enhanced stability has only recently been established experimentally [14]. Under radiative collapse conditions, a one-dimensional simulation [15] predicts the occurrence for 1 ps of a density of $10^5 \times$ solid hydrogen limited only by degeneracy pressure and opacity. However, this again assumes stability, which experimentally was found not to occur when employing frozen deuterium fibres as initial conditions. (More recently it has been shown that ion-viscous heating associated with the nonlinear development of short wavelength $m = 0$ MHD modes would in any case prevent radiative collapse at high currents. Indeed this heating mechanism has produced record temperatures of 200–300 keV in stainless-steel wire arrays. See section 5.8.) Meanwhile with the spectacular results of short, high power x-ray pulses coming from wire implosions at Sandia, the MAGPIE generator was switched to study this subject in 1998. The physical processes could be explored in detail using the many diagnostics, laser probing and x-ray and optical, streak and framing cameras, which have easy access to the wire arrays.

Z-pinches have also been studied at CERN for use as a magnetic lens for focussing high energy charged particle beams [16]. Rocca *et al* employed the Z-pinch as a compact table-top x-ray laser in a capillary configuration [17]. Z-pinches can be used as a source of x-rays or neutrons for diagnostic purposes. In laser-plasma Z-pinch-like phenomena also occur due to $\nabla T \times \nabla n$ generation of azimuthal magnetic fields [18], while fields of opposite sign also arise in the fast-ignitor concept [19].

In this review we will cover all the basic physics of the Z-pinch especially its susceptibility to instabilities, and its applications.

The Z-pinch is the name of a unique class of magnetically driven or confined plasma in which a current is passed through a cylinder of plasma parallel to the axial or z-direction. The resulting interaction of the azimuthal self-magnetic field and the axial current produces an inward radial $\underline{J} \times \underline{B}$ or magnetomotive force. This force can be employed either dynamically to collapse a hollow plasma cylinder or quasi-statically to confine the plasma through the pinch effect. Unlike most other magnetic confinement schemes that are employed for fusion studies, there is no obvious limit to the magnetic field amplitude such as found when solid-state coils are employed. Magnetic fields in the 100–1000 T (or 1–10 MG) range are routinely produced in present-day Z-pinch experiments. The advantages of the Z-pinch are that larger volumes of plasma can be produced of very high energy density, and with greater efficiency than in, say, laser-produced plasmas. The potentially high power density and hence compactness of a Z-pinch is an important reason for the renewal of interest. There are, however, difficulties arising both from the intrinsic instabilities present and from the intense damage to electrodes at high power densities.

There are many ways of forming a Z-pinch in an experiment. The earliest approach was the compressional Z-pinch to which the capillary discharge is related. The effect of walls can be removed in a gas-embedded Z-pinch which is triggered by means of a laser or needle electrodes. For x-ray production a dynamic hollow gas-puff Z-pinch is effective, from which has evolved the wire-array Z-pinch mentioned above. In addition such imploding plasmas could collide with a central cylinder of plasma or a fibre, or with secondary cylindrical shells. At the other extreme the Z-pinch can be formed from a single fibre of material on the axis, including cryogenic deuterium fibres. A coupling plasma consisting of a pre-ionized sleeve can help to control the tendency of a single fibre to explode in an unstable way, and a recent idea is to induce a large sheared axial flow of plasma in this outer layer in order to nonlinearly saturate the MHD instabilities. (See sections 3.9 and 7.7.)

The present intense interest in dense Z-pinches has arisen from the spectacular increase in x-ray power and efficiency from the dynamic collapse of cylindrical wire arrays mounted between electrodes. As the number of wires is increased beyond some critical number Sanford *et al* [20] demonstrated a remarkable increase in power radiated at the time of the pinch or stagnation on the axis with aluminium wires. With over 400 tungsten wires in a double array a record >230 TW of soft x-ray power or 1.8 MJ in 5 ns has been produced using the 11 MJ Z-accelerator at Sandia National Laboratory by Deeney *et al* [21]. These results and their possible application to controlled fusion through energizing a soft x-ray hohlraum for inertial confinement is occupying contemporary thinking in the field. The carefully built up scientific knowledge of the Z-pinch using modern diagnostic techniques, computer simulations and theory, is all very relevant, and a new understanding of the complex phenomena at work is coming about. It is hoped that this review paper will assist in this regard, and lead eventually to a predictive capability for operation at higher currents.

1.1. History

At the 4th International Conference on Dense Z-pinches (Vancouver 1997), Rudakov drew our attention to what is probably the earliest demonstration of the Z-pinch. This was work done by Martinus van Marum in Amsterdam in 1790 [22] in his entrepreneurial endeavours related to the defence industry of the day. He employed a 1 kJ capacitive energy store composed of 100 Leyden jars, which was discharged into a 1 m long wire causing an explosion and vaporization (see figure 1).

A later independent discovery in Australia by Pollock and Barraclough in 1905 [23] arose from the radial pinching of a copper tube used at the Hartley Vale kerosene refinery as a
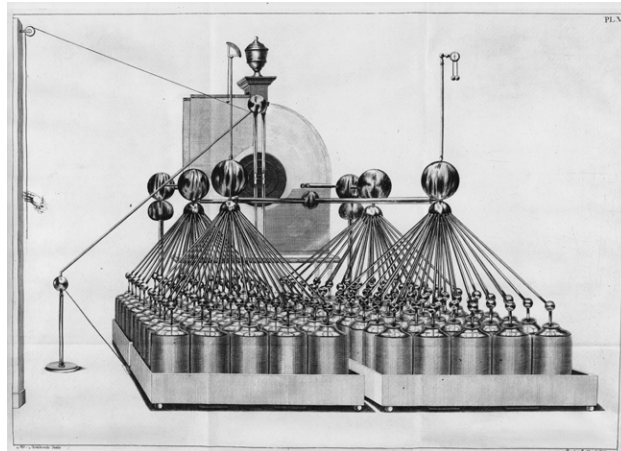
Figure 1. A print of the apparatus used by Martinus van Marum in 1790 to discharge a bank of Leyden jars into a 1 m long wire. Courtesy of the Teylers Museum, Spaarne 16, Haarlem, The Netherlands.

lightning conductor, an experiment drawn recently to our attention by Pease [24]. In the USA Northrupp in 1907 [25] devised a Z-pinch discharge in a liquid conductor which led to a continuous circulatory flow of the mercury driven by the $J_r B_\theta$ upward force. (See [24] for further details.)

In 1934, Bennett [26] derived his important pinch relation for the special case of uniform charged particle streams (see section 2.1). In the late 1940s experiments on Z-pinches were devised by Thomson and Blackman in 1946 at Imperial College resulting in a patent, figure 2, on a toroidal fusion reactor [27]. Theory by Blackman [28] and an experiment by Cousins and Ware [29] of the Z-pinch were published later. Parallel experimental work was undertaken also by Reynolds and Craggs [30] and also by Allen and Craggs [31] at the University of Liverpool. During the 1950s there were also several experiments on linear Z-pinches in the USA and USSR as well as the UK. An important landmark was the famous Kurchatov lecture at Harwell in 1956 [32] when the Russians essentially declassified their Z-pinch research, which had been led experimentally by Artsimovich [33], and theoretically by Leontovich [34], as an attempt to obtain thermonuclear reactions. It was these experiments showing the simultaneous emission of neutrons and hard x-rays, but existing even at comparatively low currents of 150 kA that demonstrated that the reactions were not thermonuclear in origin. Anderson *et al* [35], Carruthers and Davenport [36], and many papers at the 1958 Geneva Conference on Peaceful Uses of Atomic Energy also came to the conclusion that the neutrons arose from an ion acceleration process. The nature of this process, consistent with the overall conservation of axial momentum, is still not fully understood and will be discussed later in this review, in particular in section 3.14.

By the early 1960s disappointment over the inherent MHD instabilities, formulated theoretically by Kruskal and Schwarzschild in 1954 [37], Tayler [38], led to a considerable reduction in activity. Also at this time, the dynamic, compressional Z-pinch was shown to be unstable also to the Rayleigh–Taylor (RT) instability and growth rates were measured at Imperial College in experiments led by Latham and Folkierski [39]. This instability would turn out to be important in wire-array Z-pinches and indeed throughout inertial confinement. Attention switched mainly to toroidal magnetic confinement such as the reversed field pinch, e.g. ZETA, and the tokamak. Other plasma physicists, striving for a high beta (the ratio of

PATENT SPECIFICATION

Inventors: SIR GEORGE PAGET THOMSON and MOSES BLACKMAN

817,681

Date of filing Complete Specification April 28, 1947.

Application Date May 8, 1946.   No. 13963/46

Complete Specification Published Aug. 6, 1959.

Index at acceptance: —Class 39(4), P3E.

International Classification: —G21.

COMPLETE SPECIFICATION

Improvements in or relating to Gas Discharge Apparatus for Producing Thermonuclear Reactions

We, UNITED KINGDOM ATOMIC ENERGY AUTHORITY, of London, a British Authority, do hereby declare the nature of this invention and in what manner the same is to be per-
5   formed, to be particularly described and ascertained in and by the following statement: —
This invention relates to gas discharge apparatus for producing thermonuclear reactions in light elments.
10   For the initiation of nuclear reactions in light elements, particularly for the production of neutrons, effort has hitherto been primarily directed to bombarding targets of or containing deuterium compounds or light elements
15   with protons, deuterons or helium nuclei as constituents of an ionised gas and accelerated to a sufficient degree to attain conditions for the nuclear reaction.
It is now proposed to accelerate nuclei in
20   such a way that they interact between themselves to a significant degree. Their energy is then not lost in bombardment of a relatively massive target, nor is released nuclear energy lost in the target; on the contrary energy
25   released by nuclear reactions becomes available in the body of high speed nuclei to maintain their speed and to compensate for losses by radiation.
One requirement which arises is that the
30   nuclei be accelerated in such a way that they have an irregular distribution of velocity so that frequent collisions occur. In other words energy should be imparted to them in a way to increase the temperature of the gas and not
35   merely to accelerate the nuclei in parallel paths to constitute a beam of fast ions. To meet this requirement, it is proposed to accelerate the nuclei of a body of ionised gas of low density by subjecting them for a sufficient time to the
40   pressure of electromagnetic waves.
Another requirement which arises is that of containing the nuclei in an accelerating field for a substantial time without allowing them to bombard substance of a larger order of

density. Attainment of this objective involves   45
providing for the localising of gas particles without interposing material barriers in the path of the gas particles. In general a gas, by reason of the thermal motion of its particles, tends to bombard its containing walls; such   50
walls in fact are or tend to be material barriers in the path of the gas particles. Hence means other than material containing walls   are required for exerting a localising effect upon the gas.   55
It is accordingly proposed to establish, within an ionized gas of low density and high particle energy and by means of magnetic or electric fields, a pressure gradient falling in all radial directions from a central point or in all   60
directions normal to a circular or other endless axis within the gas so that the gas is largely contained by the field and its bombarding effect upon material containing walls is substantially reduced.   65
In carrying out the invention provision is made for maintaining the electrons of an ionised gas at high speed in an endless path to set up a field tending to contain the gas.
The circulating high-speed electrons con-   70
stitute a closed loop of current of large amperage. An electron attaining as the result of a collision a radial component of velocity with respect to the main electron stream is deflected by the lines of force encircling the stream to   75
follow a trochoidal path in the general direction of the main stream.
The positive ions or nuclei of the gas are bound to the electron stream by electrostatic attraction. Outward movement from the bound   80
electrons leaves a space-charge the effect of which is to limit such movement.
Since the nuclei are thus largely contained by the magnetic field and suffer only a minor loss of energy by bombardment of physical   85
containing walls, their energy can be continuously increased over a substantial period of time, for example by injecting electromag-

[Price 3s. 6d.]

Figure 2. Facsimile of the first page of the Thomson and Blackman patent of 1946 [27, p 645].

plasma pressure to magnetic pressure) plasma concentrated on theta pinches and cusps which had better stability properties, but at the expense of plasma end losses and lower power density. The plasma focus device, a variant of the *Z*-pinch and based on the configurations of either Mather [40] or Filippov [41], see Gentilini *et al,* [42], led the neutron Derby with an empirical scaling law of neutron yield being proportional to current to the fourth power. Up to 10^{12}

D–D neutrons were produced at 1 MA on the Frascati 1 MJ machine, greater at the time than any other controlled fusion experiment (see [43]). The merit of the plasma focus probably lies in the opportunity during the axial flow stage of building up the current and locally stored magnetic energy which is then used to compress a reduced mass of plasma. Unfortunately the main neutron pulse was again associated with a necking or sausage MHD instability, and the subsequent disruption.

It was during the 1970s that a remarkable technological development occurred. Pioneered by Martin and co-workers at AWRE (Aldermaston) [6], pulsed power was developed, based at first on work of Blumlein (1948), [44], a plaque to whom is displayed on his home in Ealing. What emerged is a technique in which a Marx generator (based on the switching of charged capacitors from being in parallel to being in series, leading to a large voltage multiplication) charges up a pulse-forming line to 1–10 MV. At this stage the main inventive step is to realize that insulators behave perfectly for short enough times. Furthermore the use of oil or water as the dielectric medium allowed self-healing of the medium after each discharge, and attention could be given to designing the solid-state insulators at interfaces in a carefully graded way. From these ideas machines are currently operating at currents rising to 20 MA in 150 ns at voltages of 8 MV (the Z machine at Sandia National Laboratory, Albuquerque).

In 1978 Haines [45] showed that under fusion conditions with heat losses to electrodes taken into account the ion Larmor radius is about 0.1–0.3 of the pinch radius. Also, with a current only somewhat higher at about 1.5 MA, radiative collapse to very high density might occur [45]. A new programme of Z-pinch research commenced at Imperial College with the construction of the MAGPIE generator. However, the direct application of pulsed power to single frozen deuterium fibres gave disappointing results, with the dynamics dominated by ionization, expansion and MHD $m = 0$ instabilities before the hot collisionless large Larmor radius regime could be accessed [46]. Experimental interest then switched to studying the physics of wire-array implosions. In a renewed effort in 2001, a compression Z-pinch did indeed demonstrate the stabilizing effect of large ion Larmor radius effects [14].

Meanwhile in the USA and USSR, Z-pinch experiments using the new pulsed power technology were aimed at producing intense x-ray sources. Exploding wires [47], gas-puffs [48] and finally wire arrays [49, 50] were explored. A review of x-ray emission from imploding Z-pinches was given by Pereira and Davis in 1988 [51].

1.2. Various Z-pinch configurations

Figure 3, taken from [52], illustrates the many Z-pinch configurations that have been studied. The first is the compression Z-pinch in which a cylindrical vessel bounded axially by the two electrodes is filled with gas. On applying a voltage, breakdown occurs near the insulating wall and a current shell forms. This current and its self-magnetic field create an inward radial force. Several models of the inward compression have been developed: the snowplough, a shock model and a slug model. These will be discussed in section 4.

If the diameter of the vessel is reduced to the order of up to a few millimetres, the compression pinch becomes a capillary discharge. The wall plays an important role in controlling the plasma and indeed it can itself ionize and form a conducting path for the current. The capillary discharge has been remarkably successful in producing a plasma uniform enough to form a lasing medium [17]. If the plasma density increases towards the ionizing wall, this plasma can be used to guide a laser beam, and extend the focal region beyond the Rayleigh length. This idea is being explored in the wakefield acceleration of electrons (see section 8.9).

If the Z-pinch vessel is filled with a high pressure gas ($\sim \frac{1}{3}$ atm) and an ionization path is created along the axis, e.g. by a focused pulsed laser, then, on applying a high voltage, current
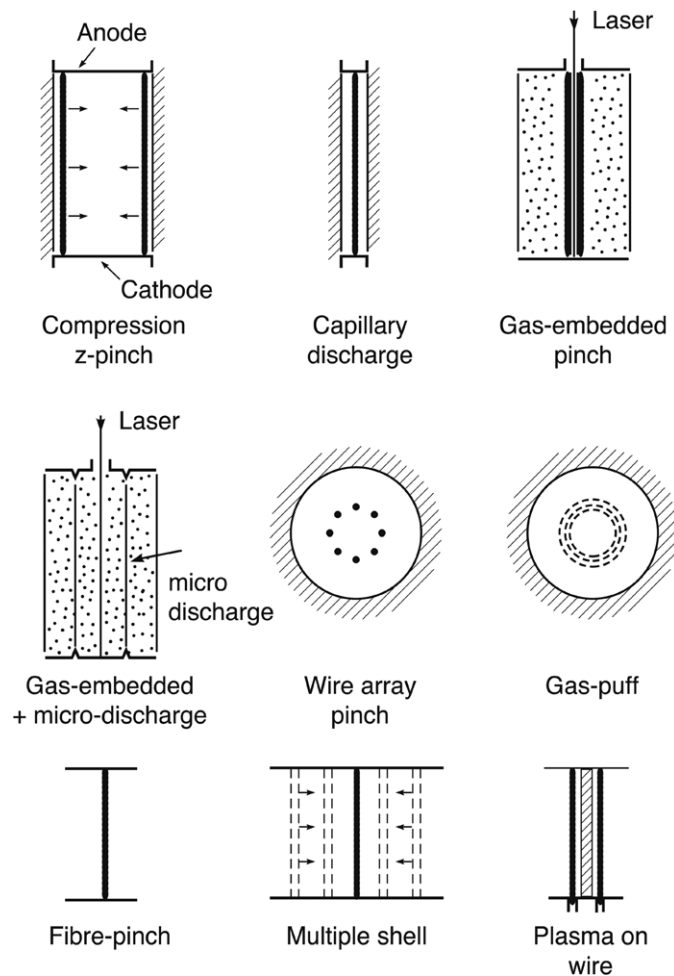
Figure 3. Various Z-pinch configurations. Reprinted from [52], copyright 1948, with kind permission from Springer Science + Business Media B.V..

will flow at first along the axis of the vessel. This is the gas-embedded Z-pinch [53]. This type of Z-pinch is the only one to be dominated by the $m = 1$ or kink instability, which we will discuss in section 3. A variant of this employing an additional hollow micro-discharge has been studied by Soto *et al* [54], figure 3.

The fibre pinch or exploding wire Z-pinch is illustrated in figure 3 [46, 47]. The fibre can be carbon, cryogenic hydrogen or deuterium, or metal wires such as aluminium or tungsten. A variation of this is if a preformed plasma is formed on the surface either by preionization [55], or by collapsing an additional plasma source onto the surface [56], figure 3. A further variation, is for the additional plasma to have a large axial velocity, so that the possible stabilization by sheared axial flow [57] can be studied.

The solid fibre can be replaced by a gas jet which will subsequently be ionized by an applied voltage. This configuration, figure 3, tends to have properties intermediate to the compression pinch (but without wall) and an exploding wire. Instead, a dynamic pinch can be devised using a hollow gas puff [48] shown in figure 3. The x-ray yield from, say, a krypton gas puff can be substantial, though the axial uniformity is difficult to control because of the

tendency of the hollow gas jet to expand radially as it flows out of a nozzle from one electrode to the other, leading to a zippering effect at the implosion.

This axial non-uniformity is overcome by using an array of very fine wires, shown in figure 3 [20]. The properties of these wire arrays will be discussed in detail later. They could in principle be replaced by a thin shell metal liner [58], but to keep the mass per unit length the same as a typical wire array, e.g. 240 wires of 4 μm diameter on an array radius of 12 mm, would mean a shell thickness of only 40 nm. However for slower compression Z-pinches with large currents, thicker shells can be employed.

One of the major limitations of the wire-array Z-pinch is the development of RT instabilities [59]. These instabilities can be partly mitigated by employing double shell or nested wire arrays [60] shown in figure 3. Further modifications can be considered such as a central foam or fibre load inside such arrays, as employed in the dynamic hohlraum [61–63]. The staged Z-pinch [64] is one such idea. Recent work by Lebedev *et al* [65] shows that the RT instability can be reduced by having incomplete merger of the wire plasmas before the final implosion, which will have features similar to a snowplough pinch (see section 4.1).

There are a few other variants, e.g. if the Z-pinch is made into a toroidal discharge threading through multiple cusp magnetic fields (the Polytron configuration [66, 67]), the toroidal current changes to an ion current through the Hall acceleration effect. Then a plasma stabilized by the cusp magnetic fields and with greatly reduced ring cusp losses can be formed. See section 8.5. This configuration has also been studied more recently by Dawson *et al* [68, 69]. However, because of the need for cusp magnetic fields provided by external coils which have to be limited to 5–10 T, the high power-density properties of the Z-pinch cannot be exploited for this configuration. Reviews of plasma confinement in cusp magnetic fields are to be found in [70, 71].

Another variant is the X-pinch in which two wires are stretched between electrodes in an X configuration (Kalantar and Hammer [72]). This crossing point carries twice the current and this leads to a very hot localized plasma region which is currently being exploited as an x-ray backlighter source. Another x-ray source can be produced at lower powers using a needle as the anode [73] in a development of the vacuum spark.

The magnetic fields spontaneously created by $\nabla T \times \nabla n$ effects in laser–plasma interactions [18] are also in the configuration of a Z-pinch and can develop [74, 75] to the MG level. Many mechanisms for generation and convection of this azimuthal magnetic field in laser–plasma interactions have been reviewed [76]. Indeed in the more extreme fast ignitor scheme [19] the laser-produced channel will have a net current and a similar or larger magnetic field. When an intense short-pulse laser beam (10^{19} W cm^{-2}, 1–2 ps) is incident on a solid target an azimuthal magnetic field of up to 0.7 GG has been measured [77, 78] similar to that predicted in particle-in-cell simulations [79], in a hybrid model [80] and analytically [81]. It can be considered as driven by the absorption of photon momentum [81, 82] and leads to a magnetic field in the opposite direction to that associated with $\nabla T \times \nabla n$ effects. This is a most extreme Z-pinch. These studies are unfortunately beyond the scope of this review and will be only briefly discussed in section 7.8.

1.3. Outline of the review

Having presented an introduction to the Z-pinch, highlighting the present exciting results from high current, wire-array pinches, giving a brief history, and outlining the many Z-pinch configurations, the review will proceed as follows. In section 2, the properties of the equilibrium Z-pinch will be explored, followed by the stability analysis (section 3) including the nonlinear evolution of a disruption and the origin of electron and ion beams. In section 4 the dynamic

pinch models will be presented. A detailed account of the wire-array Z-pinch will be presented in section 5, with its application to hohlraums and inertial confinement fusion in section 6. In section 7 experimental results from other Z-pinch configurations will be discussed. Other applications of Z-pinches ranging from x-ray lithography to a magnetic lens for relativistic charged particle focusing will also be included in section 8.

Earlier reviews of the Z-pinch include those by Kadomtsev [83], Haines [52, 84], Dangor [85], Peireira and Davis (especially on x-ray emission) [51], Matzen [86], Liberman *et al* [87] and Ryutov *et al* [88]. In addition there have been several volumes of papers from the International Conference on Dense Z-Pinch series [89] as well as special issues of the IEEE Transactions on Plasma Science [90], Laser and Particle Beams [91] and earlier Proceedings of Workshops on the Plasma Focus and Z-pinch [92].

2. Physics of the equilibrium Z-pinch

We first present some of the basic physical properties of a uniform Z-pinch in pressure balance.

2.1. Bennett relation

This was first derived by Bennett in 1934 [26] for charged particles streaming with a uniform axial velocity. It can be extended to cover the general case of any current density distributions in a Z-pinch under a radial pressure balance which is described by

$$\frac{\partial p}{\partial r} = -J_z B_\theta. \tag{2.1}$$

Employing the axial component of Ampère's law,

$$\frac{1}{r}\frac{\partial}{\partial r}(r B_\theta) = \mu_0 J_z \tag{2.2}$$

we obtain, on integration

$$B_\theta = \frac{\mu_0}{r}\int_0^r J_z r\,\mathrm{d}r \tag{2.3}$$

and hence, from equation (2.1)

$$\frac{\partial p}{\partial r} = -\mu_0 \frac{J_z}{r}\int_0^r J_z r\,\mathrm{d}r. \tag{2.4}$$

The ion line density N_i is defined by

$$N_\mathrm{i} = \int_0^a 2\pi n_\mathrm{i} r\,\mathrm{d}r, \tag{2.5}$$

where a is the plasma radius. Taking the *mean* electron and ion temperatures to be T_e and T_i, respectively, we can write

$$N_\mathrm{i} k_\mathrm{B}(Z T_\mathrm{e} + T_\mathrm{i}) = \int_0^a 2\pi p r\,\mathrm{d}r, \tag{2.6}$$

where Z is the ionic charge number and k_B is Boltzmann's constant. Equation (2.6) can integrated by parts, as follows:

$$\begin{aligned}
N_\mathrm{i} k_\mathrm{B}(Z T_\mathrm{e} + T_\mathrm{i}) &= \pi \int_0^a p\,\mathrm{d}(r^2) \\
&= [\pi p r^2]_{r=0}^a - \pi \int r^2 \frac{\partial p}{\partial r}\,\mathrm{d}r \\
&= 0 + \pi \mu_0 \int_0^a J_r r \left[\int_0^r J_z r\,\mathrm{d}r\right]\,\mathrm{d}r,
\end{aligned}$$

11

where equation (2.4) has been employed. Writing $x = \int_0^r 2\pi J_z r \, \mathrm{d}r$ this becomes

$$N k_\mathrm{B} (Z T_\mathrm{e} + T_\mathrm{i}) = \frac{\mu_0}{4\pi} \int_0^a x \, \mathrm{d}x = \frac{\mu_0}{4\pi} \left[\frac{x^2}{2} \right]_{r=0}^a$$

or finally the Bennett relation

$$8\pi N k_\mathrm{B} (Z T_\mathrm{e} + T_\mathrm{i}) = \mu_0 I^2 \qquad (2.7)$$

is obtained, where the total current I is defined by

$$I = \int_0^a 2\pi J_z r \, \mathrm{d}r. \qquad (2.8)$$

Equation (2.7) is remarkable in that the average temperature of the equilibrium pinch can be calculated knowing only the line density and current.

Another aspect of Bennett's paper is the derivation of what is called the Bennett equilibrium. This is a special density (and current) profile associated with a spatially uniform axial velocity of current carriers and no ion flow. Taking this velocity as $v_{\mathrm{e}z}$ the combination of Ampère's law and pressure balance leads to

$$-n_\mathrm{e}(r) e \, v_{\mathrm{e}z} = \frac{1}{\mu_0 r} \frac{\partial}{\partial r} (r B_\theta(r)) = \frac{1}{\mu_0} \frac{\partial}{r \partial r} \left[\left(\frac{r k_\mathrm{B} (T_\mathrm{e} + Z^{-1} T_\mathrm{i})}{n_\mathrm{e}(r) e \, v_{\mathrm{e}z}} \right) \frac{\partial n_\mathrm{e}}{\partial r} \right] \quad (2.9)$$

the solution of which is

$$n_\mathrm{e}(r) = \frac{n_\mathrm{eo}}{(1 + b r^2)^2}, \qquad (2.10)$$

where

$$b = \frac{n_\mathrm{eo} \mu_0 e^2 v_{\mathrm{e}z}^2}{8 k_\mathrm{B} (T_\mathrm{e} + Z^{-1} T_\mathrm{i})}. \qquad (2.11)$$

Such an equilibrium is useful in the Hall fluid or the Vlasov models, but is not compatible with one based on collisional transport such as the parabolic profile which is based on uniform resistivity and axial electric field.

There is an interesting feature of this profile; namely that the characteristic radius of the pinch, $b^{-1/2}$ is given by

$$b^{-1/2} = \lambda_\mathrm{D} \frac{c}{v_{\mathrm{e}z}} 2\sqrt{2} \left(1 + \frac{T_\mathrm{i}}{Z T_\mathrm{e}} \right)^{1/2}. \qquad (2.12)$$

Thus when the drift velocity approaches the speed of light c, the pinch radius shrinks to one Debye length, $\lambda_\mathrm{D} = (\varepsilon_0 k_\mathrm{B} T_\mathrm{e} / n_\mathrm{eo} e^2)^{1/2}$, while a normal Z-pinch has $v_{\mathrm{e}z} \ll c$ and it has macroscopic dimensions much greater than λ_D. The former could be relevant during a disruption (see section 3.14). This also shows the necessity of having a magnetically neutralizing return electron current in the fast ignitor where the fast electrons are indeed relativistic.

2.2. Particle orbits

In the absence of ion centre-of-mass motion the ion radial pressure balance equation is

$$0 = Z n_\mathrm{i} e E_r - \frac{\partial p_\mathrm{i}}{\partial r}. \qquad (2.13)$$

This equation shows that a radial electric field is required to confine the ion pressure. This is despite the fact that a magnetic field exists which can cause the ions to be magnetized, i.e.

move in circular Larmor orbits. From the *fluid* point of view, if the ion centre-of-mass velocity is zero there is no net magnetic force on the ions per unit volume, only the electric field force.

In general the azimuthal magnetic field is both curved and radially non-uniform. At the axis B_θ is zero and here and nearby conventional guiding-centre theory breaks down. At larger radius where guiding-centre theory holds there are three types of ion guiding-centre drift: E_r/B_θ, i.e. the axial component of the $\underline{E} \times \underline{B}/B^2$ drift; $-(m_i v_{i\perp}^2/Z_e B_\theta^2)(\partial B_\theta/\partial r)$, the gradient B drift which depends on the velocity component $v_{i\perp}$ in the plane perpendicular to the magnetic field, i.e. the r–z plane; and $m_i v_{i\parallel}^2/Z e B_\theta r$, the curvature drift associated with the velocity of the particle parallel to the magnetic field $v_{i\parallel}^2$, and the curvature of the magnetic field $1/r$.

Following [45] the relationship between the mean values of these drifts, which are all parallel to the z-axis and the centre-of-mass ion velocity v_{iz} in the z-direction is that they differ by the axial component of the diamagnetic velocity $-(1/n_i m_i)\mathrm{curl}_\perp(P_{\perp i}\underline{\Omega}_i/\Omega_i^2)$, where $P_\perp$ is the perpendicular pressure and $\underline{\Omega}_i = Ze\underline{B}/m_i$ is the vector cyclotron frequency.

This can be seen by generalizing the radial ion pressure balance equation (2.13) to include both a net c.m. axial velocity v_{zi} and anisotropic pressure,

$$0 = Zn_i e E_r - Zn_i e v_{iz} B_\theta + \frac{P_{\parallel i} - P_{\perp i}}{r} - \frac{\partial P_{\perp i}}{\partial r} \tag{2.14}$$

and rearranging it to give an equation for the axial ion centre-of-mass velocity,

$$v_{zi} = -\frac{1}{Zn_i e r}\frac{\partial}{\partial r}\left(\frac{rP_{\perp i}}{B_\theta}\right) - \frac{P_{\perp i}}{Zn_i e B_\theta^2}\frac{\partial B_\theta}{\partial r} + \frac{P_{\parallel i}}{Zn_i e B_\theta r} + \frac{E_r}{B_\theta}. \tag{2.15}$$

The first term on the right-hand side is the diamagnetic velocity; the other terms can easily be recognized as the average gradient B drift and curvature drift plus the $\underline{E} \times \underline{B}/B^2$ drift.

It is perhaps useful to recall the meaning of the diamagnetic velocity. In the frame of reference in which the mean guiding-centre velocity is zero the Larmor (circular) orbits of charged particles of each species will lead to a contribution to the magnetization per unit volume of $\underline{M}_v = n\overline{\underline{\mu}}$ where $\underline{\mu}$ is the magnetic moment $-\frac{1}{2}mv_\perp^2\underline{B}/B^2$ and $\overline{\underline{\mu}}$ is the mean averaged over the distribution function. The value of curl $\underline{M}_v$ gives the contribution of that species to the magnetization current density; $(1/ne)(\nabla \times \underline{M}_v)_\perp$ is therefore the diamagnetic velocity which becomes $-(1/nm)(\nabla \times (P_\perp \underline{\Omega}/\Omega^2))_\perp$. An alternative description can be given in terms of the contribution to momentum in a small element of volume of particles passing through this element as they execute circular motion (see [93]).

Electron motion can be similarly described, their radial pressure balance, by analogy with equation (2.14) being

$$0 = -n_e e E_r + n_e e v_{ez} B_\theta + \frac{P_{\parallel e} - P_{\perp e}}{r} - \frac{\partial P_{\perp e}}{\partial r}. \tag{2.16}$$

Addition of equations (2.14) and (2.16) together with the assumption of quasi-neutrality yields

$$J_z B_\theta = -\frac{\partial P_\perp}{\partial r} + \frac{P_\parallel - P_\perp}{r}, \tag{2.17}$$

where $P_\perp$ is $P_{\perp e} + P_{\perp i}$ and $P_\parallel$ is $P_{\parallel i} + P_{\parallel e}$. Equation (2.17) represents MHD pressure balance for an anisotropic plasma, but with zero off-diagonal stresses, as the distribution functions in the rest frame of each species are bi-Maxwellian.

Equation (2.15) contains what might seem a paradoxical result: namely that even if v_{zi} is zero there can be a net flow of guiding centres of ions in the z-direction. It would appear that the particles flow on average from one end of the Z-pinch to the other, but their c.m. velocity could be zero. There therefore must be a return flow of ions somewhere. It will now be shown that this flow is associated with the singular ion orbits caused by snake-like orbits
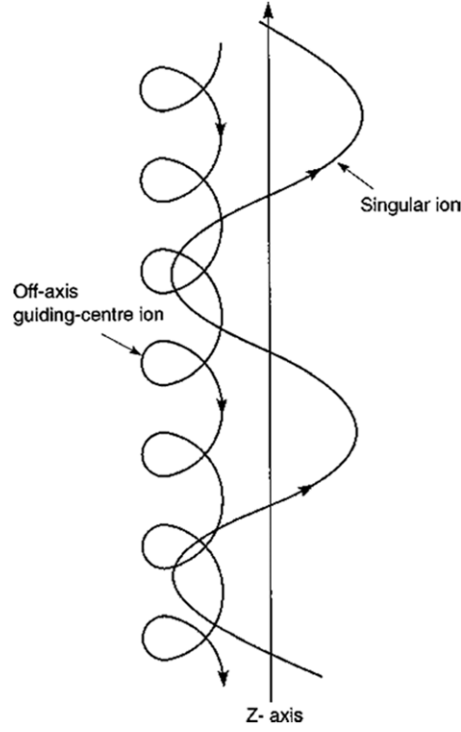
13

Figure 4. A sketch of ion guiding-centre and singular orbits. Reprinted with permission from [349, figure 2]. Copyright 2000, American Institute of Physics.

of ions within one Larmor radius of the axis as illustrated in figure 4. The net guiding-centre flow of ions is

$$\int_0^a 2\pi n_{\mathrm{i}} r \left(\frac{E_r}{B_\theta} - \frac{P_{\perp\mathrm{i}}}{Z n_{\mathrm{i}} e B_\theta^2} \frac{\partial B_\theta}{\partial r} + \frac{P_{\|\mathrm{i}}}{Z n_{\mathrm{i}} e B_\theta r} \right) \mathrm{d}r.$$

Using equation (2.15) this becomes

$$\int_0^a 2\pi n_{\mathrm{i}} r \left[v_{z\mathrm{i}} + \frac{1}{Z n_{\mathrm{i}} e r} \frac{\partial}{\partial r} \left(\frac{r P_{\perp\mathrm{i}}}{B_\theta} \right) \right] \mathrm{d}r = N_{\mathrm{i}} \overline{v_{z\mathrm{i}}} + \left[\frac{2\pi}{Ze} \frac{r P_{\perp\mathrm{i}}}{B_\theta} \right]_{r=0}^{r=a}, \quad (2.18)$$

where N_{i} is the ion line density and $\overline{v_{z\mathrm{i}}}$ is the mean ion centre-of-mass velocity in the z-direction. At $r = a$, $P_{\perp\mathrm{i}}$ will vanish. The last term in equation (2.18) is therefore

$$-\frac{2\pi}{Ze} \left(\frac{r P_{\perp\mathrm{i}}}{B_\theta} \right)_{r=0} = -\frac{2\pi}{Ze} \left(\frac{2 P_{\perp\mathrm{i}}}{\mu_0 J_z} \right)_{r=0}, \quad (2.19)$$

where equation (2.3) has been integrated for small r. Equation (2.19) represents the return singular flow of ions with their mean thermal speed within one Larmor radius of the z-axis where B_θ vanishes. It corresponds to a singular ion current, I_{si} [45], given by

$$I_{\mathrm{si}} = \left(\frac{4\pi P_{\perp\mathrm{i}}}{\mu_0 J_z} \right)_{r=0}, \quad (2.20)$$

$$= n_{\mathrm{i}} Z e v_{\perp\mathrm{i}} \pi R_{\mathrm{i}}^2, \quad (2.21)$$

where R_{i} is the distance from the axis at which the mean ion Larmor radius is also R_{i}, i.e.

$$R_{\mathrm{i}} = \frac{v_{\perp\mathrm{i}}}{\Omega_{\mathrm{i}}(R_{\mathrm{i}})} = \frac{2 m v_{\perp\mathrm{i}}}{Z e \mu_0 J_z R_{\mathrm{i}}}, \quad (2.22)$$
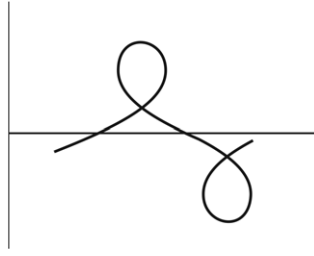
Figure 5. A retrograde singular orbit.

where $P_{\perp i}$ is $n_i m_i v_{\perp i}^2$. When $\overline{v_{zi}}$ is zero, this singular flow exactly balances the off-axis guiding-centre flow as illustrated in figure 4.

There is a corresponding singular electron current I_{se} given by

$$I_{se} = \left(\frac{4\pi P_{\perp e}}{\mu_0 J_z} \right)_{r=0}. \tag{2.23}$$

For the special case of $T_e = T_i$, $Z = 1$ and uniform current density J_z, I_{si} becomes equal to I_{se}, the ∇B and curvature drifts cancel, and the electrons and ions have the same E_r/B_θ guiding-centre drift, i.e. there is no net current associated with the guiding-centre flow. The total current I is then the sum of I_{si} and I_{se}, each of which for $Z = 1$ constitutes half the total. But because of diamagnetism the actual current density is spread uniformly from $r = 0$ to $r = a$. Another interesting special case is when the ion pressure is negligible: equation (2.13) then states that $E_r = 0$. If in addition the current density is uniform, there is then no net electron or ion guiding-centre flow. The current is effectively carried only by the singular electrons close to the axis, but the current density is distributed over the radius of the Z-pinch through diamagnetism.

There are, of course, rather more types of particle orbit than discussed above. Grateau [94] describes many of these. One interesting example is the retrograde orbit which is also well known to those studying the neutral sheet in the magnetosphere or in astrophysics, shown in figure 5 [94]. The Hall parameters ($\Omega_i \tau_i$, $\Omega_e \tau_{ei}$) must be $\gg 1$ for applicability of guiding-centre theory, a condition not always satisfied in experiments.

A special case of equation (2.23) arises for relativistic electron beams propagating in an electrostatically neutralizing medium with a velocity $v_{ze} = \beta c$ and having a perpendicular pressure $\gamma m_e n_e \beta^2 c^2$. The singular current becomes the Alfvén limiting current, 17 000 $\gamma\beta$ Ampère where $\gamma = (1 - \beta^2)^{-1/2}$. It should be stressed that the Alfvén–Lawson current [95] is only a limit if there is no other contribution such as a return cold current or a higher electron pressure than that of the electron beams.

This is how we can have, for example, a stationary Boltzmann distribution of ions on the axis, yet have a net *flow* of ions in the preferred direction from anode to cathode. The angle dividing ions into those that proceed towards the cathode from the retrograde particles that go towards the cathode is less than $\pi/2$. It has been calculated by Howell [96]. Only a unique class of particle orbit will actually cross the axis. Most particles will possess some azimuthal motion; each of which if collisionless and for an azimuthal symmetric system will have its angular momentum $m r v_\theta$ conserved. (If an axial magnetic field B_z with magnetic vector potential A_θ is also present then in azimuthal symmetry the canonical angular momentum ($m r v_\theta + Z e r A_\theta$) will be conserved, a point that requires care in considering rotation in theta pinches [93]).

15

In section 3.8 the effect of large ion Larmor radius (LLR) on stability will be analysed, but first the effect of axial energy loss will be evaluated.

2.3. Axial heat loss to electrodes

Four models of heat loss to the electrodes will be discussed. In the first [97], the worst case of electron thermal conduction in a zero magnetic field is employed, in the second model [97] the Hall parameter $\omega_e \tau_e$ is set to infinity. A third model employs the full Braginskii [98] transport with zero radial heat flux and arbitrary $\omega\tau$ (Hall parameter), while in the fourth the heat flux arising from drift and singular orbits is evaluated. In all cases a steady state model with Joule heating balancing axial heat loss is employed.

An order of magnitude estimate of the results can be obtained. In all cases the ratio of voltage V to current I gives the resistance

$$\frac{V}{I} \approx \frac{z_0}{\pi a^2} \cdot \frac{1}{\alpha T^{3/2}}, \tag{2.24}$$

where z_0 is the axial length of the Z-pinch and the electrical conductivity σ is written as $\alpha T^{3/2}$, α being approximately constant.

In the first model, if we neglect thermoelectric effects, the heat flux q_z is $-\lambda T^{5/2} \partial T / \partial z$ where λ is approximately constant. The power balance therefore scales as

$$IV \approx \pi a^2 \lambda T^{5/2} T / z_0. \tag{2.25}$$

Eliminating the current and voltage in turn from these two equations gives

$$V \approx \sqrt{\frac{\lambda}{\alpha}} T \tag{2.26}$$

$$I = \frac{\pi a^2}{z_0} \sqrt{\alpha\lambda} T^{5/2}. \tag{2.27}$$

For the second model the axial heat flux is entirely the electron enthalpy carried by the current, namely,

$$q_z \approx \frac{5}{2} \frac{kT}{e} \frac{I}{\pi a^2}.$$

The power balance is then

$$IV \approx \frac{5}{2} \frac{kT}{e} I. \tag{2.28}$$

Cancelling I, this gives a simple equation of proportionality between V and T,

$$V = \frac{5}{2} \frac{k}{e} T, \tag{2.29}$$

which is exactly the same form as equation (2.26). Substitution of equation (2.29) into equation (2.24) then gives

$$I = \frac{\pi a^2}{z_0} \frac{5}{2} \frac{k}{e} \alpha T^{5/2}, \tag{2.30}$$

which is the same form as equation (2.27). Indeed when a proper numerical integration of the nonlinear differential equations is carried out with thermoelectric terms included [97] it is found that the coefficients in the two models differ by only 30%. These results can therefore be considered to be robust and model independent.

The first and second models are given in detail in [97] in which the transport coefficients in a magnetized plasma of Marshall [99] were employed. An asymmetry in heat flow is introduced by the inclusion of the enthalpy flow in the heat-flow equation and the thermoelectric field in Ohm's law, which are

$$q_z = -\kappa \frac{\partial T}{\partial z} + \psi J_z \tag{2.31}$$

$$J_z = \sigma E_z + \phi \frac{\partial T}{\partial z} \tag{2.32}$$

when the coefficients are $\kappa = \lambda T^{5/2}$, $\psi = -\zeta T$, $\sigma = \alpha T^{3/2}$ and $\phi = \alpha\gamma T^{3/2}$, λ, ζ, α and γ being constant apart from a weak $\ln \Lambda$ dependence. The energy balance equation with bremsstrahlung loss included is

$$\underline{J} \cdot \underline{E} = \frac{\partial q_z}{\partial z} + \beta_b n_e^2 T^{1/2} + \frac{1}{r}\frac{\partial}{\partial r}(r q_r), \tag{2.33}$$

where β_b is the bremsstrahlung coefficient.

On averaging equation (2.33) over radius, i.e. integrating $\int_0^a 2\pi r\, dr$ to the outer radius a at which the radial heat flux q_r is assumed to be zero, it becomes

$$\pi a^2 \frac{\partial q_z}{\partial z} + \frac{4}{3}\beta_b \frac{N^2}{\pi a^2} T^{1/2} = I E_z \tag{2.34}$$

On introducing equations (2.7), (2.31) and (2.32) to eliminate $N(z)$, $E_z(z)$ and $q_z(z)$ a second order, nonlinear ordinary differential equation for $T(z)$ is found

$$\pi a^2 \lambda \frac{d}{dz}\left(T^{5/2}\frac{dT}{dz}\right) + I(\zeta - \gamma)\frac{dT}{dz} + \frac{I^2}{\pi a^2 a T^{3/2}}\left(1 - \frac{I^2}{I_{PB}^2}\right) = 0, \tag{2.35}$$

where the Pease–Braginskii current I_{PB} [8, 9] is defined by

$$I_{PB} = \left(\frac{192}{\alpha\beta_b}\right)^{1/2}\frac{\pi k}{\mu_0} = 0.433(\ln \Lambda)^{1/2} \times 10^6 \, A \tag{2.36}$$

and is derived later in section 2.8.

The variables can be changed to ξ and x, defined by

$$\xi = \frac{\pi a^2 T^{5/2}}{z_0 I}, \tag{2.37}$$

$$x = \frac{z}{z_0} \tag{2.38}$$

so that equation (2.35) becomes

$$\frac{2}{5}\alpha\lambda\xi\frac{d^2\xi}{dx^2} + \frac{4}{25}\alpha\lambda\left(\frac{d\xi}{dx}\right)^2 + \frac{2}{5}\alpha(\zeta - \gamma)\frac{d\xi}{dx} + 1 - \frac{I^2}{I_{PB}^2} = 0. \tag{2.39}$$

When Marshall's transport coefficients are employed it is found there is a limiting negative value of $d\xi/dx$ in the domain of interest. This can be seen in a plot of the first term of equation (2.39) versus $d\xi/dx$ in figure 6 where $(d^2\xi/dx^2) \to 0$ as $(d\xi/dx) \to -(5/4\lambda)(\zeta - \gamma)(1 - s) = \xi_1'$ where s is given by

$$s = \left[1 - \frac{4\lambda}{\alpha(\zeta - \gamma)^2}\left(1 - \frac{I^2}{I_{PB}^2}\right)\right]^{1/2} \tag{2.40}$$

the coefficient $4\lambda/\alpha(\zeta - \gamma)^2$ having a value of 1/1.47. This limitation means that the heat flux to the cathode is very small and negative, while all the Joule heating apart from that radiated is transferred to the anode. Equation (2.39) can be analytically integrated once to give ξ as a
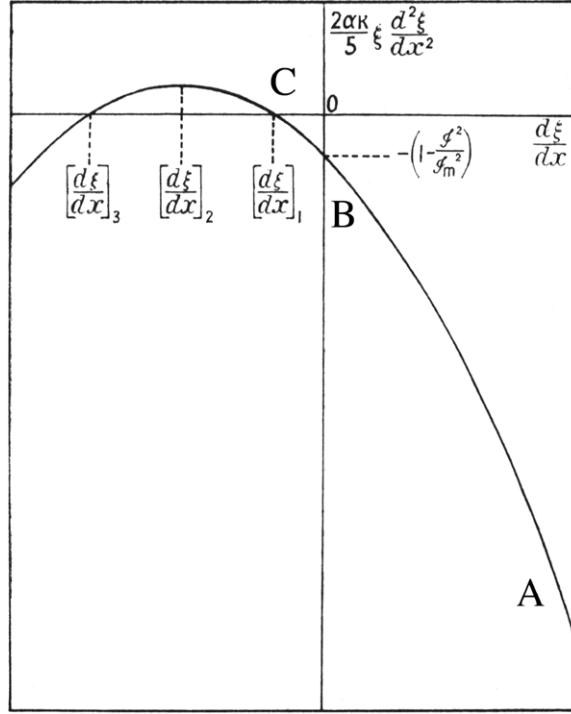
Figure 6. The curve ABC represents the allowable domain for the continuous solution from the anode (A) to the cathode (C) of equation (2.39) for real s [97, figure 1].

function of $\mathrm{d}\xi/\mathrm{d}x \equiv v$,

$$\left(\frac{\xi_{\max}}{\xi}\right)^{4/5} = \frac{\frac{4}{25}\alpha\lambda v^2 + (2\alpha/5)(\zeta - \gamma)v + 1 - I^2/I_{PB}^2}{1 - I^2/I_{PB}^2} \cdot \left[\frac{\frac{4}{5}\lambda v/(\zeta - \gamma)(1 + s) + 1}{\frac{4}{5}\lambda v/(\zeta - \gamma)(1 - s) - 1}\right]^{1/s},$$

(2.41)

where the boundary condition $v = 0$ at $\xi = \xi_{\max}$ has been applied. At the electrodes $\xi \ll \xi_{\max}$ (i.e. $T \ll T_{\max}$) and it follows that at the cathode where $v \to \xi_1'$ the heat flow is $-\frac{1}{2}T_0 I[\zeta(1 + s) + \gamma(1 - s)] < 0$ and negligible compared with the Joule heating. At the anode the quadratic term in v is dominant, giving

$$\left(\frac{T_{\max}}{T_0}\right)^2 = \left(\frac{\xi_{\max}}{\xi}\right)^{4/5} \to \frac{4\alpha\lambda}{25(1 - I^2/I_{PB}^2)}\left(\frac{\mathrm{d}\xi}{\mathrm{d}x}\right)_{\text{anode}}^2 \left(\frac{1 - s}{1 + s}\right)^{1/s}.$$

(2.42)

Inserting this value of $(\mathrm{d}\xi/\mathrm{d}x)_{\text{anode}}$ into the overall power balance equation

$$IV\left(1 - \frac{I^2}{I_{PB}^2}\right) = \frac{2}{5}\lambda T_0 I\left(\frac{\mathrm{d}\xi}{\mathrm{d}x}\right)_{\text{anode}},$$

(2.43)

which represents Joule heating minus bremsstrahlung being equal to the heat flow to the anode, a more exact relation than equation (2.26) is found, namely

$$V\left[1 - \frac{I^2}{I_{PB}^2}\right]^{1/2} = \left(\frac{\lambda}{\alpha}\right)^{1/2}\left(\frac{1 + s}{1 - s}\right)^{1/2s} T_{\max},$$

(2.44)

where the proportionality of the maximum temperature on the voltage is noted. In the absence of bremsstrahlung this numerically gives $T_{\max}(\mathrm{K}) = 3.62 \times 10^3\,V$ (volt).
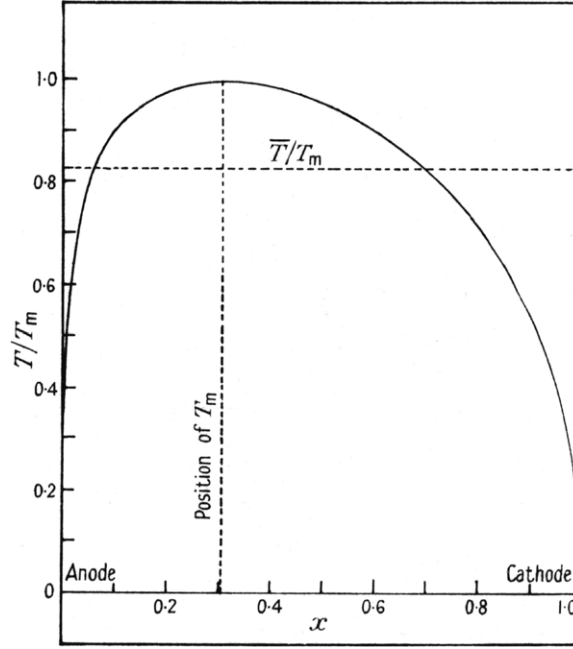
18

Figure 7. The axial profile of the temperature, showing the asymmetric drift associated with the thermoelectric terms [97, figure 4].

A numerical second integration of equation (2.41) yields $T(x)$ which is shown in figure 7.

From this integration (which is most easily performed in a plot of $1/v$ versus $\xi/\xi_{\max}$), $\xi_{\max}$ is found to be 5.89×10^6 in the absence of bremsstrahlung. This is analogous to equation (2.27) which more generally can be written as

$$T_{\max}^{5/2} = 1.36 \times 10^7 \frac{z_0}{\pi a^2}(1-s)I. \tag{2.45}$$

The second model leads to a first order equation showing that the peak temperature occurs at the anode itself, and with numerical results corresponding to equations (2.28) and (2.29) with bremsstrahlung included, namely

$$T_{\max} = 4.64 \times 10^3 V \left(1 - \frac{I^2}{I_{PB}^2}\right), \tag{2.46}$$

$$T_{\max}^{5/2} = 2.04 \times 10^7 \frac{z_0}{\pi a^2} I \left(1 - \frac{I^2}{I_{PB}^2}\right). \tag{2.47}$$

The third model is intermediate to the first ($\omega\tau = 0$) and second ($\omega\tau = \infty$) models, and allows for intermediate values of $\omega\tau$. Using the more accurate transport coefficients of Epperlein and Haines [100] and by assuming $a \ll z_0$ (or rather $\omega\tau a < z_0$) we can assume in a radially isolated Z-pinch that the radial electron heat flux is zero for all r. Then, in Braginskii's notation equations (2.31) and (2.32) become

$$q_z = -\kappa_\perp \left(1 + \frac{\kappa_\wedge^2}{\kappa_\perp^2}\right) \frac{\partial T}{\partial z} - \left(\beta_\perp + \frac{5}{2} + \frac{\kappa_\wedge \beta_\wedge}{\kappa_\perp}\right) \frac{T}{e} J_z, \tag{2.48}$$

$$E_z = \left(\frac{\alpha_\perp}{n^2 e^2} - \frac{\beta_\wedge^2 T}{\kappa_\perp e^2}\right) J_z - \left(\beta_\perp + \frac{\beta_\wedge \kappa_\wedge}{\kappa_\perp}\right) \frac{1}{e} \frac{\partial T}{\partial z}. \tag{2.49}$$

19

As shown by Haines [101] the function $((\alpha_\perp/n^2e^2) - (\beta_\wedge^2 T/\kappa_\perp e^2))$ is to a very good approximation independent of $(\omega\tau)$ for any Z and equal to $(\alpha_\|/n^2e^2)$ while $(\beta_\perp + \beta_\wedge\kappa_\wedge/\kappa_\perp)$ is close to $\beta_\|$. Thus equations (2.48) and (2.49) for arbitrary $(\omega\tau)$ are the same as equations (2.31) and (2.32) with the exception of the coefficient $\kappa_\perp(1 + \kappa_\wedge^2/\kappa_\perp^2)$ which is generally less than $\kappa_\|$ but only by a factor of order one. The factor $4\lambda/\alpha(\zeta - \gamma)^2$ in equation (2.40) becomes $\frac{16}{25}\gamma_0\alpha_0$ in the notation of Epperlein and Haines and when $\omega\tau \neq 0$ becomes $\frac{16}{25}\alpha_0((\kappa_\perp^{c2} + \kappa_\wedge^{c2})/\kappa_\perp^c)$. This is tabulated for $Z = 1$ in table 1 and shows that for no radiation loss ($I_{PB} = \infty$) the parameter s becomes imaginary for low $\omega\tau$ but for $\omega\tau \gtrsim 1$ becomes real, and will give similar conclusions as model 1 with Marshall's coefficients.

Table 1. The tabulated function varies from > 1 to < 1 as $w\tau$ is increased. This leads s going from imaginary to real; and the heat flow switching from almost equal heat-flow to anode and cathode to the heat flowing entirely to the anode.

$\omega\tau$	0	10^{-2}	10^{-1}	1	10	10^2	∞
$\frac{16}{25}\alpha_0\left(\dfrac{\kappa_\perp^{c2} + \kappa_\wedge^{c2}}{\kappa_\perp^c}\right)$	1.037	1.033	1.004	0.849	0.518	0.444	0.434

For the fourth model the heat is carried by the singular and guiding-centre currents of ions and electrons from the cathode to the anode, except for the singular ions which move from the anode to the cathode. The total heat flow is $5(kT/e)I$ since the singular and guiding-centre currents each constitute about half the total current. The result is the same form as equations (2.29) and (2.30) with the coefficients up to a factor of two greater because of the equal contribution of the ions.

If instead of $\underline{q}_r = 0$ we have the condition $\partial T_e/\partial r = 0$, perhaps through equipartition between electrons and ions, the latter having a higher cross-field thermal conductivity, there is a far greater dependence of the resulting transport on $\omega\tau$. However for $\omega\tau \gg 1$ the results of equations (2.28), (2.29), (2.46) and (2.47) are obtained.

In conclusion, the results of the various heat-flow models are largely insensitive, indeed even robust as to whether $\omega\tau$ is zero or infinite. Most of the heat is transferred to the anode with equations (2.46) and (2.47) being useful formulae for power balance, as considered in the next section. However the order of magnitude of the heat flow to the electrodes is $\frac{5}{2}IT_e$, and it strongly implies that even for $I \sim 10^7$ A and $T_e \sim 4$ keV a characteristic loss rate of $\sim$0.1 TW which, while small compared with the $\sim$100 TW radiation pulse of wire arrays, makes a quasi-steady state Z-pinch for fusion unlikely.

2.4. Fusion conditions if magnetically confined and stable

If we assume that the Z-pinch has to be in a stable, quasi-steady state for an energy confinement time τ_E in order to satisfy the Lawson conditions [102]

$$n\tau_E > 10^{20}\,\text{m}^{-3}\,\text{s},$$
$$T_{\max} > 10^8\,\text{K or }10\,\text{keV}, \tag{2.50}$$

τ_E can be defined as the stored energy divided by the power input

$$\tau_E = \frac{\frac{3}{2}Nk(T_e + T_i)z_0}{IV}. \tag{2.51}$$

Therefore, using $\bar{n} = N/\pi a^2$ and equations (2.7), (2.46) and (2.47) with bremsstrahlung neglected ($I_{PB} \to \infty$) [10, 45] the Lawson criterion, equation (2.50), becomes

$$n\tau_E = 1.71 \times 10^{-11} N T^{3/2}. \tag{2.52}$$

Table 2. Four cases of a Z-pinch satisfying Lawson conditions. Only one parameter is specified, e.g. the length.

z_0 (m)	A (μm)	$\bar{n}$ (cm^{-3})	τ_E (s)
10	200	4.5×10^{19}	1.1×10^{-5}
1	63	4.5×10^{20}	1.1×10^{-6}
0.1	20	4.5×10^{21}	1.1×10^{-7}
0.01	6.3	4.5×10^{22}	1.1×10^{-8}

Therefore if $n\tau_E$ and T are chosen, this determines N in equation (2.52), V in equation (2.46), I in equation (2.7) and $z_0/\pi a^2$ in equation (2.47). These are, respectively, $N = 5.6 \times 10^{18} \, \text{m}^{-1}$, $V = 6.5 \times 10^4 \, \text{V}$, $I = 0.97 \, \text{MA}$, for $n\tau_E = 10^{20} \, \text{m}^{-3} \, \text{s}$ and $T = 10^8 \, \text{K}$.

The other Z-pinch parameters are completely determined when one of them is specified, i.e. one out of τ_E, n, z_0 or a. In table 2 a set of consistent parameters for various lengths, z_0, of discharge is given.

Because of the power input IV being in the terawatt range, and at high voltage, especially during the initial resistive plasma formation stage, the constraints of the technology of pulsed power would suggest a time for energy confinement of $10^{-7} \, \text{s}$. Therefore a Z-pinch of about 10 cm in length, 20 μm in radius and about 10% of solid density is indicated as being suitable.

Regardless of the choice of these parameters, the constraints on N, V and I lead to the following fortuitous coincidences of nature:

 (i) It is known that the ratio of ion Larmor radius to pinch radius for a Z-pinch satisfying the Bennett relation depends only on $N^{-1/2}$ (as will be shown later, equation (3.11)) and for $N = 5.6 \times 10^{18} \, \text{m}^{-1}$ is 0.34. Therefore ideal MHD stability theory will not apply, and there could be a strong stabilizing effect (see section 3.8).

 (ii) The value of the current required for fusion is very close to the Pease–Braginskii current (equation (2.36)). Therefore it may be possible to compress the pinch by radiative cooling to obtain the required pinch radius and density. The possibility of obtaining radiative collapse to very high density (see section 2.8) for generator parameters of slightly higher values of current was pursued at Imperial College. But, apart from the question of stability, it is now known that radiative collapse can be prevented by the increase in ion pressure arising from the ion-viscous heating associated with nonlinear, fast growing, short wavelength MHD instabilities (see section 5.8). This phenomenon is not included to date in the numerical simulations which therefore have to be artificially constrained to prevent radiative collapse.

 (i) and (ii) are genuine coincidences of nature, the first depending on nuclear cross-sections for establishing $n\tau_E$ and T, and the second depending on Planck's constant and quantum mechanical in nature.

There are several more general results from these parameters:

(iii) The ion transit time, $z_0(m_i/kT)^{1/2}$ is $0.8\tau_E$. Therefore the particle confinement time scales almost exactly as the electron thermal conduction time. In [46] the ion transit time replaces τ_E as the confinement time in evaluating the Q for various currents. Since impurity ions generated at the electrodes will travel much more slowly than deuterons at the same energy by a factor inversely proportional to the square root of the masses, there should be no problems of impurity radiation or fuel dilution.

(iv) The electron–ion equipartition time is half the energy confinement time. In Haines [10] a self-similar model of Joule heating with unequal temperatures reveals that $(T_e - T_i)/T_i$ is only a function of line density; for the value written here T_e is only 10% higher than T_i.

(v) The mean electron drift velocity is 0.96 times the ion thermal speed. This should be too low to cause ion-acoustic turbulence, particularly since $T_e \approx T_i$, but lower hybrid drift turbulence remains a possibility in the low density corona. See section 3.13.

(vi) The time taken to heat the Z-pinch ohmically with pressure balance is three times τ_E when following the so-called Haines–Hammel curve [103, 104] (see section 2.5). If a faster $\dot{I}$ is employed the heating time could be comparable to τ_E and is accompanied by compression.

2.5. Self-similar solutions and radial heat loss

We consider next the class of Z-pinch equilibria (i.e. profiles satisfying radial pressure balance) which are time dependent, but in which we neglect any axial or azimuthal variation. All plasma parameters are functions of radius r and time t only. The earliest example that led to a self-similar solution, i.e. one for which a profile shape is maintained in time and is a function of a similarity variable (in this case radius), is when Joule heating occurs in a stationary Z-pinch. Then the current I follows the so-called Haines–Hammel curve of $I \propto t^{1/3}$ ([103, 104]; also found independently by Braginskii and Shafranov [105]).

This example assumed spatially uniform temperature (infinite thermal conductivity) and found a self-similar current density profile proportional to $I_0(\xi r/a)$ where ξ is the root of $I_0^2(\xi) = \frac{5}{2} I_1^2(\xi)$, i.e. $\xi \approx 1.656$, i.e. a weak skin effect.

More general cases have been considered by Coppins *et al* [106, 107]. The importance of self-similar solutions to nonlinear coupled partial differential equations is that they can act as attractors in more general situations. The set of nonlinear equations are equation (2.1) radial pressure balance, equation (2.2) Ampère's law, together with Ohm's law for, in general, a non-stationary pinch

$$E_z = \eta J_z - v_r B_\theta, \tag{2.53}$$

where $\eta^{-1} = \alpha T^{3/2}$ is the Spitzer resistivity, and an energy equation

$$\frac{n^\gamma}{\gamma - 1} \frac{\mathrm{d}}{\mathrm{d}t}\left(\frac{p}{n^\gamma}\right) = \eta J_z^2 - \frac{1}{r}\frac{\partial}{\partial r}(r q_r) - \beta_b n^2 T^{1/2}. \tag{2.54}$$

Self-similar behaviour is not necessarily obtainable when there are more than two terms in an equation. The energy equation can therefore be problematical, and so far the bremsstrahlung loss term has been neglected in searching for self-similar solutions. The radial heat flow can be fitted into a self-similar scheme in the limit of strong ion magnetization, $\omega_i \tau_{ii} \gg 1$. Then q_r is given by

$$q_r = -\kappa_{\perp i} \frac{\partial T}{\partial r} = -\frac{\alpha_0 n^2}{B^2 T^{1/2}} \frac{\partial T}{\partial r} \tag{2.55}$$

and each of the three remaining terms in equation (2.54) has the same time dependence.

In [106] two cases have been studied: the generalization of the stationary pinch with $I \propto t^{1/3}$, and the expanding pinch with the inertial term strictly zero, i.e.

$$\frac{\mathrm{d}v_r}{\mathrm{d}t} = \frac{\partial v_r}{\partial t} + v_r \frac{\partial v_r}{\partial r} = 0, \tag{2.56}$$

where all functions are now separable in v_r and t, with $v_r = r/t \equiv u$. In the first case there is one free parameter, designated Ω, which represents the ratio of the Ohmic heating time to the characteristic time for current or pressure change. It is found that there is a critical value of Ω, $\Omega_{crit} \approx 3.42$, at which both the number density $n(r)$ and heat flux $q(r)$ tend to zero at $r = r_0$, the pinch radius. This represents a thermally isolated pinch, and has $J_z(r)$, $n(r)$ and $T(r)$ profiles as shown in figure 8(a). For $\Omega < \Omega_{crit}$ there is a minimum in $n(r)$ which
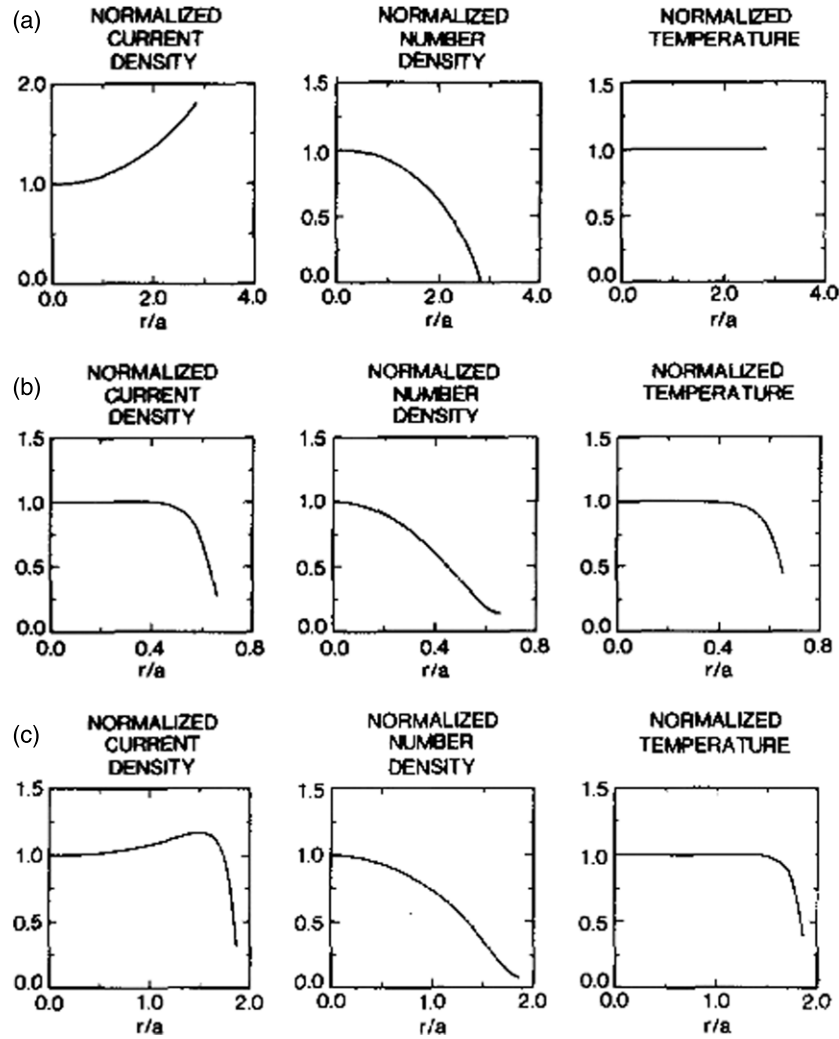
Figure 8. Radial profiles of $J_z(r)$, $n(r)$ and $T(r)$ for self-similar solutions (a) $\Omega = \Omega_{crit}$; (b) $\Omega = 0.1$; (c) $\Omega = 10$. Reprinted with permission from [106]. Copyright 1988, American Institute of Physics.

we call the plasma edge, $r = r_0$, beyond which $T(r)$ and $J_z(r)$ are very small. This we call the gas-embedded type of Z-pinch, and $q_r(r_0)$ is positive, i.e. outward. Figure 8(b) shows this case for $\Omega = 0.1$. The profiles resemble those of Falthammer [108] and Scudder [109] who earlier considered an exact energy balance for gas-embedded Z-pinches. Indeed it is interesting that Falthammer found similar scaling laws for radial heat loss as [97] found for axial heat loss, though Haines [10] later showed that the radial loss is only about 15% of the axial loss. Scudder's contribution was to include bremsstrahlung losses for $I \leqslant I_{PB}$, where at $I = I_{PB}$ the Z-pinch becomes thermally isolated. For $\Omega < \Omega_{crit}$ there is a plasma edge where $n(r_0)$ is zero, but q_r is finite and inward. This is the result of a skin current with large Joule heating at $r = r_0$. The plasma is isolated and this skin heating is transferred inwards, and is illustrated in figure 8(c) for $\Omega = 10$. When more physics is added as in section 2.6 there is an additional reason for inward heat flow. Defining the radial scale length a by field diffusion,
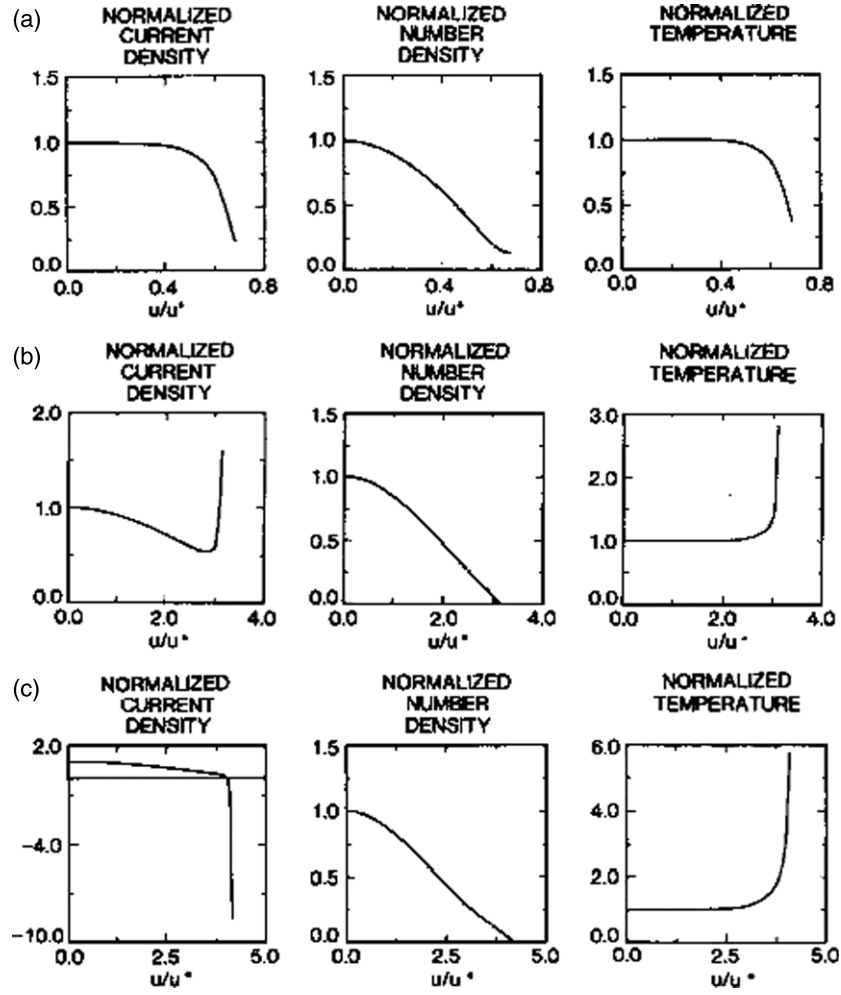
Figure 9. Profiles of J_z, n and T as a function of u for (a) $\Omega = 0.1$, (b) 1.5 and (c) 1.95. Reprinted with permission from [106]. Copyright 1988, American Institute of Physics.

i.e. $a = \sqrt{[\eta(r=0)t/\mu_0]}$, it is found that for $\Omega \gg \Omega_{\text{crit}}$, r_0/a and the ratio of skin current to the bulk current both scale as $\ln \Omega$.

For the second case of the expanding pinch with $I \propto t^{1/3}$ there is a similar occurrence of a critical value of Ω, though it has a lower value of ≈ 1.25. For $\Omega < \Omega_{\text{crit}}$ the solutions are of the gas-embedded type with $q_r > 0$ at the minimum of n at $r = r_0$, but for $\Omega > \Omega_{\text{crit}}$, the skin current case, there appears a maximum $\Omega_{\text{max}} \approx 1.96$ close to which the skin current reverses, a phenomenon known as the inverse skin effect [110]. Profiles of $J_z(u)$, $n(u)$ and $T(u)$ for $\Omega = 0.1$, 1.5 and 1.95 are shown in figure 9. For $\Omega > \Omega_{\text{max}}$ the density has no zero and the solutions are rejected because an inward heat flow is required at the plasma radius. The expanding pinch with falling current is characterized by a centrally peaked J_z and n.

In [107] self-similar profiles are found for the (early) cold pinch in which the radial heat-flow term is small compared with Joule heating. With $I \propto t^{1/3}$ stationary equilibria
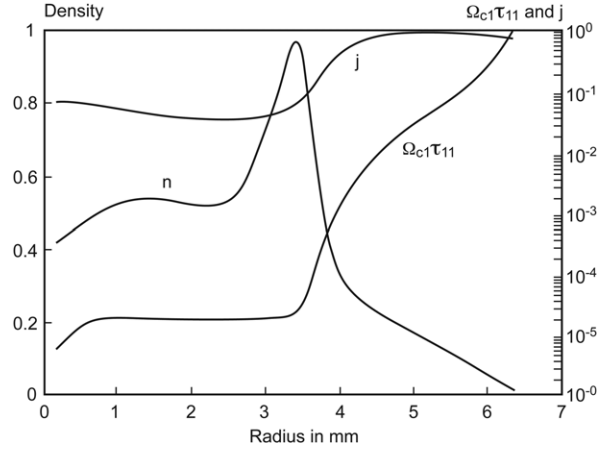
Figure 10. Evolution of the spatial profiles of n, J_z and $\Omega_i \tau_i$ in a 1D simulation [107].

are found which have $dn/dr > 0$ everywhere but centrally peaked temperature, pressure and current which scale as n^{-10}, n^{-9} and $n^{-1/2}$, respectively, leading to equilibria which are stable to $m = 0$ ideal MHD (i.e. they satisfy the Kadomtsev (1966) criterion, equation (3.21)). Such equilibria can be considered as the result of an electrothermal or thermal instability (see section 3.12).

One-dimensional time dependent simulations have been undertaken by Rosenau *et al* [111], Glasser [112] as well as Coppins [107] in order to study the onset of self-similar behaviour. Because of the two very different profiles for zero thermal conductivity compared with cross-field ion thermal conductivity (with $\omega_i \tau_i \gg 1$) there is a transition from one to the other as the spatial and temporal value of $\omega_e \tau_e$ passes through one. This can be appreciated by considering the ratio $\nabla \cdot \underline{q}/\eta J^2$ for $T_e = T_i$, i.e. forcing equal temperatures and $Z = 1$, which for a Bennett equilibrium is

$$\frac{\nabla \cdot \underline{q}}{\eta J^2} \approx 0.4 \left[\frac{(\Omega_e \tau_e)^2}{1 + \Omega_e^2 \tau_0^2} + \sqrt{\frac{m_i}{m_e}} \frac{(\Omega_i \tau_i)^2}{1 + \Omega_i^2 \tau_i^2} \right]. \tag{2.57}$$

Since for $T_e = T_i$, $\Omega_i \tau_i = \sqrt{(m_e/m_i)} \Omega_e \tau_e$ it follows paradoxically that thermal conduction can only be neglected if the condition $\Omega_e \tau_e \ll 1$ is satisfied. The transition to temperature gradient scale length being of order of the pinch radius occurs from $\Omega_e \tau_e = 1$ to $(m_e/m_i)^{1/4}$, and for higher values of $\Omega_e \tau_e$ ion thermal conduction dominates, leading to most of the pinch having a uniform temperature. $\Omega_e \tau_e$ and $\Omega_i \tau_i$ both scale as $I^4 a/N^{5/2}$ (see section 3.1, equations (3.2), (3.13)). Figure 10 illustrates the spatial evolution of profiles of n, J_z and $\Omega_i \tau_i$ in a 1D simulation, the inner region tending to a zero heat-flow self-similar solution while the outer tends towards the strong thermal conduction self-similar profile.

The condition of equal electron and ion temperature can be relaxed in the case of $\Omega_e \tau_e \gg 1$, i.e. when the temperature profiles are flat. Then, for $Z = 1$ and $I \propto t^{1/3}$ Haines [10] found

$$\frac{T_e}{T_i} = 1 + \frac{2\pi m_i}{\mu_0 N e^2} = 1 + \frac{4}{\pi} \frac{a_i^2}{a^2}, \tag{2.58}$$

where a_i/a is the ratio of mean ion Larmor radius to pinch radius. For $a_i/a < 0.3$ it is a good approximation in Joule heated pinches in pressure equilibrium to put $T_e = T_i$.
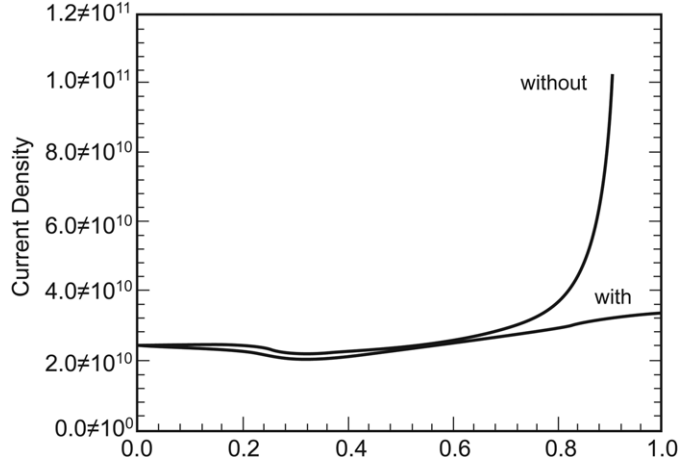
Figure 11. Inclusion of Ettingshausen and Nernst effects (simulations show that the self-similar solution acts as an attractor) in a 1D time-dependent simulation [113, figure 4].

2.6. Nernst and Ettingshausen effects

In the previous section we ignored two cross-phenomena that arise from the velocity dependence of the collision frequency ($\nu \propto v^{-3}$). The radial component of the electron heat flux q_{er} and the axial component of Ohm's law in a 1D model are

$$q_{er} = -\kappa_{\perp e} \frac{\partial T_e}{\partial r} - \frac{T_e}{e} \beta_\wedge J_z, \tag{2.59}$$

$$E_z + v_r B_\theta = \eta_\perp J_z + \frac{\beta_\wedge}{e} \frac{\partial T_e}{\partial r}, \tag{2.60}$$

where in Braginskii's notation [98] $\eta_\perp$ is $\alpha_\perp/(ne)^2$. The Ettingshausen effect in equation (2.59) is an additional heat flux in the direction of $\underline{J} \times \underline{B}$ while the Nernst term in equation (2.60) describes the convection of the magnetic field by the hotter electrons associated with the heat flux, having a common coefficient $\beta_\wedge$ through Onsager's relations. In the limit of $\Omega_e \tau_{ei} \gg 1$ the ratio of the Ettingshausen term to the thermal conduction term is $0.32 J_z B_\theta / n_e \partial T / \partial r$ while the ratio of the Nernst term to $\eta_\perp J$ is half the inverse of this. Therefore at least one of these two effects will always be important. From [101] we note that equations (2.59) and (2.60) can be combined to give

$$E_z + v_r B_\theta + \frac{q_{er} B_\theta}{\frac{5}{2} n_e T_e} \approx \eta_\perp \left(1 - \frac{\beta_\wedge^2 T}{e^2 \kappa_{\perp e} \eta_\perp} \right) J_z \approx \eta_\parallel J_z, \tag{2.61}$$

where for $Z = 1$, the parallel resistivity is 0.506 times the perpendicular resistivity. This clearly shows the advection of magnetic field by the heat flow with a velocity approximately $q_{er}/(5/2n_e T_e)$. The physical meaning of the Ettingshausen effect can best be envisaged as an inward E_z/B_θ radial guiding-centre drift of the hotter, relatively collisionless electrons in the applied axial electric field.

Chittenden and Haines [113] included these two terms in a 1D time-dependent two temperature simulation. The main effect, shown in figures 11(a) and (b), is to remove the sharp electron temperature rise and the associated skin current from the plasma edge, and to cause a slight peaking of the electron temperature at $r = 0$, i.e. an inward heat-flow occurs.
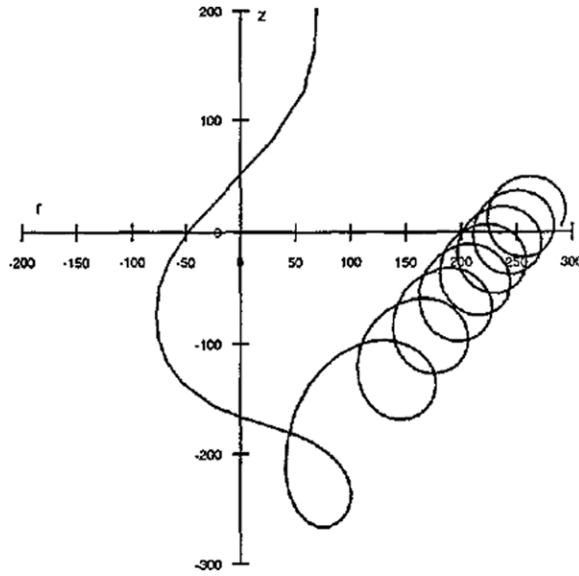
Figure 12. Trajectory of an electron with zero angular momentum as it drifts towards the axis in the presence of an axial component of electric field [113, figure 12].

2.7. Runaway electrons

Because the electron–ion collision frequency ν is inversely proportional to the cube of the electron velocity, there are, in the absence of magnetic fields, always electrons in the high energy tail of the distribution function which will gain more energy in an applied electric field than will be lost in one collision time. Dreicer [114] defined a critical electric field at which the bulk of the electrons will 'run away'. This is given by

$$E_{\mathrm{c}}(V\,m^{-1}) = \nu\frac{m_{\mathrm{e}}}{e}\sqrt{\frac{eT_{\mathrm{e}}}{m_{\mathrm{e}}}} = 6.5 \times 10^{-18} Z \ln \Lambda \cdot \frac{n_{\mathrm{e}}(\mathrm{m}^{-3})}{T_{\mathrm{e}}(\mathrm{eV})}, \qquad (2.62)$$

i.e. when the acquired drift velocity is the thermal speed. But even with an electric field, 1% of E_{c}, the tail of the distribution function will run away.

It is clear from section 2.2 that the off-axis electrons are magnetized and are not able to run away in an applied axial electric field. Only those electrons within one electron Larmor radius of the axis where $B_\theta = 0$ are free to run away, i.e. from equation (2.22), those at a distance $R_{\mathrm{e}} < \sqrt{(2\nu_{\perp\mathrm{e}}m_{\mathrm{e}}/\mu_0 e J_z)}$. However, we have just shown in the previous section that the hotter electrons, especially the high energy tail, have a preferential inward drift towards the axis. This is illustrated in figure 12 for the trajectory of an electron with zero angular momentum as it drifts towards the axis and becomes a singular (and runaway) electron. This filter for hot electrons will be more marked in the case of a hollow dynamic pinch, e.g. of a gas puff or wire array, and runaway electrons are likely to occur on the inside surface of such a plasma. In contrast, a solid fibre Z-pinch will tend to have such a high density on axis that collisions will dominate, preventing most electrons from running away. Electron beam formation on axis has been observed experimentally [115] in a plasma focus as well as a gas-puff Z-pinch [53]. Runaway electrons will particularly be generated at an $m = 0$ disruption (section 3.14).

2.8. The Pease–Braginskii current and radiative collapse

Over forty years ago Pease [8] and Braginskii [9] independently predicted that a pure Z-pinch pressure equilibrium would have a unique critical current I_{PB} when the Joule heating balances bremsstrahlung radiation loss. For a hydrogen plasma and for a parabolic density profile and uniform current I_{PB} is $0.433 \, (\ln \Lambda)^{1/2}$ MA. How this arises can easily be shown from simple arguments. The bremsstrahlung loss rate per unit volume is $\beta_b Z n_e^2 T^{1/2}$ where β_b is a constant equal to 1.69×10^{-38} W m^3 (eV)$^{-1/2}$. The Joule heating per unit volume is $\eta_\perp J^2$ where the cross-field or transverse Spitzer resistivity $\eta_\perp$ is $1.03 \times 10^{-4} Z \ln \Lambda \, T^{-3/2} = (\alpha T^{3/2})^{-1}$ Ω m. On balancing the Joule heating against the radiation loss

$$\eta_\perp J^2 \cong \beta_b Z n_e^2 T^{1/2} \tag{2.63}$$

the temperature dependences of the two phenomena combine to give $J \propto p = n_i k_B T (1 + Z)$. However, pressure balance for a volume distributed current is approximately $J B \cong p/a$ where a is the pinch radius. Therefore it follows that Ba is approximately constant. Ba is just $\mu_o I/2\pi$ and here demonstrates that there is a unique critical current. For a parabolic density profile associated with uniform current density and temperature and one or several ion species the critical current is

$$I_{PB} = \frac{8\sqrt{3} k_B}{\mu_0 \sqrt{\alpha \beta_b}} \frac{1+Z}{2Z} = 0.433 (\ln \Lambda)^{1/2} \left(\frac{1 + \langle Z \rangle}{2 \langle Z^2 \rangle^{1/2}} \right) \text{MA}. \tag{2.64}$$

This is a generalization of equation (2.36) for arbitrary Z showing that for pure bremsstrahlung (no line radiation or opacity effects) the maximum effect of $Z > 1$ in a single species plasma is to halve the Pease–Braginskii current. However, for an optimum doping of a $Z = 1$ plasma with a fraction $2Z/(Z^2 - 1)$ of $Z \geqslant 3$ ions the factor $(1 + \langle Z \rangle)/2\langle Z^2 \rangle^{1/2}$ is $\sqrt{(2Z + 1)^{1/2}/(Z + 1)}$ and can be much less than 0.5.

Pease pointed out that such a current should depend only on fundamental constants, and $I_A F(\alpha_{fs})$ where I_A is the Alfvén–Lawson current (see section 2.2) given in terms of r_e, the classical radius of the electron defined by

$$r_e = \frac{e^2}{4\pi \varepsilon_0 m c^2} \tag{2.65}$$

such that

$$I_A = \frac{ec}{r_e}. \tag{2.66}$$

The fine structure constant is given by

$$\alpha_{fs} = \frac{e^2}{4\pi \varepsilon_0 \hbar c} \cong \frac{1}{137} \tag{2.67}$$

and $F(\alpha_{fs})$ is proportional to $\alpha_{fs}^{-1/2}$. Pereira [116] developed these ideas further showing the relationship of the analysis to fundamental atomic parameters and $\ln \Lambda$. The Alfvén–Lawson current (see equation (2.36)) is related to the maximum electron current that can propagate as a beam in a stationary ion background, i.e. all electrons originate from 'the cathode' and no return electron flow or even E_r/B_θ electron guiding-centre flow are allowed. This current is entirely a singular electron current (equation (2.19)) where now $P_{\perp e}$ is $n_e m_e v_e^2$ and J_z is $n_e e v_e$. Thus, for relativistic electrons where $m = \gamma m_e$, $\gamma = (1 - \beta^2)^{-1/2}$ and $\beta = v_e/c$ the current is $I_A = 17\,000 \gamma \beta$ A. It could be, but has not yet been proven, that this is the maximum runaway electron current that can occur in a disruption (see section 3.14).

The first calculation of radiation collapse assumed constant current and temperature [117]. With the current fixed above the Pease–Braginskii value indefinite collapse would occur until
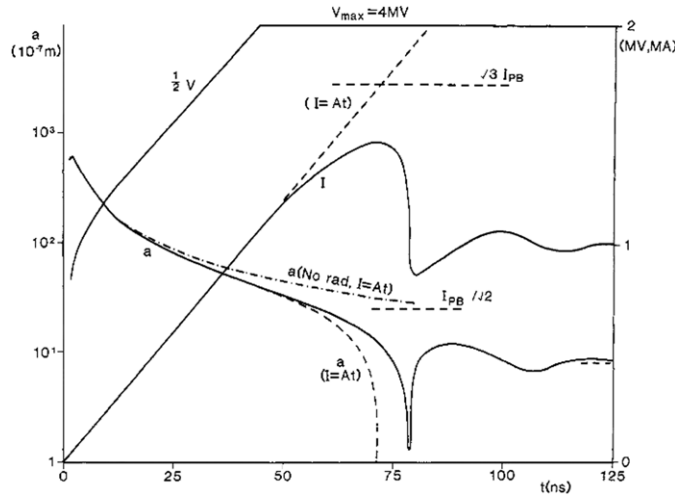
Figure 13. Analytic zero-dimensional model showing that radiative collapse is transient. The pinch radius $a(t)$ and current $I(t)$ are plotted [122, figure 1].

some additional physics such as electron degeneracy or opacity. Vikhrev [118] in a zero-dimensional model of a dynamic pinch with an external circuit, anomalous resistivity, viscous heating, transition of bremsstrahlung to black-body radiation and degenerate electron pressure modelled the collapse of deuterium with 1% xenon added to enhance radiation loss. Initial currents of 1 or 10 MA were used, the latter leading to a radiative collapse despite the inclusion of axial outflow of plasma. This was extended by Vikhrev and Gureev [119] for an initial current of 100 MA in an MHD model with axial outflow, leading to a loss of plasma from the constriction at a degenerate density of 10^{33} m^{-3} when the current is 78 MA. The inclusion of anomalous resistivity by Vikhrev *et al* [120] led to the expansion of the coronal plasma.

With the quasi-static evolution of a Z-pinch from an initially cryogenic fibre in mind Robson [121] and Haines [122] developed semi-analytic 0D models of a radiative collapse. Robson and Haines both found that a collapse to infinite density would occur at a current of $\sqrt{3}I_{\mathrm{PB}}$. This arises from a solution of the energy equation giving $a(t)$ for a given $I(t)$ in the form

$$I^3 a^2 = B \int (1 - I^2/I_{\mathrm{PB}}^2) \, \mathrm{d}t, \tag{2.68}$$

where the constant B is

$$B = \frac{8}{3\mu_0 \alpha_\perp} \left(\frac{16\pi N k_{\mathrm{B}}}{\mu_0} \right)^{3/2}. \tag{2.69}$$

By including the circuit of a pulse-forming line Haines showed that a finite collapse to $10^4 \times$ solid density could transiently occur. It is interesting to see how the large voltage (perhaps 100 MV) needed to drive a mega-ampère through a very narrow collapsed Z-pinch is provided by a large value of $L \, \mathrm{d}I/\mathrm{d}t$ as is shown in figure 13. By including the variation of $\ln \Lambda$, Chittenden *et al* [123] showed that the collapse was not limited by the dissipation and fall of the current flow below I_{PB} because I_{PB} itself also fell. Robson [124] showed that the lower initial value for I_{PB} for $Z = 2$ fully ionized helium led to a weaker collapse since the stored magnetic energy at the time of collapse was smaller. In Robson [125] a 0D model in which anomalous resistivity was introduced in the outer corona gave an enhanced value of I_{PB} while
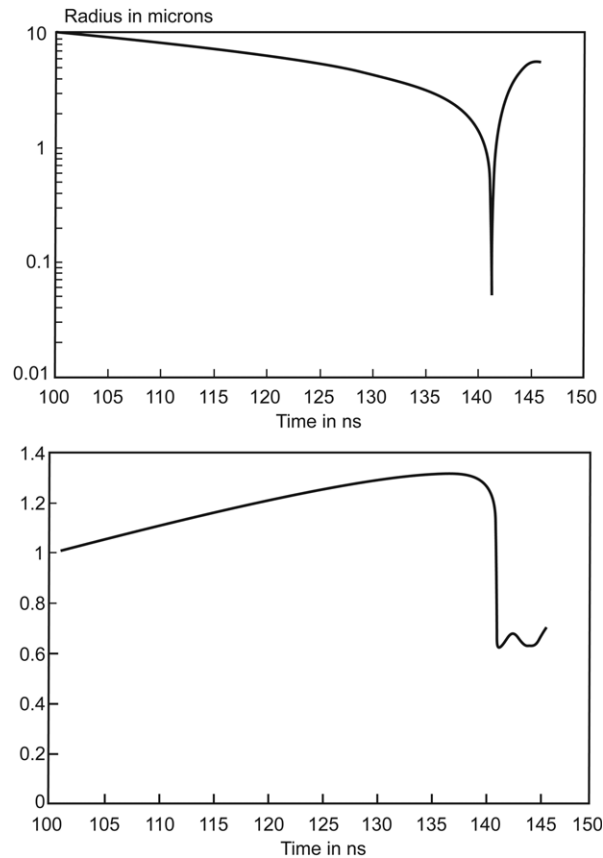
29

Figure 14. Radius of the pinch and current as a function of time. Reprinted with permission from [129, figure 6]. Copyright 1990, American Institute of Physics.

end losses [97] led to a smaller current in energy balance (section 2.3). Thornhill *et al* [126] in another 0D model included degeneracy pressure of the electrons bremsstrahlung and opacity effects, but maintained a Spitzer resistivity.

Meirovich [127] in a broad ranging paper, applied also to astrophysical situations, considered radiative collapse to an electron degenerate state. In this and his later paper [128] he postulated a relative drift velocity much greater than the thermal speed. As can be shown a relativistic beam leads to a breakdown of quasi-neutrality, but it is likely to lead also to micro-instabilities and anomalous resistivity.

In a full 1D time-dependent resistive MHD simulation Chittenden and Haines [129] employed a realistic external circuit, a radiation transport package including opacity, magnetized electron transport and equation of state. The limit of radiative collapse was found to be the onset of opacity effects and degeneracy pressure. In figure 14, the pinch radius and current are shown as a function of time, while figure 15 shows the radiative power and density. It is interesting to note that at the peak density of $10^5 \times$ solid the high plasma frequency prevents even propagation of x-rays of wavelengths longer than 10 Å from the central core.

However recent work on nonlinear growth of $m = 0$ instabilities, to be discussed in section 5.8, indicates that the conversion of magnetic energy to ion thermal energy and pressure through viscous dissipation will prevent radiative collapse altogether [130]. Furthermore the
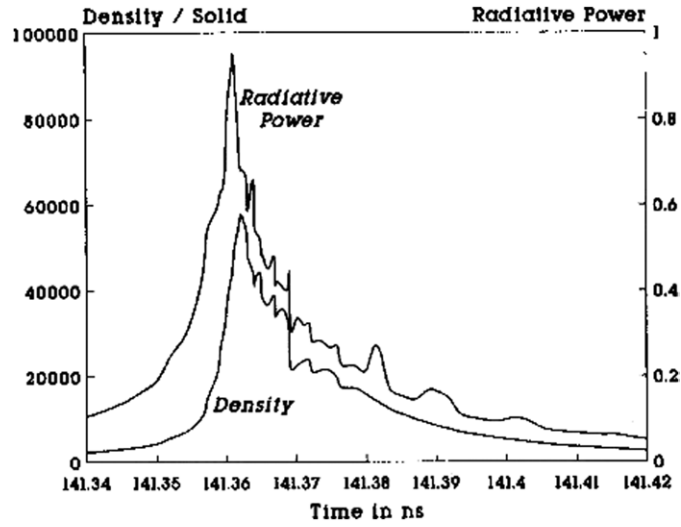
Figure 15. Radiated power and density as a function of time in a 1D simulation of radiative collapse of a hydrogen Z-pinch. Reprinted with permission from [129, figure 7]. Copyright 1990, American Institute of Physics.

characteristic time for radiation loss usually exceeds the growth times for MHD instabilities and these cannot be ignored.

3. Stability of an equilibrium Z-pinch

3.1. Regimes for stability models

Many of the earliest Z-pinch experiments, e.g. Kurchatov [32], Carruthers and Davenport [36], showed violent MHD instabilities. The theoretical models available at that time, e.g. Kruskal and Schwarzchild [37], Tayler [38], were analytic and based on ideal magnetohydrodynamics (MHD), and showed that both sausage ($m = 0$) and kink ($m = 1$) modes could be present. Whilst many researchers then added axial magnetic fields or, in toroidal discharges, a toroidal magnetic field component in order to find a more stable equilibrium, the price that is paid for this is that one is then limited to low density ($n < 10^{16} \, \mathrm{cm}^{-3}$) discharges and, for fusion also, large volume devices, because of the practical upper limit of magnetic field that can be produced by coils. Further exploration of the Z-pinch in which magnetic fields in the megagauss range can be produced, indicated that some enhancement of stability could be possible due to finite ion Larmor radius effects, e.g. Bayley *et al*, [131] Struve [132], Davies *et al* [14], or finite resistivity, e.g. Culverwell *et al* [133], Cochran and Robson [134]: or sheared axial flow, e.g. Arber and Howell [57], Shumlak and Hartman [135].

Haines and Coppins [136] have identified the regimes when resistivity, finite ion Larmor radius effects and other physics omitted in ideal MHD are important. By identifying the corresponding dimensionless parameters a universal diagram in $I^4 a - N$ space has been found which allows all equilibrium Z-pinches to be categorized according to which physical model applies.

Turning first to the introduction of resistivity, Faraday's law becomes

$$\frac{\partial \underline{B}}{\partial t} = \nabla \times \left[\underline{v} \times \underline{B} - \frac{\eta}{\mu_\mathrm{o}} \nabla \times \underline{B} \right]. \tag{3.1}$$

The ratio of the convective to diffusive terms in the bracket of equation (3.1) gives the dimensionless magnetic Reynolds' number $R_m = \mu_0 \sigma v L$; where $\sigma (= \eta^{-1})$ is the electrical conductivity, $\underline{v}$ is the plasma flow velocity and L is the characteristic length over which the magnetic field varies ([137]). When L is replaced by the wavelength of an Alfvén wave and $\underline{v}$ by the Alfvén speed it becomes the Lundqvist [138] number S relevant to the damping of the Alfvén waves. For the Z-pinch we define $\overline{v_A}$ as the mean Alfvén speed,

$$\overline{v_A} = \frac{B_\theta(r=a)}{2(\mu_0\overline{\rho})^{1/2}}, \tag{3.2}$$

where a is the effective plasma radius and $\overline{\rho} = N_i m_i / \pi a^2$ the mean density. σ is taken from Spitzer and Härm [139] in the plane perpendicular to the magnetic field

$$\sigma = \frac{3}{4} \frac{(4\pi\varepsilon_0)^2 (k_B T_e)^{3/2}}{(2\pi m_e)^{1/2} e^2 Z \ln \Lambda} = \frac{9.7 \times 10^3 T_e^{3/2}(\text{eV})}{\alpha^c Z \ln \Lambda_{ei}}, \tag{3.3}$$

where $\alpha^c(Z)$ is given by Epperlein and Haines [100]. For a dense Z-pinch, $\ln \Lambda$ can be quite low, and when a numerical value is needed in this section, a value of 5.36 is chosen [136]. Using the Bennett relation (equation (2.7)) $B_\theta(r=a) = \mu_0 I / 2\pi a$, and assuming that $T_e = T_i$ (see equation (2.52)), S can be expressed as

$$S = \frac{3\mu_0\varepsilon_0^2}{64\sqrt{2\pi} m_e^{1/2} e^2 \ln \Lambda} \frac{2^{3/4}}{Z(1+Z)^{3/2}} \frac{I^4 a}{N^2} \rightarrow 3.86 \times 10^{23} \frac{I^4 a}{N^2} \tag{3.4}$$

for $m_i = m_D$, $Z = 1$. More generally S can be written as

$$S = \frac{8.215 \times 10^{24} I^4 a}{Z(Z + T_i/T_e)^{3/2} A^{1/2} N_i^2 \ln \Lambda_{ei}}. \tag{3.5}$$

The case of $S = 100$, $Z = 1$ is shown in figure 16 in a logarithmic plot of $I^4 a$ versus N, this being the value below which significant resistive effects occur.

The viscous damping of Alfvén waves depends on a Reynolds number R in which the fluid velocity is replaced by the Alfvén speed,

$$R = \frac{\overline{\rho} v_A a}{\mu_\parallel}, \tag{3.6}$$

where the parallel ion viscosity is $n_i k_B T_i \tau_i$ and τ_i the ion–ion collision time is given by

$$\tau_i = \frac{3}{4} \left(\frac{m_i}{2\pi}\right)^{1/2} \frac{(k_B T_i)^{3/2}(4\pi\varepsilon_0)^2}{n_i Z^2 e^4 \ln \Lambda_{ii}}. \tag{3.7}$$

For values of Z greater than 5 and for $T_e = T_i$ the electron viscosity, which is $p_e \tau_{ei}$ [98], or rather $p_e/(\tau_{ei}^{-1} + \tau_{ee}^{-1})^{-1}$, will exceed the ion viscosity, and in general the sum of the two viscous coefficients should be used. Indeed the ratio of the parallel viscosities is

$$\frac{\mu_{\parallel e}}{\mu_{\parallel i}} = \frac{R_{\parallel i}}{R_{\parallel e}} = 0.0233 \frac{T_e^{5/2}}{T_i^{5/2}} \frac{Z^3}{A^{1/2}} \frac{\ln \Lambda_{ii}}{\ln \Lambda_{ei} + Z^{-1} \ln \Lambda_{ee}}. \tag{3.8}$$

Then, in terms of I, a and N, and for $T_e = T_i$, R $(= (1/R_{\parallel i} + 1/R_{\parallel e})^{-1}$ is given by

$$R = \frac{16}{3\sqrt{\pi}} \frac{e^4 \ln \Lambda}{\varepsilon_0^2 \mu_0^2} \frac{Z^4(1+Z)^{5/2}}{1 + (m_e/m_i)^{1/2} Z^4} \frac{N^3}{I^4 a}. \tag{3.9}$$

Like the form of S, R depends only on $I^4 a$ and N.

Related to this the condition that the perturbed ion pressure should remain isotropic during the growth of an MHD instability is given by $\gamma \tau_i < 1$ where $\gamma = \overline{v_A}/a$ is the characteristic growth rate for an ideal MHD instability. Using equation (2.7) $\gamma \tau_i$ becomes

$$\gamma \tau_i = \frac{3\sqrt{\pi}}{64\sqrt{2}} \frac{\varepsilon_0^2 \mu_0^2}{e^4 \ln \Lambda} \cdot \frac{2^{3/2}}{Z^4(1+Z)^{3/2}} \frac{I^4 a}{N^3} \Rightarrow 2.07 \times 10^{39} \frac{I^4 a}{N^3} = \frac{1}{R} \qquad \text{for } Z = 1 \tag{3.10}$$
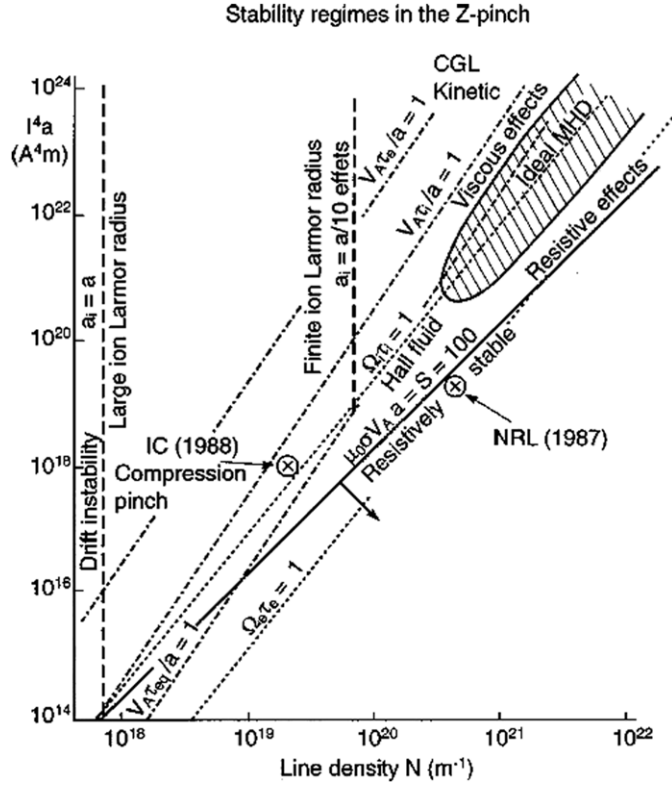
Stability regimes in the Z-pinch

Figure 16. Stability regimes shown in a plot of $I^4 a$ versus line density N for deuterium–tritium mixture [349, figure 4] or [136, figure 1]. Reprinted with permission from [136]. Copyright 1991 by the American Physical Society.

or more generally

$$\gamma \tau_{\mathrm{i}} = \frac{3.13 \times 10^{40} I^4 a}{Z^4 (1 + Z T_{\mathrm{e}}/T_{\mathrm{i}})^{3/2} N_{\mathrm{i}}^3 \ln \Lambda_{\mathrm{ii}}}. \tag{3.11}$$

The critical value $\gamma \tau_{\mathrm{i}} = 1$ for $Z = 1$ is shown in figure 16. Above this line a more appropriate model for anisotropic pressure in a collisionless magnetized plasma has been developed by Chew, Goldberger and Low (CGL) [140], but close to this line viscous effects will dominate.

The corresponding condition

$$\gamma \tau_{\mathrm{e}} = \gamma \tau_{\mathrm{i}} (m_{\mathrm{i}}/m_{\mathrm{e}})^{1/2} Z^3 \tag{3.12}$$

for electron pressure anisotropy is usually not so important, and if it were to occur would isotropize by the Weibel velocity-space electromagnetic instability [141].

We can similarly compare the electron–ion equipartition time τ_{eq} with the MHD growth time to give

$$\gamma \tau_{\mathrm{eq}} = \gamma \tau_{\mathrm{i}} (m_{\mathrm{i}}/m_{\mathrm{e}})^{1/2} Z^2, \tag{3.13}$$

which turns out to be relevant at the time of stagnation of aluminium wire-array pinches. The line $\gamma \tau_{\mathrm{eq}} = 1$ for $Z = 1$ is drawn in figure 16. Freidberg [142] imposes the stricter condition $\gamma \tau_{\mathrm{eq}} < 1$ for the applicability of ideal MHD theory. Generally, for $T_{\mathrm{e}} \neq T_{\mathrm{i}}$ it becomes

$$\gamma \tau_{\mathrm{eq}} = \frac{6.69 \times 10^{41} A^{1/2} I^4 a}{Z^2 (Z + T_{\mathrm{i}}/T_{\mathrm{e}})^{3/2} N_{\mathrm{i}}^3 \ln \Lambda_{\mathrm{ei}}}. \tag{3.14}$$

Under pressure balance the ratio of ion Larmor radius a_i to pinch radius, a, is

$$\frac{a_i}{a} = \left(\frac{2k_B T_i}{m_i}\right)^{1/2} \frac{m_i}{Ze\overline{B}_\theta a} = \left(\frac{2\pi m_i}{\mu_o e^2 N}\right)^{1/2} \frac{2^{1/2}}{Z(1+Z)^{1/2}} \to 8.08 \times 10^8 N^{-1/2} \qquad \text{for } D^+$$

(3.15)

and depends only on ion line density. The lines $a_i/a = 0.1$ (finite ion Larmor radius or FLR) and $a_i/a = 1$ (large ion radius or LLR) are shown in figure 16. However, FLR effects only apply if the ions are magnetized, i.e. $\overline{\Omega}_i \tau_i > 1$ where $\overline{\Omega}_i$ is the mean ion cyclotron frequency. In terms of I, a and N under pressure balance, $\overline{\Omega}_i \tau_i$ is given in terms of $I^4 a$ and N by

$$\overline{\Omega}_i \tau_i = \frac{3}{64\sqrt{2}} \frac{\varepsilon_o^2 \mu_o^{5/2}}{m_i^{1/2} e^3 \ln \Lambda_{ii}} \frac{2^{1/2}}{Z^3 (1 + ZT_e/T_i)^{3/2}} \frac{I^4 a}{N^{5/2}} \to 3.64 \times 10^{30} \frac{I^4 a}{N^{5/2}} \qquad \text{for } D^+$$

(3.16)

$\overline{\Omega}_i \tau_i = 1$ is plotted in figure 16, and it is interesting that it passes through the wedge-shaped region in which ideal MHD is applicable, indicating that, strictly, anisotropic viscosity should be employed in the $R = 1$–10 range. For completeness the $\overline{\Omega}_e \tau_e = 1$ line, with

$$\overline{\Omega}_e \tau_e = (m_i/m_e)^{1/2} Z^2 \overline{\Omega}_i \tau_i$$

(3.17)

is plotted in figure 16, showing that magnetized electron transport is important for all but very resistive plasmas.

We have thus constructed a universal diagram in $I^4 a$–N space, which determines the appropriate theoretical model for an equilibrium Z-pinch. We now consider theory and experiments in the various regimes.

3.2. Ideal MHD stability

The linear stability problem in ideal MHD has been shown by Bernstein *et al* [143] to be reduced to the eigenvalue equation

$$-\rho_o \omega^2 \underline{\xi} = \underline{F}(\underline{\xi}),$$

(3.18)

where ρ_o is the equilibrium mass density, the eigenfunction $\underline{\xi}$ is the displacement of the fluid plasma from its equilibrium position, ω^2 is the eigenvalue for a time dependence of $\underline{\xi}$ on $e^{-i\omega t}$ and the perturbed force density $\underline{F}$ is in general

$$\underline{F}(\underline{\xi}) = \nabla(\Gamma p_o \nabla \cdot \underline{\xi} + \underline{\xi} \cdot \nabla p_o) + \frac{1}{\mu_o}[(\nabla \times \underline{B}_o) \times \nabla \times (\underline{\xi} \times B_o)]$$

$$+ \frac{1}{\mu_o}[\nabla \times \nabla \times (\underline{\xi} \times \underline{B}_o)] \times B_o,$$

(3.19)

where p_o and $\underline{B}_o(r)$ are the equilibrium pressure and magnetic field, respectively, and Γ is the principal ratio of the specific heats. The operator $\underline{F}$ has been shown for general boundary conditions to be self-adjoint [83, 143, 144] and thus the eigenvalues ω^2 are real, positive values corresponding to stable oscillations and negative values to growing instabilities.

For an infinitely long cylinder equation (3.19) can be reduced to a second order ordinary differential equation [145] of the Stürm–Liouville form

$$\frac{d}{dr}\left[f(r)\frac{d}{dr}(r\xi_r)\right] - g(r)r\xi_r = 0,$$

(3.20)

where Fourier harmonics in the θ- and z-direction are considered for $\underline{\xi}$ of the form

$$\underline{\xi}(\underline{r}, t) = \underline{\xi}(r)e^{i(m\theta + kz - \omega t)}$$

(3.21)

and f and g can be found, for example, in Kanellopoulos *et al* [146]. Equation (3.20) can be rewritten as a pair of coupled first order ordinary differential equations [147, 148] for $r\xi_r$ and p^*, the total perturbed pressure,

$$p^* = p_1 + \frac{\underline{B}_o \cdot \underline{B}_1}{\mu_o}, \tag{3.22}$$

which is in a suitable form for employing a shooting code [149]. The boundary conditions that apply are $(r\xi_r)_{r=o} = 0$ and, for a plasma cylinder of radius a centred inside a perfectly conducting wall of radius r_w, $\underline{B}_1$ and p^* are continuous at $r = a$ and B_{1r} is zero at $r = r_w$.

Unlike a diffuse pinch or a tokamak the pure Z-pinch, i.e. with no equilibrium z component of magnetic field, has no mode rational surfaces, which would lead to regular singular points for equation (3.20) at zeros of f. When f is zero it is zero for all r, and this corresponds to the $m = 0$ mode which is a purely interchange mode. As a result we can employ the relatively simple theory for the $m = 0$ mode to find the equilibrium that gives marginal stability by postulating that there is no net change in energy when plasma on one hoop-like flux tube of volume V_1 is exchanged with that on a neighbouring tube of volume V_2 and carrying the same magnetic flux, $B_1 A_1 = B_2 A_2 = \Phi$ through their respective cross-sectional areas A_1 and A_2. There will be no change in magnetic energy with such an interchange, while the plasma interchange will obey an adiabatic law $pV^\Gamma = $ constant. On interchange the increase in internal energy is

$$\frac{1}{\Gamma - 1} \left\lfloor p_1 \frac{V_1^\Gamma}{V_2^\Gamma} V_2 - p_1 V_1 + p_2 \frac{V_2^\Gamma}{V_1^\Gamma} V_1 - p_2 V_2 \right\rfloor.$$

For $V_2 = V_1 + \delta V$ and $p_2 = p_1 + \delta p$, $\delta V \ll V_1$, $\delta p \ll p$ this becomes to second order

$$\delta p \delta V + \Gamma \frac{p_1}{V_1} (\delta V)^2$$

On equating this to zero and writing $\delta p = \delta r \, dp/dr$ and $V = 2\pi r \delta \phi / B_\theta$ we obtain the local condition for zero internal energy change

$$\frac{dp}{dr} = \Gamma p \frac{B_\theta}{r} \frac{d}{dr} \left(\frac{r}{B_\theta} \right), \tag{3.23}$$

which together with the pressure balance, equations (2.1) and (2.2), gives

$$\frac{dp}{dr} = -\frac{B_\theta}{\mu_o r} \frac{\partial}{\partial r} (r B_\theta), \tag{3.24}$$

which leads to the Kadomtsev's marginal stability condition [83]

$$-\frac{r}{p} \frac{dp}{dr} = \frac{2\Gamma}{1 + \frac{1}{2} \Gamma \beta}, \tag{3.25}$$

where $\beta(r)$ is $2\mu_o p / B_\theta^2$. To find the pressure profile we integrate equation (3.23) to give $p/p_0 = Z^\Gamma$ where

$$Z(r) = \frac{B_\theta(r)}{r} \left(\frac{r}{B_\theta} \right)_{r=0}. \tag{3.26}$$

Defining a scale length $r_o = [\mu_o \Gamma p_o / (\Gamma - 1)]^{1/2} (r/B_\theta)_{r=0}$ and $x = r/r_o$, equation (3.24) can be integrated to give

$$1 - Z^{\Gamma - 1} = x^2 Z. \tag{3.27}$$

This gives the Kadomtsev profile for $p(r)$, which is characterized by a centrally peaked current density as well as pressure, and which must extend as far as the conducting wall, i.e. no vacuum region. It is plotted in figure 17.
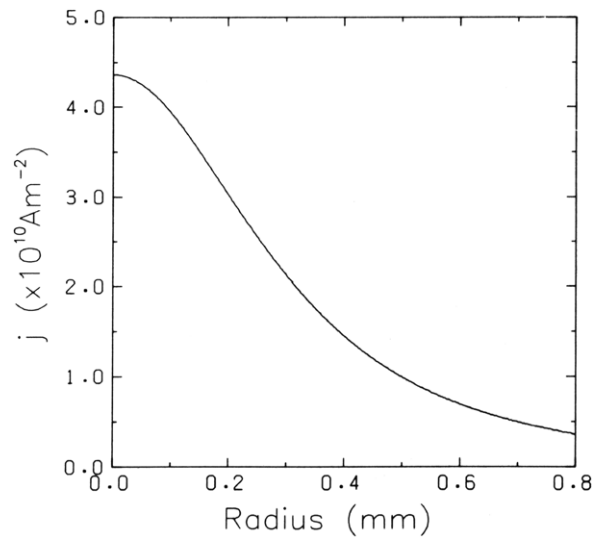
Figure 17. The Kadomtsev pressure profile which is marginally stable to the $m = 0$ sausage instability [149, figure 1].
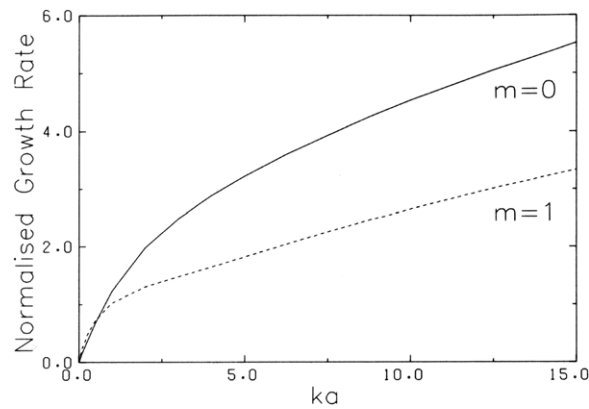

Figure 18. Growth rate γ versus ka for the $m = 0$ and $m = 1$ modes for a flat current profile [149, figure 2].

It follows that a pinch with uniform current density is unstable to both $m = 0$ and $m = 1$. Tayler [38] showed that it is however stable for $m \geqslant 2$.

The early theory of Kruskal and Schwarzchild [37] of $m = 1$ instability for a skin current equilibrium was generalized by Tayler for all m showing that it was unstable to $m = 0$ and $m = 1$ for all values of ka but for $m \geqslant 2$ there is a value of ka below which it is stable.

For the case where the current density varied as r^n, Tayler showed that a sufficient condition for stability is

$$m^2 \geqslant 2n + 4. \tag{3.28}$$

With the advent of computers a more detailed study of stability could be undertaken, and Coppins [149] has computed the growth rates and eigenfunctions for the flat current profile and for the Kadomtsev profile. Figure 18 shows the growth rate versus ka for the $m = 0$ and
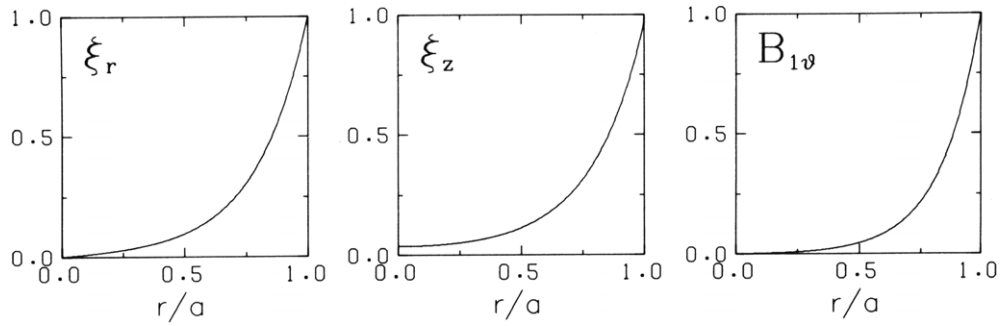
Figure 19. Eigenfunctions for the $m = 0$ mode and a flat current profile for $ka = 4$ [149, figure 3].
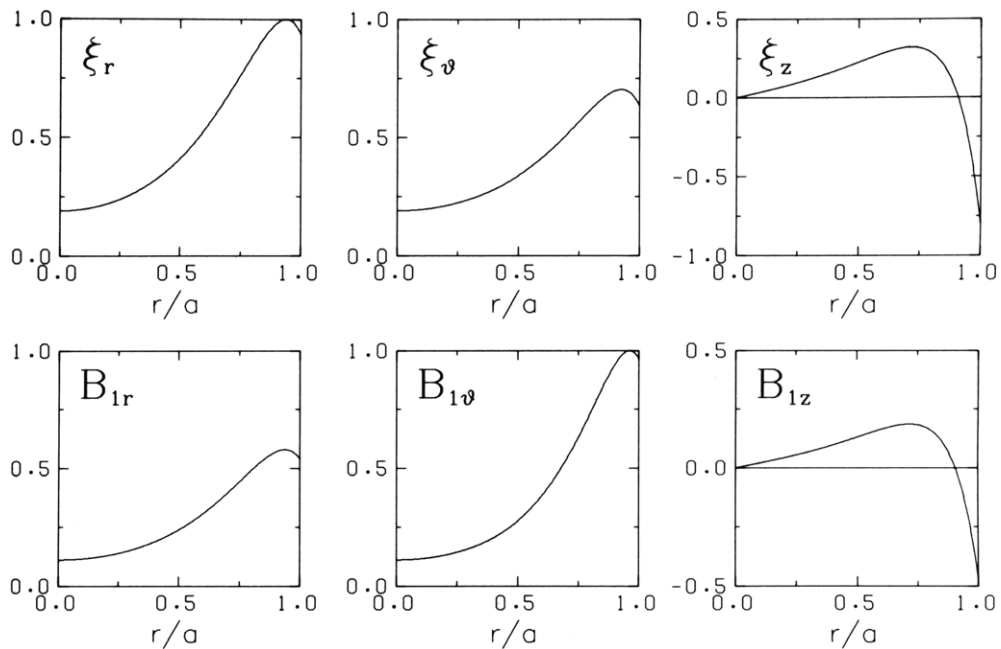

Figure 20. Eigenfunctions for the $m = 1$ mode and a flat current profile for $ka = 4$ [149, figure 4].

$m = 1$ modes. For small ka the $m = 1$ mode grows faster, while for larger ka the $m = 0$ mode dominates. Both have a growth rate increasing with ka. Figures 19 and 20 show the corresponding eigenfunctions for the $m = 0$ and $m = 1$ modes, respectively. It should be noted that these eigenfunctions correspond to the fastest growing modes, which as can be seen have $n = 0$ where n is the number of radial modes. For higher n the growth rates are lower, consistent with the oscillation theorem of Goedbloed and Sakanaka [150], and is termed Sturmian. The theorem can be extended to the stable side of the spectrum when n increases monotonically with ω^2 (Sturmian) or decreases (anti-Sturmian) depending on whether f (in equation (3.20)) is >0 or <0, respectively [146].

The eigenfunctions for the $m = 1$ mode when current density and pressure are centrally peaked and satisfy the Kadomtsev profile are shown in figure 21. Suffice to state that there is a marked change compared with the flat current profile, which will later be discussed in the context of the gas-embedded Z-pinch.
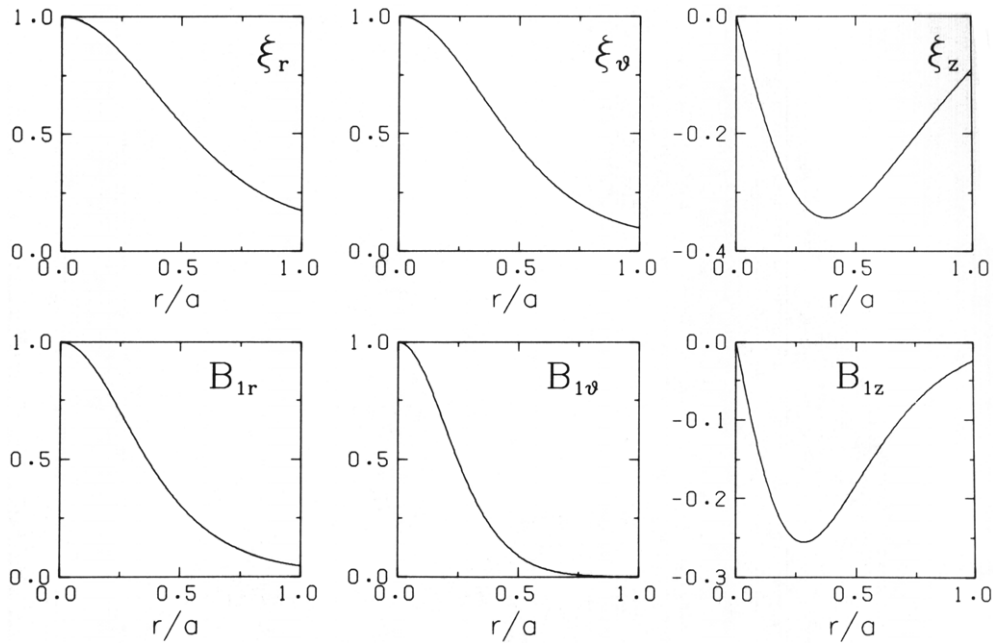
Figure 21. Eigenfunctions for the $m = 1$ mode for a Kadomtsev profile for $ka = 4$ [149, figure 8].

3.3. Resistive MHD stability

Because of the absence of singular surfaces where $\underline{k} \cdot \underline{B}_{\mathrm{o}}$ is zero the introduction of resistivity does not trigger tearing modes (with subsequent magnetic islands and reconnection), which would occur even at high values of Lundqvist number S (equation (3.4)). Instead both resistive diffusion and Joule heating are the effects that would modify ideal MHD, and values of S of order 1 to 10^2 will be considered. This does not imply very cold plasmas, because the pinch radius for a Z-pinch can be small ~ 1 mm. Rather the motivation was to explain the apparently anomalous stability of initially cryogenic deuterium fibre experiments [151, 152] where the small plasma radius leads to small S.

Because of the perceived importance of Joule heating both in the equilibrium and in the perturbed state we have to consider the stability of a time-evolving Joule heated Z-pinch. Culverwell and Coppins [133, 153] took an equilibrium constant radius pinch in which the current varied as $t^{1/3}$, satisfying the Haines–Hammel (see section 2.5) curve. S commenced at a low value of ~ 1 and rose in time to 100. An initial perturbation is applied and its growth is followed by the linearized equations. At high S it becomes an ideal MHD mode; exponential growth of this mode implies that the logarithm of the kinetic energy of the perturbation will grow as $v_{\mathrm{A}}t/a$; since $v_a \propto B \propto t^{1/3}$ it follows that at large S linear growth will be proportional to $t^{4/3}$ or S. Figure 22 shows how the growth of the MHD mode is delayed; specifically until a critical S is reached of about $50(ka)^{-0.86}$. Concurrent work by Cochran and Robson [154] employed a nonlinear 2D time-dependent resistive MHD code, and similar conclusions were reached.

However, a simplified analytic model by Lampe [155] claimed that growth rates were only reduced by a factor of 2 from ideal MHD and that an error occurred in Culverwell and Coppins arising from the neglect of pinch radius change in the perturbed Joule heating.
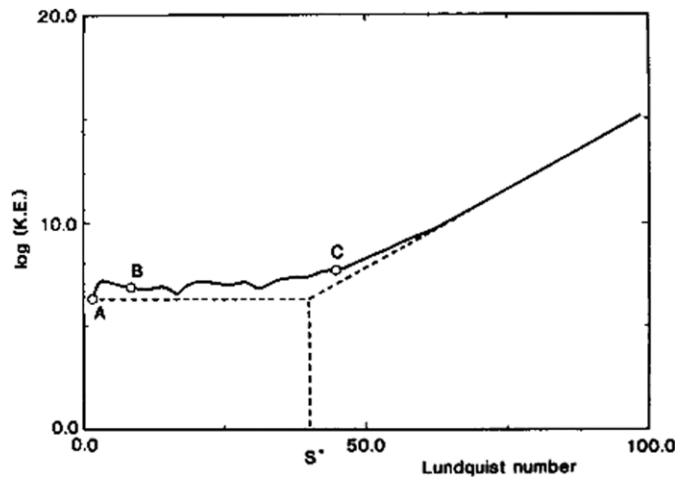
Figure 22. The stabilizing effect of resistivity is illustrated by the delayed growth of the MHD mode until a critical *S* is reached through Joule heating [133] or [153].

In a footnote Neudachin and Sasarov [156] state that they could not reproduce the stabilizing effect of resistivity found by Cochran and Robson. In their paper the stability of various heterogeneous resistive equilibria was studied with varying thermal conduction added, and thermal instabilities can exist in equilibria of high dissipation (see section 3.11). For heterogeneous equilibria with a cold dense core, it is the corona that is subject to MHD instabilities.

Finally, a more careful analysis by Coppins and Culverwell [157] reveals that at early times the pinch is not stable but a thermal instability [158] driven by Joule heating occurs. This is out of phase with the MHD mode which at low R_m is more slowly growing.

3.4. Visco-resistive models of stability

Several authors have included viscosity in addition to resistivity to the fluid model of stability. It might be considered that such a model is of more hypothetical interest, as can be seen from figure 16, the only regime where both effects are simultaneously important is where the ion Larmor radius is about one tenth of the pinch radius. The Hall effect and the FLR terms in the stress tensor at least should therefore be included, though the conventional stress tensor does not correctly include the effect of singular orbits (section 2.2) nor of strong curvature of the magnetic field (see section 3.5). Furthermore for $Z > 5$ it is necessary to include electron viscosity in the equation of motion, and more generally in Ohm's law. The triggering of some anomalous resistivity such as that caused by hybrid turbulence should also be included, particularly in the low density regimes (section 3.12).

Mathematically the damping of Alfvén waves in an homogeneous plasma by resistivity is identical to the damping by isotropic viscosity. Spies [159] employed this and studied the combined effect of scalar viscosity and resistivity to short wavelength modes in the incompressible limit. He found that for $ka > (SR)^{1/4}$ the Z-pinch was stable. However the product SR is equal to $2.86 \times 10^{-16} N$ for $Z = 1$ or $122a^2/a_i^2$. Thus a small value of SR implies large ion Larmor radius and Hall effects, which are not included in this model. Cox [160] considered the $m = 0$ and $m = 1$ linearized modes without resistive or viscous heating, extending the work of Spies to longer wavelength. He found that taking the full
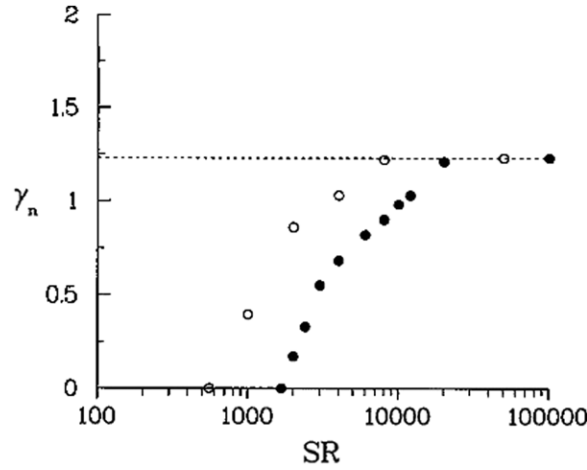
39

Figure 23. Normalised growth-rate variation with (SR)* illustrating the simultaneous stabilizing effect of viscosity and resistivity. Reprinted with permission from [161]. Copyright 1993, American Institute of Physics.

anisotropic viscosity in a magnetic field, as $\Omega_i\tau_i$ became $\gg 1$ the solutions essentially reverted to ideal MHD unstable behaviour, the fluid-like FLR terms having only a minor effect.

Cochran and Robson [161] added scalar viscosity to the 2D resistive MHD model to study the $m = 0$ growth in a time-evolving equilibrium. For the range of ka explored they found the critical value $(SR)^*$ shown in figure 23 which the pinch is unstable, considering the two extreme viscous models of $\Omega_i\tau_i = 0$ and ∞.

All of these papers were motivated by trying to explain the apparent anomalous stability of the early cryogenic deuterium fibre experiments, but it turns out that the critical line density implied by $(SR)^*$ is some 10^3 smaller than that in the experiments. Nonlinear 2D simulations of Lindemuth *et al* [162] show that a fibre develops into a hot unstable plasma surrounding a cold core which is largely unaffected by instabilities. There appears also to be a nonlinear saturation of the coronal MHD instability. This is similar to what has been found in later work on single fibre experiments and simulations (see sections 7.5 and 7.2).

Some mention should be made of papers by Gomberoff and co-workers [163, 164] who in various models with resistivity, thermal conduction and viscosity but also with an additional small axial component of magnetic field, predict the onset of convective cells.

Further analysis of the effect of viscosity and viscous heating is deferred to section 5.8.

3.5. The stress tensor; axial differential flow and strong curvature

Using the notation of Robinson and Bernstein [165] and taking the magnetic field to be only in the θ direction the components of the stress tensor are

$$P_{rr} = p_\perp - \frac{1}{2}\tau_{\theta\theta} + v_1\left(\frac{\partial v_z}{\partial z} - \frac{\partial v_r}{\partial r}\right) + v_2\left(\frac{\partial v_z}{\partial r} + \frac{\partial v_r}{\partial z}\right),$$

$$P_{zz} = p_\perp - \frac{1}{2}\tau_{\theta\theta} - v_1\left(\frac{\partial v_z}{\partial z} - \frac{\partial v_r}{\partial r}\right) - v_2\left(\frac{\partial v_z}{\partial r} + \frac{\partial v_r}{\partial z}\right),$$

$$P_{\theta\theta} = p_\| + \tau_{\theta\theta} = p_\| - \mu_\|\left(\frac{2}{r}\frac{\partial v_\theta}{\partial\theta} - \frac{2}{3}\nabla\cdot\underline{v} + \frac{2v_r}{r}\right),$$

$$P_{zr} = P_{rz} = -v_1 \left(\frac{\partial v_r}{\partial z} + \frac{\partial v_z}{\partial r} \right) + v_2 \left(\frac{\partial v_z}{\partial z} - \frac{\partial v_r}{\partial r} \right),$$

$$P_{z\theta} = P_{\theta z} = -\mu_1 \left(\frac{\partial v_\theta}{\partial z} + \frac{1}{r}\frac{\partial v_z}{\partial \theta} \right) - \mu_2 \left(\frac{1}{r}\frac{\partial v_r}{\partial \theta} + \frac{\partial v_\theta}{\partial r} - \frac{v_\theta}{r} \right),$$

$$P_{r\theta} = P_{\theta r} = -\mu_1 \left(\frac{1}{r}\frac{\partial v_r}{\partial \theta} + \frac{\partial v_\theta}{\partial r} - \frac{v_\theta}{r} \right) + \mu_2 \left(\frac{\partial v_\theta}{\partial z} + \frac{1}{r}\frac{\partial v_z}{\partial \theta} \right), \qquad (3.29)$$

where for ions we approximately can write

$$v_1 \cong \frac{\mu_\parallel}{1 + 4\Omega_i^2 \tau_i^2},$$

$$v_2 \cong \frac{p_{\perp i}}{2\Omega_i} \cdot \frac{4\Omega_i^2 \tau_i^2}{1 + 4\Omega_i^2 \tau_i^2},$$

$$\mu_1 \cong \frac{\mu_\parallel}{1 + \Omega_i^2 \tau_i^2},$$

$$\mu_2 \cong \frac{p_{\perp i}}{\Omega_i} \cdot \frac{\Omega_i^2 \tau_i^2}{1 + \Omega_i^2 \tau_i^2},$$

$$\mu_\parallel = 1.1 p_\parallel \tau_i, \qquad (3.30)$$

while, from Haines [93]

$$\nabla \cdot \underline{\underline{P}} = \hat{\underline{r}} \left[\frac{1}{r}\frac{\partial}{\partial r}(r P_{rr}) + \frac{1}{r}\frac{\partial}{\partial \theta}P_{\theta r} + \frac{\partial}{\partial z}P_{zr} - \frac{P_{\theta\theta}}{r} \right] + \hat{\underline{\theta}} \left[\frac{1}{r^2}\frac{\partial}{\partial r}(r^2 P_{r\theta}) + \frac{1}{r}\frac{\partial}{\partial \theta}P_{\theta\theta} + \frac{\partial}{\partial z}P_{z\theta} \right]$$

$$+ \hat{\underline{z}} \left[\frac{1}{r}\frac{\partial}{\partial r}(r P_{rz}) + \frac{1}{r}\frac{\partial}{\partial \theta}P_{\theta z} + \frac{\partial P_{zz}}{\partial z} \right]. \qquad (3.31)$$

The conventional finite ion Larmor radius (FLR) terms have the coefficients v_2 and μ_2 and persist in the collisionless limit ($\tau_i \to \infty$), but do not enter the irreversible viscous heating rate which is given by

$$-\underline{\underline{\tau}} : \nabla \underline{v} = \frac{\mu_\parallel}{3} \left(\frac{2}{r}\frac{\partial v_\theta}{\partial \theta} + \frac{2v_r}{r} - \frac{\partial v_r}{\partial r} - \frac{\partial v_z}{\partial z} \right)^2 + v_1 \left[\left(\frac{\partial v_r}{\partial r} - \frac{\partial v_z}{\partial z} \right)^2 + \left(\frac{\partial v_z}{\partial r} + \frac{\partial v_r}{\partial z} \right)^2 \right]$$

$$+ \mu_1 \left[\left(\frac{1}{r}\frac{\partial v_r}{\partial \theta} + \frac{\partial v_\theta}{\partial r} - \frac{v_\theta}{r} \right)^2 + \left(\frac{1}{r}\frac{\partial v_z}{\partial \theta} + \frac{\partial v_\theta}{\partial z} \right)^2 \right], \qquad (3.32)$$

which is positive definite, demonstrating irreversible entropy production consistent with the second law of thermodynamics. Here the traceless stress is $\underline{\underline{\tau}} = \underline{\underline{P}} - p_\perp(\hat{r}\hat{r} + \hat{z}\hat{z}) - p_\parallel\hat{\theta}\hat{\theta}$. The papers of Cox [160] and of Cochran and Robson [161] use either this or the isotropic (collisional or unmagnetized) limit ($\Omega_i \to 0$).

The FLR terms can lead to the spontaneous development of sheared axial flow. This is analogous to the differential rotation of θ-pinches proposed by Velikhov [166] and contained in a review [93]. It occurs even in 1D, i.e. with only radial dependence. Taking the collisionless limit, the axial component of the equation of motion is

$$\rho \left(\frac{\partial v_z}{\partial t} + v_r\frac{\partial v_z}{\partial r} \right) = \frac{1}{r}\frac{\partial}{\partial r} \left(r\frac{p_{\perp i}}{2\Omega_i}\frac{\partial v_r}{\partial r} \right). \qquad (3.33)$$

This indicates that, whilst the total axial momentum is conserved, a sheared axial velocity of order εv_t can be generated through radial motion where v_i is the ion thermal speed and ε is a_i/a, the ratio of ion Larmor radius to pinch radius.

The stress tensor in equation (3.29) was developed for straight magnetic lines of force. The effect of strong curvature such that $(B_\theta/r) \approx (\partial B_\theta/\partial r)$ is to increase the relative magnitude

of the curvature drift. In the collisionless FLR ordering, as developed by Rosenbluth and Simon [167] and extended to $\beta \approx 1$ by Bowers and Haines [168, 169], heat-flow terms also appear in the stress tensor, and indeed reduce the growth rate of instabilities because the higher energy ions have a higher guiding-centre drift velocity associated with the grad B and curvature drifts; hence leading to a collisionless heat flux and a spatial smoothing of inhomogeneities. To include strong curvature would at first sight appear to be contrary to the standard ordering scheme in which the growth rate γ should be of order $\varepsilon^2 \Omega_i$. Such an inconsistency manifests itself as a violation of quasi-neutrality. To overcome this $\partial/\partial z$ can be ordered as ε^2/r, i.e. only long axial wavelengths are included.

Then, for example, P_{rr} to second order becomes (omitting the subscript i)

$$P_{rr} = p_\perp + \frac{1}{4\Omega r}\frac{\partial}{\partial r}(r\theta_z) - \frac{\theta_{\|z}}{\Omega r} + \frac{p_\perp}{2\Omega}\frac{\partial v_z}{\partial r}, \tag{3.34}$$

where the heat flux terms for a doubly Maxwellian distribution are

$$\theta_z = -\frac{2p_\perp}{\Omega}\frac{\partial}{\partial r}\left(\frac{p_\perp}{\rho}\right), \tag{3.35}$$

$$\theta_{\|z} = -\frac{p_\perp}{2\Omega}\frac{\partial}{\partial r}\left(\frac{p_\|}{\rho}\right) + \frac{p_\|}{\rho\Omega r}(p_\| - p_\perp). \tag{3.36}$$

These extra terms will modify both the stability and the development of sheared axial flow. However, because of the limitations of the FLR expansion near the axis as $B \rightarrow 0$ and the need to consider singular ions, a more complete theory will be included when discussing large ion Larmor radius effects in section 3.8.

3.6. Anisotropic pressure effects

In the limit of small Larmor radius the collisionless Chew, Goldberger and Low [140] (CGL) theory applies when the collision frequency is much less than the MHD growth time (see equation (3.10)). In this general CGL theory there is always a difficulty of prescribing the undefined heat-flow parallel to the magnetic field. However, as pointed out by Akerstadt [170] this is identically zero for the case of $m = 0$ stability of a Z-pinch, and the CGL theory exactly applies. The characteristics of the CGL theory are the doubly adiabatic laws

$$\frac{\mathrm{d}}{\mathrm{d}t}\left(p_\|\frac{B^2}{\rho^3}\right) = 0 = \frac{\mathrm{d}}{\mathrm{d}t}\left(\frac{p_\perp}{\rho B}\right) \tag{3.37}$$

which together with the equilibrium pressure balance equation (2.17) lead to a more optimistic condition for $m = 0$ stability [171]. For anisotropic equilibria the pinch is stable to $m = 0$ if

$$-\frac{r}{(p_\perp + p_\|)}(p_\perp + p_\|) < \frac{3\beta_\perp + 4\beta_\| + \frac{5}{2}\beta_\perp\beta_\| + \frac{1}{8}(\beta_\| - \beta_\perp)^2}{(1 + \beta_\perp)(\beta_\perp - \beta_\|)}, \tag{3.38}$$

where $\beta_\perp$ is $2\mu_o p_\perp/B^2$ and $\beta_\|$ is $2\mu_o p_\|/B^2$.

For an isotropic equilibrium the rhs becomes $(5\beta + 14)/(4(1 + \beta))$ which is always larger than $2\Gamma/(1 + \Gamma\beta/2)$, the corresponding (Kadomtsev) ideal MHD case (for $\Gamma < 7/4$). This illustrates the sensitivity of the $m = 0$ mode to the model [172]. Coppins and Scheffel [173] showed that the CGL model gives smaller growth rates than ideal MHD for the same isotropic equilibria, i.e. the perturbed state is anisotropic. They also showed how stability is sensitive to the edge boundary condition [174].

42

3.7. Hall fluid model of stability

Ideal MHD employs the Ohm's law $\underline{E} + \underline{v} \times \underline{B} = 0$, and as discussed in section 3.1 and in particular in figure 16 it ceases to be valid at low line density. When the Hall effect and ∇p_e term are introduced into a collisionless Ohm's law to give

$$\underline{E} + \underline{v} \times \underline{B} - \frac{\underline{J} \times \underline{B}}{n_e e} + \frac{\nabla p_e}{n_e e} = 0, \tag{3.39}$$

these extra terms can be considered to be part of the FLR corrections. Indeed some authors incorrectly consider that these terms are the sole FLR terms (e.g. [87]). The connection between FLR for the ions and the Hall terms in the electron equation of motion can be seen by considering the equilibrium pressure balance for the ions, which if stationary as a fluid, is $\underline{E} = -\nabla p_i / Z n_i e$ or $E/B \cong m_i v_i^2 / Z e B L = v_i a_i / a$ where $a_i / L \equiv \varepsilon$ is the ratio of ion Larmor radius to the pinch radius or pressure scale length L. It follows that when the Hall terms are added to Ohm's law a new component of electric field arises and all are of order εv_i. However in the Hall fluid model it is assumed that the ions are collisional, i.e. $\Omega_i \tau_i < 1$, and the FLR terms in the stress tensor are ignored. The resistivity is also ignored. Thus the range of parameter space for the validity of the Hall model is very limited.

An important feature of the Hall fluid model for stability is that the growth rate is complex. This can be understood because Ohm's law now has the magnetic field frozen to the moving electrons in the equilibrium and perturbation. Tayler [175] and Schaper [176, 177] first considered the Hall fluid model for the Z-pinch, though Schaper limited his theory of the $m = 0$ mode to the incompressible limit and constant density, finding a stabilizing effect.

In contrast, using a linearized initial value code Coppins *et al* [178] showed that by increasing ε faster growth could occur for a Bennett profile. For a Kadomtsev profile, i.e. equation (3.27) (i.e. stable to ideal MHD), new instabilities could be triggered. Using one of Schaper's profiles and near incompressibility, stabilization is found but new unstable modes can be triggered.

3.8. Large ion Larmor radius (LLR) effects

For much of the parameter space in figure 16 at high $I^4 a$ and low N the LLR regime applies. This is also the regime for a deuterium–tritium Z-pinch under fusion conditions or a hydrogen pinch prior to radiative collapse. It is therefore important to understand both the linear and nonlinear stability in this regime.

As discussed earlier the standard FLR approach will fail for even $\varepsilon \cong 0.1$ because of the strong curvature of the magnetic field (section 3.5) and the absence of singular particle orbits (section 2.2) and resonant particles [179]. Therefore numerical modelling of the Vlasov equation for ions [180] with a cold electron fluid background to maintain quasi-neutrality is employed. The electron fluid includes the Hall term and so is frozen to the magnetic field. Like the Hall fluid model we find that growth rates are complex. The Vlasov model naturally allows anisotropic pressure to arise and can be used for arbitrarily large ion Larmor radius. Whilst for most MHD equilibria, formally the threshold for instability is the same as for ideal MHD [180], this is not the case for the $m = 0$ mode for a Z-pinch; indeed as $\varepsilon \to 0$ the Vlasov model should and does yield the same as the CGL ordering [11]. In figure 24 the real part of the normalized growth is plotted versus ε using both the linearized initial value code FIGARO and a variational code for two equilibria: a parabolic density profile and the Bennett equilibrium (equation (2.10)). For the former case it can be seen that the growth rate at $\varepsilon = 0.2$ is a minimum of about 0.3 times the $\varepsilon = 0$ case. The growth rate is very sensitive to the equilibrium profile, and indeed large ion Larmor radius (LLR) destabilizes the Bennett equilibrium.
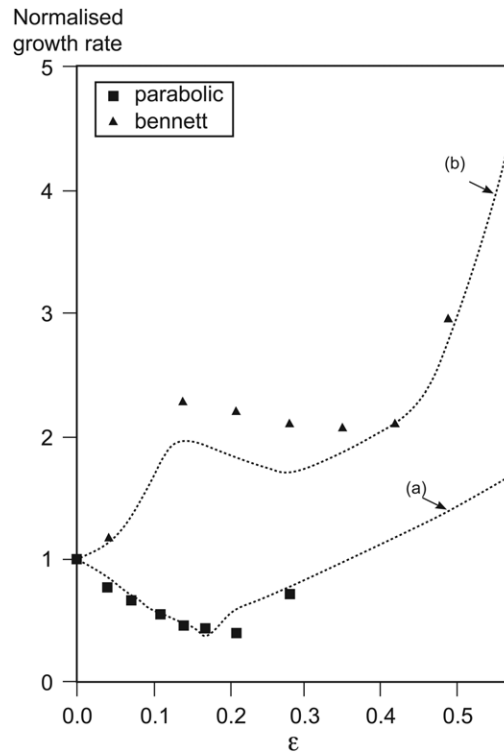
Normalised
growth rate

Figure 24. Real part of the normalized growth rate for $m = 0$ is plotted versus ε using the linearized initial value code FIGARO and a variational code for a parabolic density profile and the Bennett equilibrium. Reprinted figure 1 from [11]. Copyright 1994 by the American Physical Society.

The reason for the increasing growth for $\varepsilon > 0.2$ for the parabolic profile is not fully understood but it could be that as the ion Larmor radius increases there is less time for kinetic smoothing of the MHD mode because the ion cyclotron period approaches the characteristic growth time a/c_A. For a fixed ε the growth rate peaks at $ka = 5$ and then falls off, as expected, for larger ka. For a skin-current pinch Arber and Coppins [181] had earlier shown that the growth rate saturated at $ka = 5$.

The variational code has also been used to explore the $m = 1$ mode [12]. Figure 25 shows the normalized growth rate for three profiles. LLR has a more marked stabilizing effect here, especially on the parabolic density profile, and there is an 80% reduction in growth.

Experiments on the compressional pinch have indicated a reduction in growth rate under large Larmor radius conditions [131, 132, 182] but it is difficult to be more precise because of the time limitations of the experiments. Compression Z-pinch experiments can be devised such that at first compression $\Omega_i \tau_i$ is larger than 1 and a_i/a is optimal at ~ 0.1 [183]. Indeed a recent experiment by Davies *et al* [14] has shown a marked reduction by a factor of 2 for the $m = 0$ mode at $\varepsilon = 0.1$. Figure 26 shows the measured growth rate as a function of ε.

3.9. Effect of sheared axial flow

An intuitive view of the effect of a sheared axial flow velocity $v_z(r)$ would suggest that if a significant velocity shear were to occur over the region occupied by the zero-velocity ideal MHD eigenfunction $\xi_r(r)$ for the perturbed displacement, then the plasma, being frozen to the
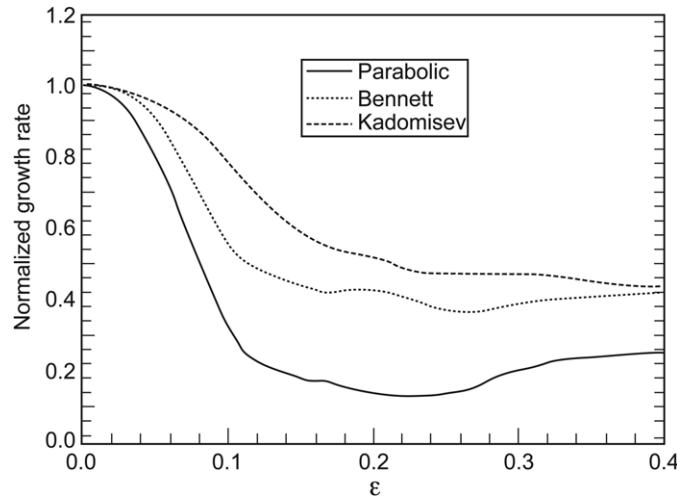
Figure 25. Normalized growth rate for $m = 1$ for three equilibrium profiles. Reprinted figure 1 from [12]. Copyright 1995 by the American Physical Society.
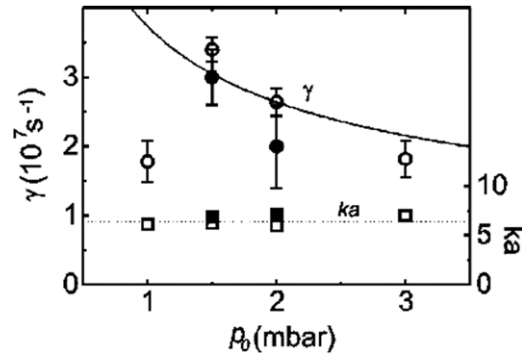

Figure 26. Experimentally measured growth rate and ka as a function of the fill-pressure p_0 showing a marked reduction to 0.21 of ideal MHD at $\varepsilon = 0.15$, corresponding to $p_0 = 1$ mbar. Reprinted figure 5 with permission from [14]. Copyright 2001 by the American Physical Society.

magnetic field, would be strongly affected. Indeed, as shown by Arber and Howell [57], this is the case, and there is a marked stabilizing effect. For high ka where $\xi_r(r)$ is localized close to the surface, a sheared velocity close to $r = a$ can reduce the growth rate (even to zero) and the eigenfunction becomes very narrow. Figure 27 shows the normalized displacement eigenfunction as a function of r for three values of the dimensionless axial velocity u_o where

$$v_z(r) = v_{Ti}u_o(1 - r^2/a^2) \tag{3.40}$$

for $m = 0$, $ka = 10$, $\beta = 1.1$ and for an equilibrium pressure profile $p = p_0(1 - r^2/a^2\beta)$, β being a parameter greater than one which determines the pressure at $r = a$. This is for an internal mode. For free boundary eigenfunctions they are non-zero at $r = a$, and the plasma is more unstable. Figure 28 shows the normalized growth rate for the three fastest free boundary modes, nevertheless showing stabilization for increasing u_o. But flow Mach numbers in excess of 1–5 are required. However at even larger values of u_o the Kelvin–Hemholtz instability can be triggered. The effect of sheared rotation, which changes the equilibrium pressure profiles, has also been studied.
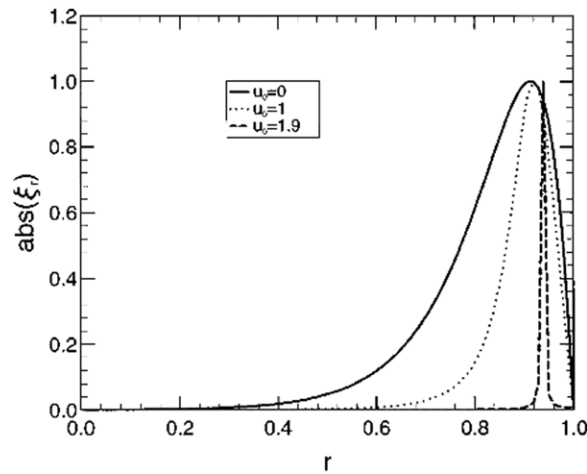
Figure 27. Normalized displacement eigenfunctions as a function of r for three values of the dimensionless axial velocity. Reprinted with permission from [57]. Copyright 1996, American Institute of Physics.
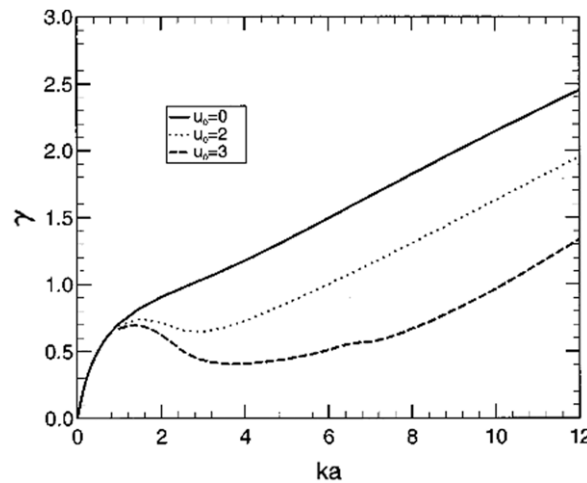
Figure 28. Normalized growth rate for the three fastest free boundary modes as a function of ka. Reprinted with permission from [57]. Copyright 1996, American Institute of Physics.

A theory which predicts even greater stabilization with axial velocity shear was published by Shumlak and Hartman [135], but this was criticized for having a discontinuity in velocity gradient at $r = 0$ [184]. This was not satisfactorily justified in [185]. It is probably this which led to the singularity in the eigenfunction at $r = 0$. Zhang and Ding [186, 187] recently studied the effects of compressibility and axial flow profiles on stability, though they seemed unaware of the earlier work of [53]. Experiments with sheared axial flow [188] are reported in section 7.7.

3.10. Addition of axial magnetic field

It is well known that an axial magnetic field can have a stabilizing effect; indeed it was the addition of such a field that led to the development of the toroidal pinch, the reversed field

pinch and the tokamak. Two important points however need to be made. The first is that the addition of an axial magnetic field component $B_z(r)$ changes the nature of the MHD mode because $\underline{k} \cdot \underline{B}$ can be zero at, say, a radial position r_s, leading to a regular singular point in the Sturm–Liouville equation; as a result adding B_z does not necessarily stabilize it. The second is that for the dense Z-pinch B_θ is typically of order 100 T (or 1 MG) and the only way in the laboratory to form a B_z of similar or larger magnitude is through compressing a seed B_z formed from a coil or perhaps dynamically creating a B_z from a helical $m = 1$ mode (see the next section). It has recently been shown that an axial magnetic field of the required magnitude can be generated from photon spin [189, 190], using a high intensity laser with circularly polarized light.

The combined effects of B_θ and B_z as first studied by Suydam [191] and extended by Newcomb [192]. The most significant result in the Suydam criterion which has been generalized for the case of anisotropic pressure [193] to give

$$\left(\frac{\mathrm{d}\mu/\mathrm{d}r}{\mu}\right)^2 + \frac{4}{r_s} \frac{\dfrac{\mathrm{d}}{\mathrm{d}r}\left(\displaystyle\sum_{\mathrm{species}}(p_\parallel + p_\perp)\right)}{B_z^2/\mu_\mathrm{o} - \displaystyle\sum_{\mathrm{species}}(p_\parallel - p_\perp)} > 0, \tag{3.41}$$

where μ is $B_\theta/(r_s B_z)$. This is a necessary condition for ideal MHD stability. In this case it is shear of the equilibrium magnetic field that provides a stabilizing effect. In a pinch of finite length line-tying at the electrodes stabilizes long wavelength global modes [194]. In contrast for a torus of major radius R the stabilization of the $m = 1$, $n = 1$ kink is provided by the Kruskal–Shafranov limit that the safety factor $q \equiv r B_z / R B_\theta$ is greater than one [195].

However the introduction of even a small amount of resistivity which allows the field lines to tear and reconnect leads to unstable modes with eigenfunctions localized at the singular surfaces where $\underline{k} \cdot \underline{B} = 0$, $\underline{k}$ being the mode wave-vector. In a hot fusion plasma where the Lunquist number might be as high as 10^9, this results in the tearing layer being very narrow with a high local current density. Aparicio *et al* [196] have shown how magnetic reconnection can occur on a fast time scale due to the triggering of micro-instabilities such as the ion-acoustic drift mode in this narrow layer, i.e. the effective resistivity in the reconnecting layer becomes anomalously high. However this rich and interesting subject lies outside the scope of this paper.

3.11. Nonlinear growth of MHD modes

The nonlinear evolution of instabilities has benefited from modern computers. In figure 29 a 2D numerical simulation of the evolution from a cold start of an exploding 33 μm diameter carbon fibre is compared with schlieren images [197] at various times. The fibre at first breaks down and the coronal plasma expands. At the same time the current is rising and in a 1D simulation it would at some point recompress because of the increasing relative strength of the $\underline{J} \times \underline{B}$ pinch force. However, due to the possibility of growth of a $m = 0$ MHD instability in a 2D simulation, this mode grows strongly at this time from (in this particular simulation) an initial random perturbation. In the necking regions bright spots of x-ray emission occur where the hot pinching plasma compresses onto the dense fibre [198]. These bright spots bifurcate axially both in the simulations and experiment as ionizing fronts propagate, driven by the $\underline{J} \times \underline{B}$ forces associated with the radial component of current density. Similar simulations have been undertaken by Lindemuth [162] to model the evolution of cryogenic deuterium fibres.

An interesting feature in both experiment and simulation is that a particular axial wavelength dominates nonlinearly, and indeed increases as the pinch radius increases. This

Figure 29. Comparison of 2D MHD simulations with schlieren images (left of each pair on top line). Lower line images are simulations at 33 ns. Reprinted with permission from [197]. Copyright 1997, American Institute of Physics.

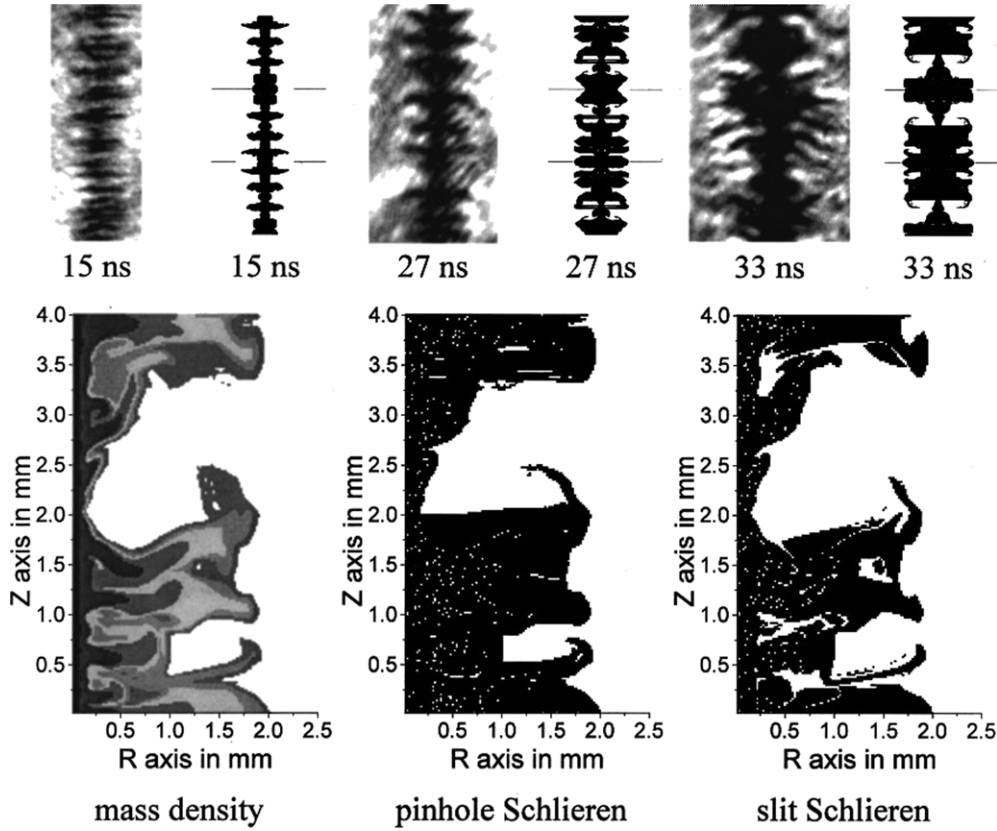is despite the fact that linear stability theory states that the growth rate increases with k, approximately as $k^{1/2}$. One reason for this can be deduced by considering the nonlinear $\rho(\underline{v} \cdot \nabla)\underline{v}$ term in the fluid equation of motion. The $m = 0$ mode leads to the development of necking regimes where there is a high $\underline{J} \times \underline{B}$ pinching force and bulges which expand almost freely with a velocity related to the sound speed. For the bulges if we assume that the nonlinear convective term balances the pressure gradient and that the $\underline{J} \times \underline{B}$ force is much weaker, i.e.

$$\rho(\underline{v} \cdot \nabla)\underline{v} \cong -\nabla p, \tag{3.42}$$

it follows that $v \cong c_s$, the sound speed $(\Gamma p/\rho)^{1/2}$, and that the radial displacement will be proportional to $c_s t$. The mode evolves to this nonlinear state when either ξ_r is $\sim \beta a$ or k^{-1}, whichever is the smaller. (The value of β depends on the radial profile of ξ_r in the linear phase, e.g. in figure 27, and is approximately 0.5.) This means that the fastest growing short wavelength modes will become nonlinear earlier and will change from exponential growth to algebraic, in this case a linear dependence on t. If this occurs at time t_1, and the linear growth rate γf is approximately $(ka)^{1/2} c_s/a$, we can write

$$\xi_k(t_1) = \xi_{0k} \exp[(ka)^{1/2} c_s t_1/a] = k^{-1} < \beta a \tag{3.43}$$

then for $t > t_1$ the displacement is given by

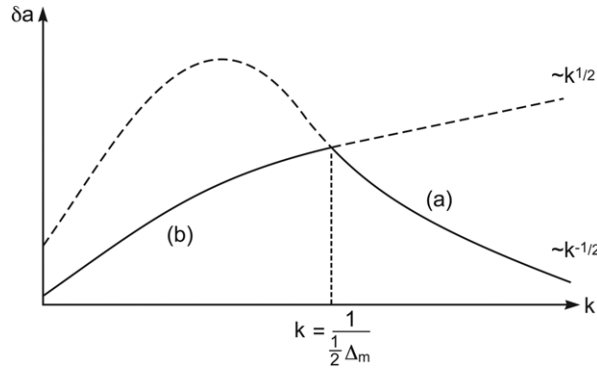$$\xi_k = \alpha_1 c_s (t - t_1) + k^{-1}. \tag{3.44}$$

Figure 30. Schematic drawing of the radial velocity associated with the nonlinear, algebraic phase of the instability as a function of ka [280, figure 4]. Copyright © 1998 IEEE.

Assuming continuity of velocity at $t = t_1$

$$\dot{\xi}_k(t_1) = (ka)^{1/2} c_s/(ka) = \alpha_1 c_s. \tag{3.45}$$

Hence α_1 is $(ka)^{-1/2}$, which shows that the short wavelength modes can have a smaller amplitude in the nonlinear phase.

For long wavelengths, which saturate at a time t_2, the linear displacement is

$$\xi_k(t_2) = \xi_{0k} \exp[(ka)^{1/2} c_s t/a] = \beta a < k^{-1} \tag{3.46}$$

and for $t > t_2$, similar arguments lead to a nonlinear displacement

$$\xi_k = \alpha_2 c_s(t - t_1) + \beta a. \tag{3.47}$$

Continuity of velocity at $t = t_2$ gives

$$\dot{\xi}_k(t_2) = (ka)^{1/2} c_s \beta = \alpha_2 c_s. \tag{3.48}$$

Hence, in the long wavelength case α_2 is $\beta(ka)^{1/2}$, and the amplitude increases as $(ka)^{1/2}$. Similar arguments will apply to the RT instability (section 4.8). As a result the maximum amplitude occurs at the boundary between these two regimes, i.e. at $ka = \beta^{-1} \cong 2$, or $\lambda \cong \pi a$. This is illustrated in figure 30. This considerably oversimplified model ignores mode–mode coupling, but nevertheless describes the main trends of both experiment and simulation.

The necking region of the $m = 0$ mode can eventually lead to a disruption with electron and ion beam formation, the former giving rise to hard x-rays and the latter, in the case of deuterium to a neutron burst. These phenomena are considered in section 3.14.

So far we have concentrated on the $m = 0$ sausage instability which is the dominant mode in compression pinches and wire or fibre pinches. However, in gas-embedded Z-pinches where the initial current channel is triggered (e.g. by laser) along the axis, a Kadomtsev type of profile develops and the $m = 0$ instability does not occur. Instead the $m = 1$ kink mode is excited. An analytic ideal MHD model of a helical perturbation in a Z-pinch by Psimopoulos and Haines [199] showed that to fourth order in time no harmonic generation occurs. In another paper [200] the inclusion of the response of an external circuit on the nonlinear development shows that for ka above a critical value of 0.802 there is an abrupt transition to a rapidly expanding plasma, as seen in experiments. The formation of a helical pinch with associated axial magnetic field can be considered as an example of a plasma evolving towards a minimum energy state [201].

The nonlinear development of an $m = 0$ instability under large ion Larmor radius conditions has been studied by Arber [202] in a hybrid model of particle-in-cell ions in a

cold collisionless electron fluid background. As discussed in section 3.8 the linear growth rate can be reduced by 70–80%. However, nonlinearly these instabilities continue to grow exponentially without saturation until the plasma column is disrupted. These results are sensitive to the plasma vacuum boundary conditions, and indeed in this low density region other physical processes such as the lower hybrid instability might occur due to the high local electron drift velocity. Further work is needed here, but at the present time it would seem that the hoped for saturation of the instability under LLR conditions does not occur.

The nonlinear development of a Z-pinch with a sheared axial flow has been studied [203]. Related to this is the stability of cosmic jets [204–206]. In Bell and Lucek it was shown that the $m = 0$ instability saturates leading to a Bennett-like structure. This is seen in some jets; indeed extra galactic jets are observed to be stable. In a 3D MHD simulation Lucek and Bell [207, 208] showed that with no additional axial magnetic field sheared, supersonic jets are indeed unstable to $m = 1$ helical modes. In a Z-pinch with sheared axial flow [209] it was shown how both $m = 0$ and $m = 1$ instabilities can saturate in amplitude. How to employ this phenomenon in a practical experiment is however difficult. An apparent reduction in instabilities was observed by Wessel *et al* [56] in wire surrounded by a flowing aluminium plasma. However a velocity of the order of the sound speed is theoretically required, and it is required to maintain this flow around the pinch for an axial transit time. Thus the apparent saturation may be a feature of the convection of the mode in a finite size system, i.e. due to the flow rather than the shear in the flow.

3.12. Electrothermal instability and the heat-flow instability

The current-driven and heat-flow driven electrothermal instability can be important in relatively dense and cold plasma carrying a current and subject to rapid Joule heating. The essential mechanism is that a spatially varying perturbation in electron temperature, T_e, orthogonal to the direction of the current density will lead to perturbed current density and Joule heating. This is due to the $T_e^{3/2}$ power law for the electrical conductivity which will lead to perturbed Joule heating that will enhance the perturbed temperature. Such an instability is called an overheating instability in a tokamak [210]. When the electron temperature is decoupled from the ion temperature, it is named the electrothermal instability and was initially studied in the context of non-equilibrium plasmas for closed-cycle MHD power generation [211, 212]. Its application to a fully ionized plasma [158] led to an explanation of early occurring instabilities in a theta pinch. Here the k vector of the perturbation is in the direction of the magnetic field, and with ion motion also included it is found that there are two essential conditions for growth of the instability. One is that the Joule heating of the electrons as measured by the equipartition rate to ions (of fixed temperature in the model) must be sufficient to lead to a ratio of electron to ion temperature given by

$$\frac{T_e}{T_i} > \frac{3 + \sqrt{57}}{8} \approx 1.32. \tag{3.49}$$

The second necessary condition is that the electron–ion mean-free path should be less than the collisionless skin depth, or more precisely

$$\lambda_{\mathrm{mfp}} < \left(\frac{4\alpha_0}{3\gamma_0}\right)^{1/2} \frac{c}{\omega_{\mathrm{pe}}}, \tag{3.50}$$

where in the notation of Braginskii [98] or Epperlein and Haines [100] the dimensionless factor $(4\alpha_0/3\gamma_0)^{1/2}$ has values ranging from 0.459 for $Z = 1$ to 0.170 for $Z = \infty$. In terms of density (m^{-3}) and temperature (eV), this condition is

$$T_e < (2.50\text{–}4.11) \times 10^{-6} n_e^{1/4} (Z \ln \Lambda_{\mathrm{ei}})^{1/2}, \tag{3.51}$$

where the lower figure refers to $Z \to \infty$ and the higher to $Z = 1$. The fastest growing mode has a wavelength λ of

$$\lambda \cong 2\pi \left[\frac{\sigma \kappa m_i}{3n^2 e^3} \right]^{1/2} = (1.52\text{--}0.56) \times 10^{20} \frac{T^2 A^{1/2}}{n_e Z \ln \Lambda_{ei}} \tag{3.52}$$

and growth rate of

$$\gamma \cong 1.2 \frac{m_e}{m_i} \frac{\alpha_0}{\tau_{ei}} = (1.03\text{--}1.77) \times 10^{-12} \frac{m_e}{m_i} \frac{n_e Z \ln \Lambda_{ei}}{T_e^{3/2}} \tag{3.53}$$

This theory satisfactorily explained the occurrence of an instability in a theta pinch during the early plasma formation [213], agreeing well on the variation of wavelength with density. Here the electron density at very early times was in the range 5×10^{20} to 3×10^{21} m^{-3}, the electron temperature 2 to 3 eV, the growth rates 5×10^5 to 8×10^7 s^{-1} and wavelengths 7.6 to 0.75 cm. A similar break-up of the current into filaments would be expected in the gaseous compressional pinch or plasma focus very soon after plasma formation if condition (3.51) holds. Such an instability however could also occur at stagnation of a highly radiating wire-array Z-pinch when the conditions ((3.50), (3.51)) can sometimes be satisfied, because of the high electron density achieved, leading to azimuthal variation with $m \sim 5\text{--}9$. However care must be exercised in this interpretation because such structure might be triggered by the slots in the return current conductor.

The reason for the optimum wavelength is that short wavelengths are damped by thermal conduction, κ, while for long wavelengths the combined effects of Faraday's law and Ampère's law ensure that an electric field perturbation will depend on k^{-2}, and this field will oppose the change in current density.

This theory has been extended to the case of nonlinear heat flow [214], particularly as it applies to the heat flux in a laser-driven implosion for inertial confinement. Here the heat flow reaches about 10% of the free-streaming limit. Indeed this is necessarily the case because the inward heat flow, the source of energy for the implosion, must exceed the outward enthalpy flux associated with the ablation process. This strong heat flux can be approximated to a relatively collisionless inward flow of hot electrons (the mean-free path varies as V^4) and an equal and opposite current of cold collisional electrons. This cold return current is driven by an inward electric field—the thermoelectric field, which only arises because of the velocity dependence of the collision frequency. Indeed the outward acceleration of ions—the ablation process—is impeded by this electric field which is of the wrong sign to accelerate the ions, and it is the frictional force between the cold return current and the ions which causes the ablation [215]. $\underline{J} \cdot \underline{E}$ for the hot electrons is negative and is equal and opposite to the $\underline{J} \cdot \underline{E}$ for the cold return current. Thus, if the conditions (3.49) and (3.51) are satisfied, the Joule heating associated with the cold return current will cause an electrothermal instability associated now with heat flux [214]. This instability is the likely cause of fine-scale filamentary structures observed at first by laser shadowgraphy [216] and recently by MeV proton probing [217] of plasmas produced by laser–solid interactions. The latter demonstrated that the instability originates at the ablation surface. In the theory [214] the hot electrons exhibit a Weibel-like response to the perturbing electric and magnetic fields, especially if they are beam-like, but if their temperature is comparable to their directed energy they have no major effect on the electrothermal instability.

Similar filamentary structures are observed on the surface of the cores of wires in wire-array Z-pinches [218, 219]. An interesting fact is that when experiments try to stimulate a different wavelength, the natural wavelength for a particular material still persists [220]. These experiments will be discussed later in section 5.4.

3.13. Micro-instabilities and anomalous resistivity

Some form of micro- or velocity-space-instability will be triggered when the drift velocity $v_d (\approx J/n_e e)$ of the current-carrying electron exceeds some critical velocity v_{crit}, which is typically of order the sound speed, c_s $(= \sqrt{[(ZT_e + T_i)/m_i]})$. The instability will rapidly grow in time and saturate in amplitude. The resulting electrostatic or electromagnetic turbulent wave structure will interact with the drifting electrons, causing them to be scattered. This scattering is usually much larger than that caused by Coulomb collisions with ions; hence an anomalous resistivity will be generated.

The microinstability that is perhaps most relevant in the Z-pinch configuration is the lower hybrid drift instability, because the current and drift velocity are orthogonal to the magnetic field. It is related to the modified two-stream instability studied earlier by Buneman [221] and Ashby and Paton [222]. Krall and Liewer [223] derived a linear electrostatic kinetic model of the lower hybrid instability. It does not have a critical velocity threshold, but nonlinearly its effective collision frequency varies as the square of the electron drift velocity.

A quasi-linear model to find a value for the anomalous resistivity was developed by Davidson and Gladd [224]. Huba and Papdopoulos [225] considered electron resonance broadening as a saturation mechanism especially in finite β plasmas. Particle simulations by Winske and Liewer [226] in contrast find that ion trapping is a saturating mechanism in the high drift velocity regime, while Davidson [227] found current relaxation and plateau formation can cause saturation at low drift velocity.

Probably the two most relevant papers to yield in 2D nonlinear modelling a value for the anomalous collision frequency at saturation are Drake *et al* [228] and Brackbill *et al* [229]. The former considered nonlinear mode–mode coupling of the electrostatic waves showing that energy is transferred from long wavelength modes to short wavelength modes which are Landau damped. The anomalous collision frequency ν_{anom} so found from this model is

$$\nu_{anom} = 2.4(\Omega_e \Omega_i)^{1/2}(v_d/v_i)^2. \tag{3.54}$$

Here $(\Omega_e \Omega_i)^{1/2}$, where Ω_e and Ω_i are the cyclotron angular frequencies of the electrons and ions, respectively, is the lower hybrid resonance frequency, while v_d and v_i are the electron drift velocity and the ion thermal speed, respectively.

Brackbill *et al* [229] employed in contrast a 2D implicit e.m. particle-in-cell code, VENUS, initially with a Harris equilibrium. The saturation mechanism was considered to be electron kinetic dissipation with wavelengths greater than the electron Larmor radius. The resulting anomalous collision frequency found in this numerical simulation differs only slightly from equation (3.43), namely

$$\nu_{anom} = \frac{C}{4\pi\beta_i}(\Omega_e \Omega_i)^{1/2}(v_d/v_i)^2, \tag{3.55}$$

where C is 0.13–0.38 and β_i is the ratio of ion pressure to magnetic pressure.

Before applying these results to the Z-pinch it is perhaps worthwhile to recall the basic physics underlying the lower hybrid resonance. Although the ion cyclotron frequency is present in the formula, the ions are in fact to a good approximation unmagnetized. Figure 31 illustrates how the lower hybrid resonance arises when the ion plasma frequency is much higher. Consider a plane e.s. wave propagating in the z-direction. The unmagnetized ions will oscillate to and fro in the $\pm z$-direction. With a steady magnetic field in the y-direction, the magnetized electrons will have an oscillatory $\widetilde{E}/B$ drift in the $\pm x$-direction. Superposed on this is the polarization drift, $\dot{E}/(B\Omega_e)$ in the $\pm z$-direction, which will convert the electron guiding-centre trajectory into an ellipse. The resonance occurs, i.e. a tendency for zero charge separation when the spatial amplitude of the ion oscillation $e\widetilde{E}/m_i\omega^2$ equals the width of the ellipse $\widetilde{E}/(B\Omega_e)$; this gives $\omega = (\Omega_e \Omega_i)^{v_2}$
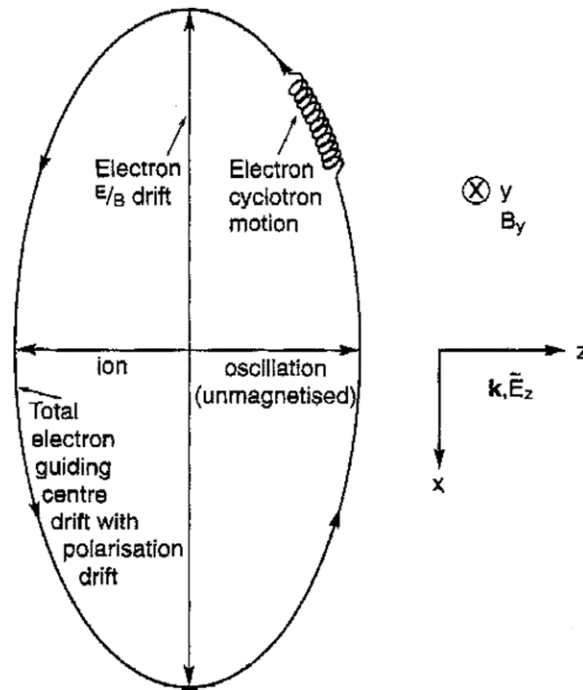
Figure 31. Schematic drawing of trajectories of oscillating ions and guiding-centre electrons, showing equal amplitude in the *z*-direction at the lower hybrid resonance [253]. Copyright © 2001 Cambridge University Press.

The lower hybrid instability arises when a density gradient is present in the −*x*-direction; then the electron elliptic motion leads to an increase in positive potential and charge at the positive peak of the wave and a similar amplification of the negative charge at the negative potential peak. The density gradient corresponds to a net diamagnetic drift of electrons in the −*z*-direction. Hence such a current is responsible for the growth in the wave amplitude.

It is to be noted that nearly all the simulations and theory have been undertaken for a collisionless plasma. However the coronal plasma around each wire of a wire array is typically so collisional that the Hall parameter $\Omega_e \tau_{ei}$ calculated using linear classical transport theory is less than unity [230]. This is also true for single wires, and it is only in the very low density outer corona that the Hall parameter is large enough to be able to apply these models of lower hybrid turbulence. However, it is very useful (see [231, 232]), to apply such an anomalous collision frequency as one approaches the plasma vacuum boundary, as it then leads to a more realistic reduction in current density. In particular, a non-singular electron drift velocity is obtained as the density approaches zero or a prescribed lower limit.

When modelling the magneto-Rayleigh–Taylor (MRT) instability in the *r*–*z* plane, e.g. [233, 234], the inward moving bubbles of plasma leave behind extended spikes. A current reconnection across these spikes in the lower density 'vacuum' would generate lower hybrid turbulence. The large, anomalous resistivity would tend to restrict the current shorting despite the low inductance path. Current reconnection is an intrinsic feature of the model proposed by Rudakov *et al* [235] to explain the dissipation of magnetic energy at stagnation (see section 5.8). A compressible electromagnetic flute mode was considered by Sotnikov *et al* [236] in a two-fluid description to explain enhanced transport across large scale structures. The model was based on a theta pinch with curvature of the magnetic field represented by a radial gravitational

53

force. Perhaps as a result the growth rate did not follow the usual $k^{1/2}$ ideal MHD dependence for a Z-pinch, but decreased with k.

Introduction of lower hybrid anomalous resistivity will also change the formula for the Pease–Braginskii current, a point followed up by Robson [125].

In section 3.14 anomalous resistivity will be introduced in a model of disruption when gaps of low density plasma exist between density islands at the time of a $m = 0$ disruption and thereafter.

It is to be hoped that with the new generation of computers further work, perhaps in 3D, full electromagnetic will be undertaken on lower hybrid turbulence, and the related modified two-stream instability.

Meanwhile attention could be drawn also to the need for better diagnosed and specially designed experiments. A paper by Takeda and Imezuka [237] presents measurements of anomalous resistivity associated with large amplitude noise at the lower hybrid frequency. Here the ratio v_d/v_i was large ($\sim 10^2$) and the anomalous collision frequency was essentially Ω_e. This leads to Bohm diffusion. It is perhaps permissible to speculate that the formula for ν_{anom} given by equation (3.54) or (3.55) is only valid up to a value of Ω_e, when it becomes independent of (v_d/v_i). For a hydrogen plasma this will occur at v_d/v_i equal to 4.2. A suitable form for the effective collision frequency ν_{anom}^* as a function of $(v_d/v_i)^2$ through equation (3.54) or (3.55) for $\Omega_e \tau_e > 1$ is given by

$$\nu_{anom}^* = \nu_{anom}/(1 + \nu_{anom}/\Omega_e). \tag{3.56}$$

3.14. Disruptions; ion beams and neutrons

During the nonlinear evolution of the $m = 0$ instability of a stagnated compressional Z-pinch or plasma focus employing deuterium as the working gas, a significant pulse of neutrons appears, typically a yield of up to 10^{12} neutrons [238, 239]. The origin of this has been a great source of debate and controversy which has still not been resolved. Some of the proposed mechanisms are fluid-like and others are kinetic in nature. An important test of any hypothetical theory is whether total axial momentum is conserved during the ion beam formation.

In fact the normally principal pulse of neutrons at the time of $m = 0$ disruption is often the second pulse [240]. The likely explanation of the first pulse is essentially kinetic in origin. It was first hinted at in Trubnikov's paper [241] and developed more realistically by Deutch and Kies [242]. Here it is considered that there is a sheet current piston which compresses the plasma as the first pinch is formed. Unlike the snowplough model, it is postulated that the ions on encountering this moving piston are reflected by it (in fact by the radial electric field in the current sheet) with twice the velocity of the piston. During this process they are essentially collisionless and also conserve their angular momentum (a point made by Trubnikov [241] and earlier by Haines [243]). On encountering the moving piston a second time, there is another gain of energy; indeed the faster ions have more reflections and gain even more energy, a feature of this Fermi acceleration mechanism. There will be, as a result, a high energy ion tail, and the ion–ion collisions which will grow in number when the piston reaches close to the axis and the density rises will also yield DD nuclear reactions, but of a suprathermal nature. If the incoming piston is conical in shape, it will also lead to a growth in axial motion. It should be noted that multiple collisions of essentially collisionless ions are needed for this, a condition which might also pertain in certain conditions in the precursor plasma of an imploding wire array.

Turning to the principal pulse of neutrons, there are important features; (i) the neutrons occur at the time of an $m = 0$ instability, a point confirmed experimentally by Bernard *et al* [238], (ii) the neutrons have an anisotropic distribution consistent with originating from an ion beam in the z-direction: This was also confirmed by Bernard who employed a deuterated
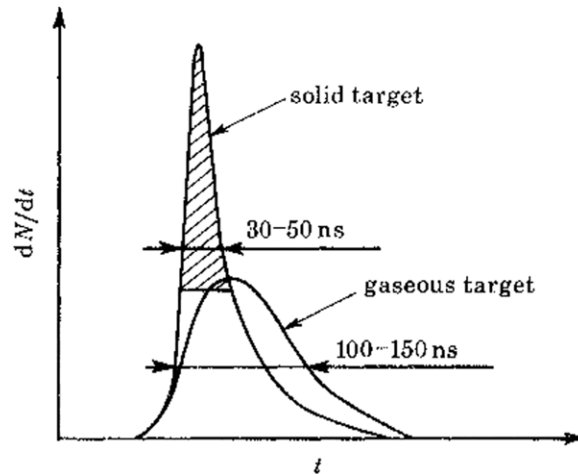
Figure 32. The rate of emission of neutrons with (shaded) and without a deuterated polyethylene target 25 mm from the anode in a plasma focus [238] or [84]. Reprinted with permission from The Royal Society.

target on axis (see figure 32) to verify this point; (iii) there is an associated relativistic electron beam travelling towards the anode, verified by measurements in a hollow anode by Nardi *et al* [244] and (iv) there is a negative voltage spike and a drop in the current. (Later on figure 77 is relevant.)

Dealing briefly with the fluid models, Anderson, Colgate *et al* [35] pointed out that at the time of the necking-off of the $m = 0$ instability, there is a large transient increase in inductance and associated electric field. In turn this electric field will accelerate the ions leading to an energetic ion beam and, by collisions, neutrons. The argument was based on ideal MHD, and as pointed out by Haines [243], in the moving plasma the electric field as seen by the ions ($\underline{E} + \underline{v} \times \underline{B}$), is actually zero. Furthermore it was shown that there is up–down (or $\pm z$) symmetry each side of a neck, even for resistive MHD, so that if any ion jets occur from the necked region, they will occur equally in both directions. It requires introduction of the Hall term and, or, the finite ion Larmor radius terms in the stress tensor to break this symmetry and allow a beam to form [243]. Filippov [245] proposed a moving boiler mechanism to explain the experimental results, a mechanism closest perhaps to that proposed by Vikhrev [246]. He postulated that a dense hot thermonuclear plasma is formed in the necks of a $m = 0$ instability, and based this on 2D MHD simulations. This is at variance with experimental measurements of Z-pinches, especially fibre pinches [247], though Kassapakis [248] has shown in a 2D simulation that a suitably tailored initial finite amplitude $m = 0$ deformation can lead to high density and temperature in a neck. Yankov [249] went further and proposed a propagating burning thermonuclear wave triggered by ignition at the $m = 0$ neck.

One of the difficulties in a kinetic model yielding ion beams is to obtain consistency with overall conservation of momentum; the question where the equal and opposite axial momentum is deposited needs to be answered. A simple electrostatic model of a diode relies on a breakdown of quasi-neutrality so that the net charge density q_v provides a force per unit volume $q_v \underline{E}$ in an electric field. Because of Maxwell's equation, this force is $\varepsilon_0 \underline{E} \nabla \cdot \underline{E}$. To explain Bernard's experiments [238] where 1.9 MA of deuteron current of energy, 300 keV was generated, it would require an electric field of over 10^{11} V m^{-1}. The equal and opposite force would occur where the corresponding negative charge is situated. Indeed in one dimension $\varepsilon_0 E_z \partial E_z / \partial z = (\partial / \partial z)(\frac{1}{2} \varepsilon_0 E_z^2)$ will clearly integrate to zero across any double layer in which

55

$E_z \to 0$ each side of the layer showing that there is no net momentum transfer. A more realistic quasi-neutral sheath acceleration was proposed by Haines [84, 243]; but this was confined to the anode sheath in which a radially inward E_z/B_θ drift of magnetized electrons would constitute the necessary $J_r B_\theta$ force, while the ions accelerated in the E_z field. The sheath thickness would lie between the Larmor radii of the electron and ion. The electrons on reaching the axis would exit axially through a hole in the anode. The equal and opposite force is transmitted to the anode itself through the magnetic pressure. It is difficult to see how such a mechanism could operate in a $m = 0$ neck in the main plasma column.

A model based on finite ion Larmor radius effects was proposed by Haines [243]. Without $m = 0$ perturbation a collisionless pinch has ion trajectories that are singular or betatron-like within one Larmor radius of the axis with a guiding-centre flow in the opposite direction off-axis, and, through diamagnetism, a net centre-of-mass velocity of zero (see section 2.2). During a dynamic creation of a $m = 0$ neck a large amount of energy is given to the ions in this region through a $\partial \underline{A}/\partial t$ electric field, leading to a beam of energetic singular ions proceeding towards the cathode, and, off axis, an equal and opposite momentum in guiding-centre ions. These ions are far more numerous and so the energy change in these is much smaller than in the beam. Nevertheless such backward moving ions have been inferred from measurements by Tiseanu and Mandache [250]. A simulation of this ion motion in a hybrid model was developed by Rickard and Lindman [251].

If the line density drops to a low value in the necked region, the drift parameter (i.e. the ratio of the electron drift velocity to the ion sound speed) increases past a critical value, leading to the onset of microturbulence. Ryutov *et al* [88] discuss the onset of this in the form of ion-acoustic turbulence, and the subsequent formation of a high energy ion tail as proposed by Vekshtein and Sagdeev [252]. Here the energetic ion tail is isotropic in the plane perpendicular to the magnetic field, rather than a beam. In this model of ion-acoustic turbulence, the fraction of ions involved in the energetic tail is $(m_e/m_i)^{1/4}$.

Trubnikov [241] considered the sudden onset of microturbulence in the neck of the unstable Z-pinch by the Buneman two-stream instability which will lead to a positive voltage spike. Keeping the total current constant, he postulated a rapid transfer of this current to an outer peripheral plasma. The drop in inductance leads to a high negative voltage in the circuit, and he considers furthermore that the peripheral plasma has a dielectric constant of (c/c_A) where c is the velocity of light and c_A is the Alfvén velocity. The ions in the peripheral plasma get accelerated in the high transient electric field by diode action and subsequently impact the adjacent dense plasma to produce neutrons.

Whilst there are difficulties over conserving the total momentum, the large electric fields needed for diode action and the concept of a dielectric under these conditions, there are some interesting and useful features for a more refined model. It can be shown that when the ion line density N_i of a Z-pinch drops below a critical value N_c based on the more general Bennett relation, (with temperature in electronvolts),

$$8\pi N_i e(T_i + ZT_e) = \mu_0 I^2 \tag{3.57}$$

when $I = ZN_i e c_s$ and $c_s^2 = e(T_i + ZT_e)/m_i$, giving

$$N_c = \frac{16\pi}{\mu_0} \frac{m_i}{e^2} = 1.3 \times 10^{18} \frac{A}{Z^2}, \tag{3.58}$$

it is impossible for a pressure balance to occur if the drift velocity is unable to exceed c_s because of microturbulence [253]. Thus in the necked region, whilst earlier the large ion Larmor radius acceleration scheme [243] might apply at first, as N_i drops to N_c microturbulence and possibly even runaway electron current will occur. Due to the large resistance at this time a transient positive voltage spike will occur. The plasma in this region will heat up by this anomalous

resistance and not be confined, but expand radially. Likewise this will lead to a redistribution of current in a time of order 1 ns (i.e. $\sim a/c_s$) and a reversal of axial electric field E_z is possible at larger radii. ($\partial B_\theta / \partial t$ is large and negative and therefore so is $\partial E_z / \partial r$). Hence there will at this time be a negative voltage spike, associated with the expulsion of magnetic flux from the necked region. The local Poynting vector will also be radially outward. The ion acceleration that could occur will be in towards the cathode near the axis and in the opposite direction at larger radii, thereby allowing axial momentum to be conserved. After this transient redistribution of magnetic field the electron current in the z-direction will be driven between these plasma density islands by a large $v_r B_\theta$ electric field, this situation then continuing in the benign decaying phase after the disruption [254]. The source of plasma for the radial outflow is the plasma islands themselves, leading to their eventual erosion as the discharge decays. This hypothesis needs to be tested both in simulations and with more experimental diagnosis of turbulence and current distribution. Indeed both Barnard [238] and Peacock [255] have found evidence of e.s. turbulence from Thomson scattering. The disruption could be a source of energetic particles in astrophysics [241]. Further discussion on neutron production in plasma focus experiments will be found in section 7.3.

4. Dynamic Z-pinch

In this section we consider the dynamic and compressional Z-pinch where the inertia and acceleration play a dominant rôle. Indeed some of the earliest Z-pinch experiments of the 1950s were in this category. In addition to the zero- and one-dimensional models of the dynamic pinch we have also to consider the RT instability. The main philosophy behind dynamic pinches is to convert stored e.m. energy rapidly into ion kinetic energy, and thence into thermal energy on stagnation.

4.1. The snowplough model

The earliest zero-dimensional model of a Z-pinch implosion is the snowplough model devised by Rosenbluth *et al* [256]. In this infinite conductivity model the current flows in an infinitesimal skin layer which acts as a piston. As the piston at radius $a(t)$ moves radially inwards due to the pinch effect, all the plasma or gas is assumed to be swept up and accumulate in this skin layer as in a snowplough. The mass of the layer is therefore continually increasing, and the momentum equation per unit length for this layer is given by

$$\frac{\mathrm{d}}{\mathrm{d}t}\left[\rho_0 \pi (a_0^2 - a^2)\frac{\mathrm{d}a}{\mathrm{d}t}\right] = -\frac{\mu_0 I^2}{4\pi a}. \tag{4.1}$$

The radial position $a(t)$ can be found for a given current waveform $I(t)$. For a linearly rising current $I = At$ the nonlinear dimensionless equation

$$\frac{\mathrm{d}}{\mathrm{d}y}\left[(1-x^2)\frac{\mathrm{d}x}{\mathrm{d}y}\right] = -\frac{y^2}{x}, \tag{4.2}$$

where $x = a/a_0$, $y = t/\tau_0$ and $\tau_0 = (4\pi^2 \rho_0 a_0^4 / \mu_0 A^2)^{1/4}$ can be integrated to give $x(y)$ for boundary conditions $x = 1$, $\mathrm{d}x/\mathrm{d}y = 0$ at $y = 0$. Assuming a solution of the form

$$x = 1 - \sum_{n=1} a_{2n} y^{2n} \tag{4.3}$$

it is easy to show that $a_2 = 1/\sqrt{12}$, $a_4 = 11/360$, etc, and a series solution can be found. Convergence as $x \to 0$ is however very slow, especially because $\mathrm{d}x/\mathrm{d}y \to -\infty$ here; a
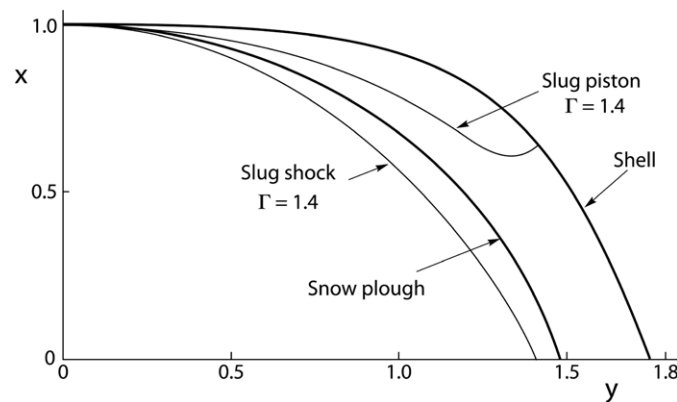
Figure 33. A dimensionless plot of pinch radius against time (a) for the snowplough model, (b) for the shell model and (c) for the slug model with the shock front trajectory given in (d).

numerical solution is tricky at $y = 0$, but a judicious mix of analytic and numerical methods leads to the result that $y \approx 1.48$ at $x = 0$. A plot of x versus y is given in figure 33(a).

Various modifications to this model can be implemented, e.g. the coupling of the pinch current to a circuit which includes the increasing inductance of the pinch with time. In section 4.4 a new analytic approach allows for the effect of increasing inductance of the imploding current shell. However the fact that the dimensionless time τ_0 depends only on the fourth root of the initial density or M_1 makes the model fairly robust and insensitive to modifications.

The snowplough model does not conserve energy, and so is strictly only applicable to a Z-pinch which can radiate the excess energy away during the implosion. It therefore might be applicable to argon or xenon discharges where the kinetic energy per ion is comparable to or less than the ionization potential. But otherwise the energy delivered to the ions through reflection in the radial Hall electric field associated with the skin current will result in shock-formation travelling ahead of the skin current 'piston'. This is the model considered next. For this the mean-free path of the particles should be small, as otherwise a collisionless reflected model [242] would be applicable.

4.2. The shock model

An analytic shock model of a fast pinch was developed by Allen [257] who used a planar model, valid at early times. Jukes [258] modified this for cylindrical geometry, making the same assumptions of infinite conductivity, an instantly rising current to a finite value and an infinitesimal shock thickness. Jukes used the classic work of Guderley [259] to find a similarity solution, in which the current I decays monotonically while with the rising inductance L the voltage LI increased almost linearly.

It soon became clear when comparing experiments with theory that to get better agreement it was necessary, especially for these early experiments in which the implosion energy per ion was comparable to the ionization potential, that dissociation and ionization energy should be included. Reynolds and Quinn [260] called this a modified shock model.

4.3. The slug model

Analytic models are however very useful for scaling purposes and for experimental design. A slug model devised by Potter [261] is a zero-dimensional (0D) model which follows the
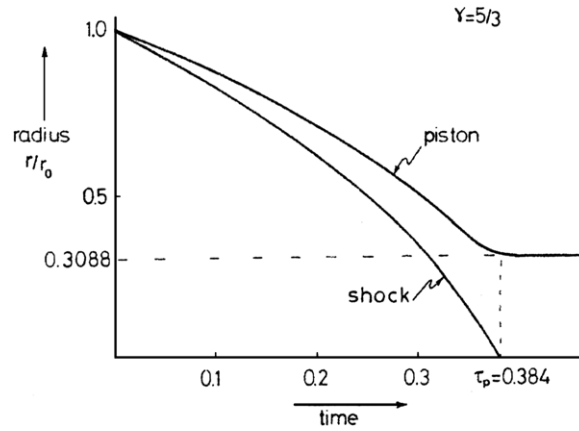
Figure 34. Trajectories calculated for the slug model with constant current [261].

trajectories of both the piston and the shock front. In many ways this aspect is similar to Kuwabara [262] who resorted to a numerical integration. Potter proceeds further to show that there is a final equilibrium, in which the ratio of the pinch radius to its initial radius becomes purely a function of Γ, the ratio of the principal specific heats.

The model assumes again a sheet current piston, and a thin shock thickness with a uniform pressure between the piston and the shock. The thinness of the shock means that planar Rankine–Hugoniot conditions can be applied to the shock transition. For a strong shock these conditions directly relate the fluid velocity u_s the density ρ_s and pressure p_s immediately behind the shock to the filling density ρ_0 and the speed of shock $v_s (= \mathrm{d}r_s/\mathrm{d}t)$ given by

$$u_s = \frac{2}{\Gamma + 1} v_s, \tag{4.4}$$

$$\rho_s = \frac{\Gamma + 1}{\Gamma - 1} \rho_0, \tag{4.5}$$

$$p_s = \frac{2}{\Gamma + 1} \rho_0 v_s^2. \tag{4.6}$$

The condition of uniform pressure between the shock and piston relies on the sound transit time being short compared with the time taken for the shock to reach the axis. This condition becomes

$$1 \gg \frac{\Gamma + 1}{[2\Gamma(\Gamma - 1)]^{1/2}} \left(1 - \frac{r_s}{r_p}\right) \left[\frac{\Gamma}{\Gamma + 1 - r_s^2/r_p^2}\right]^{\frac{\Gamma}{\Gamma - 1}}, \tag{4.7}$$

where the sound velocity immediately behind the shock is taken. As the shock converges to the axis ($r_s/r_p > 0.1$) the right-hand side is as high as 0.5 for $\Gamma = 5/3$ and 0.3 for $\Gamma = 1.4$. In addition, the sound speed decreases to about half its value towards the piston due to the temperature profile obtained by this model with no thermal conduction. Thus the assumptions are perhaps questionable.

An interesting feature of the slug model is that because of the assumption of spatially uniform pressure between the piston and shock the piston comes uniformly to rest as the shock reaches the axis as shown in figure 34, and there is no reflected shock or bouncing. The ratio

of the final piston radius r_p to initial radius r_0 is found as a function of Γ and r_s/r_p to be

$$\frac{r_p}{r_0} = \left[\frac{\Gamma}{\Gamma + 1 - r_s^2/r_p^2} \right]^{\Gamma/\Gamma-1} \tag{4.8}$$

and at $r_s = 0$ gives r_p/a equal to 0.0263, 0.1516 and 0.3088 for $\Gamma = 1.2$, 1.4 and 5/3, respectively. To obtain greater compression Potter proposes adiabatic compression of a pinch by a carefully programmed current waveform, analogous to compression in inertial confinement fusion.

The gas between the shock and piston behaves adiabatically, i.e. for a fixed mass, pV^Γ is a constant in time where V is the volume per unit length while the uniform pressure is p_s and exactly equal to the magnetic pressure, i.e.

$$p_s = \frac{B^2}{2\mu_0} = \frac{\mu_0 I^2}{8\pi^2 r_p^2}. \tag{4.9}$$

There is a subtlety in the calculation of dV and Potter shows that for an instantaneous fixed mass

$$dV = 2\pi (r_p \, dr_p - r_s \, dR_s), \tag{4.10}$$

where dR_s/dt is equal to u_s evaluated at the shock and is given by equation (4.4). The rate of change in pressure is related to the rate of change in the shock velocity by differentiating equation (4.6) to give, with equation (4.10),

$$\frac{dp_s}{dt} = \frac{4p_s}{(\Gamma + 1)v_s} \frac{dv_s}{dt} = -\Gamma \frac{P_s}{V} \frac{dV}{dt}. \tag{4.11}$$

Figure 34 is calculated for constant current [261] to consider also the case of linearly rising current so that direct comparison can be made with the snowplough and shell models. Indeed from equations (4.6), (4.9) and (4.11) a coupled pair of nonlinear equations for $r_p(t)$ and $r_s(t)$ can be derived for any given $I(t)$, namely

$$\frac{dr_s}{dt} = \frac{(\Gamma + 1)^{1/2}}{4\pi} \left(\frac{\mu_0}{\rho_0} \right)^{1/2} \frac{I}{r_p} \tag{4.12}$$

and

$$\Gamma \left[r_p \frac{dr_p}{dt} - \frac{2}{\Gamma + 1} r_s \frac{dr_s}{dt} \right] = (r_p^2 - r_s^2) \frac{r_p}{I} \frac{d}{dt} \left(\frac{I}{r_p} \right). \tag{4.13}$$

For the particular case of $I = At$ the numerical solution of equations (4.12) and (4.13) is shown also in figure 33.

4.4. Accelerating hollow shell

A zero-dimensional analytic model is a good guide for designing experiments using wire arrays, liners and hollow gas puffs. Here the mass involved in acceleration is fixed and the equation of motion is simply written as

$$M_\ell \frac{d^2 a}{dt^2} = -\frac{\mu_0 I^2}{4\pi a}, \tag{4.14}$$

where M_ℓ is the mass per unit length and $I(t)$ is either given or calculated from a circuit equation which includes the varying impedance of the load [263].

For direct comparison with the snowplough model figure 33 includes a plot of $a(t)$ for the case of a linearly rising current $I = At$ where now the dimensionless equation is

$$\frac{d^2 x}{dy^2} = -\frac{y^2}{x} \tag{4.15}$$

and τ_0 is $(4\pi M_\ell a_0^2/\mu_0 A^2)^{1/4}$ as before. It can be seen that the implosion is slower because all the mass is initially concentrated at the radius a_0, and the shell arrives on the axis at the dimensionless time of 1.752. This was found from a series solution in y up to power of y^{20}, where in a series similar to equation (4.3) only terms in powers of y^4 exist, the coefficient of y^4 being 1/12 and of y^8 1/672.

However the current waveform for Z at Sandia and for MAGPIE at Imperial College is more closely of the form

$$I = I_0 \sin^2\left(\frac{\pi t}{2t_0}\right), \tag{4.16}$$

where the current rises to a maximum I_0 in a time t_0, at least for early times. Employing the identity

$$\sin^4 z = \frac{3}{8} - \frac{1}{2}\cos 2z + \frac{1}{8}\cos 4z = z^4 - \frac{2}{3}z^6 + \frac{1}{5}z^8 - \frac{34}{445}z^{10} + \frac{62}{14175}z^{12} \cdots \tag{4.17}$$

and the dimensionless parameters, $x = a(t)/a_0$, $y = t/t_0$ and

$$\alpha^2 = \frac{\mu_0 I_0^2 t_0^2}{4\pi a_0^2 M_\ell} \tag{4.18}$$

a series solution of the form

$$x = 1 - a_6 y^6 + a_8 y^8 - a_{10} y^{10} + a_{12} y^{12} \cdots \tag{4.19}$$

can be found where $a_6 = \alpha^2 \pi^4/480$, $a_8 = \alpha^2 \pi^6/5376$ and $a_{10} = \alpha^2 \pi^8/115\,200$. The nonlinear effect of α^2 enters for higher order terms, e.g. $a_{12} = 17\alpha^2(\pi/2)^{10}/62\,370 - \alpha^4 \pi^8/1\,013\,760$. This series converges only very slowly, if at all, for practical values of α^2. Furthermore the current from a pulse-power generator is strongly affected by the impedance of the load especially due to strongly increasing inductance as the shell converges to the axis. Coupling the equation of motion to a circuit equation (as was done for example in [122]) requires a numerical solution.

However a new approach to obtain an exact, closed, analytic solution of equation (4.14) with a current waveform that peaks prior to final stagnation can be found as follows. For example, if the leading term in the above solution (equation (4.19)) is taken, i.e.

$$\frac{a(t)}{a_0} = 1 - \frac{\alpha^2 \pi^4}{480}\left(\frac{t}{t_0}\right)^6 \tag{4.20}$$

and substituted into equation (4.14) to give the current $I(t)$ as

$$I(t) = I_0 \left(\frac{\pi t}{2t_0}\right)^2 \left(1 - \frac{\alpha^2 \pi^4}{480}\frac{t^6}{t_0^6}\right)^{1/2}. \tag{4.21}$$

These values of $a(t)$ and $I(t)$ exactly satisfy equation (4.14). I has a maximum I_m at $t = t_m$ given by

$$\frac{t_m}{t_0} = \frac{12^{1/6}}{\alpha^{1/3}}\left(\frac{2}{\pi}\right)^{2/3} = \frac{1.12}{\alpha^{1/3}}, \tag{4.22}$$

$$\frac{I_m}{I_0} = \frac{3^{5/6}\pi^{2/3}}{5^{1/2}\alpha^{2/3}} = \frac{2.40}{\alpha^{2/3}}. \tag{4.23}$$

It follows that $t_m = t_0$ for $\alpha = 1.40$ while $I_m = I_0$ for $\alpha = 3.71$. A smaller value of $M_\ell a_0^2$ results in larger values of α and hence smaller values of t_m and I_m.

To further guide the choice of experimental parameters for a given generator (or vice versa) it is useful to consider the final stagnation. It is assumed to occur at a time t_s when the

kinetic energy per unit length just prior to stagnation is equal to the internal energy after one ion–ion collision time, with the Bennett relation equation (2.7) (pressure balance) holding, i.e.

$$\frac{1}{2} M_\ell \left(\frac{\mathrm{d}a}{\mathrm{d}t} \right)_{t=t_s}^2 (1-f) = \frac{N_i e T_i}{\Gamma - 1} = \frac{\mu_0 I^2(t_s)}{8\pi(\Gamma - 1)}, \tag{4.24}$$

where f is the fraction of kinetic energy lost by ionization and radiation at the moment of stagnation. Using equation (4.20) to evaluate $\mathrm{d}a/\mathrm{d}t$ together with equations (4.18) and (4.22) the ratio t_s/t_m is given by

$$\frac{t_s}{t_m} = \left[\frac{\frac{5}{2}}{1 + \frac{6}{5}(\Gamma - 1)(1 - f)} \right]^{1/6}. \tag{4.25}$$

From this it can be seen that the largest value of t_s/t_m represents the largest fractional time delay of stagnation after peak current is $(5/2)^{1/6} = 1.165$. For $f = 0$ and $\Gamma = 5/3$, the value of t_s/t_m is 1.056. These results are typically within the range of experimental data. With this model the generator essentially controls the initial rate of rise in current and the early acceleration of the load. At later times the momentum of the load controls the current which then falls prior to stagnation.

The radius at stagnation is sensitive to the value of f as well as Γ. Writing $\Gamma = (n+2)/n$ where n is the number of degrees of freedom, equation (4.20) with (4.22) yields

$$\frac{a_s}{a_0} = 1 - \frac{1}{1 + \frac{12}{5n}(1 - f)}. \tag{4.26}$$

For example, if $f = 0.5$ and $n = 3$, $a_s/a_0 = 2/7$, while $a_s/a_0 \to 0$ as $f \to 1$; but if $f = 0$ and $n = 3$, a_s/a_0 is in contrast large at 4/9. Metallic wire-array pinches tend to be excellent radiators, so f can be large and experimentally a_s/a_0 is typically $\leqslant 0.1$. On the other hand deuterium gas puffs have $f \to 0$, and the final pinch radius is a significant fraction of the initial radius. In order to obtain higher compression it would be necessary to dope the gas with argon, krypton or xenon in order to enhance the radiation loss, or as Potter [261] suggested, further raise the current in an adiabatic compression. Further terms could be added to equation (4.20) leading to additional terms in equation (4.21) if a better fit to experiment is required. In experiments with wire arrays the ratio a_s/a_0 is 1/20 to 1/10 typically, indicative of an efficient radiator, i.e. f is about 0.9 for $n = 3$. To obtain such a large and rapid conversion of energy into radiation will however probably require an additional physical mechanism as discussed in section 5.8.

4.5. Early work on numerical simulations of Z-pinches

Perhaps the earliest MHD numerical simulation was of the Z-pinch by Hain *et al* in 1960 [264] which was a 1D model of compressional pinch. It was conventionally called the 'Hain-Roberts' code. Ten years' later Roberts and Potter published a more general account of magnetohydrodynamic calculations [265]. At this time Potter [266] also published results from the 2D, two-fluid MHD code of the plasma focus (see section 7.3). The final pinch was found to be stable to short wavelength MHD modes due to damping by ion viscosity, as shown analytically earlier by Tayler [267]. Potter also found that the ions were magnetized and finite ion Larmor radius effects could be important. Viscous effects were found to be important in Z-pinch implosions simulated by Hopkins *et al* [268] in a 1D code especially at low line density and high ion temperature where the shock structure was broadened. Viscous effects will be important in ion heating with short wavelength instabilities in section 5.8.

However in many later simulations, single fluid MHD equations have been used, with an artificial viscosity replacing the real viscosity [269] and where the emphasis has been on solving compressible 3D MHD problems [270] for many Alfvén transit times.

The recent work on simulating wire-array Z-pinches will be considered in section 5.

4.6. The skin effect and inverse skin effect

One of the earliest theoretical problems in describing the dynamical behaviour of a Z-pinch was to calculate the radial current distribution. The total current is rising in time at first and then falls due to the increase in inductance as the pinch forms. For a cylindrical conductor of uniform conductivity the current density can be found knowing only the total current $I(y)$ as an arbitrary function of dimensionless time, $y = t/(\mu_0 \sigma a^2)$ [110], where a Laplace transform was employed. The formula for $j_z(x, y)$ where $x = r/a$ is

$$j_z(r, t) = \frac{1}{2\pi i} \lim_{\eta \to \infty} \int_{\zeta - i\eta}^{\zeta + i\eta} \frac{e^{yp} p^{1/2} I_0(p^{1/2}x)}{2\pi a^2 I_1(p^{1/2})} \int_0^\infty I(q) e^{-pq} \, dq \, dp, \quad (4.27)$$

I_0 and I_1 being modified Bessel functions and where a Fourier–Mellin inversion is employed. The case of a current pulse as arising from an overdamped capacitor discharge is shown in figure 35. The early skin effect is clearly identified, while after peak current the radial gradient of current density at the conductor surface becomes negative. If the rate of fall of current is sufficiently high the current density reverses, leading to an outward $\underline{J} \times \underline{B}$ force on the plasma. This was further explored theoretically by Culverwell *et al* [271].

Experiments have been carried out by Jones *et al* [272] on Z-pinches which have attributed a current density reversal to the inverse skin effect. In these experiments the outer layer of plasma is ejected by the reversed $\underline{J} \times \underline{B}$ force and this, together with its current, was measured.

More recently Lee *et al* [273] have run a 1D single fluid MHD simulation of a Z-pinch as used at CERN as a magnetic lens [274] (see also section 8.3). In this the authors find a reversed current density locally and internal to the pinch associated with the reflected shock moving radially outwards. The shock leads to compression of the azimuthal magnetic field, and so in the shock layer a large negative value of $\partial B_\vartheta / \partial r$ exists which through Ampère's law leads to a local negative j_z sheet. In this paper the authors criticize Kumpf *et al* [275] in their simulations and, more positively, draw attention to other experimental data [276, 277]. It should be noted however that many terms are omitted in this single fluid code which might significantly modify the results.

4.7. The Rayleigh–Taylor instability

The RT instability is important in all dynamic pinches where the acceleration of the plasma or shell is caused by the $\underline{J} \times \underline{B}$ magnetomotive force in the outer, lower density plasma. This instability is also the most damaging phenomenon in capsule implosions and the later fuel expansion into the denser shell in inertial confinement fusion (ICF).

Classical RT concerns the stability of the interface of a heavy incompressible fluid of density ρ_2 supported against gravity g by a lighter one of density ρ_1. It was first considered theoretically by Lord Rayleigh [278] and experimentally verified by Taylor [59] sixty years' later. The linear exponential growth rate γ is given by

$$\gamma = (kgA)^{1/2}, \tag{4.28}$$

where the Atwood number A is given by

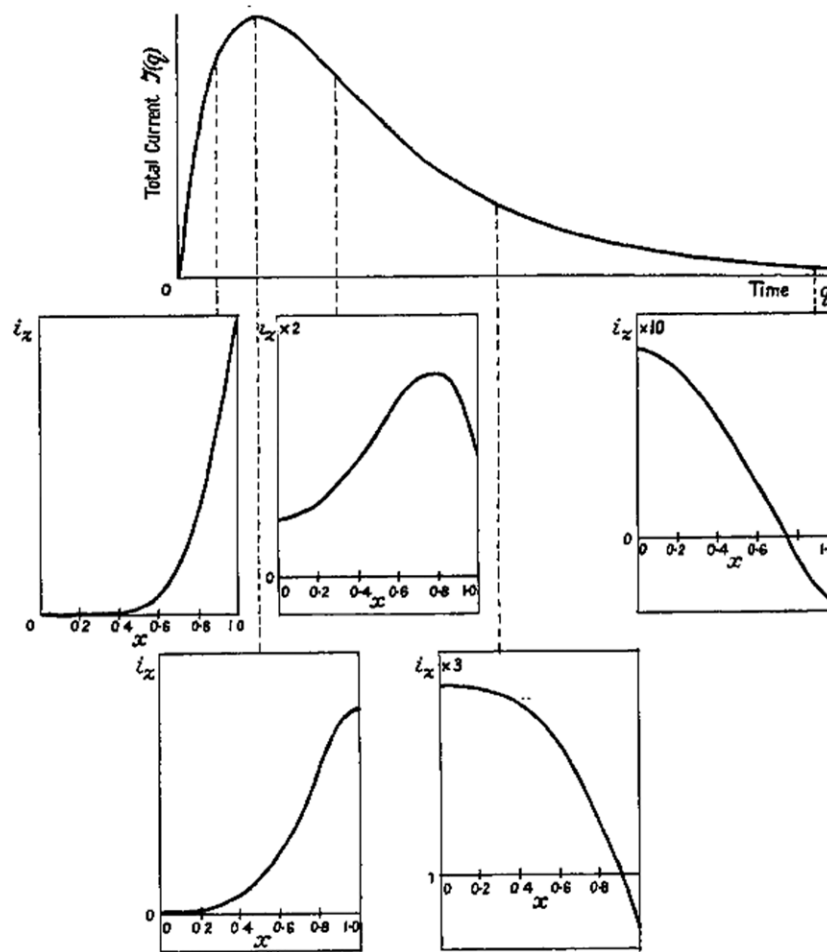$$A = \frac{\rho_2 - \rho_1}{\rho_2 + \rho_1} \tag{4.29}$$

Figure 35. Current density distributions for normalized total current $I(t) - \exp(-\alpha y) - \exp(-\beta y)$, showing early skin effect and later inverse skin and reversed surface current effects [110].

and k is the wave number orthogonal to the direction of g. Instead of gravity acting downwards the system could be accelerated upwards, with the same result. A sinusoidal perturbation at the interface will release potential energy, the heavier fluid falling and, π out of phase, the lighter fluid rising.

Some ten years later Latham *et al* [279] attributed the surface instabilities found in a dynamic Z-pinch in argon following the first bounce on axis as being due to RT, and growth rates were measured for the wavelengths found. Reference [39] presents this work in more detail. In this case the light fluid can be considered to be the magnetic field and so $A = 1$. Of course the MHD $m = 0$ compressible mode is also unstable and the competition between these modes is discussed in [39]. Later an accelerating shell will be considered, and here the RT will dominate over MHD, by the square root of the ratio of the shell radius to its thickness [280]. In general the combined mode is termed MRT, and cannot easily be dissected in simulations. However an important effect of the azimuthal magnetic field is that the MRT is essentially confined to the r–z plane.

If the magnetic field lines were straight as in slab geometry, the magnetic field has a neutral effect on the RT instability for the $\underline{k} \cdot \underline{B} = 0$ mode. To derive the RT growth rate for this case the approach of Rosenbluth and Longmire [281] can be extended to finite β (β being the ratio of plasma to magnetic pressure). For a distributed density gradient $\mathrm{d}\rho_0/\mathrm{d}x > 0$ in the x-direction, opposing g in the $-x$-direction with an axial magnetic field $B_{z0}(x)$ pressure balance is given by

$$0 = -\rho_0 g - T\,\mathrm{d}\rho_0/\mathrm{d}x + J_{y0}B_{z0}. \tag{4.30}$$

For a perturbation of the form $f(x)\exp(\gamma t - \mathrm{i}ky)$ the x and y components of the equation of motion give

$$\rho_0 \gamma v_x = -\rho_1 g - T\,\mathrm{d}\rho_1/\mathrm{d}x + J_{y1}B_{z0} + J_{y0}B_{z1}, \tag{4.31}$$

$$\rho_0 \gamma v_y = \mathrm{i}kT\rho_1 - J_{x1}B_{z0}, \tag{4.32}$$

while incompressibility is a reasonable assumption for RT, giving

$$\partial v_x/\partial x - \mathrm{i}k v_y = 0 \tag{4.33}$$

and

$$\gamma \rho_1 + v_x\,\mathrm{d}\rho_0/\mathrm{d}x = 0. \tag{4.34}$$

Ampère's law gives

$$\mu_0 J_{y0} = -\partial B_{z0}/\partial x; \qquad \mu_0 J_{y1} = -\partial B_{z1}/\partial x; \qquad \mu_0 J_{x1} = -\mathrm{i}k B_{z1}. \tag{4.35}$$

Employing the ideal Ohm's law $\underline{E} + \underline{v} \times \underline{B} = 0$, Faraday's law gives, with equation (4.33),

$$\gamma B_{z1} = -v_x\,\mathrm{d}B_{zo}/\mathrm{d}x. \tag{4.36}$$

Equation (4.32) can be simplified using equations (4.33), (4.20) and (4.34) to give

$$\rho_0 \gamma^2 \frac{\partial v_x}{\partial x} = -k^2 \rho_0 g v_x, \tag{4.37}$$

which can be integrated to give

$$v_x = v_0 \exp\left(-\frac{k^2 g x}{\gamma^2}\right), \tag{4.38}$$

where v_0 is the constant of integration. (This eigenfunction needs to be modified to satisfy boundary conditions at two finite values of x, but gives adequate results for short wavelengths.) On substituting this into equation (4.31) and again using equation (4.30), the dispersion relation

$$\gamma^4 = k^2 g^2 \tag{4.39}$$

is obtained. Thus $\gamma^2 = \pm kg$ and the $+$ sign is taken for real γ giving

$$\gamma = (kg)^{1/2}. \tag{4.40}$$

This is the same $k^{1/2}$ dependence as found for the $m = 0$ MHD instability in section 3.2, yet it is independent of the magnetic field.

The RT instability can be mitigated by many effects:

(i) Ablation of plasma, which is important in ICF both during compression [282, 283] and the deceleration phase of the confining shell [284]. This changes the growth rate to

$$\gamma = 0.9\frac{(kg)^{1/2}}{(1+kL)^{1/2}} - 3.1kV_a, \tag{4.41}$$

where V_a is the ablation velocity and L is the density gradient scale length. A more complete formula is derived in [283] while a similar formula to equation (4.41) applies in the deceleration phase [284]. This tends to stabilize short wavelength modes. It might have application to the ablative phase of wire-array Z-pinches, and compete with the nonlinear heat-flow instability [215] for the origin of filamentary structures.

(ii) Sheared flow could also reduce the growth rate of the RT instability, in analogy with sheared axial flow on MHD modes. Shumlak and Roderick [285] showed that rather high flows of order $10^5\,\mathrm{m\,s^{-1}}$ or greater are required at the outer surface of a 0.5 thick Al foil falling linearly to zero velocity on the inner edge. Large sheared flows however could trigger the Kelvin–Helmholtz (KH) instability. The authors suggest that the necessary flows could be generated with conical liners. Hammer and Ryutov [286] also discuss rotation as well as axial shear flow and give references to earlier work in this field. Douglas *et al* [287] have shown how sheared axial flows can arise through foil shaping like an hour-glass with a consequent reduction in RT growth.

(iii) Rosenbluth, Rostoker and Krall [288] consider the effect of finite ion Larmor radius on the gravitational instability. An attempt to extend this to large Larmor radii by Hassam and Huba [289] was criticized by Lehnert and Scheffel [290], mainly because the ion Larmor radii were greater than the characteristic scale length and a Vlasov treatment is required. However, during most linear or wire-array implosions the ions are too collisional for FLR to be important.

(iv) Viscosity can in principle damp high kRT modes, but the ion temperature in most implosions at this stage is too low to be effective. Ryutov [291] suggests fine scale multi-layering normal to g which will lead to sheared velocities and viscous damping on this scale. But the global mode is hardly suppressed.

(v) Bud'ko *et al* [292] found that the addition of even a relatively weak axial magnetic field can reduce the growth rate in dynamic pinches and that experiments by Felber *et al* [293, 294] show agreement. However an axial magnetic field requires a substantial energy input probably through additional coils or twisted wires [295] and the final compressed state will be weaker. (See sections 5.4 and 8.7.)

(vi) A profiled density of a gas fill can be tailored to suppress the RT instability for a certain time [296]. It requires that a shock wave propagates into increasing density thus slowing down the shock which in turn slows down the magnetic piston (not unlike the slug model), and causing a reversed acceleration. Of course an initial velocity requiring a brief, large acceleration of the piston is required but the overall growth of kinetic energy in the perturbation is reduced. The initial shock acceleration leading to a temporary RT instability is usually termed the Richtmyer–Meshkov instability [297, 298] and is finite in amplitude. However after the shock has reflected on axis there will be growth of RT associated with the hot doubly shocked plasma accelerating into the denser plasma at larger radius. So with this technique the onset of serious RT fragmentation can be delayed until late on in the discharge. Earlier theoretical work on structured profiles has been carried out for smooth density and velocity gradients by Bud'ko and Liberman [299].

(vii) The early snowplough and shock dynamics of a uniform gas fill was shown to impede the growth of RT until the reflected shock and bounce occurred [39, 300]. This was further explored by Gol'berg and Liberman [301] theoretically.

(viii) Related to these ideas are nested loads, e.g. the double-puff Z-pinch load studied experimentally by Baksht *et al* [302]. Multiple shells were studied theoretically by Cochran *et al* [303]. Nested wire arrays also give enhanced performance as x-ray radiators but here we will see in section 5.6 that there are several modes of operation including a transparent mode. There is however always significant reduction in the RT stability.

4.8. Nonlinear Rayleigh–Taylor instabilities

The nonlinear behaviour of RT instabilities has been studied for several decades especially in the case of pure hydrodynamics. In two dimensions an initial sinusoidal perturbation at

the interface grows into a bubble and spike. The bubble is rising low density fluid driven by buoyancy, while the spike is high density fluid falling almost freely under gravity. In turn the sides of the spike can be unstable to KH instabilities leading to a characteristic roll-up as the heavier fluid passes through the light fluid. In the case where the light fluid is a magnetic field, no KH instabilities will occur.

An overview of classical hydrodynamic RT in the nonlinear state has been given by Sharp [304]. 2D simulations of the nonlinear growth leading to turbulent mixing has been reviewed by Youngs [305, 306] while experiments using solid fuel rocket motors to accelerate downwards rectangular tanks of two immiscible fluids have been reported by Read [307] with accelerations of $750 \, \text{m s}^{-2}$ over distances of 1.25 m. The main conclusion of the experiments is that the denser fluid penetrates the lighter fluid at a rate $0.07 Agt^2$ in 3D. Narrow tanks were also employed to give comparison with 2D simulations where the coefficient of 0.07 is replaced by 0.06 in experiment compared with 0.04 to 0.05 in simulations. The bubbles of lighter fluid had displacements also proportional to Agt^2, with a constant of 1/2 to 1/3 that of the spike growth.

Following the bubble and spike formation, the next stages are bubble amalgamation, spike break-up and turbulent mixing, discussed briefly in [304]. Of course bubbles and spikes are purely 2D: in 3D spherical implosions Town and Bell [308] have shown that, dependent on the nature of the initial perturbation, either spikes and (connecting) valleys, or bubbles and (connecting) ridges are formed. Such spherical simulations are important for ICF capsule modelling, ideally with thermal conduction and ablation also present. A 2D representation of a spherical shell implosion with these processes present is given by Henshaw *et al* [309], where the bubble evolution is particularly important for shell integrity. The nonlinear growth of bubbles is shown to occur immediately for a perturbation amplitude greater than 0.04 times the wavelength. 2D nonlinear RT has been explored in ablation-driven shells by McCrory *et al* [310], who showed spike amplitude saturation due to ablation while the distortion of the remaining shell by the bubble development poses a limit to 3D spherical compression.

Some interesting analytic approaches to nonlinear RT in 2D are given by Ott [311], Basko [312] and by Infeld and Rowlands [313]. These have been used by Haines [280] in developing a heuristic model of the wire-array pinch. The MRT relevant to Z-pinch implosions has mainly been studied in the r–z plane as a 2D problem, assuming that the unperturbed plasma is a uniform shell. This will be discussed in more detail in section 5.5.

5. The wire-array Z-pinch

5.1. Overview

It might seem rather odd that the dynamic Z-pinch with the highest and most reproducible performance starts off as a cylindrical array of many wires stretched between two electrodes only 1 or 2 cm apart. Figure 36 is a photograph of nested arrays as typically used in high performance shots at Sandia. There is however great precision in the mounting and spacing of these wires. Even though each wire plasma at early times develops axial instabilities, the wavelength of the mode appears to only be material dependent, but their phases on different wires are uncorrelated. Thus as proposed in [280] the resulting amplitude of the seed perturbations at merger of the wire plasmas varies as $n^{-1/2}$ where n is the number of wires, a result verified by experiments at Imperial College [314]. The physical nature of this early instability which leads to many separate inward flowing plasma jets is will be discussed later in section 5.4. The single most important experimental discovery was by Sanford *et al* [20] who showed that above a critical wire number, or, rather below a critical size of gap of the order 1 mm, the resulting x-ray power increases dramatically as shown in figure 37. This is
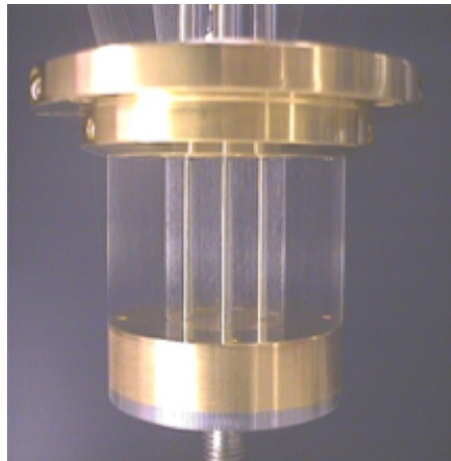
Figure 36. Photograph of nested arrays of tungsten wires strung between gold plated electrodes. Courtesy of Sandia National Laboratory.
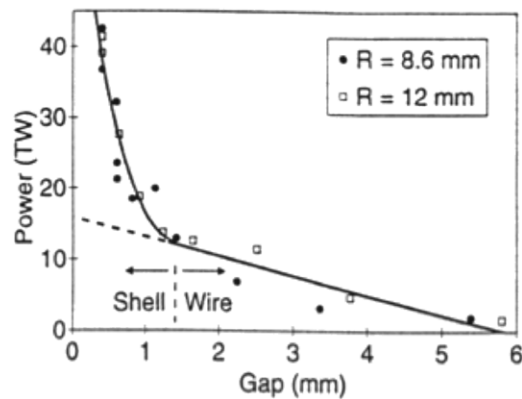

Figure 37. X-ray power versus wire spacing for two array radii. Reprinted figure 4 with permission from [20]. Copyright 1996 by the American Physical Society.

illustrated also in figure 38 where going to 90 Aluminium wires on the Saturn generator at 8 MA demonstrated not only increased power but also a sharpening up of the pulse. As a result of this, Sandia reoriented their research programme, and converted the PBFA-II generator for use as a Z-pinch driver of 11 MJ, 20 MA in 100 ns. A typical current pulse and radiated power [323] is shown in figure 39 showing a 5 ns FWHM x-ray pulse of ∼120 TW peak power. At first it was thought that the critical gap size was associated with an early merger of wire plasmas to form a shell [20, 280] which then continues accelerating towards the axis, undergoing RT instabilities. Indeed most numerical modelling at that time, e.g. [21, 234] studied the evolution of the MRT instability nonlinearly for a shell in the r–z plane until stagnation. Then the ion kinetic energy of tens of keV is converted to thermal energy by ion–ion collisions partly through shock waves the amplitude of the RT determining the final pinch radius. Subsequently by equipartition to electrons, the electron temperature increases from tens of eV to ∼500 eV or more with associated ionization and radiation. Indeed for aluminium arrays, the equipartition of energy to the electrons can govern the radiation pulse [280] while for tungsten equipartition is typically faster and the Alfvén transit time at stagnation appears to be the controlling factor [315].
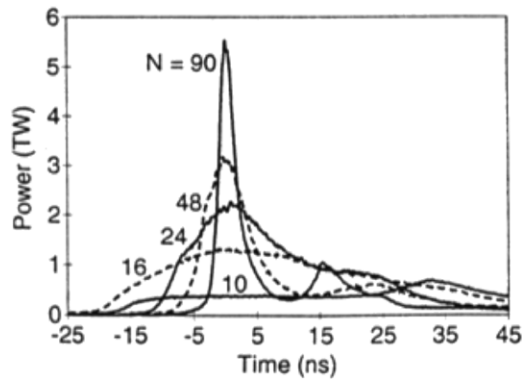
Figure 38. Aluminium K-shell x-ray power versus time on the Saturn generator for 10, 16, 24, 48 and 90 wires. Reprinted figure 4 with permission from [20]. Copyright 1996 by the American Physical Society.
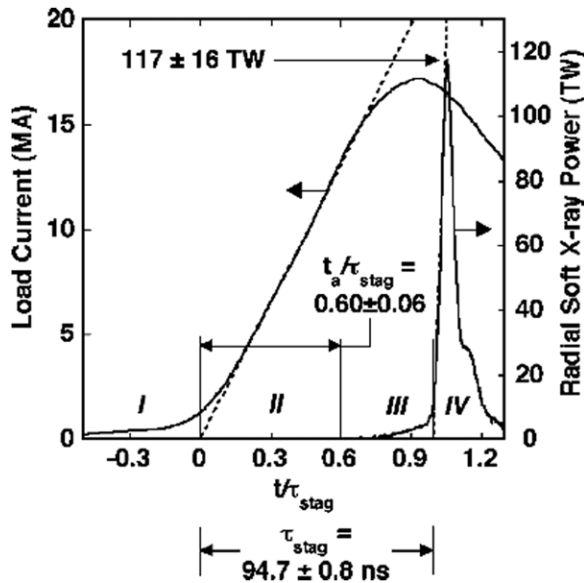

Figure 39. Current and x-ray power for a nested tungsten wire array on the Z-accelerator at Sandia showing four distinct phases; wire initiation, ablation, acceleration, and stagnation. Reprinted with permission from [323]. Copyright 2005 by the American Physical Society.

Although it has been known for some years that, at least when using a small number of wires, there is a precursor plasma [316–320], flowing from the wires towards the axis, this was ignored in the early interpretation and modelling of the data [321]. However, when following the implosion trajectory of the plasma [65] it markedly deviates from the 0D trajectory of a shell (section 4.4) as shown in figure 40. Indeed the wire cores remain stationary from 50% up till 80% of the implosion time, the inward global $\underline{J} \times \underline{B}$ force causing only the ablated coronal plasma which carries most of the current to be accelerated as a precursor, leaving the current behind. The precursor accumulates on the axis as a cylindrical column. However, when gaps appear in the wire cores (associated with necks in the $m = 0$ instability on each wire), the main
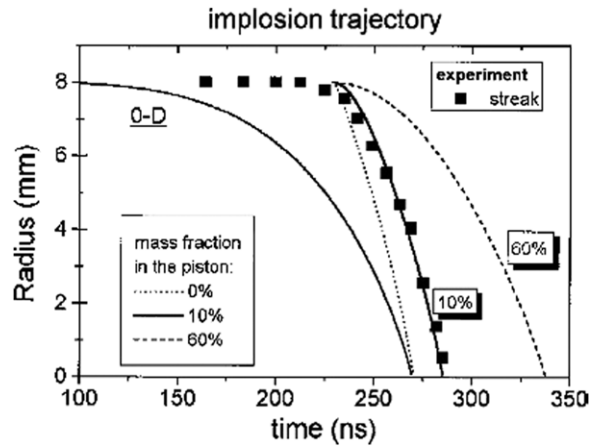
Figure 40. Experimental implosion trajectory of a $32 \times 4\,\mu$m A1 wire array on MAGPIE and implosion trajectories calculated from a model of snowplough implosion taking into account the precursor mass distribution for several cases of initial mass in the snowplough piston. The 0D trajectory is also shown. Reprinted with permission from [322, figure 5]. Copyright 2002, American Institute of Physics.
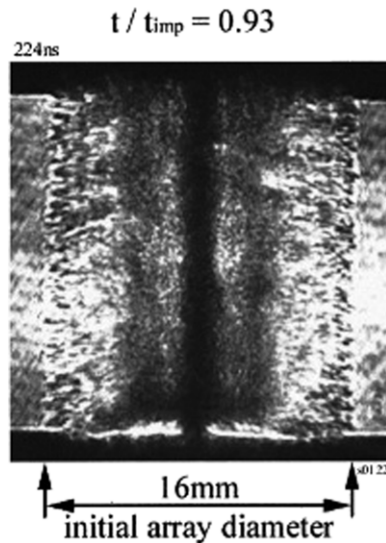

Figure 41. Side-on laser probing image of a $32 \times 4\,\mu$m W wire array showing implosion of the plasma piston onto the precursor plasma column. Reprinted with permission from [322]. Copyright 2002, American Institute of Physics.

implosion commences. Figure 41 is a laser probing snap-shot of an implosion at 93% of the time to peak x-ray power. This implosion trajectory corresponds to a snowplough as shown by Lebedev *et al* [322] in the radially distributed precursor plasma. Thus it is conjectured from the trajectories and confirmed by Cuneo *et al* [323] at higher currents that about 40–50% of the original mass is in the precursor plasma, 10–30% in the piston of the main implosion and 30–40% is left behind as 'trailing mass'. This trailing mass can be seen in figure 41 as blobs of density between azimuthally correlated gaps. 3D simulations by Chittenden *et al* [324]
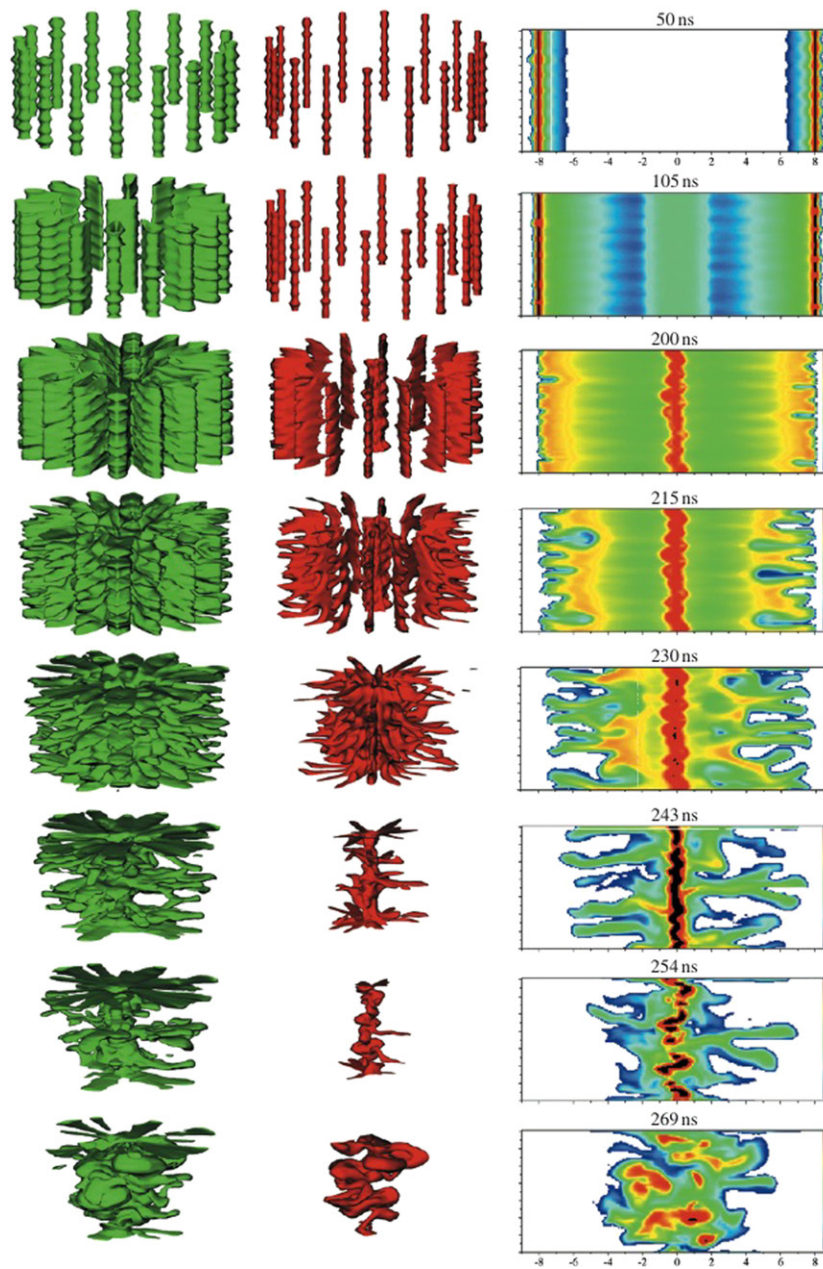
Figure 42. A 3D simulation of a 16 mm diameter array of $16 \times 15 \, \mu$m Al wires driven by the MAGPIE generator. The (red) surface of constant density equal to 0.1 kg m^{-3} is representative of the dense plasma region, while the (green) surface at 0.003 kg m^{-3} is representative of the coronal plasma. On the right are contours of ln ρ in a slice through the x–z plane [324].

shown in figure 42 have demonstrated much agreement with this interpretation of the data. It should be noted that the snowplough implosion is far less susceptible to RT instabilities. The main x-ray pulse occurs at stagnation of the snowplough implosion compressing the precursor plasma. Cuneo *et al* [323] have shown in detail that high current implosions on Z also agree

with the snowplough interpretation. Figure 43 shows x-ray images of the pinching plasma on the Z-accelerator. It is to be noted that at stagnation and during the radiation pulse the pinched plasma retains gross cylindrical symmetry, has structures, but certainly is not disrupted.

As a means of reducing the amplitude of the RT instability, Davis *et al* [60] proposed employing a second wire array of smaller diameter nesting coaxially inside the first array. It was conceived as a transparent array to which the current would switch. Experimentally Lebedev *et al* [325] showed that this would be the case, later confirmed by Cuneo *et al* [326] on *Z*. Chittenden *et al* [327] in simulations showed that there were three modes possible distinguished by the amount of momentum transfer and magnetic flux compression during collision. At this collision a radiation pulse occurs, and, if it can be enhanced in a controlled way could be the driver of one of the early shocks in a hohlraum (see section 6).

At the final stagnation the rate of conversion of kinetic and magnetic energy to radiation in high current (>10 MA) Z-pinches is generally far greater than resistive MHD models predict, by factors of up to 4, this conversion taking place in about an Alfvén transit time a/c_A. An analytic theory based on ion-viscous heating through the fastest growing, short wavelength $m = 0$ MHD instabilities gives such a heating rate and predicts, for a light stainless-steel array, record ion temperatures of 200–300 keV which have been measured by Doppler broadening of lines [130]. Earlier theories were based on larger scale $m = 0$ toroidal cavities [328] closing off and carrying magnetic flux tubes to the axis with drag heating (viscosity) and anomalous resistivity or turbulence [329–332]. At this time many bright, hot spots are observed on the axis [323] and are an important contribution to the x-ray emission. A 3D simulation of MAGPIE experiments at a current $\sim$1 MA with no viscosity and a relatively coarse mesh showed the onset of $m = 1$ instabilities leading to helical current paths increasing the Ohmic dissipation [324] and so the radiated energy. However large amplitude perturbations to the wire ablation rate had to be introduced to achieve these results. Further discussion is deferred to section 5.7.

In this brief overview it could be asked, why not use a foil instead of wires? The typical mass of a wire load on Z is 300–6000 μg cm^{-1}. A solid metallic shell would be 40–800 nm thick, i.e. as thin as a few hundred atomic spacings. Despite the difficulty in mounting such a shell, Nash *et al* [58] successfully drove an implosion but with lower performance than the equivalent wire array.

A more detailed review now follows, dividing up the processes in time as in [280, 323].

5.2. Melting and vaporizing wire cores; plasma formation

It seems crucial to understand the early phases of the evolution of the current-carrying wires in expanding liquid/vapour cores surrounded by a plasma which then carries most of the current. X-ray backlighter images of single wires of 7.5–25 μm diameter metal wires carrying currents of 2–5 kA per wire in 350 ns show that the cores are expanding and have a heterogeneous structure [333]. These novel results were obtained using an X-pinch (see section 7.6) in one of the return conductors as a hard x-ray backlighter, which yields 2.5–10 keV x-rays (when filtered by a 12.5 μm Ti foil) by a time <0.5 ns. Tungsten and molybdenum wires produced at early times what appears as a foam-like structure as vapour bubbles enlarge and coalesce. At much later times it appears instead as a vapour in which there are many liquid droplets. This occurs through a cylindrically symmetric explosion of the wire to about 10 times the initial diameter. For materials of a higher conductivity and lower melting point such as aluminium, a similar foam-like structure is seen only early on or near electrodes and is followed by complete vaporization. A titanium wire which has very low minimum conductivity was shown to have a multi-layered pancake structure on a 25 μm axial scale [219] shown in figure 44 when its diameter had expanded to 100 μm from 20 μm in 180 ns. After a few ns, the voltage to
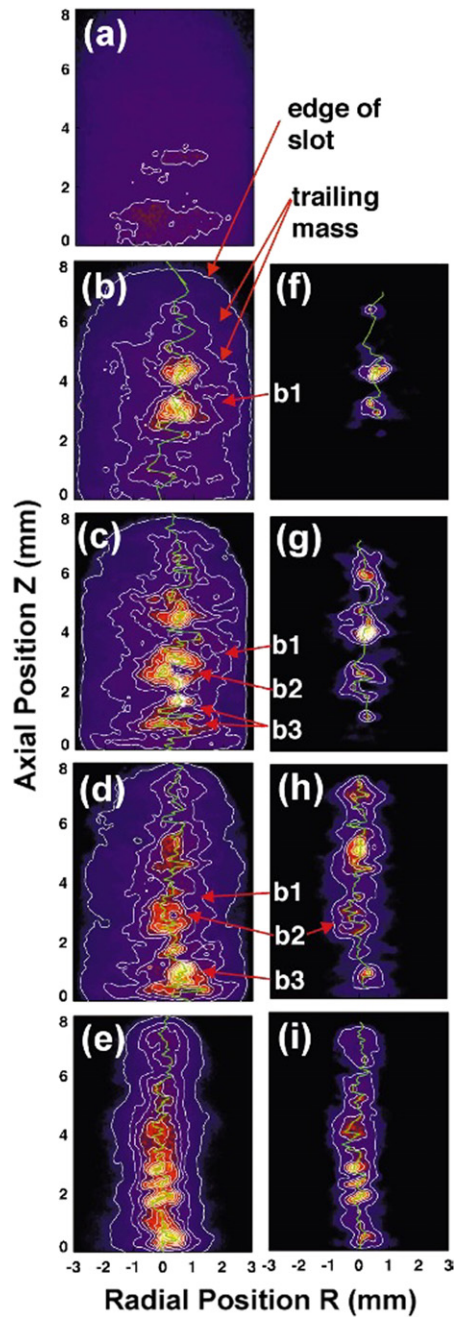
Figure 43. X-ray images of the plasma column as stagnation is reached using a nested W wire array on Z at Sandia. The large format x-ray pinhole data from shot 665 has 2 sets of filters, (a) to (e) 4.8 μm Kimfoil and 193 Å Al and (f) to (i) the Al filter is increased to 1313 Å. The times are (a) -6.6 ns, (b) and (f) -4.6 ns (c) and (g) -1.1 ns, (d) and (h) $+0.2$ ns, and (e) and (i) $+2.4$ ns relative to peak x-ray emission. The authors identify bubble regions labelled b1, b2, b3. Reprinted figure with permission from [323]. Copyright 2005 by the American Physical Society.

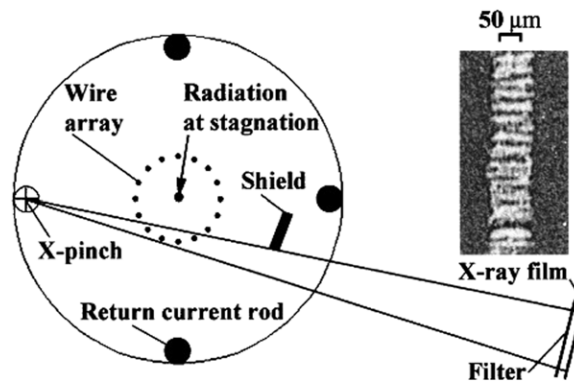**Figure 44.** Scheme of the experimental set-up for x-ray backlighting by image of a 20 μm Ti wire in a 16 wire array at 180 ns on MAGPIE. Reprinted with permission from [578]. Copyright 2001, American Institute of Physics.
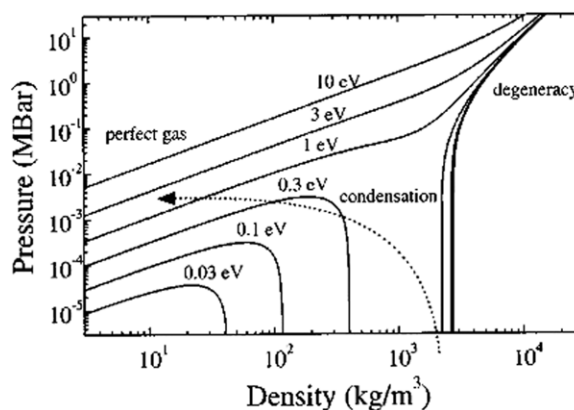

Figure 45. Electron pressure versus density for various temperatures in a modified Thomas–Fermi model. A typical trajectory for material ablated from the core and expanding into the corona is shown. Reprinted figure with permission from [336]. Copyright 2000 by the American Physical Society.

the wire induces a breakdown in the vapour (and desorbed gases) surrounding the wire core. There is a sharp voltage drop as the current transfers to the highly conducting plasma. Further experiments by Sinars *et al* measured the initial energy deposition and expansion rates of exploding wires [334]. Recently Douglass *et al* [335] employed multi-frame radiography to show the development of structure in wire cores.

This heterogeneous core structure has not been modelled and makes realistic calculations of mass ablation rates very difficult. So far the expanding cores are assumed to be in a homogeneous state, being a modified Thomas–Fermi equation of state as shown in figure 45 and used by Chittenden *et al* [336]. Here single wire 'cold-start' 2D simulations showed a persistent core surrounded by a $m = 0$ unstable coronal plasma in the r–z plane, showing excellent agreement with coronal measurements in experiments by Beg *et al* [254]. Expansion rates and coronal plasma formation have recently been studied by Shelkovenko *et al* [337].

A paper by Yu *et al* [338] shows that radiation transport is greater than thermal transport in most of the dense plasma surrounding the wire core. Yu employs r-ϑ simulations of a wire in an array to obtain the mass ablation rate in an asymptotic steady state, using a single-group radiation diffusion model. To gain physical insight and to obtain analytic scaling laws Yu
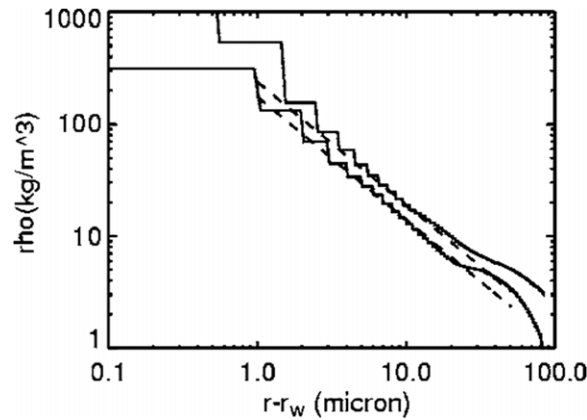
Figure 46. Plot of ρ (kg m^{-3}) as a function of $(r - r_{\mathrm{w}})$ (μm) on a log log plot for wire radius $r_{\mathrm{w}} = 5\,\mu$m (lower curve) and 15 μm (upper curve) for 100 wires and a current of 3 MA. The dashed lines show $\rho \propto [(r - r_{\mathrm{w}})(\mu m_{\mathrm{w}})]^{-1.1}$. Reprinted with permission from [338]. Copyright 2007, American Institute of Physics.
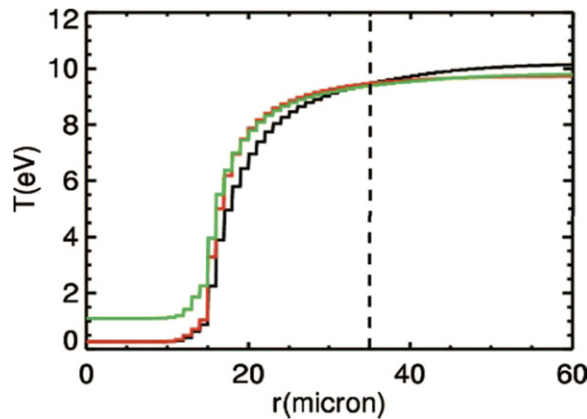

Figure 47. Lineout of T_{e} (eV) (black), radiation temperature T_{r} (red) and $T_{\mathrm{rfit}} = 2.46 T_{\mathrm{e}}^{0.6}$ (green), this being a good fit to the simulations. Reprinted with permission from [338]. Copyright 2007, American Institute of Physics.

examines what physics is dominant in a given region and compares a simplified analytic model with simulations. He finds that up to 35 μm from the wire-core surface the inward radiation energy flux approximately balances the outward enthalpy flux but beyond this Joule heating is the dominant heating mechanism. This is consistent with earlier modelling by Alexandrov *et al* [339]. In [338] rather than use the Lee–More–Desjarlais [340] transport coefficients in the core, better agreement with experiment is found by reducing the core conductivity by a factor of 10–100. As in liquid-metal MHD power generation, the effective conductivity is strongly dependent on whether there are vapour bubbles in connecting liquid or liquid droplets immersed in vapour. Percolation theory [341] gives a critical density of the mixture as one third of the liquid density below which it becomes a poor conductor. Figures 46 and 47 show density and temperature profiles computed away from the wire core radius. Note that ρ is approximately proportional to $(r - r_{\mathrm{w}})^{-1.1}$ from 1 to 35 μm from the core surface.
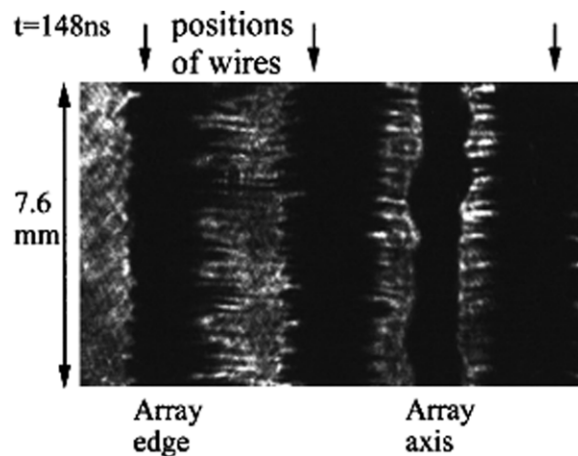
Figure 48. Side-on schlieren probing of an 8 wire Al array at 136 ns showing only a pair of wires at the array radius and another pair. The array axis is indicated and shows the accumulating precursor plasma column. Note the separate filamentary jets of plasma. Reprinted with permission from [348]. Copyright 1999, American Institute of Physics.

The onset of plasma formation in a wire array was shown very clearly in an experiment by Bland *et al* [342]. Here a magnetic probe, located in a top-hat extension of the anode (for elongated wire nested array studies), showed a sudden drop in current in the internal array when plasma formation and current transfer occurred in the outer array, indicating a drop in resistance voltage there.

Early papers on the behaviour of metal wires carrying a current should perhaps include reference to some little known work on fragmentation of wires, namely experimental work by Nasilowski [343] and by Graneau [344]. These Al wires were 1 m in length and 1.2 mm in diameter and subjected to underdamped current discharged to 7 kA over up to 10 ms. The wires broke into 20 or 30 pieces. A theory by Molokov and Allen [345] involves the dynamical response to both the Lorentz force and the thermal expansion with axially propagating waves. Tensile stress appears at the clamped ends whereas the rest is subject to compressional stress. Longitudinal waves are excited and grow in amplitude due to the stress caused by Joule heating. The ultimate strength of Al reduces with increasing temperature and when $T > 320\,^\circ$C fracture under tensile stress can easily occur. The axial wavelength could be of order the wire diameter in this model, though longer in the experiment. However in typical wire arrays as discussed here, the Joule heating rate is some 10^6 times faster and the fragmentation effect will not occur before vaporization and plasma formation, as discussed above.

The behaviour of metal wires under rapid heating by currents of up to 10^7 A cm^{-2} including the melting and liquid state and the electrical explosion and thermionic emission was carried out on the microsecond time scale by Lebedev and Savvatimskii [346].

Stratification of a liquid-metal conductor carrying a current was considered by Volkov *et al* [347] involving vortex structures with a wavelength comparable to the conductor radius.

5.3. Ablation phase and the precursor plasma

The importance of the radially inward flow of ablated plasma leading to a precursor plasma column was shown by Lebedev *et al* [348] using the MAGPIE generator [7]. Figure 48 shows side-on schlieren probing of an 8-wire Al array at 136 ns showing inward jets of precursor plasma. End-on laser probing of a 16-wire array at 97 ns in figure 49 shows the individual
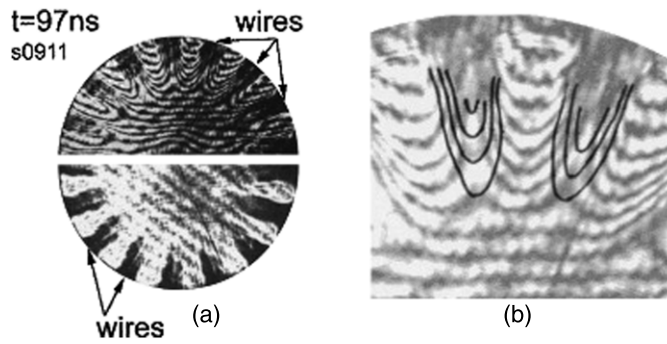
Figure 49. End-on laser probing of a 16-wire Al array at 97 ns (upper half, interferometry; lower half, shadowgraphy). On the right is a constructed isodensity plot from two wires with an increment of density of 10^{17} cm^{-3}. Reprinted with permission from [348]. Copyright 1999, American Institute of Physics.
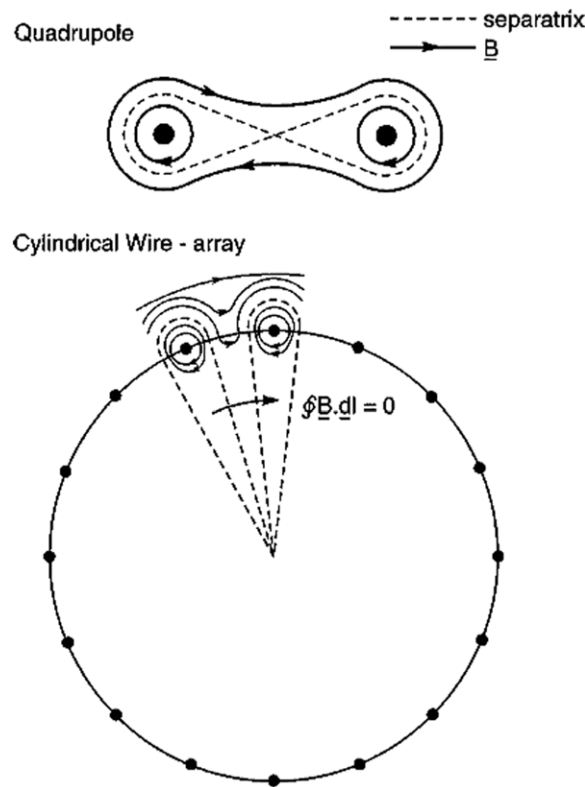
Figure 50. Magnetic field topology (*a*) for a pair of wires and (*b*) for a wire array, showing field lines and separatrices. Reprinted with permission from [349 figure 15]. Copyright 2000, American Institute of Physics.

streams from each wire. The magnetic topology experienced by the plasma is shown in figure 50; for two wires a quadrupole with a figure of 8 separatrix, while for a cylindrical wire array the separatrices cross on the array axis [349]. In both cases there are private flux lines around each wire and global field lines. For the array the latter must interpenetrate the gaps

Figure 51. A side-on laser shadowgram of a $16 \times 15 \, \mu$m Al wire array on MAGPIE at 180 ns after the start of the current [65]. On the right is a similar result from a tungsten $16 \times 7.5 \, \mu$m array. Reprinted with permission from [65]. Copyright 2001, American Institute of Physics.

between wires so that inside the current-carrying region, the closed line integral $\oint \underline{B} \cdot \underline{d\ell}$ is zero. Yu [338] found that the ablation proces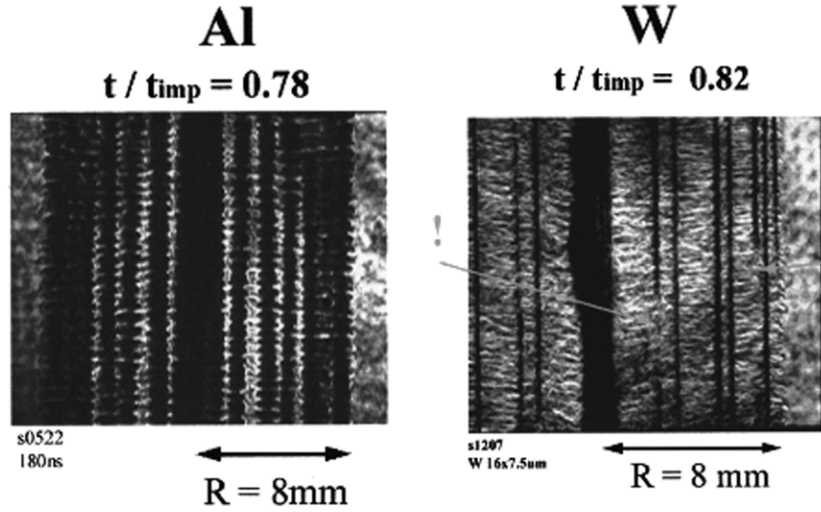s was confined to an almost azimuthally symmetric private flux region with $R_{\mathrm{m}} < 1$, and, as described above, developed a theory for the mass ablation rate.

The mass ablation rate $\dot{m}$ was very successfully modelled phenomenologically by Lebedev *et al* [65] in a rocket model. Assuming $R_{\mathrm{m}} \ll 1$ and that all the current flows in a narrow shell-like region, the magnetomotive force leads to ejection of the precursor plasma with an ablation velocity V_{a} which experimentally is found to be a constant for each material during a discharge, the rocket equation gives

$$\dot{m} = -\frac{\mu_0 I^2}{4\pi R V_{\mathrm{a}}} \; (\mathrm{kg\,m^{-1}\,s^{-1}}). \tag{5.1}$$

Knowing all the terms on the rhs from experiment $\dot{m}$ can be found and integrated in time to find the mass that has been ablated up to any time t. V_{a} is typically $10^5 \, \mathrm{m\,s^{-1}}$.

A model developed by the Angara group [339] gave a slightly modified equation for tungsten

$$\dot{m}^* = -0.4\pi \frac{I^{1.8} \, (\mathrm{MA})}{R^{0.8} \, (\mathrm{cm})} \; (\mu\mathrm{g\,cm^{-1}\,ns^{-1}}), \tag{5.2}$$

where the ablation velocity is implicitly included. Cuneo *et al* [323] claim that both formulae agree with experiment within the accuracy of measurement. Yu *et al* [338] also provide scaling laws but in terms of current and wire core radius and wire number.

A side-on laser shadowgram, figure 51, clearly shows both the inward filamentary precursor flow with a wavelength of ~ 0.5 mm in Al and the accumulated precursor cylinder on axis. As can be seen from the radial streak picture in figure 52, the precursor arrives on axis in MAGPIE at approximately half the time to full implosion, and is a bright emitter. Figure 53 shows gated soft x-ray images of precursor in carbon, aluminium and tungsten. In all cases the cylindrical column is straight with no sign of MHD instabilities, consistent with it carrying negligible current. The confinement of the column is because of the ρV_{a}^2 kinetic pressure of
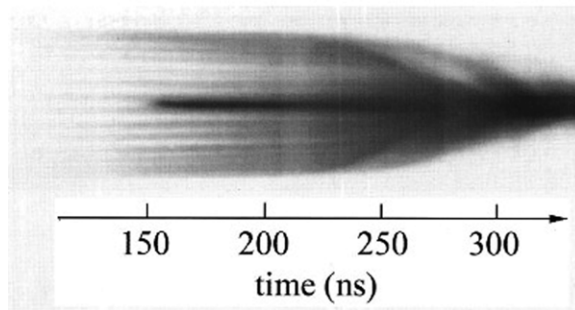
Figure 52. A radial streak picture of a typical wire array on MAGPIE. Reprinted with permission from [65]. Copyright 2001, American Institute of Physics.
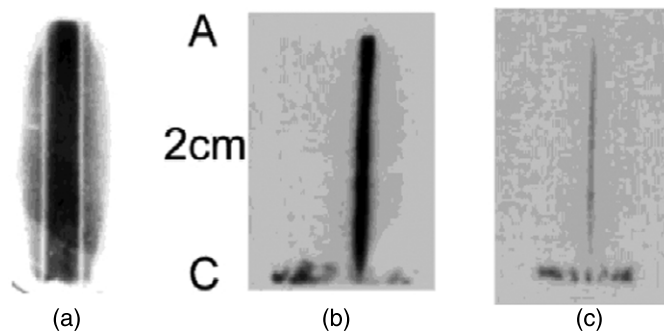

Figure 53. Gated soft x-ray images of the precursor column in carbon, aluminium and tungsten taken on MAGPIE. Reprinted with permission from [65]. Copyright 2001, American Institute of Physics.

the precursor streams impinging on it. Because of radiative cooling of the higher Z plasma there is a radial contraction of the column in W; the diameters of the columns in MAGPIE are 3 mm for C, 1.25 for Al and 0.2 mm for W. Benjamin *et al* [350] and Aivazov *et al* [319] earlier had shown the formation of a precursor column.

In a hybrid $r-\theta$ Monte Carlo treatment of the Fokker–Planck equation Sherlock *et al* [351] show that for tungsten the precursor flow is relatively collisionless, while for aluminium it becomes collisional almost immediately a significant amount of plasma arrives on axis. The precursor column forms after a critical density occurs on axis through convergence, allowing a nonlinear compression by collisional interaction with the incoming streams. The W ions are more collisionless than Al ions because the W ions have a higher kinetic energy (because of their higher atomic mass), causing an increase in the mean-free path not compensated by the higher Z value. Figure 54 shows the evolution of ion number density profile with time and also the ion–ion mean-free path and ion temperature. In contrast as shown by experimental end-on laser probing by Lebedev *et al* [352] in figure 55, the Al is more collisional and shock interactions between individual streams can be seen.

The low magnetic Reynolds number in the ablation zone was first shown by Haines [230] in a 3D analytic model of the ablation process in the presence of localized $m = 0$ necks in which Joule heating was concentrated. This led to flux limited heat flow to the cores, this providing the energy for ionization and ablation. (It should be noted that while radiation transport is dominant in the outer regions, the final heat flow to the cold cores is thermal transport.)
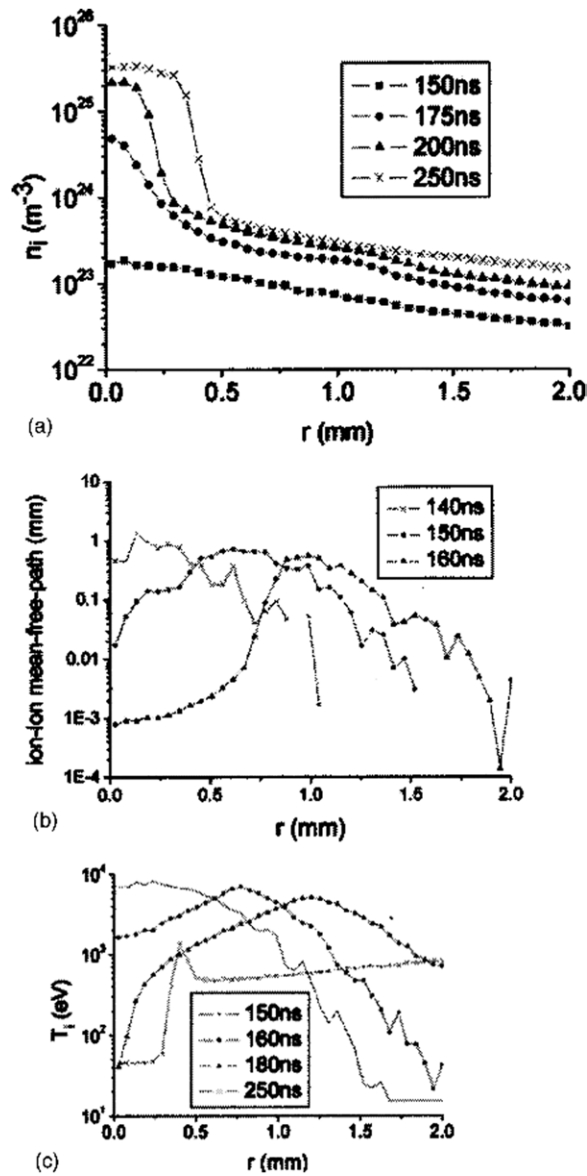
Figure 54. The precursor W ion density radial profiles at successive times, showing column formation at 200 ns, (*b*) the ion–ion mean-free path to be compared with the typical 1–4 mm scale length and (*c*) the ion temperature showing a drop on axis is at late times. Reprinted with permission from [351]. Copyright 2004, American Institute of Physics.

This plasma flows axially to the lobe regions where the global $\underline{J} \times \underline{B}$ force accelerates the jetting plasma to the axis by rocket action. It is the cooling of the Joule heated plasma by the energy flow to the cores which leads to a low magnetic Reynolds number R_m both here and in [338]. In contrast Ratakhin and Baksht [353] propose a higher current in the precursor. Currently miniature magnetic probe measurements are being undertaken at Cornell University and Imperial College. Estimates of the maximum current that could flow yet yield less than 1 e-folding time for any $m = 0$ or $m = 1$ MHD instability have been carried out by Bott
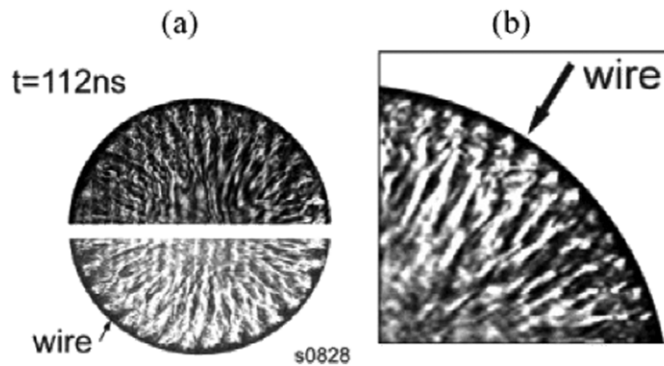
Figure 55. End-on laser probing of 32 (a) and 64 (b) Al wires showing collision of plasma streams from neighbouring wires [352, figure 9]. Copyright © 2001 Cambridge University Press.

et al [354]. This showed that less than 1% of the current could be present in the precursor on axis for W or Al wire arrays of 16 wires.

In a more academic problem, Haines [355] considers the equilibrium problem of a cylinder of plasma under pressure balance in which the Joule heating was balanced by radially inward heat flow to a cold wire acting as a heat sink. The nonlinear second order differential equation has just one free parameter, which is the ratio of the applied axial electric field to the mean radial temperature gradient. The inverse of this ratio scales as $T^2 n^{-1/2}$, thus demonstrating again that low magnetic Reynolds' number, a low Hall parameter and a mean-free path less than the collisionless skin depth occurs in the corona close to the wire core. This last condition is a criterion for the onset of nonlinear heat-flow driven electrothermal instabilities [214]. These dimensionless parameters are discussed further in [315].

A rising total current during the precursor phase and a low R_m ensures a skin current and a very small axial electric field in the flowing precursor, which in effect becomes a super-Alfvénic flow e.m. accelerator. Resler and Sears [356] considered various regimes for steady 1D resistive MHD flow, and this was extended by Haines and Thompson [357] for a spatially varying and self consistent magnetic field, finding exact integrals for the flow. In a related model of steady cylindrical 1D precursor flow Chittenden *et al* [358] have compared a steady-state analytic model with 2D r–θ simulations of precursor flow. Figure 56 is a 2D simulation of plasma ablation from one of 32 wires in an array, showing a concentration of current density on the outside of the wire core and the precursor jets flowing towards the axis (on the left of the diagram). The simulations [359] tend to show far more current in the precursor plasma than is implied by experiments, especially by the lack of $m = 1$ instabilities, but more data are required. Garasi *et al* [360] found that in 2D simulations in the r–θ plane the mass ablation rate was overestimated by factors of 10–100, and advects $5\times$ current to the axis in the precursor. Their 3D modelling was closer to experiment. A 1D Cartesian steady-state analytic ablation model by Sasorov *et al* [361] compares thermal and radiation transport. A transition from subsonic to supersonic flow is claimed in the absence of areal change in the flow, in contrast to [356, 357]. But in addition in a plasma flowing sonically against the heat flow the latter should be nonlinear as discussed later.

In contrast to steady models, it can be shown that for a rising current of the form in equation (4.16) and writing $\gamma = \dot{I}/I$ and a magnetic field of the form $\exp(\gamma t - kx)$ in a plasma of conductivity σ and ablation velocity V_a, k is given by

$$k = -\mu_0 \sigma V_a/2 + [(\mu_0 \sigma V_a/2)^2 + \mu_0 \sigma \gamma]^{1/2}. \tag{5.3}$$
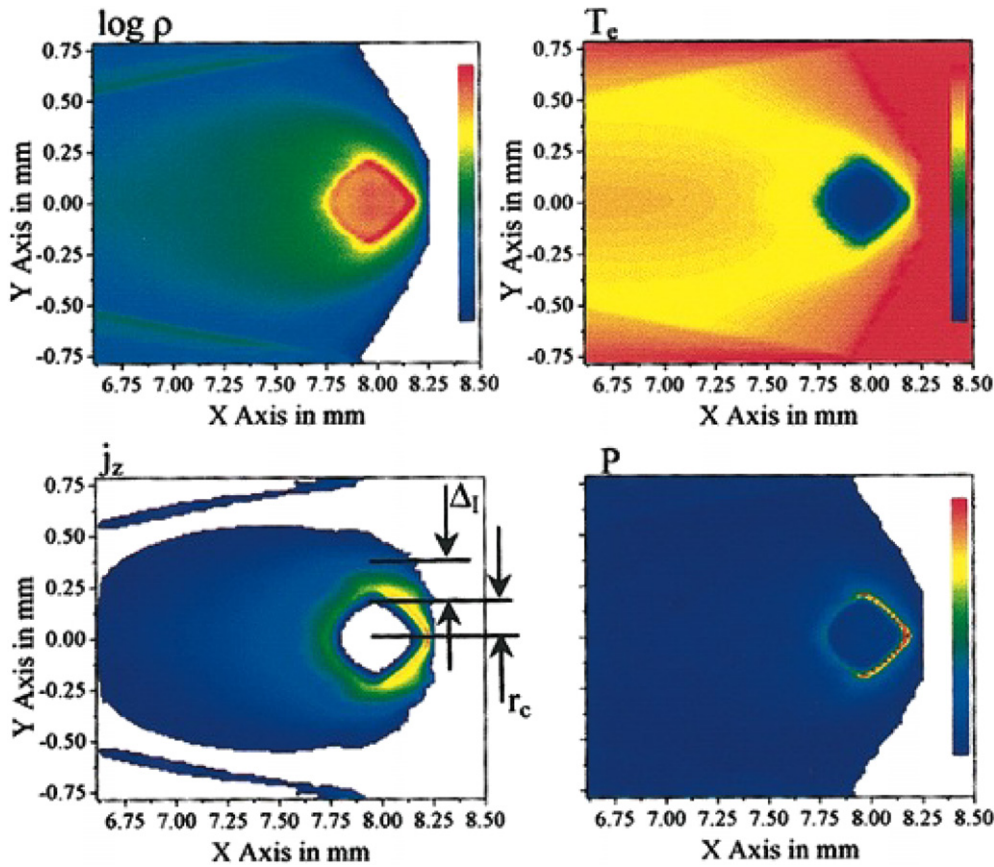
Figure 56. Contour plots of $\ln \rho$, T_{e}, j_{z} and pressure ρ at 130 ns from a 2D simulation of 1 of $32 \times 15\,\mu$m Al wires in an array on MAGPIE. Reprinted with permission from [358]. Copyright 2004, American Institute of Physics.

For typical precursor plasma conditions, $V_{a} \sim 10^{5}\,\mathrm{m\,s^{-1}}$, $\sigma \sim 2.5 \times 10^{5}$, the value of k^{-1} is not sensitive to the value of σ or V_{a} but gives 1.3 mm to 5 mm for $\gamma = (8-2) \times 10^{7}\,\mathrm{s^{-1}}$. Thus the effective skin depth for fast rising currents appears to dominate even though $\gamma \ll \mu_{0}\sigma V_{a}^{2}/4$.

If the wires are preheated Beg *et al* [362] has shown that using a linear ramp current 500 ns long of 1 kA per wire a low density precursor plasma column ($n_{e} \sim 2 \times 10^{17}\,\mathrm{cm^{-3}}$) is formed on the array axis before the start of the main current. After the main current pulse the soft x-ray emission shows the growth of an $m = 1$ helical instability; without a prepulse current the precursor plasma shows no instability. The x-ray pulse at stagnation on axis is at least 30 times smaller. Similar results of onset of a helical instability and reduced x-ray power was found by Lebedev *et al* [363] in an experiment in which additional current could be diverted into the precursor column on axis. Recent studies by Sarkisov suggest that there is an optimum prepulse condition on current, and also a polarity issue [364]. This is developed further in section 6.4 where improvements in long pulse performance is reported.

In [363] there is a study of how the ablation velocity V_{a} varies with gap/core size, x. The mean core size was measured by x-ray radiography as $250\,\mu$m approximately when the final implosion begins. The experimental results shown in figure 57 are compared with the
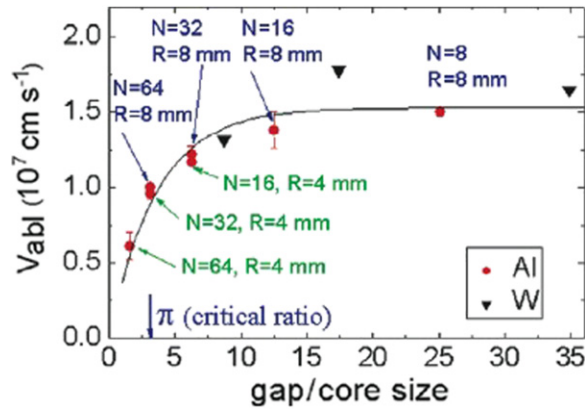
Figure 57. Ablation velocity as a function of inter-wire separation to core size for both Al and W wire arrays. The core sizes were measured by x-ray radiography [363].
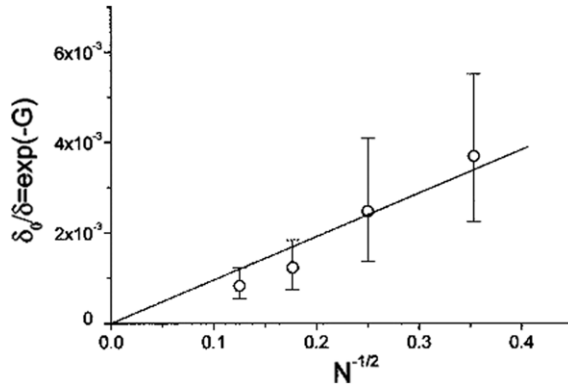
Figure 58. Fit of the experimental data to the scaling law, $\exp[-\int_0^t \gamma(t)\,\mathrm{d}t] \propto N^{1/2}$ where N is the number of wires. The error bars are due to uncertainty in the time of appearance of bright spots, equal to half the x-ray camera's interframe separation [314, figure 6] or [348, figure 9]. Reprinted figure with permission from [314]. Copyright 1998 by the American Physical Society.

phenomenological fit

$$V_{\mathrm{a}} = 1.5 \times 10^7 (1 - \exp(-x/3.4))\,\mathrm{cm\,s^{-1}} \qquad (5.4)$$

indicating for smaller gaps there is a large reduction in V_{a} and hence a large increase in ablation rate (equation (5.1)). This change is consistent with the change in magnetic topology when the private magnetic field B_θ at the core surface equals the global magnetic field (see [280]) when $d/a = \pi$. At merger, the global magnetic field would be π times the private field. Hence it can be argued as in [280] that if pressure balance (equation (2.7)) holds for each wire of line density N_j and current I_j with its private magnetic field, it cannot hold for the array as a whole, which will dynamically implode. Indeed it is possible for each wire to be exploding while the array plasma as a whole is imploding. This is because the overall line density $N = n N_j$ and current $I = n I_j$, whereas pressure balance connects N with I^2. The sharpening of the x-ray pulse at small values of the gap size, i.e. with more wires, seen originally by Sanford [20] is consistent with these ideas, as there will be significant improvement to azimuthal symmetry as well as the $n^{-1/2}$ statistical reduction in the seed amplitude of the RT. This reduction in seed amplitude, predicted in [280] is illustrated in figure 58 from experiments on MAGPIE [314, 348]. As

even more wires are used Coverdale *et al* [365] and Mazarakis *et al* [366] have shown that there is an optimum number of wires for Al and W, respectively. This could be that earlier merger and plasma shell formation permits a longer time for RT growth, reducing the tightness and symmetry of the final stagnation. Indeed it is now being recognized in simulations by Lemke [367] that the precursor could provide an optimal density profile and precursor column to maximize x-ray power. An alternative explanation could be that with more and finer wires the final radius could be smaller due to better symmetry, and this smaller radius limits the area for black-body radiation loss. A detailed experimental study of the precursor plasma has been carried out by Bott *et al* [354]. Three stages of the precursor plasma were identified; an initially broad density profile, with a critical density on axis for formation of the column, then a shrinkage to a small diameter due to radiative collapse, followed by a slow expansion. Al, W and other material arrays were compared and modelled, a kinetic model [351] being required for the first stage. A dynamic pressure balance of the column was found to hold throughout, where ρV_a^2 balances the pressure.

Single and nested nickel wire arrays (8 or 16 wires) are observed to behave rather differently to aluminium or tungsten [368] in that the precursor plasma column on axis experiences a $m = 1$ instability, implying a significant current in the precursor plasma (i.e a higher magnetic Reynolds' number), and centrally peaked. Recent low wire number (6) experiments on the 1 MA Zebra facility using copper revealed higher than expected electron temperatures of the precursor column in the range ∼450 eV [369]. Here there is a significant pulse emission of soft x-rays prior to that of the main implosion, which might be of interest for multi-shock capsule implosions.

5.4. Axial structures on wires

The cause or causes of the instability which arises at plasma formation around each wire is still not fully understood, though it is extremely important as it acts as the seed for the RT instability in the later implosion phase. It also leads to a filamentary structure of the precursor plasma, and to the occurrence of trailing mass.

The main experimental features are that the wavelength appears to be only material dependent (0.5 mm for Al, 0.25 mm for W) for all conditions. It seemed at first that the wavelength was just equal to the expanded core size [218] but later work by Bland *et al* [370] showed that for unequal core sizes on the same wires the wavelength was the same. Jones *et al* [219, 220] seeded the instability with controlled modulations on the wires. For Al wires it was found that for imposed wavelengths of the modulation much larger than the natural $m = 0$ mode, magnetic bubbles grow and at the implosion may hit the axis early. On the other hand, for a seed wavelength of 0.125 mm, smaller than the natural mode of 0.5 mm, while early flares are seen at the shorter wavelength close to the core, soon the natural wavelength occurs. This indicates that the natural mode is not seeded by surface perturbations on the wire nor by mass modulations in the core. Where the instability first arises was partially answered by x-ray backlighting [218] where the natural mode was found to occur at quite high density in the plasma around the wire core, as shown in figure 59.

Four theoretical types of instability can be considered; resistive MHD, RT, thermal and heat-flow-driven electrothermal. But first the parameter space where the instability grows will be identified, guided by experiments and the simulations of Yu [338]. An electron temperature in the range 6–12 eV will be taken and a density range (see figure 45) 3–100 kg m^{-3}. A density of 3.6 kg m^{-3} at $r = 55\,\mu$m and a mass ablation rate $\dot{m}$ of 4.8 kg m s^{-1} [338] (for $r_w = 5\,\mu$m W) leads to a flow velocity from the core to a further 50 μm of 3.9×10^3 m s^{-1}, (i.e. at approximately the thermal speed) and a transit time of 13 ns.
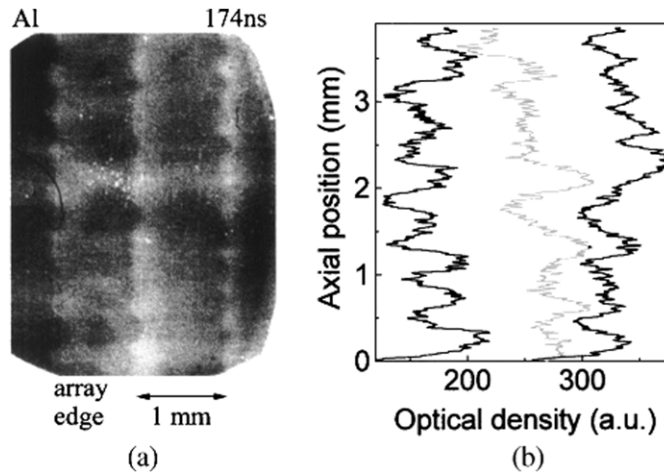
Figure 59. Radiographic image showing instabilities in cores of A1 wire array and corresponding axial profiles of film optical density (averaged over 0.2 mm). Reprinted figure with permission from [218, figure 4]. Copyright 2000 by the American Physical Society.

Therefore up to $50\,\mu$m from the core surface the magnetic Reynolds' number $R_{\rm m}$ with $L = 50\,\mu$m, $T_{\rm e} = 12\,$eV, $\sigma = 9.1 \times 10^4\,\Omega^{-1}\,{\rm m}^{-1}$ will be

$$R_{\rm m} = \mu_0 \sigma v L = 0.022. \tag{5.5}$$

This flow velocity is close to sonic and the Alfvén speed and so represents the Lundqvist number S approximately also. As discussed in section 3.3 and in [153, 154], the resistive MHD $m = 0$ instability is significantly modified by the Joule heating in these circumstances. Indeed the velocity times length can increase significantly before $R_{\rm m}$ approaches one and Alfvén waves can propagate.

In the region immediately surrounding the wire cores for 50–$100\,\mu$m the density gradient is in the opposite direction to the ablative acceleration, and so here it is RT stable. Only further away in the more tenuous regions experiencing the global $\underline{J} \times \underline{B}$ force will there be RT instability. The rising current pulse ensures a skin effect with a skin depth δ given by

$$\delta = [t/(\mu_0 \sigma)]^{1/2}. \tag{5.6}$$

At $50\,$ns this will be $0.7\,$mm. Lebedev *et al* [348] measured a precursor velocity from side-on schlieren of $3.2 \times 10^4\,{\rm m\,s}^{-1}$, while from end-on looking at lower density contours it was $1.5 \times 10^5\,{\rm m\,s}^{-1}$. The latter was employed in figure 57 taken from [363]. Thus the acceleration $g = v^2/2s$ is $1.6 \times 10^{13}\,{\rm m\,s}^{-2}$ where the acceleration distance is $0.7\,$mm. The acceleration time v/g is $9\,$ns, while the growth rate $\gamma = (kg)^{1/2}$ for a wavelength of $0.25\,$mm is $6 \times 10^8\,{\rm s}^{-1}$ or an e-folding time of $1.6\,$ns giving 5.7 e-folding times. Thus the RT, or rather MRT, will be important at distances $\gtrsim 100\,\mu$m from the wire cores. The fastest growing mode in the presence of resistive damping could have the natural wavelength. But it is only a secondary instability because it cannot occur within $50\,\mu$m of the wire core, contrary to observation and there is no natural wavelength.

Nonlinearly the plasma is considered to flow at first axially away from a $m = 0$ MHD neck due to pinching by the private magnetic flux. Then due to the dominance of the global magnetic field, it will accelerate radially inwards towards the array axis [230]. Recently a 3D resistive MHD simulation by Chittenden and Jennings [371] for Al has found such flows, and they conjecture that it is the r–θ geometric dimension involved here that determines the axial

wavelength. Initial fine-scale random perturbations of temperature in the core were introduced in order to seed the instability. Earlier 2D and 3D simulations by Frese *et al* [372] as well as Garasi *et al* [360] also contributed usefully to understanding the physics. The emphasis here was to question the notion that merger of plasmas from separate wires occurs and leads to the formation of a shell, rather than to the inward flow of separate plasma jets.

Axial wave numbers would be characteristic of a thermal instability in a conductor in which the resistivity η *increases* with temperature T and the current is in the axial direction. The instability arises because in a region of increased temperature but current density continuous, the heating rate ηJ^2 will be increased, so increase the temperature further. However $d\eta/dT$ is > 0 for W at solid density only below 1 eV and as the density is dropped the point where $d\eta/dT = 0$ moves to lower temperature. For Al, $d\eta/dT$ is >0 at solid density below 6 eV and is less pronounced as the density drops. Short wavelengths would be damped by thermal conduction, but there does not appear to be a mechanism to give a natural wavelength, and certainly for W, the $d\eta/dT > 0$ effect disappears in typical corona close to the wire core. Further discussion on this can be found in [738] including the composition with MHD modes.

The fourth candidate is the heat-flow driven electrothermal instability, proposed for conditions of nonlinear heat flow such as near the ablation surface of an ICF capsule [214], where the heat flow is $\geqslant 3\%$ of the free-streaming limit. It is discussed in detail in section 3.12. A second necessary condition is given by equations (3.50) and (3.51). Taking equation (3.52) and inserting for W with $Z = 6$ and $T_e = 12$ eV and a wavelength λ of 0.25 mm this instability will occur at an electron density of n_e of 6.8×10^{25} m^{-3} or a density of 3.5 kg m^{-3}. Referring to figure 46, it can be seen that this is the density at 50–100 μm from the wire core. Further in, at high density this and shorter wavelengths will be locally unstable, but the shorter wavelengths will be damped by thermal conduction as the plasma ablates and the density drops. Perhaps this occurs in the experiment of Jones *et al* [219]. The condition (3.51) is well satisfied. The growth rate (equation (3.53)) is 6.3×10^8 s^{-1} or an e-folding time of 1.6 ns compared with the ablation transit time of 13 ns. For Al with $Z = 2$; $T_e = 12$ eV and a wavelength of 0.5 mm, this will be the fastest growing mode at a density of 0.43 kg m^{-3}. Shorter wavelengths will occur at higher density or lower temperatures. In this theoretical model there is no radiation transport, but very close to the high density wire cores the thermal conduction is more important. Furthermore the process of ablation of ions requires, in this range of density, the frictional drag by the cold return current associated with the nonlinear heat flow [215]. The perturbations in return current flow will lead to perturbations in the mass ablation rate, leading eventually to gaps. It can also be argued that radiation transport also leads to a thermoelectric field due to photon momentum deposition, and hence a return cold current which can be thermally unstable. To summarize, the electrothermal heat-flow instability will occur close to the wire cores and a natural wavelength emerges as the fastest growing mode where the plasma exits the core interaction region. Unfortunately, it cannot be modelled by present fluid simulations, and requires at least a hybrid code. Probing the wires with MeV protons [217] should resolve the issue as the electrothermal instability occurs at high density and low temperature, i.e. close to the cores.

In a recent experiment using the Cornell Beam Research Accelerator (COBRA) by Knap *et al* [373] the axial wavelength and amplitude of the instability together with the core radius were measured as a function of time using laser shadowgraphy. It was found that both grew from ~0.1 mm to ~0.5 mm over 30 ns from breakdown. At this time there is saturation, and the wavelength is essentially the fundamental wavelength that had been measured in earlier experiments. The saturation is believed to be associated with the inward flow of precursor plasma and change in magnetic topology, similar to MHD simulations [371]. *B*-dot probes show the reduction in the initial private magnetic flux around each wire and the dominance of the global field (see figure 50(*b*)) by this time.
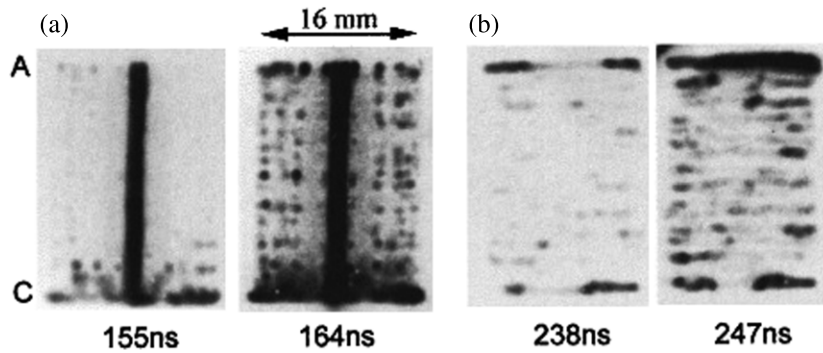
Figure 60. A sequence of side-on soft x-ray images on MAGPIE for an array of 16 wires at 155, 164, 238 and 247 ns. Reprinted figure with permission from [314, figure 4]. Copyright 1998 by the American Physical Society.

Novel experiments have been carried out using coiled or helical Al wires in an array by Hall *et al* [295]. The complex 3D Lorentz forces were modelled by MHD simulations. It was found that outside the diameter of each helix the flow of ablated plasma is now modulated at the wavelength of the coils rather than at the fundamental wavelength. Furthermore with only eight helical wires the resulting x-ray power at stagnation was surprisingly increased to that of a 32 wire implosion on MAGPIE. However more recently Hall *et al* [374] have shown that the fundamental mode does occur initially close to the wire cores. Further details of an experiment with etched wires can be found in [375].

5.5. Main implosion

The ablation of the wire cores is axially non-uniform due to the occurrence of the instability, discussed in the previous section and an early implosion adjacent to the cathode. At a certain stage, typically at a time of 80% of the total time to implosion, gaps appear in the necks of the instability on each wire, accompanied by correlated bright spots due to the development of the global MRT instability. A sequence of soft x-ray images is shown in figure 60 from [348]. With no wire cores in the gaps the plasma heats up; the magnetic Reynolds' number can be inferred to exceed one, and the $\underline{J} \times \underline{B}$ global pinching force causes the main implosion. The implosion's trajectory is shown in figure 40, and, as discussed in section 5.1, figure 41 illustrates the imploding current shell which acts to a good approximation as a snowplough, sweeping up the precursor plasma still in its path. This considerably reduces the growth of RT because the piston is forced to move at almost constant velocity. Lebedev *et al* [65, 376] estimated the radial mass distribution $\rho(r, t)$ at a position r at a time t, taking into account the time delay required for the precursor material to reach the position r to be

$$\rho(r, t) = \frac{\mu_0}{8\pi^2 R_0 r V_a^2} \left[I \left(t - \frac{R_0 - r}{V_a} \right) \right]^2, \tag{5.7}$$

where $I(t - ((R_0 - r)/V_a))$ is the current in the array at the earlier time $t - (R_0 - r)/V_A$. With $r = R_p$, the radius of the precursor column, the total mass in the precursor column can be found by integrating equation (5.1) to the time $t - (R_0 - R_p)/V_a$.

Using a snowplough model of the implosion as in section 4.1 with $\rho(r, t)$ given by equation (5.7) and by varying the initial mass in the piston a fit can be made to the trajectory of the final implosion as shown in figure 40. Similar detailed fitting of Z data from Sandia can be found in Cuneo *et al* [323]. A small correction could be made for the motion of the gas being swept up.
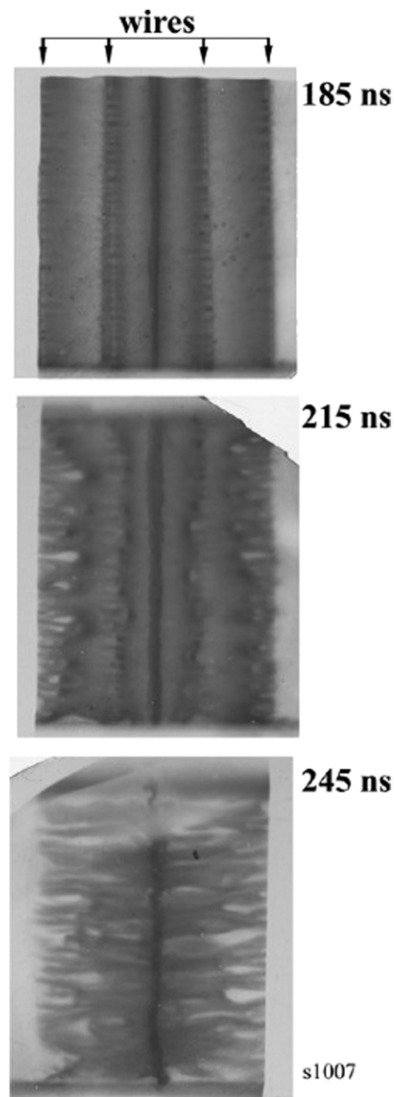
Figure 61. XUV images of the transition from the ablation phase to the implosion phase and stagnation in a $8 \times 10\,\mu$m Cu wire array on MAGPIE [363, figure 53(a) only].

During this final implosion, the RT instability will continue to develop albeit at a greatly reduced rate. The r–z simulations, if they include precursor plasma ahead of the piston [377] are relevant here. Furthermore shock heating and reflection together with compression of the precursor column are now important additions. The skin depth of the current and magnetic field will increase with time due to both diffusion and cylindrical convergence [110]. The final pinch radius will depend on these two effects, the RT wavelength having now grown to typically 2 mm, i.e. approximately the effective thickness of the shell as discussed in [280] and section 4.7. Figure 61 shows three consecutive XUV images of an implosion in a $8 \times 10\,\mu$m Cu wire array, the first at 185 ns is at the end of the ablation phase, showing the characteristic $\sim$0.5 mm wavelength of the modulation, with the emission concentrated near the wire cores. The precursor column on the axis is clearly seen, having formed by 130 ns, and has compressed
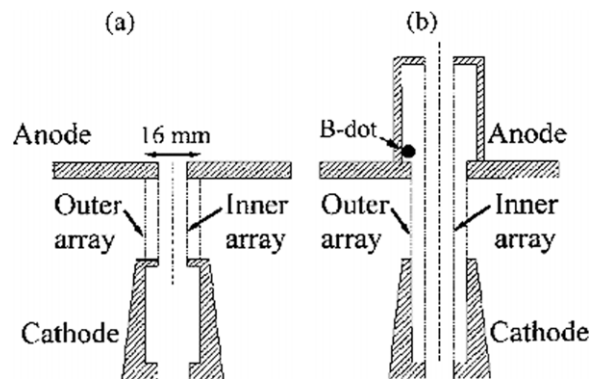
Figure 62. Schematic of nested wire arrays with (*a*) low inductance and (*b*) high inductance connection of the inner array. Reprinted figure with permission from [325, figure 1]. Copyright 2000 by the American Physical Society.

by radiative cooling coupled with the kinetic pressure ρV_a^2 of the impinging precursor streams. At 215 ns, figure 61 shows the structure of the 'magnetic piston' half-way through the implosion phase, and consists of a large number of axisymmetric $m = 0$ magnetic bubbles moving towards the axis. To the extent that it is a snowplough mechanism which requires energy loss, inelastic collisions (excitation and ionization) will lead to XUV radiation, and this is stronger in front of the larger bubbles that move faster. By now the wavelength of the modulations has grown to ~ 2 mm. Even with the small number of wires in this particular array the onset of global correlation is very evident, and represents the same phenomenon as observed in high wire number arrays. The RT structure is similar to that simulated by Peterson *et al* [233]. Note that in the laboratory frame as opposed to the accelerating frame represented in theories by gravity g, the bubbles are accelerating inward while the spike tips remain at the original wire-array radius. These spikes form the trailing mass, clearly obvious at 245 ns in figure 61, which will be considered in section 5.11. During the ablation and implosion phases, there appears to be no evidence of kink and azimuthal displacement instabilities as proposed by Felber and Rostoker [378], Marder *et al* [379] and Hammer and Ryutov [380] which would probably be only slowly growing anyway. Ivanov *et al* [381] imaged bubble formation in 8- and 4-wire cylindrical arrays, and employed Faraday rotation techniques to measure the magnetic field strength. However such fields are unlikely to be characteristic of high wire-number implosions.

5.6. Nested arrays

The use of a nested, inner array has led to a significant improvement in the performance of the wire-array Z-pinch, and was used in high performance shots [1, 2] and in recent detailed studies [323]. It was proposed by Davis *et al* [60] so that, as the outer array plasma passed through the inner array, the current would switch to the inner array, because of the high conductivity of the inner wires and the inductive coupling between the two arrays. At this time the driving force behind the RT growth would also transfer to the inner array which would start to ablate and implode with initially no RT amplitude; thus at the final stagnation a much more symmetric plasma should result.

Simulations by Chittenden *et al* [327] show three modes of operation as discussed in section 5.1 while experiments on MAGPIE [325] distinguished two modes, dependent on the fraction of total current induced in the inner array. Experiments were conducted with a 16 mm diameter outer array and an 8 mm diameter inner array each $16 \times 15\,\mu$m aluminium. Figure 62

shows (*a*) the (standard) low inductance scheme while (*b*) shows a novel high inductance inner array. The former had wires of 2.3 cm length while the inner array in (b) was 8.3 cm. Calculations by Chittenden *et al* [231] of magnetic diffusion in the r–θ plane indicated that the inner array in (a) carried 20% of the total current, while for case (b) measurements by the B-dot probe showed that the inner current was only $\sim$8 kA during the first 20 ns while the outer array was highly resistive, and it fell to lower values by the time of the collision of the two arrays. In case (a) at early times comparable wire-core expansion of both inner and outer arrays was measured by laser shadowgrams, while in case (b) very little expansion of the inner array wire cores was seen. The optical streak photographs and the plot of trajectories indicate two very different modes of operation. In figure 63 for the low inductance case shows the inner array accelerating inwards before the arrival of the outer array and both arrive on axis together. In contrast, for the high inductance case, a clear 'transparent' mode occurs with the outer array plasma proceeding between the wires of the inner array which then accelerate from rest with 100% transfer of the current. In both cases the streaked images show a precursor plasma on axis at $\sim$135 ns. Soft x-ray emission at early times is believed to be due to the impact of precursor streams from the outer array, as current alone does not lead to such emission. With more wires and higher current and rate of rise in current, the transparent mode appears to be dominant in nested W wire arrays on Z up to 19 MA [326]. This suggests that very little current flows at early times in the inner array, and after the outer passes through it, there is a rapid current transfer. After which, the inner behaves as a single array with its own precursor streams from each wire, axially non-uniform delayed implosion with trailing mass.

This current transfer was first modelled by Terry *et al* [382], reasoning that it was caused by the higher radius path and lower inductance of the inner array after the outer passed through. Experimental confirmation of current transfer was shown by Bland *et al* [383] on MAGPIE while Sanford *et al* [384] demonstrated that the transparent mode applies to nested arrays as used for dynamic hohlraum studies at currents up to 20 MA. The normal mass ratio of the outer to inner is 2, but when reversed it was clear from the timings of the x-ray emission peaks that the transparent mode applied. Numerical simulations were complemented by analytic theory, which showed that the current switching was driven by the larger electric field $\sim$7 $\times$ 10^7 V m^{-1} experienced by the stationary inner array, while the highly conducting moving outer array had a greatly reduced effective electric field, $(E_z + v_r B_\vartheta) \approx 3 \times 10^6$ V m^{-1} due to the large negative radial velocity v_r. The current transfer can occur in a time $<$2 ns. By Lenz's law opposite image currents are induced in the neighbouring moving plasma, resulting in the latter carrying closed loops of current which resistively decay on a 5 ns time scale.

5.7. Stagnation on the axis

Both the precursor plasma and the outer wire array will stagnate on axis. If the current is still flowing in the imploding inner array, only relatively small x-ray peaks will characterize these earlier stagnations. Here the ion kinetic energy is randomized to yield an ion temperature and then equipartition of energy to electrons raises the electron temperature, causing further ionization and radiation loss.

The presence of the precursor column on axis can lead to this being further heated by radiation from the imploding plasma [323] causing a large rise in temperature from 25 to 75 eV, and an expansion on Z. The presence of the precursor column has been shown by Hall *et al* [385] to lead to hollow radiation profiles. For Al wire arrays Al XII line emission occurs from the compressed precursor column, while continuum and Al XIII line radiation occurs in the surrounding pinch in hot spots. It should be recalled that significantly higher temperatures were found with low wire-number Cu experiments [369].
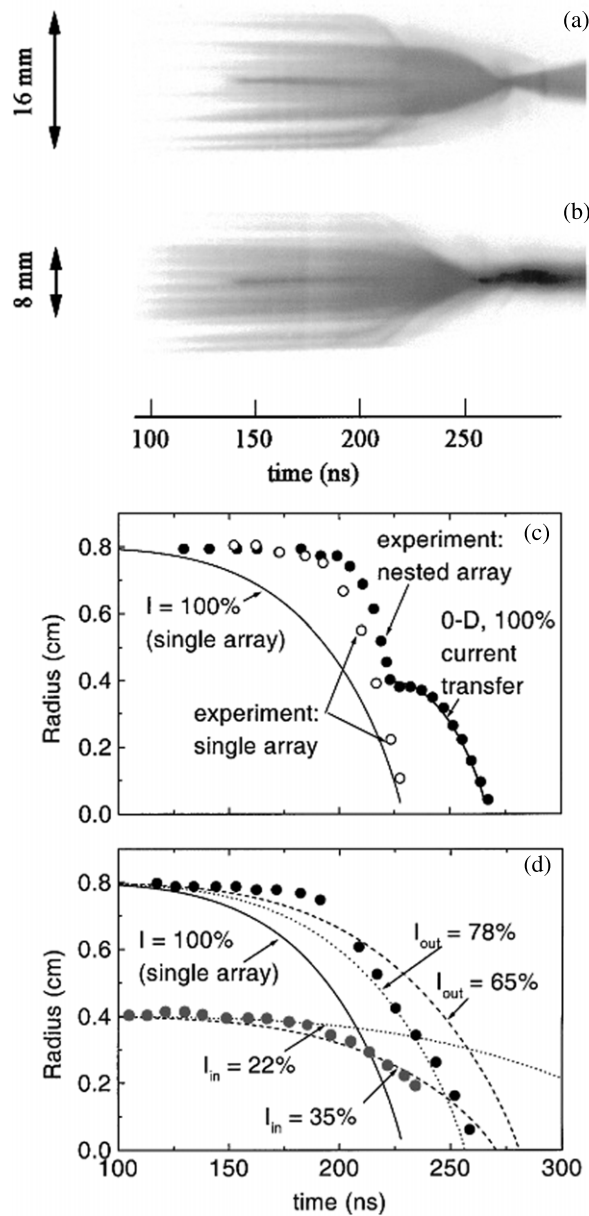
Figure 63. Radial optical streak photographs and comparison of the inferred radial positions of the inner and outer arrays with the 0D model. Reprinted figure with permission from [325]. Copyright 2000 by the American Physical Society.

It is only when the current-carrying final implosion (of the inner array for a nested array operating in a transparent mode) stagnates on axis that the large x-ray pulse occurs. For small ion–ion mean-free paths a shock will recompress the precursor plasma on the axis, and there will be conversion of directed ion energy into thermal ion energy on the τ_{ii} time scale. This is followed by equipartition on the longer τ_{eq} time scale accompanied by soft x-ray radiation as proposed in the heuristic model [280]. Indeed for low wire number Al implosion it is τ_{eq}

that determines the x-ray rise time, while, when this is shorter than the Alfvén transit time $\tau_A \equiv a/c_A$, which determines the bounce time and subsequent plasma expansion, it is the latter which determines the pulse rise time and width.

Another phenomenon which broadens the x-ray rise time and pulse width is axial non-uniformity associated with zippering which in turn can be associated with the axially varying radial electric field. This will be considered in section 5.10.

The pinch radius, or rather the FWHM density profile of the hot plasma (excluding trailing mass), is probably determined by several physical mechanisms; the radial amplitude of the RT instabilities; the radius of the imploding current shell when it responds to the reflected shock from the axis; if the implosion is very three dimensional with kink modes and local angular momentum (see [324]) it is the angular momentum or rather the centrifugal force together with the generated axial magnetic field pressure which prevents further compression.

In 1D and 2D simulations a problem arises when the current greatly exceeds the Pease–Braginskii current [8, 9] in that a radiative collapse will occur as the radiation loss at pressure balance exceeds the Ohmic (or Joule) heating. Since experimentally collapse does not occur, it has to be prevented artificially in the codes. In section 5.8 we will find that inclusion of $m = 0$ modes and ion viscosity provide a natural physical process for preventing radiative collapse.

5.8. $m = 0$ instabilities and ion-viscous heating

In some experiments the radiated energy could be 3 or 4 times the kinetic energy [1, 365, 386–388], and, if it were assumed that the ion temperature is equal to the electron temperature the plasma pressure was too low to balance or overshoot the magnetic pressure at stagnation. A resolution of these two mysteries was proposed [130] in which the fast growing, short wavelength $m = 0$ interchange MHD instabilities would grow and nonlinearly saturate. Then ion-viscous heating associated with the velocity shear and compression is sufficient to raise the ion temperature T_i in a few nanoseconds to a very high temperature, sufficient for $T_i \gg Z T_e$ (in a low mass array) and for pressure balance. The equipartition of energy to the electrons leads to the elevated radiation levels.

For the particular stainless-steel array experiments on Z employing a relatively low line density record ion temperatures of 200 to 300 keV (over 2 billion degrees Kelvin) were predicted and measured from Doppler broadening of optically thin lines [130]. The choice of wavelength of the instability was based on a viscous Lundqvist number of 2, to give a maximum linear growth rate and maximum viscous heating, this wavelength being in the range 10–100 μm, just a little greater than the ion mean-free path. It would be difficult to detect these instabilities because of both the fine scale and the small amplitude at saturation, the amplitude of the perturbed velocity being only $c_A/\sqrt{ka}$ where k is the wave number.

At this ion temperature pressure balance, i.e. the Bennett relation, equation (2.7) holds at stagnation. Ideal MHD instabilities grow at a rate $\gamma_{MHD} \cong c_A(k/a)^{1/2}$, i.e. increasing as $k^{1/2}$. The critical damping of Alfvén waves by viscosity occurs at a viscous Lundqvist number L_μ of 1 where

$$L_\mu = \frac{2\rho(c_A^2 + c_s^2)^{1/2}}{(\mu_\parallel/3 + \nu_1)k}, \tag{5.8}$$

c_s is the sound speed, $\mu_\parallel$ is the parallel ion viscosity equal to $p_i\tau_{ii}$ and proportional to $T_i^{5/2}$ and ν_1 is the perpendicular ion viscosity given approximately by $\mu_\parallel/(1 + 4\Omega_i^2\tau_{ii}^2)$ where Ω_i and τ_i are the ion cyclotron frequency and ion–ion collision time, respectively.

The saturation amplitude of the perturbed velocity $\tilde{v}$ can be found by equating $(\tilde{v} \cdot \nabla)\tilde{v}$ to $\gamma_{MHD}\tilde{v}$ giving an eddy velocity amplitude of $c_A/(ka)^{1/2}$. Since in the example considered

in [130] $ka \simeq 200$, it would be very difficult to detect these perturbations. Nevertheless the viscous heating rate arising from the fine scale of the mode gives a relatively high value of $\nabla \cdot \tilde{v}$. For $\mu_\parallel \gg 3\nu_1$ (since $\Omega_i \tau_{ii}$ is ~ 3) and recalling that the $m = 0$ MHD mode is a compressible interchange mode, i.e. $\nabla \cdot \tilde{v} \neq 0$ a value for the heating water per unit volume is approximately

$$\frac{1}{3}\mu_\parallel |\nabla \cdot \tilde{v}|^2 \cong \mu_\parallel c_A^2 \frac{k}{a} \tag{5.9}$$

and the linear dependence on k should be noted. As a result, by fixing the maximum k such that L_μ equals 2, then gives

$$\rho \frac{c_A^2}{a} (c_A^2 + c_s^2)^{1/2} = \frac{3n_e e}{2\tau_{eq}} (T_i - T_e), \tag{5.10}$$

where the lhs is the viscous heating rate and has been equated to the equipartition rate where the equipartition time τ_{eq} is defined by

$$\frac{1}{\tau_{eq}} = \frac{8(2\pi m_e)^{1/2} e^{5/2}}{3m_i (4\pi\varepsilon_0)^2} \frac{Z^2 n_i \ln \Lambda_{ei}}{T_e^{3/2}} \tag{5.11}$$

and $T_e \gg (m_e/m_i)T_i$. Thus equation (5.10) shows that the viscous heating rate is essentially an Alfvén transit time a/c_A which for the example is 1–2 ns. This is consistent with the measured ion temperature rise shown in figure 64, where τ_{eq} is over 5 ns, and so the ion temperature T_i continues to be much larger than the electron temperature T_e. In contrast the ion–ion collision time τ_{ii} is 37 ps, allowing rapid thermalization of the ions. In terms of global quantities equation (5.10) can be combined with the Bennett relation to give

$$(T_i - T_e) = 2.1 \times 10^{36} \frac{aI^3 T_e^{3/2} A^{1/2}}{Z^3 N_i^{5/2} \ln \Lambda_{ei}}, \tag{5.12}$$

where A is the atomic number (55.8 for iron). For the measured current I and estimated line density N_i the Bennett relation gives T_i of 219 keV while equation (5.12) gives a pinch radius a of 3.6 mm. Including the viscous heating associated with ν_1 and other k-modes reduces a to ~ 1 mm. This formula is not very sensitive to the effects of trailing mass (see section 5.11) since there will be comparable reductions in both I and N_i.

It would be expected that at the start of stagnation there would be a skin current, and the instabilities would lead to the rapid diffusion towards a Kadomtsev profile (see section 3.2), converting magnetic energy to ion vortex motion but conserving magnetic flux. Assuming that the electrodes are perfect conductors and that at this time there is a current short across the AK gap the magnetic flux can only decay if the line integral $\int_A^K E_z \, dz$ along the axis is non-zero. If only axisymmetric $m = 0$ modes are present, and if the resistivity is negligible then this can only be achieved if there are many hot spots formed on the axis with a component of number density variation out of phase with the temperature variation [389]. A contribution from electron viscosity through the electron stress in Ohm's law might be important. All experiments reveal the occurrence of many bright spots on the axis. Figure 65 illustrates this from Z, [388]. Indeed the voltage drop can be roughly estimated as T_e (in eV) times the number of bright spots. Anomalous resistivity, as suggested in section 3.14, applies at a disruption and can also dissipate magnetic flux.

In comparing the current and voltage waveforms with a lumped circuit model, e.g. Waisman [390], it would be necessary in order to model this viscous heating process to equate $\pi a^2 \ell$ (i.e. the pinch volume) times the lhs of equation (5.10) to $R_{vis} I^2$. Then R_{vis} is rather like the inductance divided by the Alfvén transit time; in fact

$$R_{vis} = \frac{\mu_0 \ell}{4\pi a} \cdot (c_A^2 + c_s^2)^{1/2}. \tag{5.13}$$
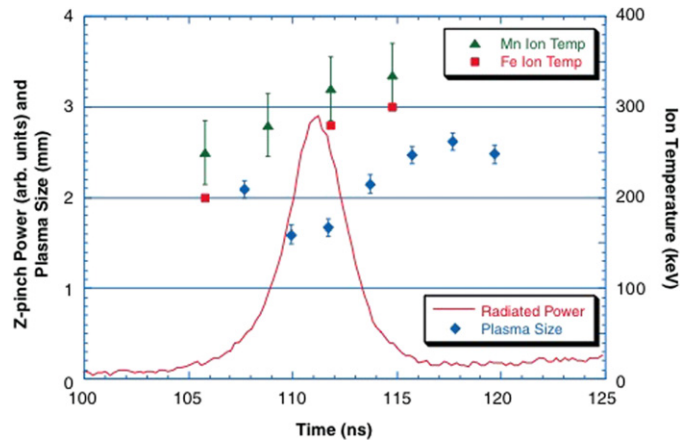
Figure 64. Measurements of ion temperature, plasma size, and radiated power as a function of time. Reprinted figure with permission from [130]. Copyright 2006 by the American Physical Society.
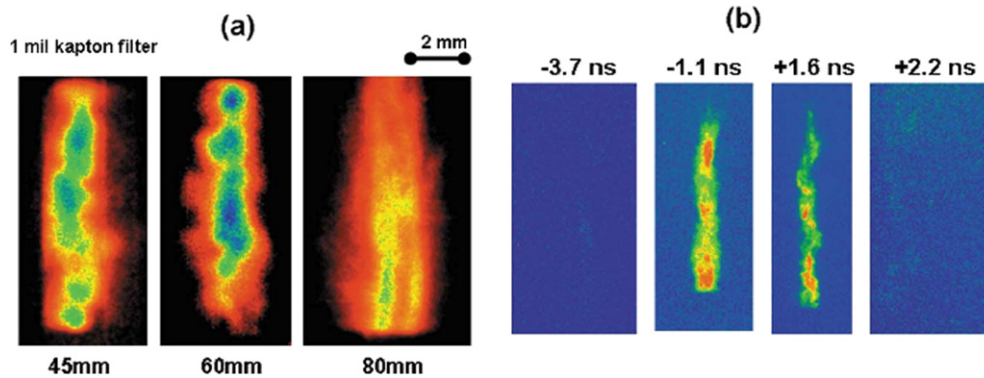
Figure 65. (*a*) Time-resolved pinhole images of >1 keV emissions within 1 ns of peak radiation for 45 mm, 60 mm, and 80 mm outer diameter nested stainless steel wire-arrays of length 20 mm; (*b*) Time-resolved images of K-shell radiation for a 55 mm outer diameter array with times relative to peak x-ray output. Reprinted with permission from [388]. Copyright 2008, American Institute of Physics.

This is typically of the order of 0.3 Ω and for *Z* will give a dissipation rate of several hundred TW, comparable to the radiation power, as found experimentally. In section 7.2 another mechanism originated by Lovberg [329] and later by others [331, 332] involving magnetic bubbles is found to give a similarly enhanced effective resistance. Further discussion of viscous heating and when it will occur will be found in section 7.2.

5.9. Atomic physics

It is beyond the scope of this review paper to include all the relevant detailed atomic physics such as the equation of state (EOS) transport, radiation transport and opacity. Atzeni *et al* [391] have developed a simplified EOS for matter in the density range $10^{-3} < \rho < 10^{7}\,\mathrm{kg\,m^{-3}}$ and

for electron temperatures up to 100 keV. Refinement of the Lee and More [392] transport model for strongly coupled plasmas has been carried out by Dejarlais [340] while for partially degenerate, magnetized plasmas a complete set of transport coefficients has been derived by Brown and Haines [393, 394].

Pereira and Davis [51] have reviewed the experimental data of x-rays from dense Z-pinches and compared the results with theoretical modelling. The experimental I^4 scaling of x-ray yield for neon K shell and krypton L shell radiation is explained. Also there is a marked radial distribution of radiation emission, the XUV emission coming broadly from the pinched region but the harder radiation, i.e. the soft x-rays, being emitted from many hot spots along the axis. This is particularly true for higher Z materials such as tungsten. Even harder radiation (inner shell transitions) from 10 to 100 keV electrons is also detected at stagnation. The origin of this electron acceleration process is still not firmly established, and in [51] is usually assumed to be caused by a resistive or inductive axial electric field. However it should be noted that runaway electrons have singular orbits and can only occur within one electron Larmor radius of the axis. Such orbits are discussed in section 2.2; furthermore as shown in [113] off-axis energetic relatively collisionless electrons drift towards the axis with a E_r/B_ϑ drift—a sort of high energy filter—where they are free to accelerate in the applied electric field. In linear transport theory the velocity dependence of the collision frequency leads to the Ettingshausen heat flows (see section 2.6) in the direction of $\underline{J} \times \underline{B}$, of which the runaway electron drift is an extreme example. Thus on the axis when the axial electric field has convected or diffused in (perhaps anomalously quickly by the vortices of the fine scale $m = 0$ instabilities discussed in section 5.8) the electron distribution function could be very non-Maxwellian. In the presence of fine-scale instabilities and viscous heating, the rapid conversion of magnetic energy to thermal energy will be accompanied by a greatly enhanced E_z field, and hence enhanced Ettingshausen advection of hotter particles to the axis, leading to hot spots and runaway electrons [395].

Due to the limitations of resolution in x-ray images of the pinch at stagnation, the fastest growing but small amplitude $m = 0$ MHD instabilities that are most effective for viscous heating of the ions accompanied by rapid conversion of magnetic energy, have not yet been detected. However the more slowly growing and larger wavelength modes will overtake these in a time of order of the radial Alfvén time, and probably are the origin of the large amplitude hot spots which radiate many of the soft x-rays. Axial flows away from the high pressure hot spots will occur, and the line density at each spot could drop below the critical value leading to anomalous resistivity and electron and ion beam formation as discussed in section 3.14. Such a disruption would occur several Alfvén transit times after the main soft x-ray pulse has peaked.

This tendency for runaways is greatly enhanced in vacuum spark experiments, and quite hard x-rays are generated here. Bright spots in vacuum sparks have been modelled by Vikhrev *et al* [396] and for a Z-pinch [328] and also Maxon *et al* [397]. Sotnikov *et al* [398] have employed a hybrid 3D MHD code including the Hall term, modelling both $m = 0$ and $m = 1$ modes. The development of an electromagnetic flute mode in a precursor plasma carrying a current [399] showed the evolution of large scale structures and the generation of shorter wavelength turbulence. But simulations would require $\lesssim 2\,\mu$m resolution in order to model the fast-growing short wavelength modes and their associated viscous heating of [130]. There is clearly a need to understand the energy conversion process to x-rays. Whilst it is difficult to calculate the ion kinetic energy of the implosion accurately, there is a consensus that the energy radiated can be much greater than the kinetic energy [400]. Candidates for this are reversible $p\mathrm{d}V$ compressional heating by the $\underline{J} \times \underline{B}$ forces [321]; magnetic bubbles from $m = 0$ instabilities coupled to resistive dissipation [331, 332]; $m = 1$ instabilities leading to helical structures and enhanced resistive losses [324] associated with the current

Figure 66. Laser shadowgrams at $1\,\mu$s after voltage maximum (a) (c), and time-integrated open-shutter images (b) (d) of fast exploding $20\,\mu$m Ti wire with $E_r > 0$ (a) (b) and $E_r < 0$ (c) (d). The anode is on the right for (a) (b) and on the left for (c) (d). Reprinted figure with permission from [405]. Copyright 2002 by the American Physical Society.
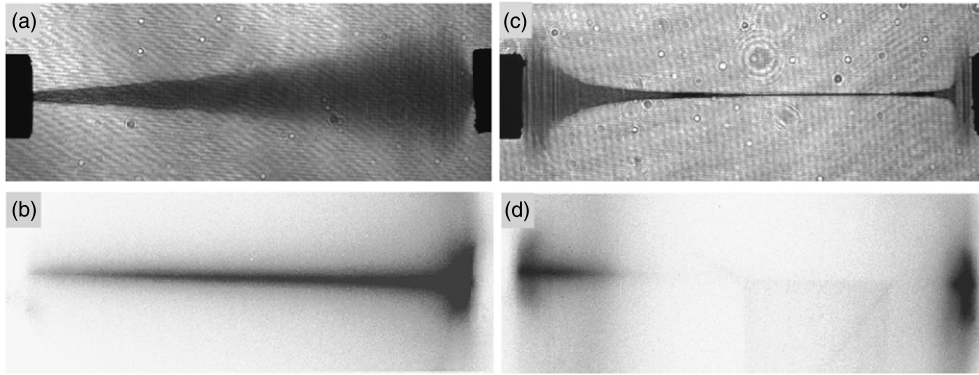
path length; anomalous resistivity [401] (but the conditions for this to occur require high drift velocity, usually associated with a low line density as could occur in a disruption (see section 3.14)); multiple shock waves, particularly attributed in simulations [324, 402]; and, lastly, the viscous heating of ions through small amplitude, fast growing, short wavelength $m = 0$ instabilities [130], discussed above. Apruzese *et al* [400] employed spectroscopic techniques to discriminate between these mechanisms by employing detailed collisional–radiative equilibrium (CRE) calculations. In particular they found that in a 1D model that the K-shell peak power involved only 1% of the original load. However it is clear that a 2D or 3D model would be needed to capture the multiple hot spots seen in the time-resolved images; but these are limited in resolution by the pixel size ($\sim$300 μm). A useful tutorial paper by Apruzese *et al* [400, 403] outlines the methods used in modelling radiation transport in dense plasmas. Whilst it is too early to be conclusive, the high ion temperature observed spectroscopically in [130] lends strong support to the ion-viscous heating model in this high magnetic Prandtl regime. A detailed presentation of non-LTE effects and the CRE model in particular is given by Davis *et al* [404] and applied to a titanium wire array as well as argon and krypton gas puffs. It was found that the CRE model is in better agreement with experiment than LTE with radiation transport of diffusion. The transition from weakly to strongly coupled regimes is also discussed.

5.10. Axial asymmetries and flows; radial electric fields

Experiments show that, apart from the filamentary instabilities on the wires (see section 5.4), there is a systematic long-scale axial variation. For single $20\,\mu$m diameter Ti wires exploding in vacuum, shown in figure 66, Sarkisov [405] has shown that there is a marked polarity effect dependent on the sign of the radial electric field E_r. It was interpreted that when E_r is positive the electrons are driven into the wire core and there is more energy deposition leading to a conical core expansion. A negative electric field would lead to electron field emission when E_r exceeds $300\,\text{kV}\,\text{cm}^{-1}$ [406], followed by vapour breakdown. Then a current shunt to the plasma forms around the wire requiring a lower voltage to drive the current. In addition there is enhanced energy deposition near the electrodes for reasons to be discussed. In contrast, explosion in air at 1 atm pressure led to identical homogeneous columns with no current

shunting [405]. Increasing the wire diameter reduced the asymmetries of polarity which is consistent with the following theory.

Whilst the wire core is surrounded in general by a quasi-neutral coronal plasma of radius a_p, it itself is surrounded by an electron sheath formed by emission of electrons by the negative radial electric field. The Maxwell equation $\nabla \cdot \underline{D} = \rho$ in the sheath gives

$$\varepsilon_0 \frac{1}{r} \frac{\partial}{\partial r}(r E_r(r)) = -n_e(r)e \qquad \text{for } r > a_p. \tag{5.14}$$

This outer sheath shields the coronal plasma from the radial electric field and also leads to E_r/B_θ guiding-centre drift of the electrons, so causing an axial current density $J_z(r)$ and a magnetic field from Ampère's law given by

$$J_z(r) \simeq -e n_e \frac{E_r(r)}{B_\theta(r)} = \frac{1}{\mu_0 r} \frac{\partial}{\partial r}(r B_0(r)). \tag{5.15}$$

On integrating this with the boundary conditions that at $r = a_p$, $E_r = 0$ and $r B_\theta = \mu_0 I_p/2\pi$ where I_p is the current flowing in both the coronal plasma and core the fundamental sheath relation

$$1 > \frac{1}{c^2}\left(\frac{E_r}{B_\theta}\right)^2\Big|_{a_s} = 1 - \frac{I_p^2}{I_T^2} > 0 \tag{5.16}$$

is obtained where $a_s > a_p$ is the outer radius of the sheath and I_T is the total current in the sheath, coronal plasma and core. It should be noted that significant shunting of current into the sheath can only occur at early times when B_θ is small, and E_r/B_θ approaches the velocity of light. The theory is relativistically correct for $|E_r/B_\theta| < c$ only. If $|E_r/B_\theta| > c$ no guiding-centre drift in the frame moving with E_r/B_θ will occur; instead there is a local inertial frame in which $B_\theta = 0$ and free acceleration of the electron in the negative radial electric field will occur, causing the electron to hit the return conductor.

To find what determines the value of the radial electric field at the sheath edge, a closed line integral $\int \underline{E} \cdot \underline{dl}$ is taken along the (assumed perfectly conducting) return conductor and anode, along a distance z outside the sheath of the wire, and across the vacuum gap to the return conductor as illustrated in figure 67. There will be a resistive contribution to this along the wire proportional to z where Ohm's law

$$E_z = \eta J_z \approx \frac{\eta_p I_p}{n \pi a_p^2} \tag{5.17}$$

holds, and the plasma current I_p is now distributed among n wires, The corresponding inductive contribution from Faraday's law is also proportional to z and is the time derivative of the magnetic flux enclosed, $z \mu_0 I_T \ln(R_c/a_s)$, R_c being the radius of the return conductor. Thus the radial electric field E_r is proportional to z, the distance from the anode, where for the usual case the power feed is at the cathode. In addition in the vacuum outside the sheath $r E_r$ is essentially independent of r. Thus the charge per unit length in the sheath Q_ℓ to yield this electric field is

$$Q_\ell = 2\pi \varepsilon_0 r E_r. \tag{5.18}$$

For a wire array as opposed to a single wire an approximation has to be made. Without going into detail, it can be shown that for a large number of wires radial electric field E_r^1 at the outer surface of the sheath on each of the n wires is approximately

$$E_r^1(z) \cong -\frac{z}{2 n a_s}\left[\frac{\eta_p I_p}{n \pi a_p^2 \ln R_c/R_a} + \frac{\mu_0 \dot{I}_T}{2\pi}\right], \tag{5.19}$$
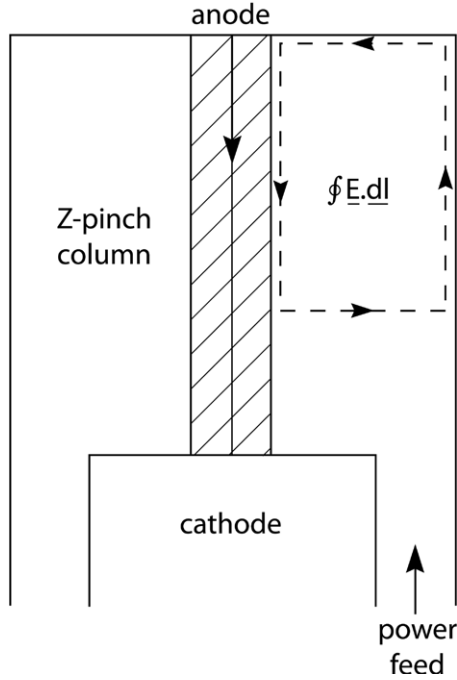
Figure 67. Diagram of path of the closed line integral $\oint E \cdot \underline{d\ell}$.

where R_a is the radius of the wire array. It can further be shown that at early times and during the current prepulse when a_s and a_p are small and close to the original radius of each wire a_w the resistive contribution is dominant, but later the inductive term is more important. For the former case $-E_r^1/E_z \rightarrow Z/(2na_s \ln R_0/R_a)$; and close to the cathode at early times is typically ~ 10 to 10^2. This formula approaches that of Sarkisov [405] when $\ln(R_c/R_a) \rightarrow \Delta/R_a$ where $R_c = R_a + \Delta$ and $\Delta \ll R_a$. Another dimensionless number (somewhat like an inverse Reynolds number)

$$- \frac{E_r^1}{cB_\theta^1}(z = \ell) = \frac{\eta\ell}{cn\mu_0 a_p^2 \ln(R_c/R_a)} \tag{5.20}$$

describes the relative importance of the radial electric field, in particular the electron drift velocity compared with c as in equation (5.16). Here ℓ is the anode to cathode separation, and E_r^1 and B_θ^1 are the fields at the surface of each sheath, the sheath radius a_s being assumed small compared with $\pi R_a/n$. In Sanford *et al* [407] it is shown that the axial asymmetry of the imploding wire array is sensitive to the value of $-E_r^1/E_z$, small values leading to the least asymmetry in the axial x-radiation power between top and bottom. The asymmetry is also manifested in a zippering of the main implosion with stagnation occurring first near the anode. As argued in an earlier paper by Sanford *et al* [408], the wire core receives greater heating near the anode because here the radial electric field is zero, and no current shunting occurs. In [407] a simulation using the RMHD code GORGON [324] showed that a hotter core had less precursor plasma and a faster implosion (nearer the anode), while a colder core had significant precursor and a later implosion. However, very close to the cathode there is even earlier stagnation and x-ray emission. This could be caused by several effects; first, a local heating of the core due perhaps to a poor wire-cathode contact [409, 410] resulting in

an effect similar to the GORGON simulations mentioned above; second a local depletion of line density due to the radial Hall current in the plasma adjacent to the cathode giving an axial flow of plasma towards the cathode surface; however, in a simulation using LASNEX it was shown that this effect could be swamped by gold vapour and plasma emitted from the cathode surface, [408], but the Hall effect would be the reason for the apparent necking-off at the anode seen by Sarkisov *et al* in his figure 7 [405] and also in images of early *Z*-pinches [300]. However when there is a hole in the bottom electrode this Hall-driven axial flow can occur unimpeded. It was in such an experiment that the unexpected axial asymmetry in radiated power was first identified [406]. This process is the basis of a plasma opening switch.

A related paper by Bland *et al* [370] in which a wire array is extended by a factor of 3 in length by mounting it within holes in the cathode and anode, shows markedly different behaviour in the upper (anode) half where E_r is negative compared with the lower half. There is no gradual transition as in [405] but a sharp change in behaviour occurs at the mid-point where E_r reverses sign. The upper half has wire cores which have expanded to only 100 μm in diameter compared with the usual 300 μm in the lower half; the precursor plasma has a higher ablation velocity consistent with a lower mass ablation rate, perhaps caused by the smaller area of the core surface. As a result the precursor assembles on the axis earlier, at 75 ns, and is brighter in emission. The lower half (where $E_r > 0$) precursor plasma stagnates at 90 ns, but the final implosion, which is dependent on the erosion of the core at axial positions associated with the filamentary instability, occurs first in the lower half and stagnates at 200 ns. The upper half stagnates at 230 ns. Thus there are two main x-ray pulses, which might be useful in profiling the x-rays for emission for ICF applications. This delay in implosion of the upper half requires $\dot{m}$ to be halved, thus leading to a doubling of the precursor ablation velocity from 15 to 30 cm μs^{-1}. It is interesting that the wavelength of the axial instability is the same throughout, i.e. independent of the core diameter in contrast to [373]. Surprisingly it is the lower half ($E_r > 0$) which behaves more closely like a standard short array fixed between anode and cathode (but where $E_r < 0$) on MAGPIE.

The reason for the sharp transition half-way along the wires is not understood, but it could be that the magnitude of the radial electric field is sufficiently large to cause plasma formation and current shunting uniformly in the upper half. At the transition region there could also be a local strengthening of the azimuthal magnetic field due to $\nabla T_e \times \nabla n_e$ magnetic field generation [75], which could tend to sharpen up the transition.

The early concentration of current in the liquid-vapour core when E_r is positive can also occur for $E_r < 0$ when insulating coatings around each wire are employed [411]. The vapour formed around each wire core, and emitted from the electrodes could contain contaminants which might require conditioning techniques to remove [412].

At very early times, when the current associated magnetic field is small, there could be insufficient magnetic insulation, and electrons emitted by the wires with $E_r < 0$, instead of forming an electron sheath as discussed above, will be accelerated to the return conductor. The critical value of the fields at which this occurs can be found as in a magnetron by examining the orbits of electrons leaving a cylindrical emitting surface. The equations of motion are

$$m\frac{\mathrm{d}v_r}{\mathrm{d}t} = -eE_r + ev_z B_\theta, \tag{5.21}$$

$$m\frac{\mathrm{d}v_z}{\mathrm{d}t} = -ev_r B_\theta. \tag{5.22}$$

For a large number of wires, again the near-field effects can be ignored and the global variation is dominant. Thus rE_r and rB_θ are independent of r, giving $v_0 = -E_r/B_\theta > 0$ independent
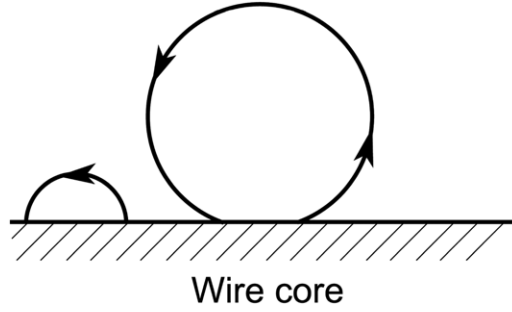
Figure 68. Sketch of orbits of ions leaving a wire core with components of axial velocity positive or negative.

of r and, with $e B_\theta(r)/m = \mathrm{d}\tau/\mathrm{d}t$ these give

$$\frac{\mathrm{d}^2 v_r}{\mathrm{d}\tau^2} = -v_r \tag{5.23}$$

and

$$v_r = v_0 \sin \tau, \tag{5.24}$$

where the boundary conditions $v_r = 0 = v_z$ at $\tau = 0$ are applied.

Writing $u \equiv (e/m) r B_\theta(r)$ equation (5.24) becomes

$$\frac{u}{v_0} \frac{\mathrm{d}(\ln r)}{\mathrm{d}\tau} = \sin \tau, \tag{5.25}$$

which integrates to give

$$\frac{u}{v_0} \ln\left(\frac{r}{R_a}\right) = 1 - \cos \tau. \tag{5.26}$$

The maximum radial excursion $r_{\max}$ of an electron occurs at $\cos \tau = -1$, giving

$$r_{\max} = R_a \, \exp\left(\frac{2v_0}{u}\right). \tag{5.27}$$

Current shorting will occur when $r_{\max} \geqslant R_c$. The current density J will be given by Child's law, which for a planar case is

$$J = 4\varepsilon_0 (2e)^{1/2} \Phi^{3/2}/(9 m_{\mathrm{e}}^{1/2} d^2), \tag{5.28}$$

where Φ is the potential drop over a distance d. In summary, at very early times electron shorting to the return conductor can occur until the azimuthal magnetic field builds up; such a radial current will cause axial plasma flows. As B_θ increases the electrons are confined to an electron sheath, carrying a current described by equation (5.16). The radial electric field varies approximately linearly (equation (5.19)) from the anode to the cathode (where the feed point is at the cathode) and there is increased shunting of axial current from the plasma core to the electron sheath at the cathode end. The increased plasma current at the anode end is a reasonable explanation of the zippering of the implosion found by Sanford *et al* [407].

But there is another source of axial flow in addition to the $\underline{J} \times \underline{B}$ force associated with radial current shorting to the walls. This is the effect of ion orbits as plasma ablates from the outer facing wires. See figure 68. It is assumed that ions leave the core equally in all directions, the ions with a component of velocity in the z-direction will be deflected by the azimuthal magnetic field to impact the wire core after a small fraction of a Larmor period. In contrast,

ions leaving the core with a large component of velocity in the $-z$-direction (i.e. towards the anode) will almost complete a Larmor orbit before returning. Thus the cores will receive momentum in the $+z$-direction for one Larmor period, while, by conservation, the precursor plasma will acquire momentum in the $-z$-direction, i.e. towards the anode. Collisions in the precursor plasma might reduce this effect. Furthermore 3D effects will especially cause the ions with initial components of velocity in the $-z$-direction together with a θ-component to miss the core and join preferentially the precursor flow towards the axis. This is essentially a finite ion Larmor radius (FLR) effect, and will lead to a component of the inward precursor plasma flow towards the anode, regardless of the position of the power feed. It is an adaptation of a theory of the origin of rotation of theta pinches [93] in which ions leaving the vessel-wall exchange angular momentum with the wall.

Experimental data at the present time show an axial component of precursor flow towards the anode and away from the power-feed, which is at the cathode. It will be interesting when experiments with the power-feed at the anode end are undertaken: Then any shorting process will be electron emission, not from the wires, but from the return conductor. The $\underline{J} \times \underline{B}$ force will have a component driving flow away from the power-feed, i.e. towards the cathode. The FLR mechanism will continue to lead to a component of flow towards the anode.

5.11. Trailing mass and current re-strike

The implosion phase commences when there are gaps in the wire cores. As discussed above, it could be theorized that the plasma in the gaps, being no longer cooled by the heat flow to the cores necessary to cause ablation, heats up sufficiently for the magnetic Reynolds' number to exceed unity. Thus, this plasma together with the current and associated magnetic field implodes under the action of the global $\underline{J} \times \underline{B}$ force. This is illustrated in figure 61 taken from Lebedev *et al* [363] for an $8 \times 10 \, \mu$m Cu wire array. The characteristic wavelength of $\sim$0.5 mm of the modulation is seen in the x-ray image at 185 ns. The precursor plasma arrived on the axis earlier at 130 ns. At 215 ns the implosion has already started, the current sheath being formed by a large number of magnetic bubbles, moving towards the axis, snowploughing up previously launched precursor plasma, and now has $\sim$2 mm wavelength. At 245 ns the imploding plasma has stagnated leaving behind characteristic trailing mass which has a global $m = 0$ structure. Later, these fingers of trailing mass also pinch to the axis, and this is the cause of later x-ray emission. The peak x-ray emission in this $32 \times 10 \, \mu$m Al wire array occurs at 265 ns, and so the trailing mass does not contribute to the main x-ray pulse, and indeed could deprive the stagnated column of some of the current. Figure 69 shows grated x-ray images 2.3 ns before and 3.2 ns after peak x-ray emission on Z, illustrating the later implosion of the trailing mass and the relative uniformity of the pinch column.

From analysis of the trajectories it would appear that about 30% of the original mass of the wires is in the trailing mass [65] though fringe shifts from laser interferograms would merely estimate that this trailing mass is greater than 7% [363]. After stagnation there is evidence of a $m = 1$ component to the dominantly $m = 0$ stagnated pinch. Bland *et al* [413] have compared the evolution of filaments and precursor bubbles for low (8) and high (32) wire number aluminium wire-array implosions, showing correlation and merging of bubbles in the latter case. For arrays of $\sim$300 wires Sinars *et al* [414] have shown a similar evolution of trailing mass on Z using x-ray radiography.

Recently, Yu *et al* [415] have simulated the current trajectories in 3D in the trailing mass. They find that the growth of bubbles (in the sense of bubble and spike of RT) is reduced compared with 2D simulations. The trailing mass evolves towards a force-free structure, implying the presence of significant axial magnetic fields. The azimuthal perturbations and
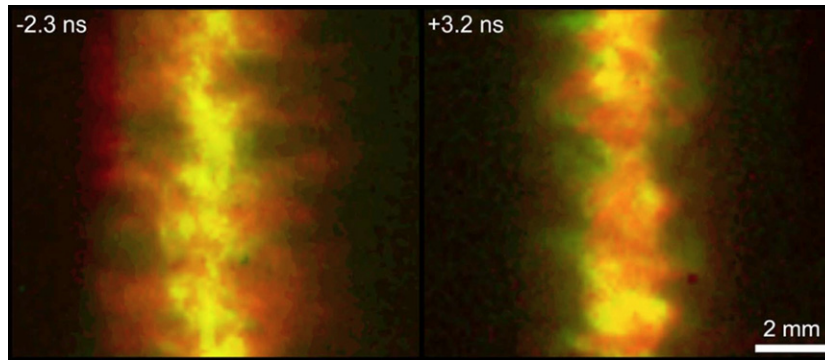
Figure 69. False colour composite 1 ns. Gated images from Al shot 1519 on Z-accelerator 2.3 ns before and 3.2 ns after peak x-ray power [739, figure 3]. Copyright © 2000 IEEE.
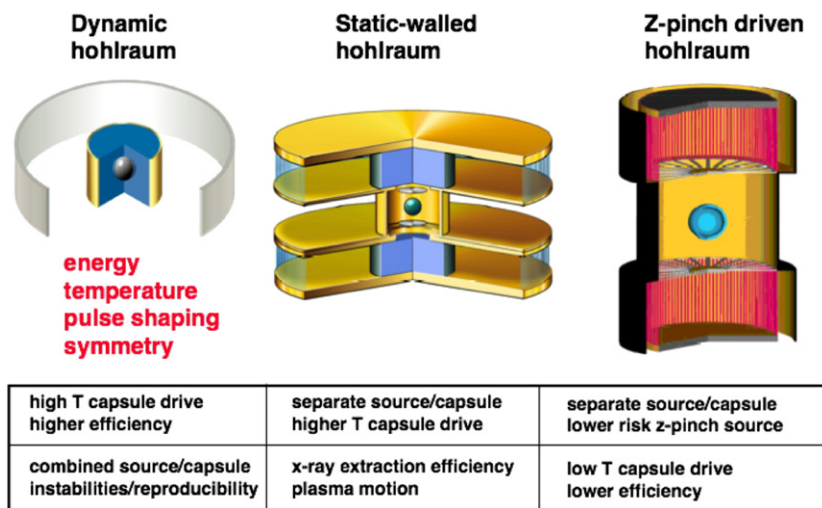
Figure 70. Three designs for hohlraums for Z-pinch driven inertial confinement fusion at Sandia: (*a*) the dynamic hohlraum, (*b*) the static-walled hohlraum and (*c*) the vacuum hohlraum. Courtesy of Sandia National Laboratory.

correlations introduced initially will, however, strongly affect the result, and whether this occurs in experiments conducted with a high degree of azimuthal symmetry is an open question.

5.12. Planar arrays

Recently some small scale experiments have been undertaken with planar arrays [416] which showed that current stays on edge wires and cascades inwards from wire to wire, giving an implosion at the centre of the array with significant x-ray yield [417]. Ivanov *et al* [418, 419] have extended the data and given a more thorough review of planar arrays. Their application to larger-scale experiments was undertaken by Jones *et al* [420] at currents of 3–6 MA. There is a significant amount of trailing mass here, and there appears to be saturation of peak x-ray power.

Double planar arrays were explored by Kantsyrev *et al* [421, 422], for Mo and W at ∼1 MA and gave increased x-ray yield. Star arrays have also given interesting results in experiments

by Ivanov *et al* [423]. Star arrays are multi-nested cylindrical arrays (up to 6 so far) with equal numbers (so far small) of wires in each array and exact azimuthal alignment of the wires. An unexplained increase in radiated energy was reported for these loads [424]. It will be interesting to see how these configurations scale at higher currents, and whether new and more compact hohlraums can be designed as a result. Modelling of planar arrays has also been undertaken [425].

Mention should be made of two-wire experiments by Yadlowsky *et al* [426] and by Beg *et al* [427]. A precursor plasma accumulates on the axis midway between the two wires. Because this plasma experiences the applied voltage, an axial current flows, and results in a $m = 1$ instability, indicating a centrally peaked current.

6. Hohlraums and inertial confinement fusion (ICF)

Because the wire-array Z-pinch is the most efficient ($\sim 15\%$) and most powerful (~ 230 TW) x-ray source, it is a strong candidate for energizing a hohlraum for driving a fusion capsule. Compared with laser-driven hohlraums, it is also energy rich, but the problem is how small a hohlraum could be made; and how can the x-ray drive be profiled in time to yield a low entropy adiabatic compression of the fuel. These are two issues which are currently being addressed. In addition, for inertial fusion energy (IFE) the development of repetitive pulsed power and a realistic engineering reactor system is at the early stage of conceptual design [428].

There are three principal configurations of hohlraums employing wire-array Z-pinches [429]. They are illustrated in figure 70 and will be briefly described below.

6.1. The dynamic hohlraum

The dynamic hohlraum is the most compact design [61–63]. It has a capsule containing the D–T fuel buried in plastic foam on the axis of the wire-array Z-pinch [430]. The foam is a cylinder which has an external coating of gold as shown in figure 70(*a*). When the Z-pinch stagnates onto the foam the gold is heated and radiates, the inward radiation creating a supersonic radiative shock through the foam. The gold acts as the wall of the hohlraum, but it is compressed to a smaller diameter by the Z-pinch, hence the name, dynamic hohlraum. From an initial diameter of 5 mm a dynamic hohlraum compression to 0.8 mm diameter has been measured on Z [431–433]. The peak Planckian radiation temperature was measured to be 230 ± 18 eV. A plastic spherical shell filled with deuterium gas gave a neutron yield of $> 10^{10}$ which originated from an isotropic thermal source [434–436]. More recently, with further optimization the DD neutron yield was increased to 3×10^{11}, which is a record for indirect drive capsules [437, 438]. Whilst early simulations did not agree with experiments [439] more recent radiation hydrodynamics gave spectral features similar in duration to measurements [440]. Integrated 2D simulations, including the implosion of the wire arrays on to the foam converters followed by radiation transport to the embedded capsule gave better agreement [441] and led to the concept of ablative stand-off by the capsule of the incoming shock, thus preserving spherical symmetry of the capsule. This work also employed analytic modelling of the wire-array implosion for a linearly rising current. Palmer *et al* [442] have recently made radiographic studies of foam targets. The importance of the MRT instability on the radiating shock has been studied by Lemke *et al* [443], and the simulations accurately reproduced the shock trajectory. Indeed the capsule implosions were shown to be relatively free from random radiation asymmetries associated with instabilities.

6.2. The static-walled hohlraum

The static-walled hohlraum uses the radiation emitted axially from two Z-pinches with foam cylinders on the axis, as shown in figure 70(*b*). Using only one Z-pinch, a one-sided energized static-wall hohlraum of NIF scale (7 mm height and 6 mm diameter) has produced a radiation temperature of ~130 eV [444–446]. To raise this temperature a reduced volume of 4 mm height and diameter has been studied [447, 448]. The radiation temperature achieved in this reduced NIF scale hohlraum using Z is ~160 eV [431–433].

Apruzese *et al* [449] have compared spectroscopically the properties of the plasma of the interior hohlraum with that of the blow-off plasma which accompanies the axial flow of radiation. They compared the spectral emission of K-shell Al lines from a tracer buried 2 mm deep within the foam with Mg at the end of the foam. The Mg lines can be seen in absorption while the Al lines are observed in emission, the background radiation being the broadband sources from the optically thick ionized carbon foam. The end tracer becomes part of the blow-off plasma and shows cooling relative to the hohlraum interior. It is found that the radiation temperature created by the dense interior hohlraum plasma (~200–250 eV) is the same as that seen by the cooler blow-off plasma a few millimetres away. The deduced electron temperatures agree with 2D RMHD calculations.

However, as stated earlier, Sanford *et al* [410] found up-down asymmetry in the radiated power. Furthermore in another paper [450] Sanford *et al* found a length scaling of the axial radiation flow. The length of the dynamic hohlraum was varied from 5 to 20 mm keeping M_ℓ (the mass per unit length) constant. The increasing inductance with length led to the peak current decreasing with length. However the axial radiation power had an unexpected maximum of ~11 TW at a length of ~8 mm, the dramatic fall-off at 5 mm being probably due to end effects including instabilities near the radiation exit-holes on the electrodes. Two independent techniques for measuring the radiation field in a static-walled hohlraum gave temperatures of 147 ± 3 eV and 145 ± 5 eV, respectively, the first from an active shock break-out measurement in aluminium, and the second from x-ray re-emission from the gold wall [451].

An overview of the x-ray source for producing 10 TW of axial radiation from a dynamic hohlraum by Sanford [452] gave emphasis on the need to include the discrete wire dynamics in any simulation.

6.3. The vacuum hohlraum

This hohlraum has the largest volume and hence the lowest temperature for given x-ray sources. However the capsule will have more open diagnostic access, and will be far from the irreproducible Z-pinch instabilities which might affect the other hohlraum concepts. Proposed by Hammer *et al* [453] it is the configuration studied most for IFE (inertial fusion energy) [428], and two Z-pinches each of >60 MA will likely be required [454]. In a 17 mm diameter and 15 mm high hohlraum driven by a single pinch, a radiation temperature of 90 ± 5 eV has been obtained [5]. In 2D rad-hydro simulations, Vesey *et al* [455] have modelled a high-yield capsule design with a 4 step rise in radiation temperature to 230 eV in 80 ns, shown in figure 71. For the 2.65 mm radius capsule with a 190 μm thick beryllium ablator surrounding a 280 μm layer of cryogenic DT fuel (30 times the fuel mass in the standard NIF capsule) an absorbed energy of 1.21 MJ would lead to 520 MJ yield with a ρR of 3.1 gm cm^{-2}. This energy-rich implosion is shown in simulations to be controllable to radiation symmetry using suitable shields to obtain optimized P_4 (Legendre polynomial) symmetry. Indeed time-averaged radiation fields uniform to 2–4% have been measured [456, 457], while control of selective modes by shields has been developed by Vesey *et al* [458].

104
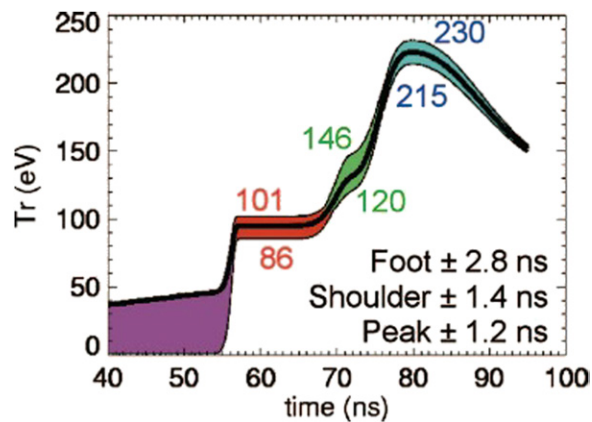
Figure 71. Radiation temperature as a function of time for the *Z*-pinch baseline design at Sandia. Reprinted with permission from [455]. Copyright 2007, American Institute of Physics.
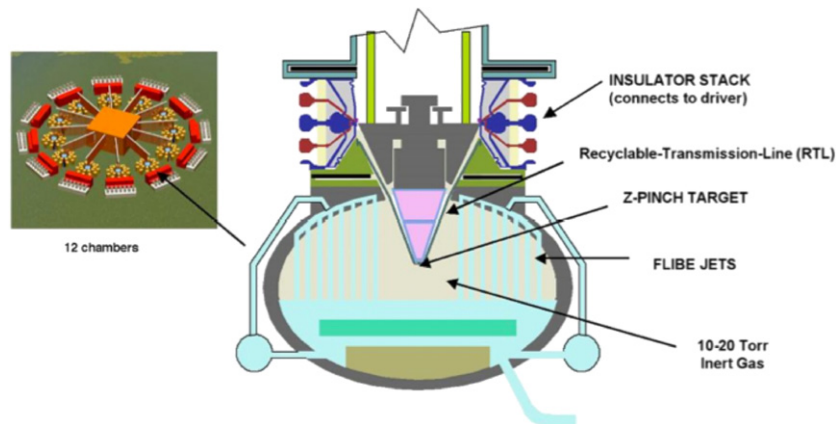
Figure 72. Conceptual design of Z-pinch reactor based on the vacuum hohlraum, ZP3 elliptical IFE chamber [463]. Copyright 2003 by the American Nuclear Society, La Grange Park, Illinois.

Various simplified models of hohlraums have been developed. Cuneo *et al* [459] considered 0D models for four configurations and found consistency with measured x-ray powers and wall temperatures. Stygar *et al* [460] proposed analytic models coupling x-ray sources to hohlraums and capsules in a more general way, but gave special attention to the *Z*-pinch source. Lastly, numerical simulations have been used to examine fast ignition [19] and the scaling of hot-spot break-even in both tamped and untamped compressed fuel [461].

The subject is discussed in a review by Cuneo *et al* [462].

6.4. Z-pinch hohlraum reactor

Figure 72 illustrates the conceptual design of Sandia's ZP3 fusion reactor [463, 464] based on the vacuum hohlraum. It is to be repetitively operated at about 0.1 Hz. In each cycle about 3 GJ is released mainly as 14 MeV neutrons and x-rays. This energy is planned to be absorbed by thick curtains of flowing flibe molten salt (BeF_2–LiF), which acts both as a tritium breeder (from the lithium) and as a heat transfer agent. The current from the repetitively pulsed power source is coupled to the *Z*-pinch load through a recyclable transmission line (RTL).

This alleviates the need for complex liquid–vacuum geometry, as the pulsed power energy is coupled to the Z-pinch by direct contact. It also eases the vacuum requirements in the chamber which will have a 10 Torr pressure background of argon. However the inner gap of the RTL must operate in high vacuum to prevent electric breakdown, and a sliding seal arrangement has been devised to allow the pre-pumped RTLs to be inserted and connected to the pulsed power source, without opening the full chamber to high vacuum between each shot. After that the RTL will be destroyed, and a new RTL inserted. Therefore the RTL can be built either of frozen flibe which will melt in the coolant, or of a material immiscible in the molten salt which could then be separated and recycled. To alleviate shock generation arising from the pulsed energy absorption the flibe is in the form of curtains, with voids between, and the bubbling pool at the bottom of the chamber is two phase. Aspects of the nuclear technology involved are being studied in separate experiments. One of these considers low mass recyclable transmission lines theoretically and experimentally to determine the ability of the electrodes to carry the current required as a function of electrode thickness [465]. It was concluded that a transmission line of only a few tens of kilograms of material could carry the large currents require for fusion.

6.5. Technology of pulsed power; longer pulses

The further development of pulsed power to achieve more powerful x-ray sources and ignition of indirect drive ICF requires a greater understanding of the present technological approach and its limitations, together with the development of alternative techniques such as linear transformer drivers (LTDs) pioneered at Tomsk. In brief LTD accelerating cavities contain the pulse-forming capacitors. These are switched at low voltage, inductively adding the pulses and using soft iron-core isolation. Higher currents can be obtained by employing many capacitors in parallel, while higher voltage can be achieved by inductively adding the output voltage of several cavities in series.

In addition the scaling of the Z-pinch itself to higher currents and the trade-off of longer current pulses with lower voltages should be explored.

A three-dimensional e.m. model of pulsed power has been developed recently by Rose *et al* [466]. It has been applied to the new ZR-accelerator at Sandia which is designed to give 27 MA. This represents a major computational step compared with the earlier development of the Z-accelerator [467]. Extrapolating to new designs however assumes a knowledge of the scaling laws of the Z-pinch itself. Empirical scaling relations have been developed by Stygar *et al* [468], but these ignore the fact that the radiated energy can be three or four times the kinetic energy of the implosion, which is discussed in sections 5.8 and 7.2. Indeed the analysis assumes competition between ablation-dominated and RT-dominated pinches, each of which has its own scaling law, and concludes that a decrease in implosion time is preferential.

In contrast, experiments were undertaken ten years ago by Deeney *et al* [386] and Douglas *et al* [469] to see if x-ray powers could be maintained with a longer current rise-time ($\sim$250 ns), implying a lower voltage and fewer insulator problems. These were surprisingly successful. Characteristics of wire-array implosions on the longer 1 μs time scale are being carried out on the SPHINX machine at CEA, Gramat [470]. This leads to a longer x-ray pulse, dominated by a large plasma bubble at the cathode and the associated zippering along the axis. However there has been a dramatic improvement in the performance of SPHINX by employing a microsecond prepulse [471]. Previously the long x-ray pulse [470] was a result of a cathode bubble (see section 5.10) which collapsed onto the axis first, starting the main x-ray pulse. During the prepulse the wires are heated, but after $\sim$4 μs at 400 V there occurs plasma breakdown, presumably of vaporized low Z impurities, dropping the voltage to 40 V. The current at this time is 1750 or 8 A per wire and the deposited energy is far below that needed to cause melting of

the aluminium or tungsten. The prepulse current supply can rise to 10 kA. By varying the time of the main LTD 5 MA current an optimum value of $\sim$7 μs delay was found. Amazingly the cathode bubble disappeared, and an almost 1D snowplough-like and reproducible implosion with no zipper occurred. The x-ray pulse is reduced to 20 ns (a quarter of its previous value) and the peak power was increased by a factor of six to 1.5 TW cm^{-1}, with 25% conversion efficiency. Single arrays performed as well as nested arrays, thus simplifying future loads.

Finally the design of petawatt-class pulsed-power accelerators has been considered by Welch *et al* [472] and Stygar *et al* [473]. In [473] a comparison between Marx/pulse-forming line and LTD is made, favouring the latter. Both systems require a magnetically insulated transfer line (MITL), and Stygar *et al* [474] have studied in a relativistic model the critical issue of electron current shorting here. By varying the charging voltage of the module cavities and the timing, Stygar *et al* [475] have shown how the output current pulse of a LTD can be shaped. A LTD is compact and can be rep-rated. These features are discussed by Mazarakis *et al* [476]. Already small LTD experiments are being undertaken in universities: Bott *et al* [477] have made ablation studies of low number wire arrays at currents of 200 kA employing laser imaging techniques to measure the wavelength of the axial density variations and ablation velocities. A larger LTD-driven Z-pinch is being commissioned at the University of Michigan [478], while a load current multiplier is being tested at the University of Nevada [479].

7. Other experimental configurations of the Z-pinch

As earlier discussed and illustrated in figure 3, there are many configurations of Z-pinches. The experimental results from these will be reviewed, and interpreted using the theory developed in earlier sections.

7.1. Compressional Z-pinch

Most of the earliest Z-pinch experiments were compressional Z-pinches in which there is initially a uniform fill of gas inside an insulating cylinder, at the ends of which are the two electrodes. In section 1.2 and [29–36] we reported some of these early experiments. They are characterized by the formation through the skin effect of a current sheet adjacent to the insulating wall, followed by an implosion. Whilst experiments were often interpreted using the snowplough model, section 4.1 (which requires radiated energy loss for energy conservation), it was soon found experimentally that preceding the magnetic piston was a shock wave [257, 258] which caused dissociation and ionization [260] as discussed in section 4.2. A direct experimental verification of the presence of the shock was published by Folkierski and Latham [300]. Earlier, radiating luminous fronts were detected by Heflinger and Leonard [480] using a streak camera, and attributed to a shock. At this stage there is no sign of an instability. Only after the first pinch and a subsequent bounce with inward acceleration caused by the $\underline{J} \times \underline{B}$ force is the magneto- MRT instability observed and growth rates measured [39]. These instabilities in the form of $m = 0$ constrictions are found to occur first in the vicinity of the electrodes, and lead to axially moving luminous fronts which could be shocks [481]. These could be similar to the end effects found more recently in wire-array pinch experiments (see section 5.10).

A theory of ionizing strong shocks was developed by Gross [482] and compared with experiments. Further experiments on radially converging cylindrical shocks in various gases by Kogelschatz *et al* [483] and Kleist *et al* [484] confirm several aspects of Potter's slug model [261] (see section 4.3), namely very little current travels with the shock wave, and the gas pressure between the shock and piston is approximately uniform. However at higher filling pressures significant current has been found to flow even ahead of the shock [483].

The development of high voltage pulsed power technology [6] led to compressional Z-pinches with current rising at 10^{13} A s^{-1} or higher. Early experiments by Choi *et al* [485] using 100 kA from a 600 kV storage line produced a stationary pinch in 100 ns at about 0.3 of the pinch radius, as predicted by the slug model. There was no bounce or oscillation for times of interest. Later, end-on interferometry by Baldock *et al* [486] demonstrated a stable, cylindrical plasma column while side-on framing images were obtained by Bayley *et al* [131]. Recent work by Davies *et al* [14] shows that the enhanced stability is due to large ion Larmor radius effects, but there still is a slowly growing $m = 0$ instability as shown in figure 26. A simple model of how to attain LLR conditions in a compressional pinch is presented in [183].

However, if the aim of the experiment is to form a dense, high temperature pinch for fusion studies, a smaller final radius is needed. This could be obtained using a hollow, and hence dynamic, gas pinch which we consider next.

7.2. Gas-puff Z-pinch

The hollow gas puff is well suited for pulsed power as it removes the need for an insulating wall and its concomitant plasma–wall and radiation driven interactions. It also acts as an accelerating shell, rather than a snowplough, allowing the ions to be accelerated to higher energy before stagnation closer to the axis. The gas-puff is formed by releasing gas stored in a subsidiary chamber at high pressure, using a fast acting valve. The gas flows through a nozzle, and the resulting supersonic jet should have very little transverse motion. It is possible to use a 'solid' fill or a hollow fill, and, currently up to three separate, concentric jets have been employed [487–489], thus allowing great control of the initial neutral gas density profile and composition and so minimizing MRT growth (see section 4.7). The fast-rising current from a pulsed power generator is applied when the gas has reached the second electrode, which is usually in the form of crossed wires to enable the gas flow to continue without a reflected shock. The three shells of gas can be considered as pusher (outermost), stabilizer (middle) and radiator [489]. In this way MRT instability can be mitigated and optimal radiation power obtained.

One of the earliest experimental studies was a PhD Thesis by Shiloh at Irvine in 1978 [490] who studied both solid and hollow gas jets in deuterium and in high Z gases (argon and krypton) as a radiative source. Highest temperatures were obtained with a hollow jet, and he found that its implosion had similar phenomena to the collapse phase of a compressional pinch or plasma focus namely sausage instabilities, energetic electron and ion beams, and non-thermal neutrons. The instabilities were more slowly growing than given by ideal MHD. The current used here was generally a maximum of 300 kA from 5.4 kJ of a 30 kV capacitor bank.

Deuterium gas experiments were carried out on the Saturn generator at Sandia by Spielman *et al* [491] with currents up to 10 MA. The gas load was produced by a supersonic nozzle (Mach 6) tilted at 5° to eliminate the zippering effect. Up to 3×10^{12} DD neutrons were measured in a then unexplained extra apparent resistive heating of the pinched plasma.

Very recent gas-puff experiments carried out on Z at Sandia by Coverdale *et al* [492, 493] have taken a deuterium gas-puff pinch to 17.71 MA current and measured a neutron yield of 3.9×10^{13}. In contrast to earlier Z-pinch and plasma focus experiments these neutrons are probably not the result of ion beam formation followed by beam–plasma nuclear reactions, but mainly thermonuclear neutrons. This is because they appeared to be isotropic as far as limited measurements could conclude. A detailed discussion of the possibility that ion beams could be generated is to be found in Velikovich *et al* [494] and they conclude that the neutron yield in [492] is mainly thermonuclear and consistent with analytic theory and one- and two-dimensional simulations. They point out that this yield is several orders of magnitude

larger than in current direct-drive laser-capsule experiments elsewhere or in dynamic hohlraum experiments on Z, this being mainly due to the higher implosion velocities.

Recently Welch *et al* [495] have produced kinetic particle-in-cell (PIC) simulations of the Sandia deuterium experiment [492] and have found both thermonuclear and beam–plasma contributions to the neutron yield. More needs to be done with this type of modelling. Can ion viscosity or even electron viscosity [496] be included in such a model?

However, as in nearly all high current Z-pinches it appears that the final thermal energy of the pinch is over double that arising from the kinetic energy. Thus in [494] to obtain agreement with the experimental neutron yield, noting that the experimentally measured electron temperature is 2.2 keV and that the calculated equipartition time exceeds twice the Alfvén transit time τ_A (i.e. the total bounce time of the plasma column) an ion temperature of 10 keV (i.e. greatly exceeding the Bennett value) and an ion density n_D of 3×10^{20} cm^{-3} (compared with the measured 2.4×10^{20} cm^{-3} [492]) is required.

In contrast a new calculation based on the Bennett pressure balance at stagnation gives $T_i = 5.5$ keV. Using the experimental density for two ion transit times (each of 8 ns) and $\overline{\sigma v} = 2.3 \times 10^{-19}$ cm^3 s^{-1} the neutron yield is 4×10^{13}, close to experiment. Here we have used the formula

$$Y_n = \tfrac{1}{4}\pi a^2 z_0 n_D^2 \overline{\sigma v} \times (2\tau_A) \tag{7.1}$$

where a is the pinch radius and z_0 its length. The kinetic energy prior to stagnation, based on the ion radial velocity of 70 cm μs^{-1} [492] is 5.1 keV per ion with very low electron temperature. The equipartition time is 25 ns ($\gg \tau_A$), allowing the ion temperature to exceed the electron temperature over the period of neutron emission. In this model it is assumed that the increase in ion thermal energy is the result of ion-viscous heating associated with small amplitude, short wavelength $m = 0$ MHD instabilities [130] rather than just reversible $P dV$ heating. The latter in any case would be included in current 2D MHD simulations, and is usually insufficient to account for preferred ion heating. As noted in [494] these simulations generally include fudge factors to prevent radiative collapse, which can be physically prevented by ion-viscous heating [130] or some extra phenomenological ion heating source [329–332].

A puzzling result is that of Kroupp *et al* [497] who, from detailed time-resolved Doppler shifted spectroscopic measurements of optically thin lines in neon, showed that there is in this experiment a balance between the ion kinetic energy and the radiated energy, via electron energy through equipartition. There is no rise in T_i at stagnation in contrast to that measured by LePell in [130]. However it can be shown that at this relatively low current (320 kA at stagnation) gas-puff Z-pinch there is negligible viscous heating and all short wavelength MHD modes are essentially resistively damped, i.e. the magnetic Prandtl number is much less than one [253]. There are several ways of arriving at this conclusion. One is to examine where in the $I^4 a$–N_i stability regimes diagram, namely figure 16 (but altered for the higher Z value according to equations (3.4), to (3.13), this experiment at stagnation lies. $I^4 a$ is found to be 4.2×10^{18} (A^4 m) at $N_i = 1.27 \times 10^{19}$ (m^{-1}). The electrons are weakly magnetized with $\overline{\Omega_e}\tau_{ei} = 4.6$ (using the spatial average of B_θ) while the ions are unmagnetized at $\overline{\Omega_i}\tau_i = 2.4 \times 10^{-3}$ making the ratio $a_i/a = 0.025$ irrelevant. The magnetic Reynolds number S is 91, i.e. $\sim$100, on the border of resistive stabilization effects [153, 154] while the Reynolds number R is 1.7×10^4 taking into account the contribution from electron viscosity. $\gamma\tau_i = 1.2 \times 10^{-4} \ll 1$ is closely related to R^{-1}, and shows that viscous effects are negligible.

In another approach considering the relative damping of Alfvén waves by resistivity and viscosity it is found that the competing diffusivities are $\eta/\mu_0 = (\mu_0\sigma)^{-1}$ and ν (the effective kinematic viscosity), respectively. For [497] η/μ_0 is 0.386 m^2 s^{-1} while ν is 2.0×10^{-3} m^2 s^{-1} showing that resistive damping dominates over viscous damping. Thus
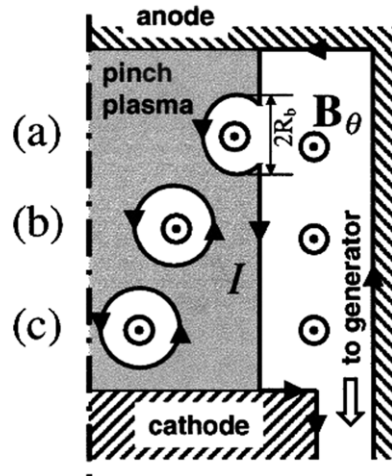
Figure 73. (*a*) A magnetic bubble is formed as a $m = 0$ RT or MHD perturbation at the pinch surface. The plasma closes back behind it, producing a flux tube. (*b*) The flux tube is driven to the axis due to both curvature stress and buoyancy force. (*c*) Near the axis, it still carries the same magnetic flux, but most of its energy has been dissipated in the plasma. Reprinted figure with permission from [235, figure 1]. Copyright 2000 by the American Physical Society.

in this experiment, in contrast to [130] and many high current implosion experiments, there is essentially no extra viscous conversion of magnetic energy to thermal energy but only resistive heating of electrons and compressional heating.

On the other hand, Coverdale *et al* [492]'s gas-puff experiment has parameters $I^4 a = 1.97 \times 10^{26} \, \mathrm{A^4 \, m}$, $N_i = 1.21 \times 10^{22} \, \mathrm{m^{-1}}$, $\overline{\Omega_e} \tau_e = 10^3$, $\overline{\Omega_i} \tau_i = 76$, $a_i/a = 7.3 \times 10^{-3}$, $S = 9.1 \times 10^5 (\gg 10^2)$, $R = 5.7$, $\gamma \tau_i = 0.45$, $\eta/\mu_0 = 4.5 \times 10^{-3} \, \mathrm{m^2 \, s^{-1}}$, $\nu = 3.0 \times 10^2 \, \mathrm{m^2 \, s^{-1}}$, showing that viscous MHD is dominant, and resistive effects are negligible.

Interestingly both experiments have relatively long equipartition times, $\gamma \tau_{eq}$ being 3.5 for Coverdale's and 0.76 for Kroupp's experiment. Thus in Coverdale T_e is expected to be much lower than T_i during the stagnation period whereas in Kroupp T_e will converge towards T_i which itself will fall as there is essentially no viscous heating, just equipartition from the thermalized ion kinetic energy. There are many other experiments which have displayed higher T_i than can be explained by resistive MHD with gas puffs. One of these by Wong *et al* [498] has measured an ion temperature of 36 keV in neon (90%) + argon (10%) while T_e is 1.25 keV with a current of 8 MA (using Saturn at Sandia). To satisfy the Bennett relation the effective line density N_i has to be half the nominal annular fill, namely $4 \times 10^{20} \, \mathrm{m^{-1}}$. From the measured electron density the ion density is $7.6 \times 10^{25} \, \mathrm{m^{-3}}$ leading to a pinch radius of 1.3 mm, consistent with x-ray profiles. From this R is 114 while S is 9×10^4. Thus viscosity dominates over resistivity ($S \gg R$) in contrast to Kroupp where $R(\sim 10^4) \gg S(\sim 90)$. A discussion of the distinction between viscous and resistive Z-pinches and the role of numerical viscosity in simulations is to be found in [395].

A detailed analysis for neon, argon and krypton gas puff Z-pinches by Labetsky *et al* [499] claimed that the additional heating was due to toroidal magnetic bubbles associated with $m = 0$ instabilities, penetrating to the axis. A model in Rudakov *et al* [235] suggests that the extra energy is not due to $p \mathrm{d}V$ work, nor Ohmic dissipation nor anomalous resistivity but that magnetic energy in the bubbles is somehow converted into thermal energy leading to an effective resistance. Figure 73 taken from [235] illustrates the mechanism. This idea was first published in 1993 in a little quoted paper by Lovberg *et al* [329] who calculated an effective

resistance (in SI units)

$$R_{\text{Lovberg}} = \frac{\ell}{4(N_i m_i)^{1/2}} \left(\frac{\mu_0}{\pi}\right)^{3/2} \frac{I}{a}. \tag{7.2}$$

This determined the rate of transfer into 'turbulent kinetic energy' of the plasma. To get agreement with HDZP-II deuterium fibre Z-pinch experiment this heating was added only to the ion energy equation, and was described as a 'boiling' of the pinch. The inward radial velocity of the bubbles is equated to the Alfvén speed. Lovberg states that only 10% of the pinch length is affected in this way, and agreement on the low neutron yield is obtained because of the drop in density resulting from a faster expansion of the corona.

In Rudakov *et al* [235, 331] there is a discussion of the inward velocity of bubbles based on buoyancy leading to a velocity v_{bubble} given by

$$v_{\text{bubble}} = 2\alpha \left(\pi \frac{r_b}{a}\right)^{1/2} \overline{v_A}, \tag{7.3}$$

where r_b is the radius of the bubble, $\overline{v_A}$ the mean Alfvén speed and α an undetermined constant. For 'definiteness' Rudakov *et al* take $r_b/a = 0.2$ and $\alpha = 0.3$ to give the effective additional nonlinear resistance

$$R_{\text{Rudakov}} = \frac{\ell}{2 \cdot (N_i m_i)^{1/2}} \left(\frac{\mu_0}{\pi}\right)^{3/2} \frac{I}{a}. \tag{7.4}$$

This mechanism is further explained and employed by Velikovich [329] to compare with experiments. It is essentially identical with the earlier work by Lovberg, differing only by a factor of 2. Both models have some arbitrariness in the numerical coefficient. The effective resistance in Haines' viscous heating model, equation (5.13) has no arbitrary constant and employs well established MHD instability growth rates, saturation levels and stress tensors. Taking the growth rates in Coppins [149] R_{visc} becomes

$$R_{\text{visc}} = \frac{\Gamma(1 + \Gamma/2)^{1/2}\ell}{8(N_i m_i)^{1/2}} \left(\frac{\mu_0}{\pi}\right)^{3/2} \frac{I}{a}. \tag{7.5}$$

For the ratio of specific heats Γ of 5/3 the coefficient becomes 0.282 which is just 10% larger than in R_{Lovberg}. Considering the large physical differences in the two models this is remarkable. One reason for this coincidence is that in choosing a viscous Lunqvist number of 2 the product of wave number and viscosity is eliminated to give the left-hand side of equation (5.10) for the local ion-viscous heating rate. The positive aspect is that the resistance formula enables 0D and 1D models to agree with experiments.

In Haines' model the wavelength is short and corresponds to the fastest growing mode. This saturates at a low amplitude, but the viscous heating for high k is substantial. Depending on the ratio of ion to electron viscosity, the heating will be distributed between ions and electrons. There is no need to postulate turbulence and associated cascading. If Menikoff's theory [500] is adapted to the MHD instability the wavelength of the fastest growing mode is increased. In contrast a 'flux limit' to the momentum transport caused by the mean-free path being only slightly smaller than the wavelength is equivalent to an increase in k. A full nonlinear Fokker–Planck stability analysis is needed in which electron viscosity is also included, not only in the equation of motion but also in Ohm's law.

In the Lovberg/Rudakov/Velikovich (LRV) model, the implied wavelength is long and in the linear phase will exponentiate only once in one Alfvén transit time. Thus there is little time at stagnation for it to grow unless it is already well established as a MRT mode. There is even less chance for the cascading to shorter wavelengths implicit in establishing MHD turbulence. In contrast Haines chooses the fastest growing mode and has no need for cascading. Indeed $\delta B/B \sim (ka)^{-1}$ here, whilst LRV requires $\delta B/B \sim 1$. In LRV there is a problem with current
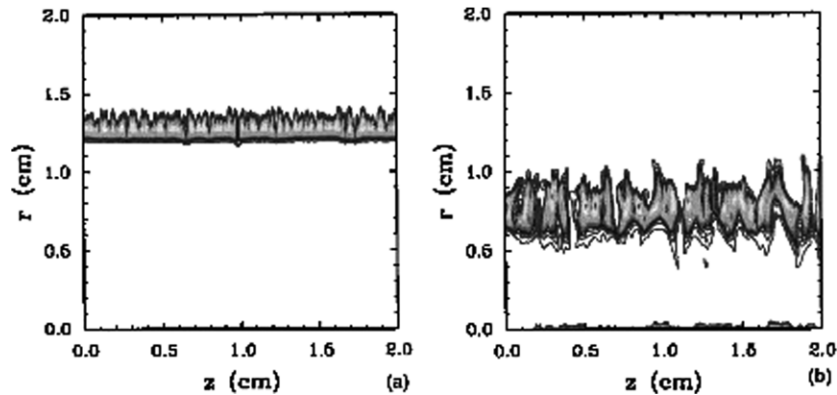
Figure 74. Density contours at (*a*) $t = 205$ ns and (*b*) $t = 218$ ns for a 2D simulation. The calculation exhibits short wavelength growth which saturates and then develops into longer wavelengths. Reprinted with permission from [321]. Copyright 1998, American Institute of Physics.

reconnection, when, prior to this the $J_r B_\theta$ forces in the outgoing $m = 0$ flares are confining the flares and preventing coalescence. But of course the axial electric field in the vacuum gaps will be enhanced by the feeding of magnetic flux into the inward-going bubble, analogous to current switching in nested arrays. When simulating this there is a problem that the vacuum regions are usually modelled with a low density plasma of high resistivity, so the results will depend on this numerical artefact. A second problem is the conversion of magnetic energy stored in each bubble to ion thermal energy. $\int P \, dV$ work is cited in some of these papers, e.g. [458]. But this is reversible and will heat both species in the ratio of their pressures. Furthermore LePell in [130] has shown that experimentally the ion temperature continues to *increase* whilst the mean pinch radius is *increasing*. Another point is that within each bubble B_θ falls off as $1/r$, and at the outer surface, as shown in figure 73 the current density is reversed leading to an outward $\underline{J} \times \underline{B}$ force which will work against buoyancy. Lovberg states that magnetic 'flux is detached from the circuit and ingested by the turbulent pinch'. How the magnetic energy is converted without resistivity is rather vague in LRV. $\underline{J} \times \underline{B}$ could lead to local $\rho \, dv/dt$ ion acceleration and then to viscous dissipation via shocks or steep velocity gradients. Indeed, insofar as numerical simulations are able to give enhanced radiation, large amplitude MHD modes with *numerical* viscosity to provide the dissipation is the probable energy route. So far no simulations have included the real physical viscosity, let alone the full stress tensor. Douglas *et al* [501] found that computationally the growth rate was limited if fewer than ten mesh points per wavelength were employed. In Peterson *et al* [321] while there is evidence for shorter wavelengths growing more quickly and saturating, emphasis is placed on the evolution of longer wavelength modes, as shown in figures 74 and 75. At stagnation, density profiles in figure 75(*a*) indicate that pronounced spikes are dominant while in (b) the contours of $r B_\theta$ which may be interpreted as current streamlines show that work can continue to be done on this outlying material by the Lorentz force. There could be a few current loops in the plasma indicative of magnetic bubbles, but they do not appear to be dominant. Recently Lemke [367; see also 392] has shown that 70% of the radiated energy arises from numerical heating associated with artificial or von Neumann viscosity. He also showed that there was an optimum ablation rate (in the precursor phase) for maximizing the x-ray power.

In Chittenden *et al* [324] a 3D MHD simulation with GORGON shows helical $m = 1$ structures as well as $m = 0$ hot spots. Agreement on x-ray emission occurs if there is significant
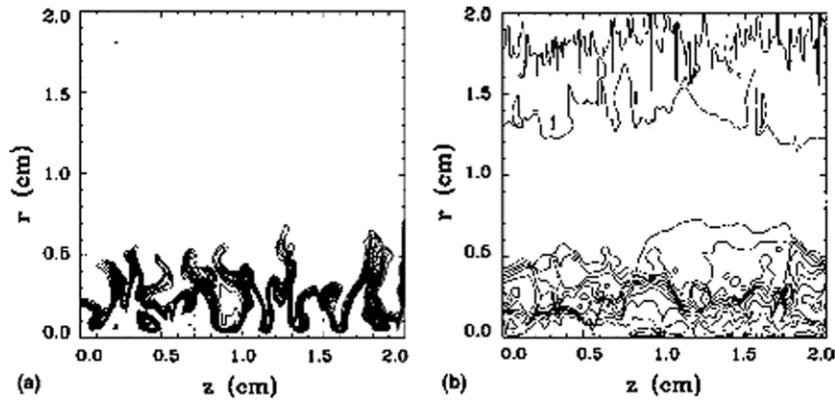
Figure 75. Contours of (*a*) density and (*b*) $r B_\theta$ at stagnation, $t = 230$ ns. Reprinted with permission from [321]. Copyright 1998, American Institute of Physics.

$m = 1$ activity in the simulation which itself is dependent on the initial, arbitrary azimuthal perturbations in the simulation. In ALEGRA simulations in order to obtain energy conservation when switching from Lagrangian to Eulerian meshes plus the numerical viscosity, Lemke [367] transfers the excess energy to ion thermal energy. This then appears equivalent *in effect* to the ion-viscous heating of Haines [130]. It is interesting that because the choice of k, the wave number of the fastest growing mode in equation (5.7) with $L_\mu = 2$, depends on the value of the viscosity, the resulting viscous heating is independent of both k and viscosity. Thus, provided $S \gg R$ holds, and provided the excess energy is the result of 2D or 3D activity, it is reasonable in simulations to deposit the excess energy into thermal energy.

Early attempts to account for the extra heating included an arbitrary increase in all dissipative processes by some assumed turbulence [401]. The 3D modelling introduces an initial chosen azimuthal perturbation, and together with artificial viscosity and a coarse mesh leads to an axial magnetic field of the same order as the azimuthal field [443] much earlier than the experimental observation of any helical structure. This means that there is a generation or injection of helicity to the pinch. Helicity per unit volume, $\underline{A} \cdot \underline{B}$ (or some authors use $\int \underline{A} \cdot \underline{B}\, \mathrm{d}V$) where $\underline{A}$ is the magnetic vector potential is governed by the equation

$$\frac{\partial}{\partial t}(\underline{A} \cdot \underline{B}) + \nabla \cdot (\underline{E} \times \underline{A} + \Phi \underline{B}) = -2\underline{E} \cdot \underline{B}, \tag{7.6}$$

where $\underline{E}$ is $-\partial \underline{A}/\partial t - \nabla \Phi$. The source term, $-2\underline{E} \cdot \underline{B}$ is usually negligible in a highly conducting plasma and so the local change of $\underline{A} \cdot \underline{B}$ must be due to a surface flux of $(\underline{E} \times \underline{A} + \Phi \underline{B})$ which in simulations has to be prescribed in effect at the outer boundary. This implies the imposition of a radial magnetic field or a radial component of $\underline{E} \times \underline{A}$ at the outer boundary.

7.3. Plasma focus

There are two main configurations of the plasma focus device; the 'Mather type' and the 'Filippov type', named after their inventors [40, 41] and shown in figure 76. The largest Mather-type device, the 1 MJ experiment at Frascati, produced 10^{12} neutrons when optimized for 500 kJ stored energy at 5–8 Torr filling pressure [42]. The neutron yield has a I^4 scaling, as does the x-ray yield, and there are many mechanisms proposed, [241, 243, 246, 503], most of which are designed to account for the anisotropy of the neutron production through the onset of an intense ion beam followed by beam–plasma nuclear reactions. As pointed out in [243] and in section 3.14 ideal and resistive MHD cannot produce a uni-directional flow of ions
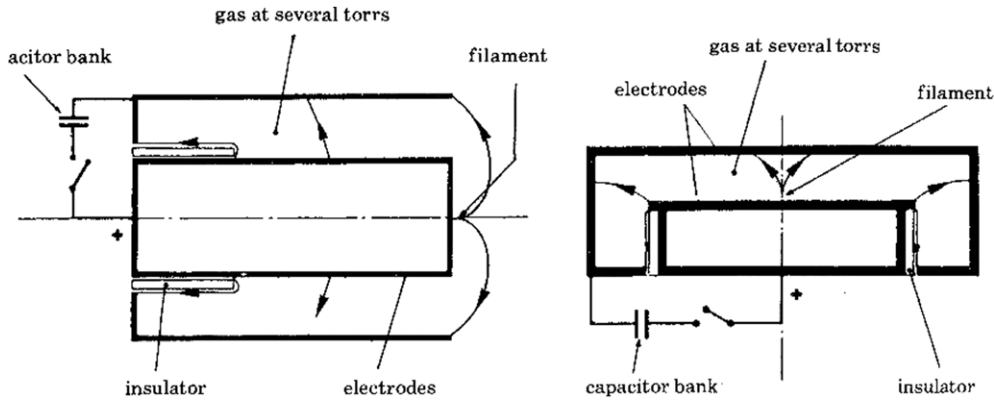
113

Figure 76. The plasma focus; (left) Mather type; (right) Filippov type [84, figure 1]. Reprinted with permission from The Royal Society.

from a $m = 0$ MHD neck in a Z-pinch because this theoretical model is symmetric above and below the axial position of the minimum radius. To merely state that the axial electric field is large [35] is insufficient (a) because in ideal MHD with $\underline{E} + \underline{v} \times \underline{B} = 0$, in the rest frame of the moving plasma itself the electric field is zero, and (b) the only force per unit volume on the plasma due to an electric field is $q_v E$ where q_v is the net charge density. Because $q_v = \varepsilon_0 \nabla \cdot \underline{E}$ it follows that the electrostatic force per unit volume is $\varepsilon_0 \underline{E} \nabla \cdot \underline{E}$ which is usually negligible compared with the magnetic force and is ignored.

In section 3.14 the mechanism of a disruption was discussed as it is a phenomenon common to all Z-pinches and not just the plasma focus. Here a model is outlined which gives a neutron yield from a single $m = 0$ neck which is close to that found in experiments. Ion acceleration towards the cathode will occur as the $m = 0$ neck forms [243] (with off-axis ions accelerated in the opposite direction to conserve total axial momentum). When the local line density drops below the critical value given by equation (3.58) anomalous resistivity with associated heating sets in, leading to a transient positive voltage spike. This is because the electron drift velocity exceeds the ion sound speed. Thereafter there is no pressure balance as the current is limited in the $m = 0$ neck and a fast, transient, and local outward flow of plasma occurs. The current and magnetic field are also swept out and there is a redistribution of magnetic field on the Alfvén transit time scale. Figure 77 illustrates this, and the associated axial electric field will have a large positive value near the axis which accelerates ions in the $+z$ direction and an e-beam in the $-z$-direction with singular orbits. Further out the electric field reverses in sign, its value at the main pinch radius a_z leading possibly to a negative voltage spike. Ions are accelerated in the $-z$-direction in this region while the axial electron current is driven by the $v_r B_\theta$ electric field associated with the outward flow of plasma. As mentioned earlier, neutrons produced off axis by this reversed ion flux have been measured by Tiseanu and Mandache [250]. By this means axial momentum is conserved. This can be confirmed by examining the induced electric field arising from the change in magnetic flux in the neck region.

If the magnetic energy released is given mainly to the ions at a line density N_{crit} an energy E_I (eV) arises given by

$$2 N_{\text{crit}} \ell e E_{\text{i}} = \frac{\mu_0 I^2 \ell}{4\pi} \ln\left(\frac{a_2}{a_1}\right), \tag{7.7}$$

where a_1 is the initial radius of the neck and a_2 is the final radius (probably greater than the radius of the adjacent bulges). The length of the $m = 0$ neck, ℓ, cancels in equation (7.7) but
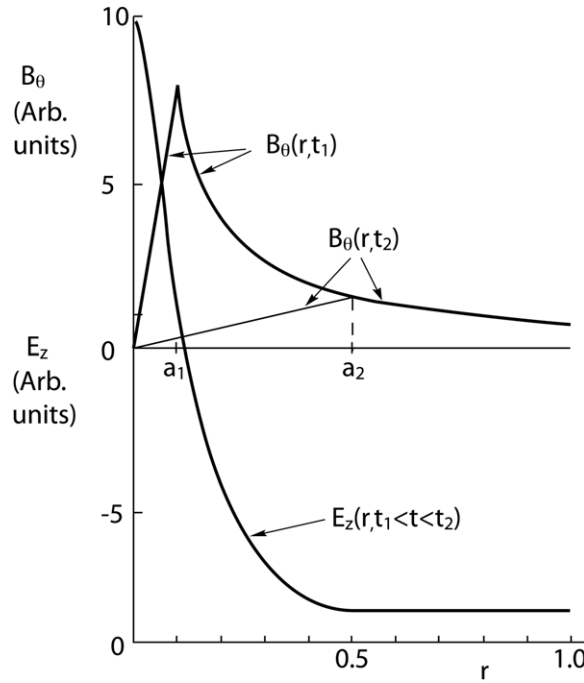
Figure 77. Schematic plot of $B_\theta(r)$ before and after the disruption. The axial electric field during this process, which depends on $\partial E z/\partial r = \partial B_\theta/\partial t$, is also shown.

an estimate is required to find the neutron yield Y_n in the formula

$$Y_n = \overline{\sigma v} N_{crit} \ell n_0 \tau_{ii}, \tag{7.8}$$

where $N_i \ell$ represents the number of accelerated ions at the energy eE_i, $\overline{\sigma v}$ is the averaged fusion cross-section × velocity, n_0 is the ion density in the stationary or target plasma and τ_{ii} is the slowing down time. It should be recalled that there are far more Coulomb collisions than fusion events, hence fusion will only occur for a time τ_{ii}. The product $n_0 \tau_{ii}$ is given by

$$n_0 \tau_{ii} = 1.5 \times 10^{13} \frac{A^{1/2} T_i^{3/2}}{Z^4 \ln \Lambda_{ii}} \tag{7.9}$$

and we put T_i equal to E_i. The value of ℓ will be taken as $2a_I$ which is approximately the pinch radius at the neck. This will allow the singular ions around the axis (see equation (2.21)) to escape as a beam away from the anode, while a larger number off axis will be accelerated to a lower velocity in the opposite direction. Such a model gives typically up to $Y_n = 10^{12}$ for currents just below 10^6 A, and with a strong dependence on current in excess of I^4 for currents below 100 kA. However, because the critical line density is a constant and $\overline{\sigma v}$ rises less steeply at higher beam energy the exponent will be reduced for higher currents. As discussed in [84] the ion beam might reach the Alfvén limiting current I_A for particles of energy eV, given non-relativistically by

$$I_A = \frac{4\pi}{\mu_0} \left(\frac{2mV}{e} \right)^{1/2}, \tag{7.10}$$

which is close to that in the Limeil experiment. The electron current as detected by Nardi [244] in a hollow cathode would be smaller by the square root of the mass ratio. At the time of the

beam-generated neutrons there is experimental evidence, observed by Barnard *et al* [238] and Forrest *et al* [255] of electrostatic turbulence using laser scattering techniques. This is consistent with the line density locally at the $m = 0$ neck falling below the critical value, described in section 3.14.

In most experiments there is an earlier neutron pulse arising at the time of the implosion. Deutch and Kies [242] have identified this with a Fermi mechanism in which the higher velocity ions are reflected several times in the inward moving sheath carrying the skin current. Neutrons resulting from D–D collisions in this case would have an anisotropy in which more neutrons would be emitted radially.

At currents greater than 1 MA there is a tendency for the neutrons to be more isotropic, and there could be a significant thermal component which would scale as I^2, more like the high current gas-puff experiments (section 7.2). Such results were found on the 1 MJ plasma focus at Frascati by Maisonnier and Rager [239]. By pinhole-imaging the charged particles from the fusion reaction zone and correlating with time-resolved neutron detectors Zakaullah *et al* [503] showed that at low pressure the neutrons were produced by beam–plasma reactions with an anisotropy of 3.5. Above the optimum pressure (for this 2.3 kJ low energy machine) of 2.5 mbar the almost stable plasma moves away as a jet-like boiler. The apparent stability at this time could be explained by Comisar [504] who theoretically showed that for a curved Z-pinch (as in a plasma focus) the $m = 0$ instability grows 10 times more slowly. Hirano *et al* [505] found a similar transition from low to high pressure.

The plasma focus does not require pulsed power on the 100 ns time scale but works conveniently with a capacitor bank with microseconds' time scale. Instead, the rundown phase allows magnetic energy to be stored inductively, prior to the final collapse, which can have a high implosion velocity due to the early shedding of mass, in the rundown phase.

There is a strong polarity dependence, the device having much higher neutron and x-ray yields with a central anode. (This is the opposite polarity to present-day wire-array experiments where the cathode and power-feed point are at the same end). There are several mechanisms which are affected by the polarity. Bostick [506] noted that the shapes of the moving ionizing shock front and current sheet behind were different. This is because of the Hall effect. Writing

$$\underline{E}^* = \underline{E} + \underline{v} \times \underline{B} + \nabla p_e / n_e e + \nabla T_e. \tag{7.11}$$

Ohm's law becomes

$$\sigma \underline{E}^* = \underline{J} + \underline{J} \times \underline{\beta} \tag{7.12}$$

where $\underline{\beta} = \varpi_e \tau_{ei} \underline{b} = \sigma \underline{B} / n_e e$ is the Hall parameter. There is an angle θ between $\underline{E}^*$ and $\underline{J}$ such that

$$\underline{b} \tan \theta = \frac{\underline{E}^* \times \underline{J}}{\underline{E}^* . \underline{J}} = \underline{\beta}, \tag{7.13}$$

where $\underline{b}$ is the unit vector in the direction of the magnetic field. If the generalized electric field $\underline{E}^*$ is normal to the surface of the conducting inner electrode, then when it is the anode the current will slope backwards, causing the plasma slug to be bullet shaped. In this way much of the plasma swept up will move radially outwards, so that in the final implosion when the current has reached its peak and is at the end of the anode, the mass is smaller and a faster implosion occurs.

In the case of a central cathode the current will slope forward, less radial motion will occur, and a greater mass will have to be collapsed to the axis.

An apparently different explanation of the polarity 'riddle' is presented by Decker *et al* [507]. Their theory is that the plasma behaves very differently in the radial electric field between the electrodes. In an experiment they show that shielding out this field by means of

a copper conductor buried in the insulator leads to almost equal behaviour of both polarities. In contrast an unshielded insulator with a central cathode leads to two orders of magnitude reduction in the neutron yield. Only with a central anode can there be electron charging on the insulator surface. The employment of a high dielectric insulator is also important. But this result is perhaps consistent with the Hall effect model, since both models depend on the angle between the current and electric field.

In the breakdown process and early heating of the plasma sheath, radial spokes or filaments can occur. This could be due to the current-driven electrothermal instability [158], discussed in section 3.12. Bostick *et al* [508] claimed that the filaments came as pairs of plasma vortices. But Mather and Williams [509] were not convinced that there was a paired effect. Nardi [510] constructed a theory for the production of filaments, which he envisages are bundles of helical field lines, in the regions of high plasma vorticity behind a shock wave. Bykovskii and Lagoda [511] investigated the occurrence of filaments in a laser-initiated vacuum discharge. However, at higher power, filamentary structures play little rôle, probably because the condition that the mean-free path be less than the collisionless skin depth is not satisfied for very long [158, see also section 3.12]. In their book Liberman *et al* [87] discuss several other mechanisms for filamentation but conclude that the electrothermal [158] overheating instability, such as discussed later by Imshennik and Neudachen [512] is the most likely explanation. Radiation loss also enhances the growth rate provided the loss rate has less than a T^2 dependence. Bremsstrahlung with a $n^2 T^{1/2}$ dependence, as used in [214], therefore enhances the instability. This is because, with ion motion included, a hot filament has a lower density, and radiates less than the higher density region surrounding it. Adding an inert gas as a dopant can increase the x-ray radiation loss; this will be discussed further below and in section 8.1.

Attempts have been made to obtain scaling laws not only for larger but also for smaller plasma focus devices. Lee and Serban [513] defined a 'drive-parameter' S by

$$S = \frac{I_{\mathrm{p}}}{a\rho^{1/2}}, \tag{7.14}$$

where I_{p} is peak current, a is the inner (anode) radius and ρ is the filling density. For plasma focus devices optimized for neutron production S is almost the same for all sizes. This was followed up by Zhang *et al* [514] for a range of currents from 180 to 400 kA and for aspect ratios which spanned Mather and Filippov types. Beg *et al* [515] studied the x-ray emission from a table-top plasma focus and its application as a backlighter. Soto [516, 517] has extended this scaling to very small repetitive plasma focus experiments, useful for field applications. A plasma focus using an energy source of only 1 J has been developed [518].

There is a transition in the structure of the x-ray emitting region as the charge number of the ion is increased beyond 18. Below $Z = 18$ there is a well defined pinch column, while above $Z = 18$ hot spots with harder x-radiation occur on the axis. These results by Beg *et al* [515] are consistent with earlier data by Lebert *et al* [519] and Kies *et al* [520]. It is likely that the transition to hot spots is the result of $m = 0$ MHD instability in which radiative collapse plays an important role. Indeed when a heavy gas dopant is added to a deuterium plasma focus, hot spots are in evidence [521, 522]. This is due to timing of the pinch to coincide with maximum current at peak compression, and the need to minimize filamentary structures at the insulator and during the rundown phase.

As in Z-pinches, the long-time behaviour of a dissipative plasma focus could be to transform via a helical or kink mode into a minimum energy state [219]. This was considered by Sestero *et al* [523]. More recently Kukushkin *et al* [524] proposed that a spheromak-like magnetic configuration might be produced from a plasma focus by means of a dynamo effect (see [525]).

At Culham Laboratory, Peacock and his team used their plasma focus as a test-bed for new diagnostics. Ion temperatures of 0.3 to 3 keV were measured by collective Thomson scattering [526], while magnetic fields of ∼1 MG were measured from Zeeman splitting of the C v 2s2p line [527].

In closing this section on plasma focus experiments, it should be said that much of the interest in this configuration has centred on neutron production. There are many incomplete and hand-waving theories concerning the production of ion beams. No theory is complete unless it can be shown where the equal and opposite momentum is deposited. It should be remembered that in the local instantaneous rest frame of an ideal MHD fluid, the electric field is in fact zero. For individual ions moving at a velocity different to the centre of mass they will experience an electric field, and indeed in a two-fluid model there is an electric field associated with the Hall effect and the electron pressure gradient. Furthermore in the presence of transport, e.g. heat flow, there will be an electric field. However, quasi-neutrality means that $q_v \underline{E}$ is much smaller than $\underline{J} \times \underline{B}$ or ∇p unless the scale length for gradients is of the order of a Debye length. This then is the condition for diode action, and the equal and opposite reaction is where the net negative charge is located. However, some of the earliest theories of the ion acceleration mechanism merely assume a given axial electric field and azimuthal magnetic field to calculate ion orbits. We consider these chronologically. Bernstein [528] calculated ion orbits in the r–z plane for a contracting Z-pinch with $E_z = 0$ on the axis. Furthermore he assumed an unexplained anomalous rise in resistivity in order to obtain a sufficiently high electric field. He was aware that there was a problem of non-conservation of axial momentum. Potter and Haines [529] included the radial electric and $\partial A/\partial t$ field with self-consistent ion particles and electron fluid. When the density is sufficiently low so that the ion Larmor radius and collisionless skin depth, c/ω_{pi}, are comparable to the pinch radius, the ion distribution function evolves to become very anisotropic, and singular orbits of energetic ions dominate. Later Bernstein and Comisar [530] extended the cross-field acceleration model of [528]. Gary and Hohl [531] postulated instead a strong E_z on axis and $E_z = 0$ outside the plasma, associated with a decreasing current in a modification of Bernstein's model. Again Gary [532] required anomalous resistivity in order to obtain ions of sufficient energy. Kondoh and Hirano [533] calculated ion orbits for a snowplough collapse with no axial dependence of fields. Unlike [529] no radial electric field was included and they criticized models in which E_z is put to zero at the plasma radius.

Hohl and Gary [534], still with $E_r = 0$, examined *electron* beam formation from (i) current filaments and (ii) a uniform current distribution. (Incidentally the magnetic topology of the filamentary case is the same as that for wire arrays.) Again the axial electric field is put to zero outside the pinch, implying no internal change in magnetic flux. There is an optimal pressure for maximum x-ray yield in any particular device. Experimental x-ray spectra have been measured with energies up to 350 keV [535], with a $E^{-3.3}$ power law in a parabolic plasma focus. Lee *et al* [536] found E^{-4} while Johnson [537] found E^{-2}. In a mainly experimental paper Stygar *et al* [538] found similar power laws for the electron and ion beams of the form $dN/dE \propto E^{-2.9+0.5}$ and $E^{-3.5\pm0.5}$, respectively, and the ratio of the number of ions to electrons accelerated was approximately the square root of the ion to electron mass ratio. The instantaneous ion current needed to produce the electrons was estimated to be 800 kA, compared with the pinch current of 560 kA. The beams are generated at the time of a large negative dI/dt, i.e. a current interruption, but neither the diode mechanism nor orbit calculations [533] could give sufficient energy $\geqslant 1$ MeV. Smith *et al* [539] considered the plasma focus as a compact electron accelerator.

Trubnikov and Zhdanov [540] found an analytic mode of a $m = 0$ instability leading to a complete break-off on the time scale of a radial Alfvén wave, accompanied by breakdown in a surrounding channel with filamentary currents and lower hybrid oscillations. In [541] Kondoh

and Mamada return to the plasma diode model with anomalous resistivity after disruption by a $m = 0$ mode. There is no conservation of axial momentum in this model, in contrast to the earlier work of Haines [243]. Vikhrev [246] and Trubnikov [241] published their two papers in 1986 to celebrate Filippov's 70th birthday. Disagreeing as to the origin of the neutrons, Vikhrev, backed by 2D MHD simulations, considered the neutrons as thermonuclear arising in the high temperature $m = 0$ necks of the Z-pinch. Trubnikov developed his earlier model further in which the ions are accelerated by a large induced electric field resulting from the redistribution of current. Again there is a problem of momentum conservation. Schmidt [542, 543] assumes in his 'gyrating particle model' deuterium ions originating at $r = 0$, $z = 0$ already with high energy. He follows their orbits with electron collisions and D–D fusion reactions in the surrounding gas in an attempt to match their energy and orientations with experimentally measured time-integrated and spectrally resolved distributions of fusion protons and neutrons. A similar method was applied by Rhee and Weidman [544] in which the acceleration process was consistent with a diode action. Hora *et al* [545] considered a double layer model for a fast decaying current, but implied that in their model the ion current would be orders of magnitude lower than the electron beam current.

In conclusion, the origin of the ion and electron beams whilst perhaps still controversial could be best explained by the breaking of symmetry each side of a $m = 0$ neck by the Hall and FLR terms. This evolves during the redistribution of current density in the neck, like Trubnikov's model, into a disruption with anomalous resistivity when the line density in the neck drops below the critical value given by equation (3.58). This leads to energetic singular ion beams and off-axis reversed ion flow (conserving momentum) [243] of lower energy deuterons as measured by Tisaneau and Mandache [250]. Electron beams which impact a solid anode typically have energies greater than 100 keV to 1 MeV.

7.4. Gas-embedded pinch

It could be said that the origin of the gas-embedded Z-pinch dates back to 1947 with the investigation in Russia of the development of a spark channel under high pressure with moderate currents. This is discussed by Braginskii [546] who developed a theory of Joule heating and expansion of a channel with classical resistivity and thermal conductivity with bremsstrahlung radiation loss, neglecting the effect of magnetic forces.

For Alfvén and Smårs [547] the magnetic pressure was important for confinement, and the surrounding gas was considered as high density gas-insulation. Fälthammar [108] investigated the steady-state cross-field thermal conduction losses of such a Z-pinch, as discussed in section 2.3. Smårs [548] reported experimental results in hydrogen, helium, and nitrogen. Kerr cell photographs showed the familiar $m = 1$ kink instability at currents of 100 kA.

Skowronek *et al* [549] described the production of an exploding plasma filament which generated a Mach 12 shock in atmospheric air. First a filament is produced between two needles 3 cm apart and 0.5 μm radius, stabilized by two rings at intermediate potentials and a current of 100 μA, stable for 10 min. A 90 kV capacitor bank is then discharged rising to 200 kA in 1 μs. The aim of this experiment was to study dense, low temperature plasmas in the regime between degenerate and non-degenerate plasmas and also when the distance between ions $n_i^{-1/3}$, the Debye length and the Landau lengths are almost equal, i.e. strong coupling. Over a large spectral region the plasma column radiates as a black body at 44 000 K, and is stable. In a later paper [550] they identified the onset of anomalous resistivity. Benage *et al* [551] extended this to 240 kA in 220 ns. The pinch always expanded reaching a radius of 8 mm with a velocity of 30 km s^{-1} with accretion of the surrounding gas. A helical instability occurred within the expanding cylindrical envelope.
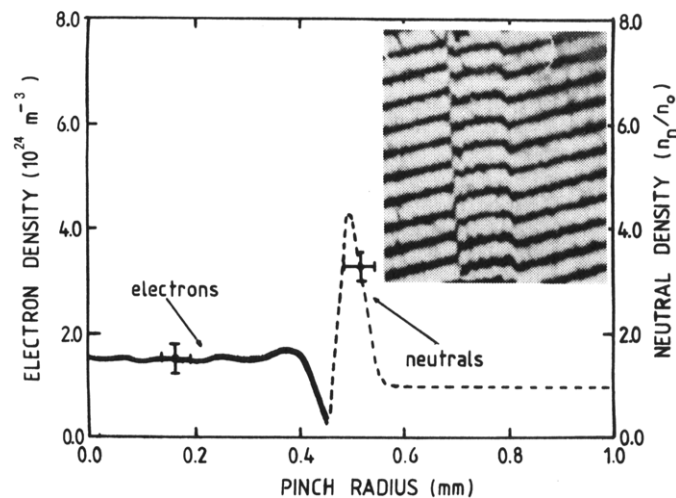
Figure 78. Imperial College gas-embedded pinch; number density profile of electrons and neutrals during preheating phase at a filling pressure of 0.3 bar [182, figure 3]. Reprinted with permission from the IAEA.

In their conceptual fusion reactor based on the high plasma density Z-pinch Hartman *et al* [552] considered that one means of isolating the Z-pinch is by a dense blanket of cold neutral gas. Two pinch cycles were considered, one where the pinch was sufficiently long to minimize plasma flow out of the ends and the other where refuelling occurred by plasma flow, e.g. using axial flow as proposed by Morozov [553] with FLR stabilization This has developed further to include sheared axial flow, considered in sections 3.5 and 7.7.

Jones *et al*'s [554] laser-initiated, gas-embedded Z-pinch experiment with a 2D MHD model indicated a 200 eV electron temperature at a density of 10^{20} cm^{-3}. The pinch was powered by a 600 kV Marx generator and (water) transmission line into 3 atm H$_2$ gas with 260 kA, rising in 200 ns.

In his thesis [555] Shlachter presented schlieren images showing the growth of helical structures inside the cylindrical, expanding envelope of the current-carrying plasma. This illustrated the dominance of $m = 1$ in a Z-pinch with a centrally peaked current density (see section 3.2). Dangor *et al* [556] found that their laser initiated, gas-embedded pinch with a preheat current to raise the initial temperature and lower the density, did not expand but maintained a constant radius during the time of the main current rise. This is because the current rise approximately satisfied the Haines–Hammel [103, 104] curve. After this time the pinch transformed into an expanding helical structure similar to that reported by Smårs [548]. No disruptive break-up occurred.

Scudder [109] undertook a more complete 1D steady-state calculation of radial heat loss and bremsstrahlung losses. Problems arise when the Pease–Braginskii current is approached. Indeed at 1.8 MA both the pressure and radial heat flux go to zero at the plasma boundary. (However we should note that radiative collapse is probably precluded by ion-viscous heating associated with short wavelength $m = 0$ MHD instabilities, section 5.8.) The Imperial College gas-embedded pinch [53] was upgraded in current to 150 kA and in the use of laser interferometry to show that three phases could be distinguished. In the preheating phase the plasma column expanded from an initial radius of 100 μm with a radial velocity of 1.7×10^4 ms^{-1} driving a shock wave in the neutral gas. The Abel inversion of an interferogram gives the electron and neutral densities in figure 78. The equilibrium phase followed when
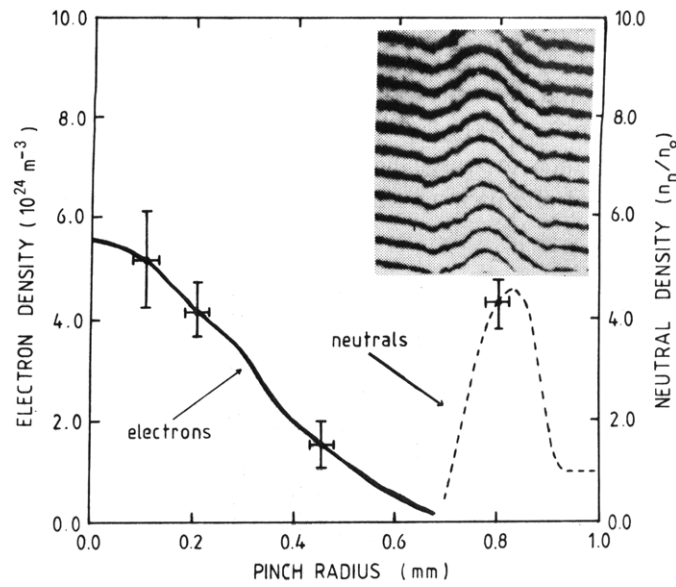
Figure 79. Number density of electrons and neutrals during the equilibrium phase at a filling pressure of 0.3 bar [182, figure 4]. Reprinted with permission from the IAEA.
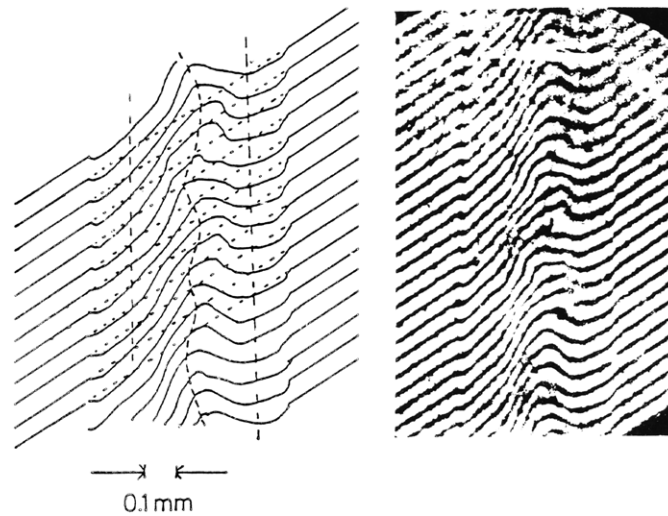
Figure 80. Interferogram showing how the spiral begins to grow from the axis. Here the fill-pressure was 1 bar [182, figure 5]. Reprinted with permission from the IAEA.

the main current was applied, the column was Joule heated at a constant radius of $400\,\mu$m Density profiles at this time are shown in figure 79. However, during this time accretion of plasma arising from the inwards radial diffusion of neutrals occurred, causing the plasma line density to double. In the third phase a spiral is formed. The interferogram in figure 80 shows that this helical perturbation occurs first with a peak on axis, consistent with MHD theory for a centrally peaked current profile [149]. The apparent delay [53] in the onset of a measurable perturbation was consistent with a 1% initial perturbation. The associated axial magnetic field

was always in the direction from cathode to anode. No attempt was made to remove perturbing fields such as the Earth's field [557], and it also was not possible to reverse the polarity of the pinch. In [53] the accretion problem was addressed, and it was suggested that by current programming to have a larger rate of rise, compression of the hot pinch will occur.

A variant of this was explored by Soto *et al* [54] who employed two stainless-steel conical hollow electrodes with 2 mm diameter with edges of 50 μm radius of curvature. A micro-discharge was set up between these. Then a few nanoseconds before the application of the main current a pulsed laser was focused through the anode on to the cathode. Thus two parallel conductive paths for the current were set up. With a peak current of 130 kA, interferograms showed a peak electron density of 3×10^{25} m^{-3} on axis. The outer annular hydrogen plasma coalesced with the central column and there was a compression of the pinch from 1 mm to an equilibrium radius of 50 μm. The Alfvén transit time was estimated to be 14 ns, and the line density grew to 1.3×10^{19} m^{-1}. This early increase in N is not maintained, inferring that the neutral gas does not cross the pinch boundary. The pinch appeared to be stable at a temperature of 150 eV. The enhanced stability is proposed to be due to resistivity at early times, and later due to FLR because a_i/a is about 0.1. It could be worthwhile to extend this compressional gas-embedded pinch to higher currents. So far with no observations of neutrons or x-rays, there are no disruptions, the achievable temperatures by Joule heating alone are rather modest. This idea of employing compression both to insulate the plasma from accretion from the neutrals outside, and to have more heating has been followed up by Veloso *et al* [558] using a laser-initiated hollow gas-embedded Z-pinch. The peak current of 150 kA led to an implosion velocity of 5 km s^{-1}, and the plasma column remained hollow and stable for 10 Alfvén transit times at a Bennett temperature of 150 eV.

7.5. Single wire and frozen deuterium fibre pinches

For single fibres distinction between insulating and conducting materials should be made at the earliest stage of electrical breakdown and plasma formation. As found by Beg *et al* [254], for insulators breakdown was observed to proceed from the cathode, coincident with a pulse of hard x-rays associated with an electron beam of about 4 kA and >50 keV. This was consistent with a magnetron type of condition,

$$I = \frac{2\pi r_0}{\mu_0 d} \sqrt{\frac{2m_e V}{e}} \tag{7.15}$$

in a radius $r_0 \gg a$, the fibre radius. This is r_0/d times the Alfvén-Lawson limiting current [95], (see section 2.2). Carbon and frozen hydrogen or deuterium are examples of insulators used, while conductors such as aluminium, tungsten, copper and nickel have been widely explored. The subject of exploding wires has a rather different motivation, but indeed it characterizes that all fibres initially explode with a typical velocity of 10^4 ms. This is illustrated in figure 81 in an optical radial streak of images of a 25 μm aluminium fibre taken on the IMP generator in which the current rises to 80 kA in 60 ns. The exploding plasma around the fibre carries the rising current, but at this stage the $\underline{J} \times \underline{B}$ pinch force is insufficient to overcome the plasma pressure, rising under Joule heating. Thus here is another example of the current being less than that given by the Haines–Hammel curve [103–105]. As the current increases further, however, simulations [197] show that a re-compression occurs accompanied by the onset of the $m = 0$ MHD instability. The experimental data and simulation are shown in figure 82. It is interesting that here the simulation reproduces from noise the same wavelength of instability as occurs in the experiment, i.e. the resistive MHD approximation is adequate. Thus the fibre pinch is dominated at the stage of confinement by the $m = 0$ instability. Furthermore, Chittenden
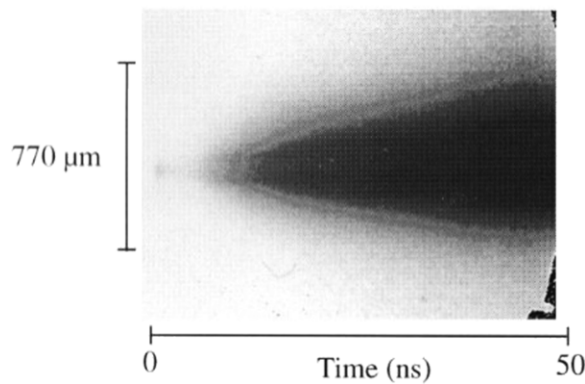
Figure 81. Optical radial streak photograph of a 25 μm diameter and 2 cm length fibre taken 5 mm from the cathode [254, figure 3].
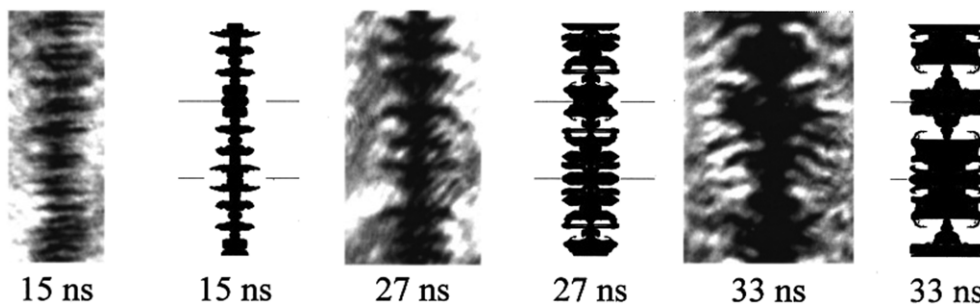

Figure 82. Schlieren images and numerical simulations of single 33 μm diameter carbon fibre on MAGPIE rising to 1.4 MA in 200 ns. Reprinted with permission from [197, figure 7]. Copyright 1997, American Institute of Physics.

et al [198] have shown in simulations that $m = 0$ MHD instabilities lead to bifurcation of bright spots as seen in experiments [254]. The x-ray yield from these short-lived, localized regions can exceed the total yield from the background plasma by orders of magnitude. The axial velocity at which the bifurcating bright spots move is $(1–3) \times 10^5 \, \mathrm{m \, s^{-1}}$, which is an order of magnitude greater than the radial expansion velocity of $2 \times 10^4 \, \mathrm{m \, s^{-1}}$. Figure 83 is an x-ray streak photograph of a 33 μm diameter carbon fibre showing typical $m = 0$ bifurcating bright spots. This behaviour is also observed in optical streak photography. Only 1% of the fibre is ionized at this time and the current is flowing in the low density ($n_e \sim 10^{24} \, \mathrm{m^{-3}}$) corona, leading to sound and Alfvén speeds comparable to the axial velocity.

Early radial expansion of coronal plasma and instabilities was identified also by Lindemuth and Sheehey [162] in the modelling of the deuterium fibre experiments at Los Alamos under Jay Hammel. However in this modelling the thermal neutron yield was below what was expected. This was hypothesized by Lovberg *et al* [329] to be due to a faster expansion associated with magnetic bubbles, and subsequent turbulent heating as they are ingested. Here the increased expansion dominates over the heating thus reducing the number density and the neutron yield. This model was also later put forward in a different context by others [331, 332] but, as argued in section 5.8 and 7.2 it is physically unlikely to occur at higher currents compared with viscous heating by saturated short wavelength $m = 0$ MHD instabilities [130].

A completely different hypothesis was put forward by Sethian *et al* [152] in explaining the neutron yield on the NRL deuterium fibre experiment. In this experiment it appeared
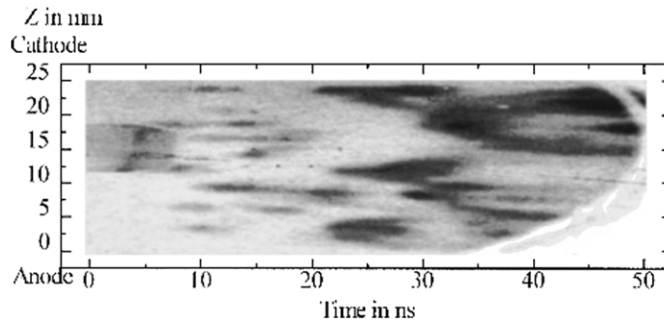
Figure 83. An axial x-ray streak photograph of the first 50 ns of the discharge in a 33 μm diameter carbon fibre. A 10 μm beryllium filter was employed, the spatial resolution was 640 μm and the temporal resolution 1.5 ns. Reprinted with permission from [198, figure 4]. Copyright 1997, American Institute of Physics.

that the plasma was stable so long as the current was rising, and the neutrons and hard x-rays appeared when the current abruptly stopped rising. However, it could possibly be that when the $m = 0$ instability became fully developed and the line density of ions in the necks dropped to the critical value (equation (3.58), the increasing inductance and anomalous resistivity caused the current rise to be interrupted, and ion beams to be generated (see section 3.14). Images of the dense fibre will show little instability compared with the surrounding plasma. The results from the Imperial College deuterium fibre experiment [47] would be consistent with this interpretation. Indeed it was shown by Lebedev *et al* [47] that yet again the neutrons were anisotropic, consistent with beam–target nuclear reactions.

A time-resolved study of the associated electron and ion beams in mega-Ampère fibre pinches was reported by Robledo *et al* [559] and Mitchell *et al* [247]. In [559] it was found that hard x-ray emission associated with energetic electrons occurred from the time of a disruption and lasted between 20 and 100 ns, indicating electrons of around 2 MeV energy in both 33 μm diameter carbon fibres and 25 μm aluminium fibres. The long time of MeV x-ray emission suggests that either the electrons are accelerated at the disruption itself and then most are confined off-axis in guiding-centre orbits, or there is a continuous heating of electrons to this energy in the low density gaps by anomalous resistivity between the plasma islands. In this region the driving voltage is due to the $v_r B_\theta$ electric field associated with the outward flow of under-confined plasma where the line density is less than critical. Both theories appear at first plausible. Confinement of energetic electrons off-axis requires a low guiding-centre velocity v_d such that $\ell/v_d = t_{\text{confinement}}$ is $\sim$100 ns. If the accelerated electrons have an isotropic distribution due to electron–electron collisions, the curvature and grad B drifts cancel on average, and in the dense plasma island region the E/B drift will be small and dependent on the ion temperature. The confinement time will be $\ell\mu_0 I/4\pi T_i$ (eV). For a length ℓ of 25 mm, a current of 1.4 MA and an ion temperature of 1 keV the time is 2.5 μs. However the individual hot electrons will have higher individual drift velocities, and at $T = 2$ MeV could traverse the length of the pinch in a few nanoseconds. In the theory of electron heating by anomalous resistivity when the local line density in the $m = 0$ neck is below the critical ion line density N_{criti} given by equation (3.58), the current I will be $ZN_{\text{criti}}ec_s$, leading to an electron temperature at pressure balance given by

$$T_e = \left(\frac{\mu_0 I}{8\pi}\right)^2 \frac{Ze}{m_i} \tag{7.16}$$

For fully ionized carbon and a current of 1.4 MA, this gives a hot electron temperature of 25 keV. This is much less than the 2 MeV electron energies measured, but if the line density
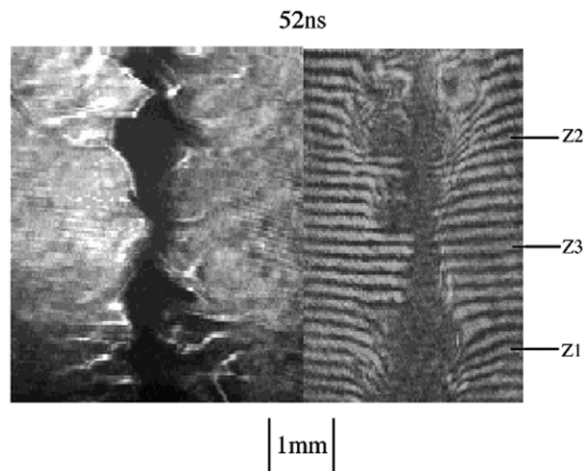
52ns

1mm

Figure 84. Simultaneous polarogram and interferogram of a 33 μm carbon fibre taken at 52 ns after the current start. (The analyzer is set at 85° anti-clockwise with respect to the input polarizer; Note that the polarogram shows a brighter image to the left and darker to the right of the unstable fibre). Reprinted with permission from [560, figure 10]. Copyright 1998, American Institute of Physics.

dropped further to a third of N_{criti} in the neck, T_e would rise to 2 MeV. More research is needed to resolve which mechanism is dominant.

In Mitchell *et al* [247] CD_2 fibres were also employed, and it was concluded that the 7×10^8 yield of neutrons at 1.4 MA was due to beam–target collisions arising from an ion beam at the time of disruption. The fastest neutrons had 3.3 and 4.8 MeV energy. With reversed polarity the fastest neutrons had 3.1 and 5.2 MeV energies arriving at scintillators 2 and 3 located, respectively, 6.8 m away radially and 16.8 m away above and at 45° to the axis.

Optical probing by Tatarakis *et al* [560] showed by Faraday rotation that at least 70% of the current was contained in a $m = 0$ neck prior to disruption. Simultaneous polarogram and interferogram, shown in figure 84, show clearly the $m = 0$ instabilities. Further experiments on optical probing by Ruiz-Camacho *et al* [561] have shown radial expansion velocities of 10^4 m s^{-1} for tungsten and 2×10^4 m s^{-1} for aluminium wires, and a perturbing wavelength of 200 μm, increasing in time, similar to work of Mosher and Colombant [562]. Aliaga *et al* [563] compared the dynamics with and without a current prepulse. The radial expansion velocity measured from schlieren images for 33 μm diameter carbon fibre was 3.6×10^4 m s^{-1} and 5.5×10^4 ms^{-1} for shots with and without a current prepulse of 35 kA in 200 ns. The prepulse reduced the delay of the breakdown and main current rise by 20–30 ns. Lorenz *et al* [55] studied prepulse effects at lower currents showing also a zipper effect from cathode to anode. Beg *et al* [368] extended it to wire arrays where it caused enough current to flow in the precursor column to drive instabilities, while Calamy *et al* [471] demonstrated optimal and beneficial preheating.

7.6. X-pinch

When two or more wires are stretched between two electrodes such that they touch at the central position, a powerful current will lead to a point x-ray source, well defined in space and time. This is a very useful diagnostic tool for backlighting experiments and is also an excellent source for high energy density plasma (HEDP) studies ($\sim$solid density, $T_e \sim 1$ keV).

In arguments similar to those for wire-array Z-pinches [280], the current in each of the wires I_n can be less than that needed to satisfy the Bennett relation, i.e.

$$\mu_0 I_n^2 < 8\pi N_n e (T_i + Z T_e), \tag{7.17}$$

while the total current at the X-point exceeds this, namely

$$\mu_0 \left(\sum_n I_n \right)^2 > 8\pi \left(\sum_n N_n \right) e (T_i + Z T_e). \tag{7.18}$$

Therefore the plasma at the X-point, experiencing the full global magnetic field at a small radius, will compress to form a localized pinch. In addition, as will be discussed in section 8.6, when considering conical arrays, the radial components of current in the wires will lead to axial components of $\underline{J} \times \underline{B}$ acceleration. The precursor plasma will flow to the axis radially, but also with an axial velocity component. Local to the X-point there will be a larger plasma pressure plus potentially radiative collapse, leading to further axial flows away from the X-point.

The small micropinch at the X-point radiates soft x-rays in the 1 to 10 keV range, from a point source of size $< 1 \, \mu$m for > 10 ps. This source is suitable for point-projection radiography, its spatial location is well defined, while the timing of the pulse can be varied empirically by varying the thickness and number of wires employed.

The X-pinch was first studied by Zakharov *et al* [564] and pioneered by Kalantar and Hammer [565] who first explored K-shell x-ray yield. Later [72] they employed the X-pinch for point-projection radiography. Using one X-pinch as a backlighting point source a second X-pinch was diagnosed by Shelkovenko, Pikuz *et al* [566, 567]. This showed that a very narrow pinch forms between dense plasma quasi-electrodes of the crossed wires, leading to a central x-ray burst followed by hard x-ray 8–100 keV associated with energetic electrons formed in the gap as in a Z-pinch disruption. Figure 85 shows the formation of the central pinch and bright x-ray spot in a time sequence set of shots. In Beg *et al* [568] and Chittenden *et al* [569] 2D and 3D resistive MHD simulations reproduced remarkably well the key phenomena of the X-pinch, as shown in figure 86. A cascading process was found in which mass depletion ceased at the centre of the fine pinch and the two ends start to form two identical, smaller collapsing necks. It is thought that this is how in some experiments multiple x-ray bursts are seen, though here in the simulation strict symmetry was imposed, and the results are sensitive to the initial perturbation. Beg *et al* [568] also compared $120°$ and $83°$ angles for the X-pinch. In studying the effective axial velocity of the precursor on axis, the $83°$ angle led to a higher velocity. Furthermore, when the jets hit the electrodes current is transferred and a $m = 1$ kink instability is observed. Bott *et al* [570] have made quantitative measurements of the wire ablation process and have found electron density profiles as a function of distance normal to the wire and time.

The effect of wire number on a table-top X-pinch discharge was explored by Green *et al* [571] at 35 kA. The hard x-ray energy (> 3.5 keV) was an order of magnitude higher, the pulse shorter and total x-ray power was double. At 160 kA with up to six thicker Al wires emission was only strong at the X-points, and greater for Al than for Mo which had extended jets. Multiple wire X-pinches were also explored by Shelkovenko *et al* [572], who found an optimal mass per unit length to maximize the x-ray power; this was in the range 1–7 mg cm^{-1}, and the parameter also determined the timing. There is a useful table of performance here. More recently the configuration at the crossing point was examined in the nested multiple wire X-pinch with various mixtures of metal elements [573]. It was found that with a higher Z material in an outer layer a single powerful x-ray burst occurred at 1 MA. Otherwise, for example [574], in a four limb X-pinch multiple x-ray bursts can occur. Useful reviews are to be found in [575, 576], while a notable advance giving a five frame point-projection x-ray image
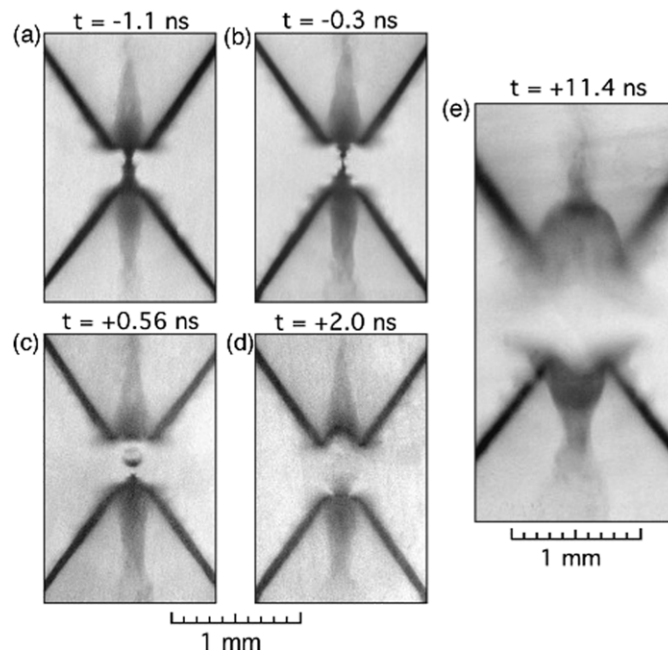
126

Figure 85. X-ray backlighter images of 17 μm Mo-wire X-pinches taken (*a*) 1.1 ns before the thermal x-ray burst, (*b*) 0.3 ns before, (*c*) 0.56 ns after, (*d*) 2 ns after and (*e*) 11.4 ns after the thermal x-ray burst. Reprinted with permission from [567]. Copyright 2005, American Institute of Physics.

has been developed by Douglass and Hammer [577] using five X-pinches each of four Mo wires in the return conductors, with relative timing controlled by varying the wire diameters.

In addition to directly backlighting wire arrays [578] the X-pinch has been used by Bott *et al* [579] to diagnose the low density foam on the axis of a wire array. Appartaim and Maakuu [580] have shown that successful X-pinches can also be produced with a more conventional long pulse ($\sim$1 μs quarter period) capacitor bank. With the right choice of wire material and x-ray filter, highly localized bright spots suitable for point-projection radiography can be produced. Beg *et al* [581] have shown how a compact X-pinch (80 kA in 50 ns) can be used to show phase contrast effects in a plastic capsule (1 mm diameter, 20 μm thick wall with a 80 μm foam inside). The high spatial resolution and short time exposure make the X-pinch suitable to examine the quality of cryogenic layered targets for ICF.

7.7. Z-pinch with sheared axial flow stabilization

Provided the sheared axial flow is not too great so as to cause KH instabilities, its presence can enhance stability. A very general theoretical dispersion equation was developed from the Vlasov equation by Wright *et al* [193] which included sheared rotation and axial flows and sheared heat flows (azimuthal and axial), axial and azimuthal magnetic fields and FLR effects. As discussed in section 3.9 sheared flow can theoretically be stabilizing, but experimental evidence for this is sparse. In 2001 Shumlak *et al* [188] claimed stabilization in the ZaP flow Z-pinch. In the transit time of the flow of only 20 μs there are nevertheless many e-folding times for instability growth, but the plasma conditions are such that LLR stabilization [12, 14] could also play a significant role. The $m = 1$ and $m = 2$ modes can be observed from magnetic
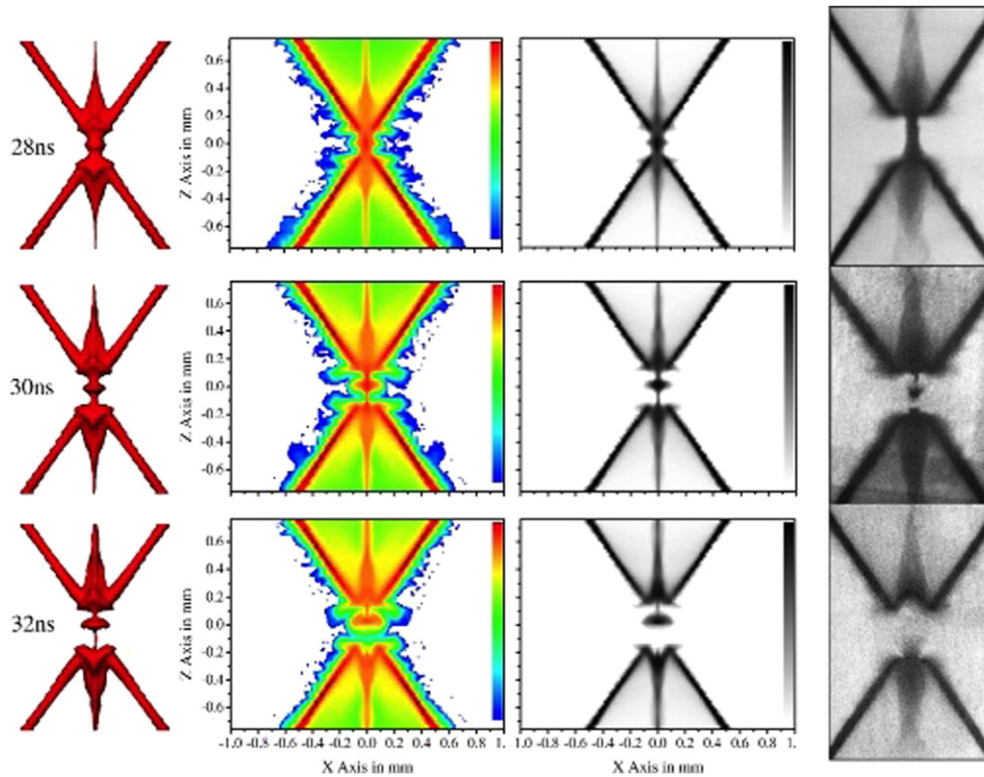
Figure 86. 3D simulations showing surfaces of constant density ($1 \, kg \, m^{-3}$), mass density contours in the plane of the wires, and synthetic and experimental radiographs. Reprinted figure with permission from [569]. Copyright 2007 by the American Physical Society.

fluctuations at the wall, but this is not possible for $m = 0$. More experimental work is needed here, not least to address how to design a suitable reactor scenario. Progress is reported in recent papers by Shumlak *et al* [582, 583].

7.8. Laser-driven Z-pinches; B_θ fields generated by $(\nabla T \times \nabla n)$ and fast ignition

It has been known for many years that the azimuthal magnetic field generated spontaneously when a laser focussed on to a solid target can lead to a pinch effect, as well as $\underline{J} \times \underline{B}$ acceleration of ions [75]. More recently an intense laser pulse ($>5 \times 10^{19} \, W \, cm^{-2}$) has been used to irradiate thin wire targets [584]. In such interactions the relativistic electrons, energized by the laser beam, will propagate away and a return current of cold electrons is induced. Using the VULCAN laser at the Rutherford Appleton Laboratory, $20 \, \mu m$ diameter copper, gold or glass wires of length 3–5 mm were employed, only one being irradiated, the others showing second harmonic emission due to optical transition radiation associated with the $\underline{\tilde{J}} \times \underline{\tilde{B}} \, 2\omega$ ponderomotive force on the accelerated electrons. The irradiated wire showed expansion velocities, similar to single fibre Z-pinch experiments, but now the current is the return current of order 4 MA composed of high density cold electrons which ohmically heat the wires. In addition short wavelength ($\lambda \sim 100 \, \mu m$) $m = 0$ instabilities have been observed, in agreement with the heat-flow driven electrothermal instability [214]. This type of Z-pinch at higher laser intensity could have currents rising in a time much shorter than the usual unstable MHD modes.

As mentioned above the generation of azimuthal magnetic fields in laser-plasma studies can lead to Z-pinches. In particular the $\nabla T \times \nabla n$ generation of megagauss magnetic fields in the underdense coronal plasma can lead to a pinch effect [75]. Under fast ignition conditions the reversed azimuthal magnetic field associated with the creation of a relativistic electron beam and a diffusing return electron current can lead to magnetic confinement of the hot electrons. Magnetic fields as high as 700 MG have been measured using the Cotton–Mouton effect [78], while a recent theory confirms this value and gives scaling laws for the hot electron temperature and absorption [81].

7.9. Liner-driven Z-pinches

Liner-driven Z-pinches have a relatively long history. In particular, Linhart [585–587], Maissonnier [588] and Turchi and Baker [589] proposed and carried out small scale experiments. The purpose of the liner which is driven by pulsed power is to compress the plasma which can be preformed inside it to attain suitable conditions for x-ray emission or even thermonuclear conditions, yet retain a longer confinement time than a radial Alfvén or sound transit time of the deuterium plasma because of the inertia of the liner. Furthermore the liner acts as a conducting wall preventing some plasma instabilities from growing. In some schemes an internal magnetic field is imposed to reduce the thermal conduction to the relatively cold liner. Such a scheme is usually called magnetized target fusion (MTF) and will be considered in section 7.10.

The accelerating liner is of course unstable to RT instabilities. Care has to be taken to ensure that seeding imperfections are minimized. Alternatively the liner could be stabilized by rotation [590]. Then of course, because angular momentum is conserved, the final compression is much more difficult. Alternatively Budko *et al* [591] adding a 'modest' axial magnetic field to produce shear in the field and hence reduce the RT interchange mode. A hollow plasma liner was analytically studied by Hussey and Roderick [592] to find the self-consistent magnetic field diffusion and plasma density profile as a preliminary model for considering the RT instability.

In endeavouring to maximize their velocity, liners as thin as in soap bubbles have been employed [593]. The Pegasus II facility (4.3 MJ, 15 MA) at Los Alamos drives a relatively massive hollow cylinder towards the axis in 1.8–2.5 μs for Al foils 5 cm in radius and 0.25–0.75 μm thick. 125 kJ of soft x-rays were emitted in a 200 ns pulse. The filtered pulse was 200 ns [594]. Simulations showed the growth of RT instabilities [595] in good agreement with experiment. The ultimate goal is a 1 to 10 MJ radiation source at $>$100 TW. Similar liner implosions are being studied by Degnan *et al* [596] using the Shiva Star 94.6 MJ, 10 MA) facility at the US Air Force Research Laboratory. The facility directly employs a capacitor bank and can also employ an intermediate inductive store. Their programme includes using shaped solid-density liners [597] and spherical liner implosions [598]. Vandevender [599] recently proposed using the Z-accelerator at Sandia to drive a quasi-spherical implosion for direct-drive fusion. An earlier scheme by Slutz *et al* [600] envisaged a quasi-spherical Z-pinch implosion followed by fast ignition using a short, intense laser pulse. This concept has evolved into magnetized target fusion (see the next section), where in this particular example the laser pulse provides the initial preheat of a plasma which is in the Z-pinch configuration [600].

7.10. Magnetized target fusion (MTF)

A Z-pinch can be used as a liner (e.g. made of aluminium) to compress a preformed and *magnetized* plasma to fusion conditions. This is called magnetized target fusion (MTF). The purpose of the magnetic field is to reduce thermal conduction from the hot fusion plasma to

the cold liner, and also to magnetize alpha particles so as to deposit their energy in the plasma, but its pressure is much less than the plasma pressure. Spherical and cylindrical configurations have been considered, while the most favoured is the magnetic theta pinch or field-reversed configuration (FRC). In Russia the subject is called MAGO [601] and the subject is intermediate in density and confinement times to magnetic and inertial fusion. Essentially the inertia is greatly increased by the relatively massive liner which usually is considered to compress adiabatically with a velocity of 10^4 to $10^5 \, \mathrm{m \, s^{-1}}$. The parameter space for MTF is discussed by Lindemuth and Kirkpatrick [602]. A useful summary of the field is given by Dahlin [603].

It is important to remember that this is still inertial confinement. An important feature of this is that the energy E to be provided to an inertially confined sphere is proportional to n_i^{-2} where n_i is the ion density. This can be seen as follows

$$E = \tfrac{4}{3}\pi R^3 \cdot 3n_i e T_i \tag{7.19}$$

and the Lawson product $n_i \tau$ for inertial confinement is $n_i R / c_s$, but now multiplied by $(M_L/M)^{1/2}$ where M_L is the sum of the liner and plasma mass M and c_s is the ion sound speed. Thus E is given by

$$E = 4\pi \frac{(n_i \tau c_s)^3}{n_i^2} e T_i \left(\frac{M_L}{M} \right)^{3/2}. \tag{7.20}$$

The final, compressed plasma is considered to be $10^{26} \, \mathrm{m^{-3}}$ at $10 \, \mathrm{keV}$ which is a density some 10^5 smaller than that usually considered for ICF. Thus the driver can be much weaker, but the energy required for the plasma is greatly increased. Furthermore the energy that has to be employed for the driver would have to be recycled with a very high efficiency of over 90%.

A reactor would be a pulsed system, which, for example, at 4 pulses a second would give an output of 160 MWe. But because of the comparatively low fuel density there would only be a fractional burn-up of $\sim 1\%$. It would appear that the higher the initial plasma density the more efficient the reactor would be for a given volume contraction.

A Z-pinch, rather than a FRC, might be one answer, as unlike the FRC there is no limitation of magnetic field or plasma density for a Z-pinch since no magnetic coils are employed. Such a scheme, the staged Z-pinch, was proposed by Rahman *et al* [604] in which a Z-pinch liner collapses on to a DT-fibre Z-pinch. However in this paper an axial magnetic field is also added to ensure magnetization of alpha particles, and also to provide some stabilization. Diffusion of this field will occur, especially if the plasma is turbulent, but the main flux compression is of the azimuthal magnetic field. An experiment by Klir *et al* [605] was conducted on the S-300 device in Moscow with an aluminium wire array imploding on to a CD_2 fibre. The x-ray pulse was almost the same with and without the central fibre, while the peak neutron yield of 2×10^8 with a fibre was not associated with a dominant x-ray pulse, and indeed was of beam–target origin.

Magnetically insulated inertial fusion applied to laser-driven ICF was proposed in 1986 by Hasegawa *et al* [606].

Simulations have been undertaken by Sheehey *et al* [607] where the DT fibre pinch is allowed to develop into a Kadomtsev ($m = 0$ stable) profile as it meets the liner wall followed by liner compression. Joint studies by Los Alamos and the Air Force Research Laboratory are concentrating on the compression by liners of field-reversed configurations [608].

7.11. Inverse Z-pinch

The inverse Z-pinch consists of a hard-core insulated cylindrical conductor on the axis, and a return current in a plasma shell around it [609]. This shell will be accelerated radially outwards, but there is an axial magnetic field applied which will then be compressed. The
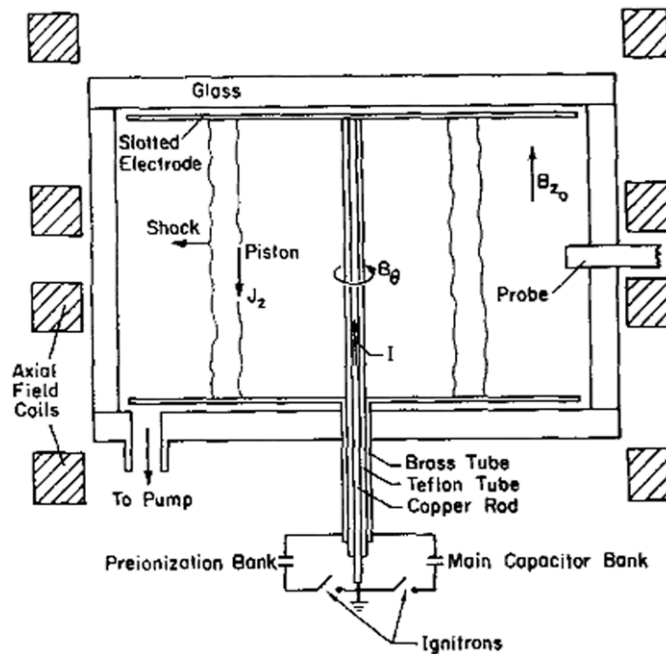
Figure 87. Schematic diagram of the inverse Z-pinch [611]. Copyright © 1963 Cambridge University Press.

resulting configuration should be MHD stable because of the favourable magnetic curvature of the B_ϑ field inside the plasma shell and the neutrally stable B_z field outside [610]. An outer conducting wall together with the field coils can provide the means of attaining an equilibrium. This is illustrated in figure 87. In the formation of the plasma shell, the current forms a piston and a radially moving shock will move ahead. This is the subject of several papers by Vlases [611]. He finds that both theoretically and experimentally there is a big difference between assuming zero or finite electrical conductivity ahead of the shock. For zero conductivity the shock velocity is larger but the shock strength is weaker.

Because of the need for applying an axial magnetic field it is difficult to match such a field with the MG azimuthal magnetic fields which can be produced with modern pulsed power. But closely related is the Z–Θ pinch and work on liner compression of axial magnetic fields discussed in section 8.4.

An inverse Z-pinch has been employed by Harvey-Thompson [612] in order to gain a greater understanding of the ablation process in a wire array. Interestingly when the technical design led to some precursor current through the wires, no axial instabilities occurred. This would be consistent with a temperature exceeding the critical value for electrothermal instabilities. This is a very recent finding, and further confirmation is needed.

8. Applications of Z-pinches

8.1. Early reactor concepts for the Z-pinch

A Z-pinch has some peculiar advantages over other magnetic confinement schemes. The most important is that no external magnetic field coils are employed. Such coils limit the

magnetic field to $\sim$5 T, unless further compressed. Indeed the azimuthal magnetic field for 20 MA in 1 mm radius is as high as $\sim$4000 T, the local β is of order 1 and the plasma density at fusion temperatures ($\sim$10 keV) is some 10^7 times that of a tokamak. The nuclear reaction rate depends on the square of the ion density, and so the confinement time becomes a critical factor, together with the instantaneous fusion power. If the confinement time is less than an ion transit time along its length, there will be no problems with impurities unlike in other magnetic confinement devices unless the plasma forms at first on an insulating wall. Wire-array and gas-puff Z-pinches do not interact with a wall, as, unlike other magnetic confinement devices, the currents for equilibria are not driven by outward diffusion of the plasma. For example the tokamak has radially outward Pfirsch–Schluter diffusion to generate the equilibrium currents. Thus in considering reactor configurations the 'first wall' can be far away, and indeed could be a liquid not limited in energy flux to 10 MW m^{-2}, and could also carry the return current [10].

The disadvantages of the Z-pinch for fusion are well documented in papers extolling the virtues of tokamaks, stellarators and other low density quasi-steady-state devices. The first is its instability to $m = 0$ (sausage) and $m = 1$ (kink) instabilities. The second is the heat loss to the two electrodes. In section 2.3 it was shown that the power loss is mainly to the anode and is of order $\frac{5}{2}IT$. For $I = 2 \times 10^7$ A and $T = 10^4$ eV this amounts to 0.5 TW. Clearly for this to be negligible a fusion power in the tens of TW at least must be considered and therefore for a reasonable size power station the Z-pinch must be pulsed.

This indeed fits in with current knowledge of dynamic Z-pinches in which, for example the intense soft x-ray power occurs over 1 or 2 radial Alfvén transit times. For high Z radiating loads this is sufficient time to radiate a significant fraction of the stored energy, especially if the viscous heating mechanism (section 5.8) applies. Indeed this mechanism takes advantage of MHD instabilities and in this context instabilities are excellent for Z-pinches. The dynamic 'bounce' of the pinch is very non-adiabatic, and is accompanied by the onset of longer wavelength modes, and later, probably a disruption (section 3.14). The disruption is characterized by the creation of electron and ion beams, the latter which for deuterium will produce neutrons from a beam–target mechanism.

To provide a longer confinement time various ideas have been employed. (a) The preparation of Kadomtsev current density profile (section 3.2) as in a gas-embedded pinch (section 7.4) can eliminate the $m = 0$ instability, or at least, for a plasma–vacuum boundary condition, reduce the growth rate. Instead the $m = 1$ instability dominates and indeed endeavours to form a helical minimum energy configuration, i.e. an axial magnetic field is spontaneously generated (presumably of arbitrary sign). (b) Sheared axial flow can also extend the stability time (sections 3.9 and 7.7) and further work at high currents is needed to explore this concept. (c) Large ion Larmor radius effects have been shown both experimentally [14] and theoretically to reduce the growth rate of the $m = 0$ instability (section 3.8). (d) An axial magnetic field could be applied and compressed by means of a liner to provide a more stable configuration (see section 7.10). Early ideas and concepts for a Z-pinch fusion reactor were summarized by Sethian [613], before some of the recent advances were known, and when it was considered that radiative collapse would limit the current dynamically to a few megampéres.

Hartmann [614] envisaged a gas-puff or a gas-embedded Z-pinch (which with present-day knowledge is, in its hollow form, a strong candidate). Later he extended this to the continuous flow pinch [615] which had earlier been proposed by Morozov [616]. This relied on sheared axial flow to stabilize the pinch. Indeed Newton *et al* [617] did find in an experiment conducted in 1967 that a continuous flow pinch could form at the end of a Marshall gun's central electrode at 0.5 MA. The pinch lasted 100 μs at several $\times 10^{17}$ cm^{-3} electron density at 100–200 eV. However reference to section 2.3 and [97] would indicate a heat loss of 2.5TI, equal to 0.25 GW to the electrodes even at this low power. At the temperature and current required

for a fusion reactor such losses would be unacceptable except for a pulsed system. Cheng and Wang [618] indeed criticized Morozov for neglecting the energy dissipation at the electrodes and for assuming adiabatic behaviour.

Winterberg, in a series of papers, has put forward several eclectic reactor concepts, but only with rudimentary theoretical backing. In 1978 he proposed the adiabatic compression of a 'super-pinch' at a current much higher than the Pease–Braginskii current [619], similar to Potter [261]. To obtain shear-flow stabilization he proposed shooting a moving rod or metal jet along the axis [620] later adding a laser fast ignition pulse and D–T fibre instead of a rod plus radiative collapse [621]. To take advantage of ion beam formation at a disruption and subsequent nuclear reactions to drive a detonation wave Winterberg proposed cutting a Z-pinch with a laser [622]. Magnetized target fusion could be achieved using the high magnetic field of the pinch by shooting DT pellets from several sides of the pinch of a plasma focus [623], followed by laser-driven fast ignition. With a helical sawtooth-shaped capillary tube and a solid DT core, he envisaged sheared flow to stabilize MHD, and rotation to prevent RT with a current compressed DT core, plus a laser-driven fast-ignition detonation wave [624]. This is a development of a two-part paper on thermonuclear detonation waves in one or two stages plus catalysed or auto-catalysed burn [625, 626]. A combination of axial shear flow and rotation could lead to vortex line confinement with stable spherical regions [627]. With a sheared flow Z-pinch Winterberg proposed using a non-neutronic fusion chain reaction for propulsion [628]. Employing two MITLs he proposed ignition at their focus [629, 630] and an auto-catalytic fusion–fission burn [631]. Winterberg proposed using one Marx generator at high current to compress the fuel and a faster, high voltage, low current Marx generator to act as an ignitor [632]. Lastly he proposed using the Nernst effect in the corona of a D–T pinch to confine it. Zakharov in the 1950s first considered using the Nernst effect for steady confinement. Both found $T^{1/4}n$ is a constant. Here Winterberg [633] requires the neutrons emitted from the pinch on axis to heat the corona by nuclear reactions.

More realistically Hagenson *et al* [634] considered a gas-embedded pinch with a gain of 30. This was a level III reactor study with no engineering issues studied. The concept of using a vortex of liquid lithium was studied by Robson [635] following ideas of McCorkle [636]. At Imperial College a series of concepts based on using liquid lithium as a return conductor and blanket were studied. Bolton *et al* [637] considered the gas-embedded pinch at high pressure. This followed earlier proposals by Haines [638] which included employing a matrix of Z-pinches immersed in liquid lithium, and using the injection of DT gas bubbles and laser initiation. Haines and Walker [639] considered the serendipitous employment of a pressure vessel of similar design to pressurized water reactors (PWRs). This was followed up by Walker and Javadi [640]. Many of these concepts are contained in a later paper by Bolton *et al* [641]. During the era of frozen deuterium fibre Z-pinches, Robson [642] ingeniously proposed the injection of fibres to intersect with two lithium jets which were the anode and cathode, respectively.

In addition to these concepts, Baronova and Vikhrev [643] have studied employing the $m = 0$ neck as a trigger for fusion reactions. This is entwined with the controversy over the origin of the neutrons during a disruption, captured by the consecutive papers by Vikhrev [246] and Trubnikov [241]. The mechanisms of beam formation have been clarified in [243, 253], as discussed in section 7.3. An important point here is overall conservation of axial momentum. In order that the $m = 0$ instability leads to a high density and temperature in the necked region, the initial perturbation must be of a particular form [248]. This has yet to be demonstrated experimentally.

In section 7.2 the deuterium gas puff experiment was extended on Z to 17 MA, producing a record 3.9×10^{13} neutrons. Furthermore it is likely that the ion temperature is achieved in

part by ion-viscous heating. The extension of this to DT and to higher currents for at least a neutron source [494], if not yet a reactor, is very promising. The important point is that viscous heating not only raises the temperature but also removes any limiting current associated with radiative collapse. Alpha particle heating will continue to heat primarily the electrons.

The addition of an axial magnetic field is considered in sections 3.10 and 8.7.

Lastly it is interesting to examine the scaling of the vector triple product $n_i \tau T_i$ which should exceed $10^{24}\,\mathrm{m}^{-3}\,\mathrm{s}$ (eV) for fusion break-even. If the pinch can be confined for $10\tau_A$ at 10 keV and at a radius of 1 mm, a current of 35 MA is required, and $n_i \tau T_i$ scales as I^2. Perhaps future experiments will explore this, perhaps extending the confinement time with axial velocity shear.

8.2. X-ray sources

The use of pulsed-power generators to power Z-pinches as x-ray sources was reviewed over 20 years' ago by Pereira and Davis [51]. Since then the generation of soft x-rays using wire arrays has reached high powers of 280 TW for a FWHM pulse of 5 ns with a 17% conversion efficiency from the wall-plug [1, 2].

Early work on soft x-ray emission from imploding aluminized plastic cylindrical liners using the SHIVA capacitor bank by Degnan *et al* [644] gave up to 240 kJ in an x-ray pulse of 130 ns FWHM. Deeney *et al* [645] as early as 1991 found that there appeared to be an extra heating mechanism during stagnation when using low mass aluminium arrays of large array diameter to study keV x-rays. Increased x-ray yield was found by mixing elements of similar atomic numbers [646]. Later at 20 MA on Z up to 125 kJ of K-shell x-rays from titanium wire arrays was obtained with electron temperatures up to 3.2 keV [647].

Zakharov *et al* [648] employed the collision of an accelerated gaseous liner with an inside shell on the Angara 5 generator producing 9 TW in a 90 ns pulse. Sharpening the x-ray pulse was the main purpose of this early work. Instabilities in liners, involving azimuthal and axial inhomogeneities, were found by Branitsky *et al* [649], and they could reduce their effect by using thin foam (50–100 μm) liners rather than gas puffs. For further discussion on gas puffs see section 7.2.

If x-ray energies greater than 1 keV are needed, Whitney *et al* [650] have developed a 1D model to give scaling laws. They define a parameter

$$\eta = K_i / E_{\min}, \tag{8.1}$$

where K_i is the kinetic energy per ion before stagnation and $E_{\min}$ is the minimum energy to promote K-shell excitation and not allow recombination back into the L shell. For aluminium this energy is about 12 keV/ion. For a small mass of 6 μg cm^{-1} figure 88 shows that there is an optimum value of η for maximum yield per unit length of x-rays above 1 keV. Here η was varied by varying the implosion time and hence the peak current. For low η there is little energy to radiate while at high η the plasma overheats and hence becomes an inefficient radiator. As the mass of the array is increased in these calculations, which are based on 1D calculations of the stagnation itself in the absence of current, the optimum value of η increases such that at 200 μg cm^{-1} η was equal to 27.5. Because at low mass the plasma is optically thin and the radiated power scales as the square of the density, it follows that the x-ray yield would scale as mass squared. At high mass the radiated energy is limited by the thermal energy at stagnation. The yield therefore is proportional to mass. This transition is clearly seen in figure 89 for two cases in each of which the kinetic energy per ion and η are fixed. Below the transition in scaling the regime is termed inefficient because the energy radiated is a small fraction of that available, while above the regime is termed efficient. As one considers other elements the
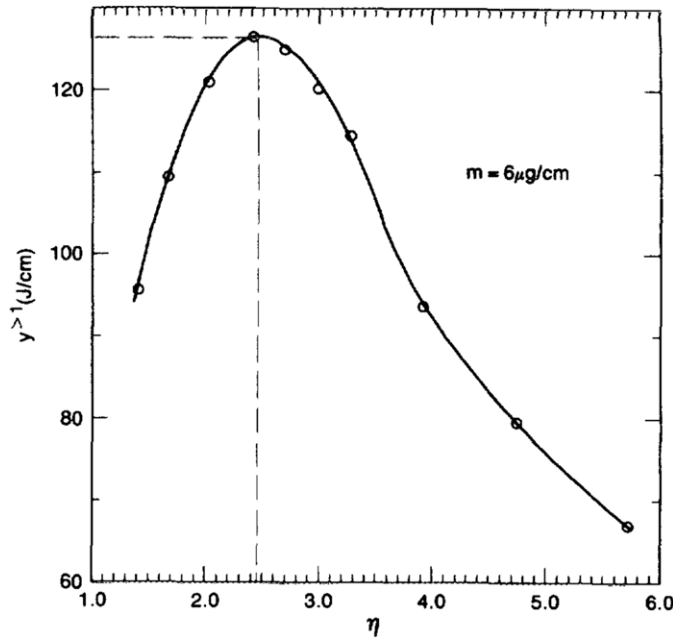
Figure 88. Calculated x-ray yield above 1 keV as a function of η for a Al wire array of 6 μg cm^{-1}. Reprinted with permission from [650, figure 3]. Copyright 1990, American Institute of Physics.

Figure 89. Calculated x-ray yield above 1 keV for aluminium for two different kinetic energies per ion K_i and for fixed η. The slopes drawn show the transition from quadratic to linear dependence on the mass per unit length. Reprinted with permission from [650, figure 8]. Copyright 1990, American Institute of Physics.

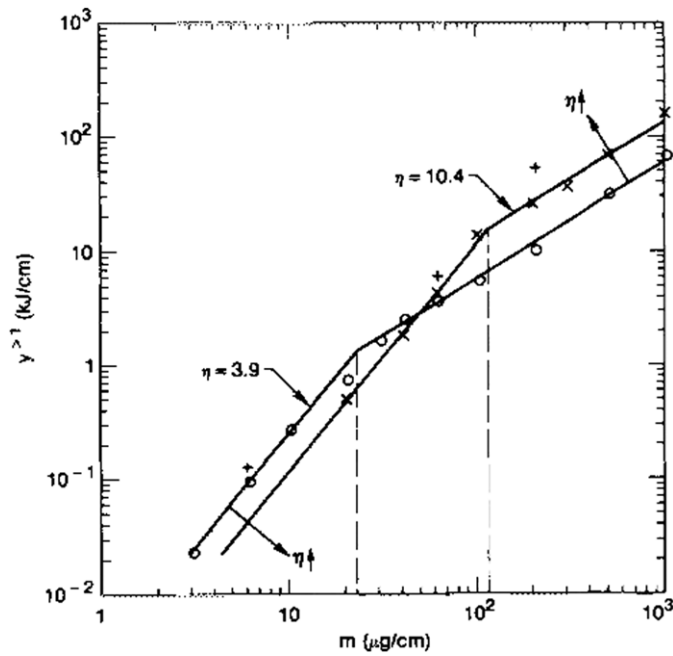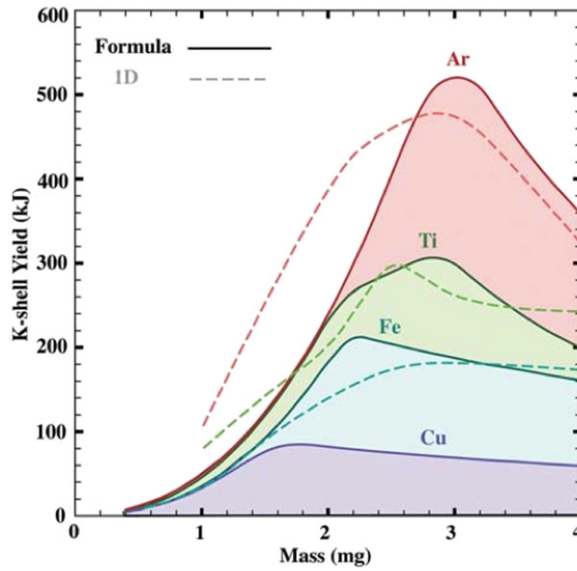**Figure 90.** Empirical formula and 1D phenomenological predictions for K-shell yields on ZR at Sandia, as a function of mass for loads 2 cm in length. Fe and Cu predictions are for 55 mm diameter single wire arrays, Ti predictions for 45 mm, while for argon a standard 1-2-3-4 nozzle configuration is used. (There is no 1D result for Cu.) [651, figure 11]. Copyright (©) 2006 IEEE.

atomic number A can approximately be related to Z by

$$A \approx 1.58 Z^{1.1}. \tag{8.2}$$

For $Z > 10$, while the ionization energy E_i is approximately

$$E_i \approx 3.8 Z^{2.64} \ (\text{eV/ion}) \tag{8.3}$$

when the plasma is 50% hydrogen-like and 50% helium-like, the minimum energy $E_{\min}$ required is approximately

$$E_{\min} \approx 1.49 Z^{3.51} (\text{eV/ion}) \tag{8.4}$$

The demands on the generator are substantial if an efficient radiator is required for high Z, e.g. for krypton $E_i > 1$ MeV/ion and a current rise time below 30 ns, though the latter could be increased by increasing the array radius beyond 1 cm.

A more recent paper by Thornhill *et al* [651] included L-shell losses and opacity, with the objective of bench marking data and employing 1D MHD to predict what the potential of the higher current (26 MA) ZR machine at Sandia is for producing multi-keV in x-rays, both from K-shell line and from free-bound continuum radiation. Argon, titanium, stainless-steel and copper were considered. The predictions are summarized in figure 90, having first bench marked the results obtained so far from the Z generator.

Stainless-steel implosions at up to 20 MA on Z have been studied by Jones *et al* [652] and show K-shell yield scaling consistent with Thornhill *et al* [651]. To minimize the effects of RT instability nested arrays in transparent mode were employed. Optimal x-ray emission and highest temperatures occurred when there was simultaneous arrival on the axis of the inner and outer masses. Low mass and large array radius are a key to obtaining electron temperatures in excess of 3 keV. It is disappointing that the 450 μg cm^{-1} case which gave record ion temperatures [130] was omitted from this series, but in terms of coupling maximum energy to the electrons and hence to radiation it might be justifiable. There is probably an optimal ratio of equipartition time to Alfvén transit time to maximize x-ray yield, yet benefiting

from the extra viscous heating which occurs at high temperature. It should be noted that all the results here are for masses below the break-point for onset of the efficient regime. A triple nested array was explored and gave up to 200 TW total x-ray power for a $4:2:1$ mass and radius ratio, with $T_e \simeq 3.8$ keV and a narrower pulse. It was noted that radiative cooling in the L-shell complicates the simple model and reduces the efficiency of K-shell radiation.

A transition from I^4 to I^2 scaling of keV radiation found by Sorokin *et al* [653] at 4 MA in a double shell gas-puff experiment in argon. They claim this is due to a very high compression of the pinch to a diameter of 0.2 mm when the inner and outer shells had mean radii of 4 mm and 13 mm, respectively, i.e. a 45-fold radial compression. This might be based on the time-integrated pinhole photographs of the pinch. A similar result was found by Sze *et al* [654].

There is a tendency for the hotter electrons to drift preferentially towards the axis (see sections 2.6 and 2.7). Indeed runaway electrons can only exist in a Z-pinch within one Larmor radius of the axis (section 2.2). Combined with $m = 0$ instabilities bright micro-pinches have been observed by Alikhanov *et al* [655] with pulsed gas injections. Indeed Kr xxxv–Kr xxxvi ions with ionization potentials ∼17 keV suggest electrons with 3–5 keV temperature. Choi *et al* [656] distinguished hard and soft x-rays from a gas-puff Z-pinch, the former being associated with bursts of ∼10 keV electron beams and emission from the anode. Li and Yang [657] showed that a thinner gas sheath gave a higher velocity of compression and a higher x-ray yield, while Bayley *et al* [658] injected argon through a hole in the anode of the speed 2 plasma focus to obtain soft x-rays from micro-pinches along the axis. Chuvatin *et al* [659] considered a two stage heating of an argon gas fill. The first stage was shock heating and thermal conduction from an imploding shell, and the second is an adiabatic compression to the required temperature. Bergman and Lebert [660] varied parameters to find the optimization of Lyman-α emission in a plasma focus. In section 7.2 the x-ray emission from a plasma focus is discussed in detail.

The X-pinch (see section 7.6) is also a very useful source of 1–10 keV photons, and its small volume of emission ($<1\,\mu$m in size) and pulse length (∼10 ps) make it ideal for point-projection radiography.

Bailey *et al* [661] have discussed what radiation science can be done with the intense x-ray source of ∼200 TW power on Z. For example, the radiating pinch can both heat a sample and act as a backlighter, enabling opacity, absorption and re-emission measurements to be made accurately with large samples.

8.3. Neutron source

The plasma focus (see section 7.2) is a notable pulsed source of neutrons when deuterium gas is employed. Neutron yields as high as 4×10^{12} have been obtained but in small devices are caused by beam–plasma collisions, rather than being thermonuclear in origin.

There is renewed interest in deuterium gas-puff experiments, as discussed in section 7.2. At a current of the yield was 3.5×10^{13} and is isotropic, almost certainly mainly thermonuclear in origin. Velikovich [494] has put forward cogent arguments as to why it is unlikely that an ion beam is the origin of these nuclear reactions. It is hoped that this work will be extended on ZR, and interest in it as a powerful 14 MeV neutron source will be increased. With some stabilizing feature such as sheared flow it is possible that the concept at higher currents could satisfy Lawson conditions for a pulsed reactor.

8.4. Magnetic lens

If an energetic ion beam is injected through a hole in the anode of a preformed Z-pinch it will be deflected towards the axis due to the $\underline{v} \times \underline{B}$ field that it experiences. Its trajectory is part of a

singular ion trajectory as discussed in section 2.2. For the 3.5 GeV anti-proton beam at CERN the Z-pinch lens would have opposite polarity. An early attempt at employing a Z-pinch as a magnetic lens for focusing an energetic ion beam was made at Brookhaven National Laboratory [662]. Unfortunately it failed after several hours of operation. At CERN a careful programme of materials testing and prototype development led to the use of graphite rather than tungsten electrodes; helium rather than hydrogen for the filling gas; and low-porosity alumina for the insulation tube [663]. Over 20 000 successful shots at 14 s intervals were obtained, limited only by the time available on the accelerator. Erosion rates of the various components were measured, and, with modifications, a further 20 000 shots were made. This proved the capability of the Z-pinch as a magnetic lens for high energy beams [664]. The specification of the Z-pinch magnetic lens at CERN is a 400 kA current in a plasma column 2 cm radius and 29 cm in length, L. This gives a peak magnetic field of 4 T and a focal length just greater than the length of the pinch. Explicitly the focal length f is given by

$$f = \frac{L}{\beta \sin \beta}, \tag{8.5}$$

where

$$\beta = L \left(\frac{q \mu_0 J_z}{2 p_z} \right)^{1/2}, \tag{8.6}$$

J_z is the pinch current density and q and p_z are the charge and relativistic momentum of a beam particle. With a line density of $2 \times 10^{22} \, \text{m}^{-1}$ and a Bennett temperature of a few eV the regime for stability is firmly in the resistive stabilization regime in figure 16. Indeed the magnetic Reynolds' number S, given by equation (3.4), is 2.7, and resistivity dominates, leading to enhanced stability. With high resistivity the skin effect is diffused, bringing azimuthal magnetic field towards the axis, so that a uniform gradient could exist by the time of maximum pinch diameter after the first bounce [665]. The occurrence of the inverse skin effect [110, 271] also led to a strengthening of the magnetic field gradient near the axis. The range of reproducible focusing is also consistent with the above discussion on stability regimes. A few per cent of nitrogen added to the helium gave a reduced pinch diameter, and hence a higher focusing strength. This is important as stability for $4 \, \mu$s or several Alfvén transit times is required.

8.5. Hall acceleration and multipole fields

Hall acceleration employing closed loops of Hall current was found by Haines [666] and independently by Hess [667, 668] at NASA.

If a short coil surrounds a Z-pinch, illustrated in figure 91(a), so that the radial components of the magnetic field B_r penetrate the plasma, it is found that the plasma is accelerated away from the anode and towards the cathode. The reason for this is that the axial current density J_z in the Z-pinch plasma interacts with B_r to give an azimuthal Hall current J_ϑ, given by

$$\eta J_\vartheta = -\frac{J_z B_r}{n_e e}. \tag{8.7}$$

In turn J_ϑ interacts with B_r to give an axial $\underline{J} \times \underline{B}$ force which accelerates the plasma. Using equation (8.7) it gives

$$\rho \frac{\mathrm{d} v_z}{\mathrm{d} t} = -J_\vartheta B_r = \frac{J_z B_r^2}{\eta n_e e} \tag{8.8}$$

showing that the direction of acceleration is independent of the sign of B_r. The equal and opposite axial force is on the coil, which experiences an anti-parallel J_ϑ in the plasma on the cathode side and a parallel J_ϑ on the anode side, the latter causing an attractive force, i.e. a
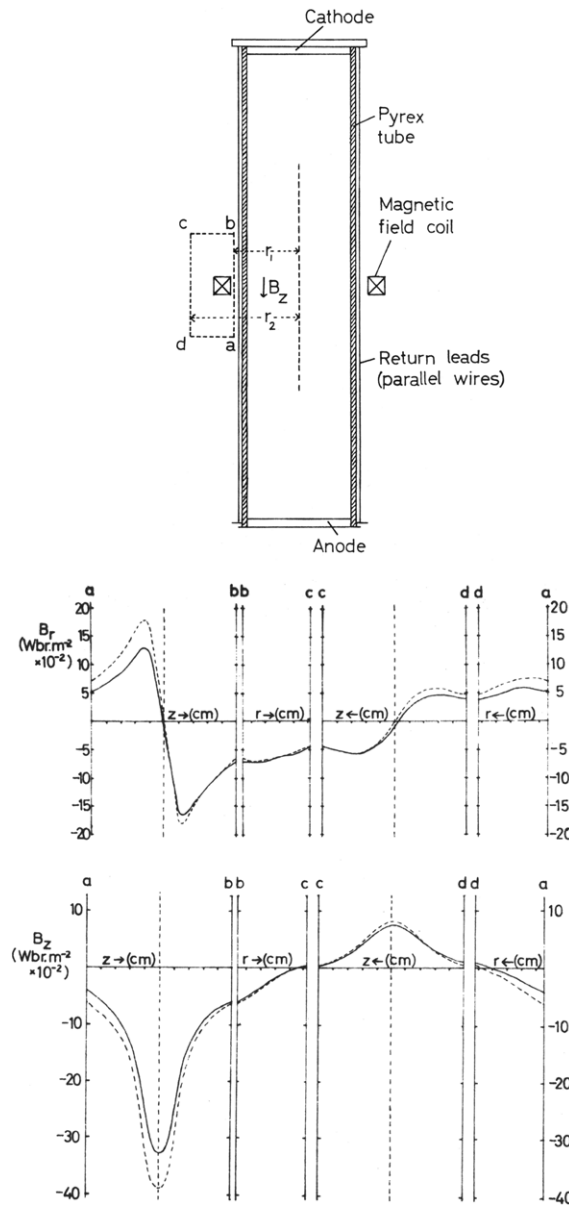
Figure 91. Hall acceleration and force found experimentally from the magnetic stress tensor [669]. The upper figure shows the schematic of the Z-pinch with a short coil added, including the closed path abcd along which the components of B_r and B_z are measured (middle figure) leading to the components of the magnetic stress tensor (bottom figure). Reprinted figure with permission from [669]. Copyright 1965 by the American Physical Society.

force towards the cathode. Correspondingly on the cathode side there is a repulsive force again accelerating the plasma (ions) towards the cathode. The magnetic field lines associated with the coil are in fact pulled towards the anode, and the tension in these field lines acts like a catapult to accelerate the plasma towards the cathode. It can be thought that the magnetic field is almost frozen to the electrons which are moving axially towards the anode. Etherington
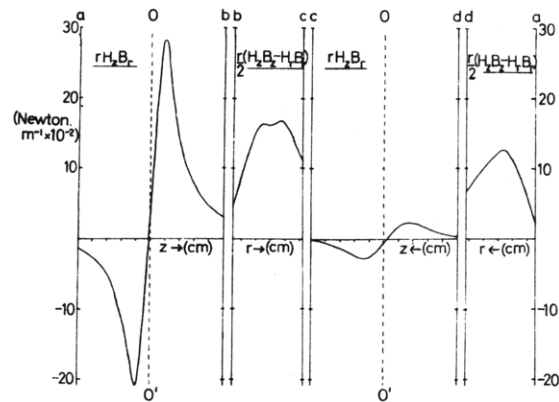
Figure 91. (Continued)

and Haines [669] measured the force on the coil as a function of time by measuring the components of the magnetic field on a surface outside the Z-pinch enclosing the coil, shown in figure 91(b); then via the stress tensor and a surface integral the force was measured as illustrated in figure 91(c). The limiting axial velocity is $v_z = J_z/n_e e$, at which $\underline{v} \times \underline{B}$ field balances the $J_z B_r/n_e e$ Hall term and no further acceleration will occur. That is, the ions are carrying the Z-current.

One application of this phenomenon is the development of the Hall thruster, which has been employed especially in Russian and more recently European space missions. In order to maximize the volume where the radial magnetic field exists the device has developed into a coaxial system, schematically shown in figure 92 from [670]. These are quasi-steady-state thrusters which can accelerate ions from 100 to 1000 eV. Whilst the instantaneous force is small, typically 0.04 to 1 N in a plasma of electron temperature of order 10 eV, these devices have a high specific impulse, e.g. in Xe, 1500 s or 15 kN s kg^{-1}. These thrusters have been used mainly for attitude control, consume some kilowatts of power with an efficiency of about 60%. Their thrust is an order of magnitude higher than electrostatic ion thrusters which are limited in current by the Child–Langmuir law. Another application of Hall acceleration is in industrial plasma processing.

At Imperial College a toroidal Z-pinch was surrounded by 36 coils of spatially alternating currents, these coils producing a series of cusp-shaped magnetic fields which dominated the configuration (figure 93). The applied induced toroidal electric field led to ion acceleration through multiple coils; hence the device was named the Polytron [66, 67, 666]. The coil separation has to be less than the accelerated ion's Larmor radius. To achieve this condition it was easier to use an argon plasma, in which it was found that a Mach number of over 2 was obtained. The equilibrium position could be controlled by an additional vertical magnetic field, thus reducing plasma–wall interactions and losses through the ring cusps. Indeed a double electrostatic sheath develops at each ring cusp. There is not only Hall acceleration of ions, but also ion-viscous heating to 100 eV, i.e. much higher than the electron temperature of 10–25 eV. In considering how this stable configuration could be improved it was proposed to have elongated cusp coils, confining the radial magnetic field to narrow regions, thus reducing ion losses and concomitant electron thermal conduction losses through the ring cusps. Furthermore, by increasing the Mach number to 5 or 7 the confinement time could be increased to satisfy Lawson's condition. 2D, two-fluid simulations by Watkins *et al* [671] followed the fast radially inward diffusion of the axial current, the computational time-step now being determined by the whistler wave. Hall acceleration, ion compressional heating
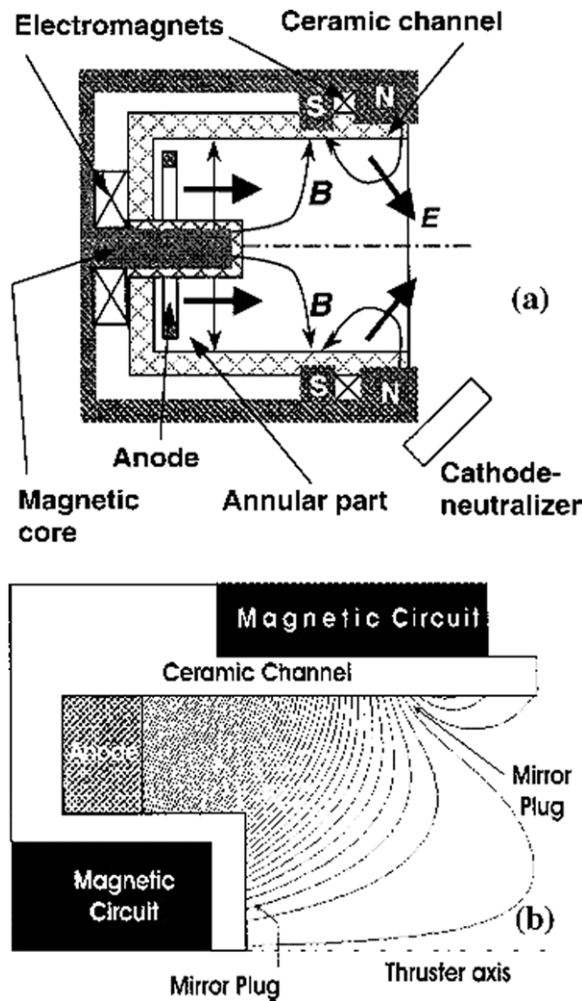
Figure 92. (*a*) Schematic of a cylindrical Hall thruster. (*b*) Typical externally applied magnetic field distribution which leads to azimuthal Hall currents. Reprinted with permission from [670, figure 1]. Copyright 2003, American Institute of Physics.

and extra Joule heating of the electrons by the Hall current was found. A central core of the plasma appeared well defined, stable and detached from the walls. But the next stage of this programme was not pursued as interest switched to pulsed-power driven Z-pinches. However a UCLA team under Dawson [68, 69] reinvented the scheme, but they too was unable to take it further.

A related experiment in Sweden was the EXTRAP concept [672]. But here the external multipole fields ($n = 4$ or 8) were added to a straight Z-pinch, and carried external currents alternately parallel and anti-parallel to the J_z current of the plasma. The objective of the multipole fields was to provide positive curvature to the fields near the plasma surface, and hence provide a stable equilibrium. A toroidal version was also experimentally studied, but the temperature was limited by radial losses through the gaps in the multipolar fields [673], as here, in contrast to the Polytron, there was no induced transverse ion c.m.-motion to reduce particle and thermal losses. This programme evolved into a reversed field pinch.
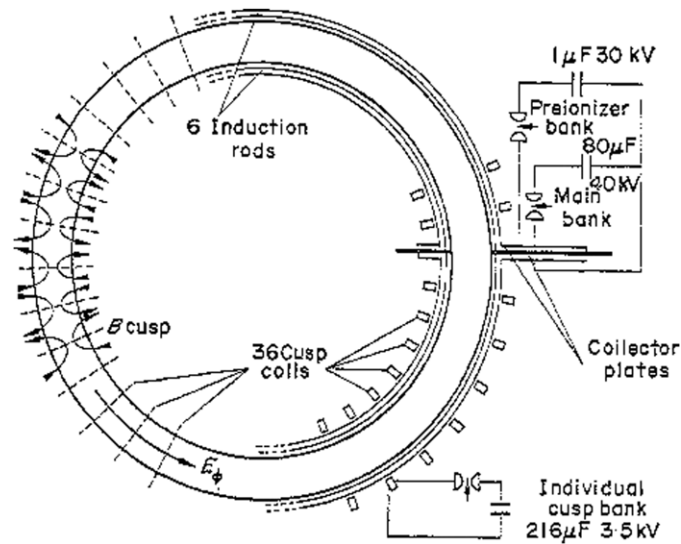
141

Figure 93. Schematic drawing of the Polytron apparatus; a toroidal Z-pinch threading through 36 cusp-shaped magnetic fields which enable both Hall acceleration leading to ion currents and stabilization of MHD modes [66, figure 1].

8.6. Multi-species ion separation

If a dynamic Z-pinch is formed with several ion species it is possible during the implosion phase to separate them because the $\underline{J} \times \underline{B}$ force is exerted on the electrons. A slight charge separation creates a radial electric field which accelerates the ions inwards radially with a value ZeE_r/Am_p. Thus ions with different Z/A will be accelerated by different amounts unless collisions between the species dominate.

In a gas-puff mixture Rahman *et al* [674] showed that the plasma shell split into two distinct annuli which imploded concentrically. This separation of species is however a little impaired by the onset of the RT instability. Perhaps a series of compressions with axial flow would be more effective. A related paper by Chakrabarti *et al* [675] employed two ion species. This has the geometry more of a plasma opening switch, and cases could be found where the ions acquired a velocity component perpendicular to the $\underline{J} \times \underline{B}$ force. In a plasma opening switch geometry Osin *et al* [676] with 150 kA of 400 ns duration showed a marked difference of behaviour of the two ion species; rapid magnetic field penetration into the heavy-ion plasma and specular reflection of the light-ion plasma, leading to ion-species separation.

8.7. Compression of axial magnetic field; the Z–Θ pinch

Two purposes exist for adding an axial magnetic field to the azimuthal field of the Z-pinch. One is to enhance the stability of the plasma configuration, especially for fusion; the other to compress the axial magnetic field to very high values, possibly for application in understanding the physics of dense matter in a uniform intense magnetic field.

One of the earliest experiments of an 'ultra-fast pinch', using a Blumlein circuit involving charged coaxial cables, was undertaken in 1963 by Adlam and Holmes [677]. An axial magnetic field of up to 1 T was first established in a Helmholtz coil and a fast Z-pinch of 30 kA rising in 20 ns (or millimicroseconds as it was then termed) applied in a silica discharge

tube 108 cm long and 2.8 cm internal diameter in pre-ionized hydrogen at 50 mTorr. The axial magnetic field was compressed from 0.2 to 0.9 T in 80 ns. The main interest of the experiment was however to find that the field diffusion was anomalously large compared with the collisionless skin depth. Indeed the growth of this was too fast to be explained even by ion-acoustic turbulence. In deuterium there were 10^3 neutrons per pulse.

Shock heating at a higher current of 200 kA by Baker *et al* [678] at Los Alamos produced a higher temperature in an attempt to avoid the drift instabilities. In 30 mTorr deuterium the peak density (from holography) 10^{16} cm^{-3} and an inferred temperature ($T_i + T_e$) of 750 eV were achieved in a 30 cm long 10 cm diameter discharge tube with a current rise of 2×10^{12} A s^{-1}. The axial magnetized field was compressed to 1.7 T peaking on axis while the azimuthal magnetic field peaked at 1.3 T at a radius of 2 cm. However anomalous Bohm diffusion was inferred, though gross stability for 8 μs was attained. This experiment was a precursor of the reversed field pinch (RFP) configuration, and a toroidal version was also reported.

The use of pulsed power technology to achieve compression of an axial magnetic field to megagauss (100 T) levels was pursued by Felber *et al* [294]. Using a neon gas-puff Z-pinch at 7.5 MA an axial magnetic field of 100 kG was compressed to 42 MG, a compression of 420. Velikovich *et al* [679] had earlier carried out some theory and simulations. Clearly the early Z-pinch acceleration leads to an inertial kinetic energy per unit length of the plasma shells $\frac{1}{2} M_\ell v^2$, which can in a conservative system subsequently compress the axial magnetic field to give a transient axial magnetic field $\pi a^2 B_z^2 / 2\mu_0$; while flux conservation gives $a^2 B_z$ a constant, a being the final shell radius. Velikovich *et al* [679] pointed out that transport effects can reduce the flux compression, but not by much. Felber *et al* extended the self-similar solutions to subsonic [680] and supersonic [681] regimes and included not only resistive and thermal diffusion but also the Nernst and Ettingshausen advection terms. Smaller compression ratios of 180 and peak fields of 1.6 MG were obtained at 500 kA with a 3 min repetition rate. Here the axial magnetic field was measured by Faraday rotation of an argon laser at 5154 Å in a quartz fibre on axis. Several radial bounces of the plasma occurred. At a similar current Appartaim and Dangor [682] compressed a 0.3 T field to 38 T in 2 μs, a factor of 126. The Z-pinch was initially either a thin cylindrical surfactant film or a uniform gas fill, the latter giving the best flux compression. Approximately half the current at peak was estimated to flow at the wall. The results above were for an optimal filling pressure of argon of 2 Torr and an optimal seed field for this current of 500 kA in the 5.5 cm internal diameter pyrex tube, driven by a modest 16 kJ capacitor bank.

The stability of the dynamic Z–Θ pinch has been studied theoretically by Bud'ko *et al*, first for a diffuse profile, [292] and second for annular and columnar profiles with sharp outer boundaries [591]. Even a relatively weak initial axial magnetic field substantially suppresses the dominant RT instability. Approximate analytic solutions are compared with numerical solutions for ideal MHD. In RT high m number ($\sim$7–10) fastest modes correspond to a filamentation of the axial current. In [292] it is found that magnetic shear is important for stabilizing bulk convective modes. This however requires $B_z \sim B_\theta$, which can occur at high compression with carefully shaped current pulses in the Z-pinches. The liner thickness and axial magnetic field need optimal choosing to minimize the effects of instabilities. Gol'berg, Liberman and Velikovich [683] extend the theoretical analysis to a break-even fusion experiment at 20 MA, but with a very small initial liner radius of 3 mm with a 30-fold radial compression.

A similar concept of inertial confinement in a Z–Θ pinch has been proposed by Rahman *et al* [64, 604]. Here the concept is having a cryogenic DT fibre on the axis, while the pulsed power driven annular Z-pinch compresses an axial magnetic field up to 100 MG, leading to the fibre forming a dense and relatively stable theta pinch.

However, in an experimental report by Wessel *et al* [684] there was insufficient coupling of energy to the fibre which largely remained unionized. This was because of the high electrical conductivity of the surrounding plasma, rather analogous to wire behaviour in an array. An experiment by Zehnter *et al* [685] concentrated on the effect of the axial magnetic field reducing the transverse thermal conduction in a helium gas puff implosion with a 6 TW generator, Ambiorix. A stable, hot, low density core plasma at 2 keV and 2.2×10^{19} cm^{-3} was measured, while the coronal cool, high density plasma was at 300 eV and 4×10^{20} cm^{-3}, in agreement with 1D MHD simulations.

There have been several attempts to compress axial magnetic flux using wire arrays. There are obvious issues at achieving this due to the tendency of the wire arrays to produce precursor streams of plasma inwards prior to the main implosion. There is indeed an interesting question of whether there is an azimuthal path of good electrical conductivity which can move radially inwards, trapping the axial magnetic flux and leading to flux compression. Leon *et al* [686] identified three negative effects of the precursor plasma, namely, closure of the gap allowing the axial magnetic field in, perturbation of the flux compression itself and closure of the seed gap between the compression and load chambers. A central rod was present, which acted as a return current path for the seed field and a stator for the flux compression armature. Flux compression was achieved, with improvement in the quality of implosion suggesting that RT was reduced. Bland *et al* [687] also studied wire-array behaviour in a high magnetic field. More recently Zukakishvili *et al* [688] employed wire arrays on Angara-5-1 Facility at currents of 2.5–4 MA to compress an axial magnetic field. Two methods were employed to generate the axial magnetic field: (i) the use of a helical wire array, and (ii) an independent multi-turn solenoid in the liner section. After some 30 ns B-dot probes indicated that there was some compression of the free axial magnetic flux within an effective radius of about 0.6 times the array radius, the plasma at this position moving with an inward velocity of $(1-2) \times 10^7$ cm s^{-1}. However this is followed over the next 100 ns by only a slow increase, followed by a second stage of rapid compression coinciding with the main array implosion, achieving a value of 300 kG from an initial 5 kG. After peak compression, the axial magnetic field continues to increase. This could be due to delay of diffusion into the probe or to further inward flux from trailing mass. Another possibility is inward Nernst convection associated with an enhanced Ettingshausen heat flux in the $\underline{J} \times \underline{B}$ direction. Several experiments were undertaken with the wires arranged in several groups. Only in the case of two compact groups were results very different; here the flux frozen in the wire plasmas was transferred to the array axis by two plasma jets. An initial axial magnetic field of 0 to 15 kG reduced the soft x-ray power from 2.5 to 0.1 TW as the volume of emission increased.

8.8. Capillary Z-pinch: x-ray laser and GeV electron acceleration

For many years researchers have explored the possibility of developing a laser in a Z-pinch discharge. For example, Illingworth [689, 690] found laser action at 4765 Å due to Ar$^+$ ions early on in a Z-pinch 5.2 cm or 2.6 cm in diameter and 92 cm long; and later Ar^{2+} ions. The peak discharge current was 15 kA in 580 ns; rapid heating is an essential feature of obtaining collisional excitation and population inversion. In contrast, Steden and Kunze [691] explored a recombination cascade scheme in a capillary discharge in which carbon from the walls of the capillary formed the plasma. The hydrogen-like Balmer-α line of C^{5+} at 18.2 nm gave amplification, but as Shin *et al* [692] found, the gain–length ($G\ell$) product was small. Lebert *et al* [693] also explored recombination laser action in Z-pinches.

A major breakthrough occurred with the work of Rocca *et al* [17] who in a 4 mm internal diameter capillary and a 40 kA discharge rising in 60 ns gave a population inversion in the

$J = 0$–1 line of neon-like Ar^{8+}. With gain G of 0.6 cm^{-1} at a wavelength of 46.9 nm, three lengths of discharge were tried; 3, 6 and 12 cm. The longest gave a gain–length product, $G\ell$, of 7.2. At this time the pinch radius was 100–150 μm. A buffer gas of hydrogen was added in a 1 : 2 mixture to reduce radiative trapping on the lower laser level; this level must quickly decay to the ground state. Neon was also explored as a buffer gas, but pure argon also lased well at a full pressure optimized at 700 mTorr. To obtain successful lasing action required hot, dense and axially uniform plasma (i.e. no instabilities), and sufficiently fast current rise to give collisional excitation.

It took some years for other researchers to master the black art. Among these should be mentioned Ben-Kish *et al* [694] and Kwek and Tan [695]. The former used an initial spark followed by a prepulse in the current range 10 to 50 A. In a capillary of 4.2 mm diameter and 80 mm length with argon pressure of 500 mTorr, the main discharge was a peak current of 40 kA in 51 ns. There was shock heating, and a pinched, uniform column of 150 μm diameter formed at the time of the lasing. The electron density was $\sim 10^{19}$ cm^{-3} and electron temperature $\sim$60 eV. The reflected shock led to an increase in radius; and it is at this time of 45 ns that for 1–2 ns lasing action occurs. It is inferred that at the time of lasing a concave electron density profile in the radial direction occurs to give beam guiding, and a thin plasma diameter avoids self-absorption of the Ne-like Ar 2p-3s line. A gain G of 0.75 cm^{-1} similar to that of Rocca *et al* was found, and the angular divergence of the laser beam was less than 5 mrad. Kwek and Tan found that lasing action could occur at discharge currents as low as 9 kA, and that timing of the prepulse relative to the main discharge is crucial, being 2–4 μs delay. Fill-pressures from 0.15 to 0.35 mbar showed an optimum pressure increasing with current and 0.24 mbar at 19 kA. The prepulse current amplitude was varied and 23 A was optimal.

In the light of the work on stability regimes [136] and section 3.1, it is instructive to ascertain in what regime are the above capillary Z-pinches. At peak compression followed by expansion at a peak current of 40 kA the Bennett relation must momentarily hold. This gives an ion temperature of 1.56 keV for $T_e = 60$ eV and $N_i = 2.45 \times 10^{17}$ m^{-1}. From this we find that $\Omega_i \tau_i = 0.02$ and $\Omega_e \tau_{ei} = 0.50$, i.e. the plasma is hardly magnetized, but the radially inward Ettingshausen heat flux is a maximum, and this with the Nernst term ensures that the current flows on axis. This could be assisted by the current-driven electrothermal instability [158] which would occur earlier at T_e below 48 eV with a radial wavelength close to the pinch radius to give a single filament. The higher temperature on axis can lead to a local drop in density, as required for focusing or optical guidance. With regard to MHD stability the Lundqvist number is 0.78, showing that the pinch is extremely resistive and more dependent on Joule heating than MHD effects. The magnetic Prandtl number is 0.016 showing that viscous effects are negligible. With this knowledge, scaling to higher or lower parameters should be possible. A fully time-dependent collisional–radiative model has been developed by Pöckl *et al* [696] in a recombining carbon/hydrogen plasma formed from the walls of a capillary Z-pinch. A useful review by Suckewer and Skinner [697] reports progress in table-top soft x-ray lasers.

Another and perhaps even more important application of the capillary Z-pinch is its use in forming a straight channel of axially uniform plasma with a radial minimum density on axis, for guiding an intense short pulse. It has been established by several research groups [698–700] that laser-driven acceleration of electrons to 200 MeV energy can be achieved in a medium of a mm-scale helium gas jet. Pukhov and Meyer ter Vehn [701] had earlier in simulations shown how a monoenergetic beam of electrons could be accelerated in the wakefield scheme proposed by Tajima and Dawson [702]. Here the electric fields, caused by charge separation, can be of order 10–100 GV m^{-1}. By using instead a capillary Z-pinch a much longer acceleration length can be achieved in principle. Leemans *et al* [703] demonstrated the production of a monoenergetic electron beam of 1 GeV energy in a 3.3 cm long hydrogen gas-filled capillary

discharge in which a 40 TW peak-power 1 μm wavelength 38 ps laser pulse was axially propagated. Without guiding by a profiled dielectric constant or thermal self-focusing the laser–plasma interaction length would be limited to the order of a Rayleigh length which is proportional to the spot size. Relativistic self-focusing extends the propagation distance but the effective dielectric constant is a function of laser intensity itself. Thus the leading edge of the laser pulse will be eroded. The self-focusing is a result of balancing the focusing effect of the dielectric profile resulting from the relativistic mass increase on axis with the centrifugal effect on the photons due to their spin [82]. The use of a channel allows a smaller spot size and hence a more efficient use of the laser energy. Much narrower capillaries of 150 and 310 diameter were used. The time delay between the peak discharge current and the laser was varied to give the optimal electron density profile at $(2.7–3.2) \times 10^{18}$ cm^{-3}. In this experiment the input intensity was $\sim 10^{18}$ W cm^{-2} and the spot radii were 25–27 μm at the entrance and 31–34 μm at the exit. The plasma channel here was preformed by a laser.

Further insights into the physics, especially the key process of injection of electrons into the laser wakefield, were found by Rowland-Rees *et al* [704]. In particular they concluded that it is beneficial if the plasma is only partially ionized near the axis: It was noted that the generation of electrons within the wakefield reduced the threshold for trapping because these electrons are born with $\sim$zero velocity while those of the background plasma have backwards momentum. The length of the channel (10 mm) here was of order of the dephasing length associated with the velocity difference between the accelerated bunch of electrons and the propagating bubble shaped vacuum generated by the ponderomotive force in the wakefield.

In summary, two important branches of physics have developed out of the capillary Z-pinch, the capillary x-ray laser and the monoenergetic acceleration to GeV energy of electron bunches by a short-pulse intense laser.

8.9. Conical and radial arrays; plasma jets

Conical arrays have been explored in depth by Ampleford *et al* [705] using both the MAGPIE generator at Imperial College and the ZEBRA generator at the University of Nevada at Reno. Figure 94 shows the schematic idea, and there is now an angle α at which the wires are inclined to the Z-axis. As can be deduced from this, even though the global magnetic field is purely azimuthal the currents have a radial component. The $\underline{J} \times \underline{B}$ force now has an axial component, and the resulting precursor velocity and final implosion velocity will have axial components leading to a flow of plasma through a hole in the anode, usually in the form of a narrow, radiatively cooled jet of high Mach number (see section 8.10).

Two types of experiment should be distinguished; (a) the overmassed, non-imploding wire array to study the precursor jet which is to a good approximation free of magnetic field and (b) the optimally massed array for implosion studies with a strong azimuthal magnetic field. In both cases there is zippering. This is because the global magnetic field at the array is larger nearer the cathode due to the smaller array radius there, and there is a shorter distance for the plasma to reach the axis.

Interestingly during the precursor phase both the wavelength of the perturbations along the length of the wires and the ablation velocity V_{abl} are constant, despite the large variation in the global magnetic field. In the case of the early stage of the instability it is more consistent with a primary role for the heat-flow-driven electrothermal instability, which is essentially only material dependent (see section 5.4). With a constant V_{abl} it is the mass ablation rate per unit length, $\dot{m}_\ell$ that responds to the larger $\underline{J} \times \underline{B}$ force, and is given approximately by [705],

$$\dot{m}_\ell(z) = \frac{\mu_0 I^2(t)}{4\pi V_{abl}(R_c + z \tan \alpha)},$$ (8.9)
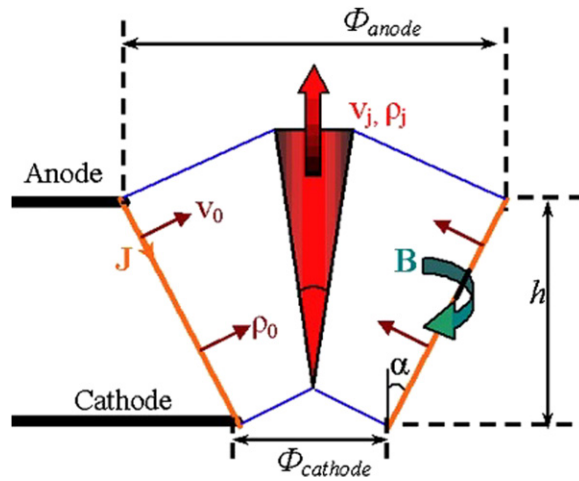
Figure 94. Set-up for the conical wire-array load, which leads to an axial component of plasma flow through the larger diameter hole in the anode. Reprinted with permission from [705, figure 1]. Copyright 2007, American Institute of Physics.
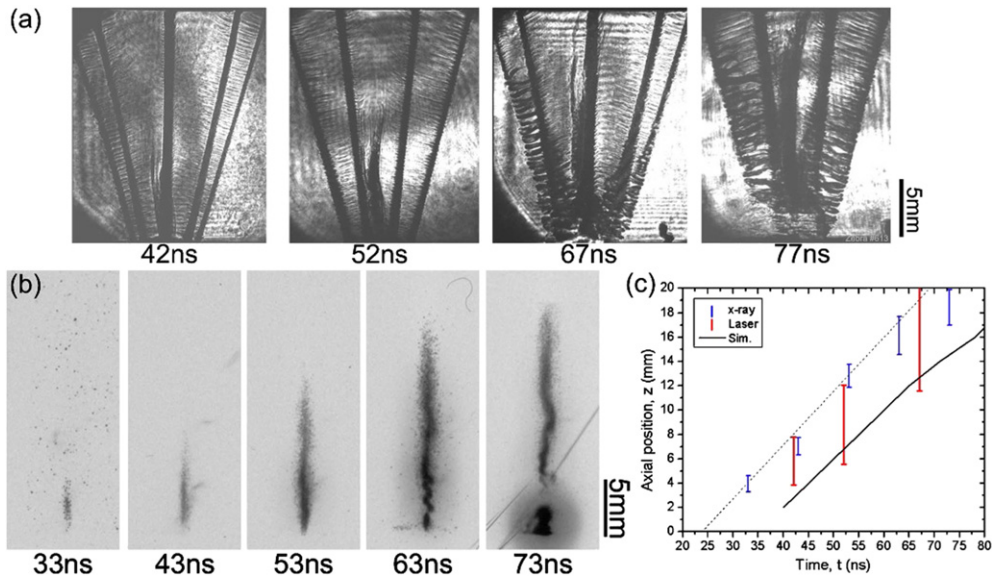

Figure 95. Formation of the precursor plasma on ZEBRA viewed at different times by (*a*) laser shadowgraphy and (*b*) time-resolved x-ray pinhole camera ($h\nu > 1\,\mathrm{keV}$) for an array with 16.7° opening angle. Plot (*c*) shows the measured axial formation positions by the two diagnostics. Reprinted with permission from [705, figure 4]. Copyright 2007, American Institute of Physics.

where R_c is the radius of the array at the cathode. Thus the gaps in the wires occur first near the cathode; the current transfers to the hot, higher R_m plasma, and the main implosion occurs first at the cathode.

Both the precursor and the main implosion therefore have a zipper effect on axis, the zipper velocity (which is essentially a phase velocity) getting large as the angle α decreases. The

higher velocity near the cathode in the main implosion phase means that there is an increased zipper effect.

Above a critical angle α the early implosion at the cathode end results in the creation of a 'magnetic bubble'. This is seen at 73 ns in the faster ZEBRA experiment illustrated in figure 95(*b*). Also in figure 95(*a*) can be seen the axially uniform wavelength and in 95(c) the axial zipper position of the precursor plasma. There are 3D MHD simulations in this paper and an earlier one by Ciardi [706] which broadly agree with the dynamical phenomena.

An interesting possible application is the broadening of the x-ray pulse in time, typically by a factor of two which would be needed by ICF. Indeed further shaping of the x-ray pulse could probably be achieved by using a mixture of conical sections to the load.

In another proposed application, Chittenden *et al* [707] have proposed using two jets of plasma as drivers for indirect inertial confinement by aiming each at a material convertor (as in heavy-ion fusion) each end of a cylindrical hohlraum in which is placed the fuel capsule.

The magnetic bubble is probably associated with a strong radial current connecting the already imploded plasma at the cathode end with the remains of the conical wire array. Thus it would be expected that a purely radial array would have a similar rising magnetic bubble or tower as its main feature. Because of its relevance to laboratory astrophysics it will be considered in more detail in the following section.

8.10. Laboratory astrophysics

The Z-pinch and laser-produced plasmas can be used to model on the laboratory scale certain astrophysical phenomena, even though the length and time scales can be up to 10^{24} times greater. The reason for thinking that the basic hydrodynamic or MHD phenomena are essentially the same is that if the corresponding dimensionless numbers such as the Reynolds' number, R_e, and Peclet number, P_e, in hydrodynamics and the magnetic Reynolds' number, R_m, in MHD are much larger than unity in both the laboratory and the astrophysical situation, then the resulting phenomena will be similar. Such astrophysical phenomena as shocks and jets formation and collimation could thus be modelled in the laboratory using lasers or Z-pinches [708, 709].

The longest highly collimated jet so far found in active galactic nuclei (AGN) is estimated as being 1.5 million light years (mℓy) or 1.4×10^{22} m long [710] emanating from an extremely massive black hole ($>10^9$ solar masses). More standard, Centauris has a jet 4.5 kilo-parsec (kpc) or 1.4×10^{20} m long (and a counter-jet) [711]. Young stellar objects (YSOs) have shorter jets, often with more structure. In particular Herbig–Haro (HH) jets [712] are associated with the birth of stars, formed from giant molecular clouds (GMCs) via accretion in a disk under gravity. These jets are typically 0.5pc or 1.5×10^{16} m in length, and, like the other jets, are moving at speeds of $100–1000 \, \mathrm{km \, s^{-1}}$ [713]. Molecular bow shocks typically occur at the ends of the HH jets due to interaction with the surrounding cloud, and emit in the infra-red (IR) or optical region. Knots have been observed [714], which is consistent with nonlinear $m = 1$ instabilities.

A large Reynolds' number, R_e, or Peclet number, P_e, implies a short mean-free path (mfp), since they are proportional to L/λ_{mfp} while, paradoxically the magnetic Reynolds' number, R_m, is *proportional* to the electron–ion mean-free path. A large magnetic Reynolds' number means that at sonic flow the mean-free path multiplied by L is much greater than the square of the ion collisionless skin depth. Another important comparison between laboratory and astrophysical phenomena is the radiative cooling time compared with L/v where L and v are the characteristic length and velocity, respectively.
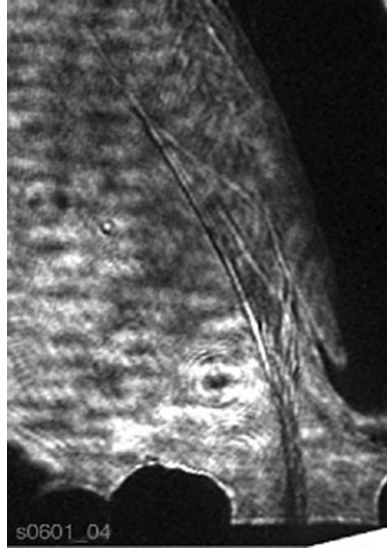
Figure 96. Deflection of a supersonic plasma jet by a plasma wind blowing from right to left, illustrated in a laser schlieren image 343 ns after the start of the current on MAGPIE. Shock-like features can be identified [715, figure 2].

Lebedev *et al* [715] showed how the approximately current-free precursor plasma from an overmassed tungsten conical array can form a jet with an axial velocity similar in magnitude to that of astrophysical jets, namely $200\,\mathrm{km\,s^{-1}}$. In this case L and t of the two systems scale in the same way, and the Euler equations, i.e. the dissipationless hydrodynamic equations,

$$\frac{\partial \rho}{\partial t} + \nabla \cdot (\rho \underline{v}) = 0, \tag{8.10}$$

$$\rho \left(\frac{\partial v}{\partial t} + (\underline{v} \cdot \nabla) \underline{v} \right) = -\nabla p, \tag{8.11}$$

$$\frac{\partial p}{\partial t} + \underline{v} \cdot \nabla p = -\gamma p \nabla \cdot \underline{v} \tag{8.12}$$

remain the same if L and t are scaled by the same factor [709]. In ideal MHD an additional term $-\mu_0^{-1}\underline{B} \times (\nabla \times \underline{B})$ arises together with Faraday's law combined with Ohm's law

$$\frac{\partial \underline{B}}{\partial t} = \nabla \times (\underline{v} \times \underline{B}), \tag{8.13}$$

which also formally remains the same. If, furthermore, the parameters $\underline{v}$, $\underline{B}$, ρ and p are the same, in the two systems, the dimensionless parameters R_e, R_m and P_e also all scale with the same factor as L or t. If this scale factor is A, the energy required to drive a scaled experiment scales as A^3 which makes laboratory experiments possible. Ryutov and Remington [716] call this a 'perfect' hydrodynamic similarity as transport coefficients are identical in both systems, including compositional effects. Gardiner *et al* [717] have presented MHD models of jets, while Ciardi *et al* has extended modelling of jets to 3D [718].

Continuing with magnetic field free jets from the precursor phase of a conical wire-array Z-pinch, Lebedev *et al* [719] caused the jet to interact with a cross-wind plasma produced by radiative ablation of a thin plastic foil placed above the anode. This cross-wind had a density of $10^{24}\,\mathrm{m^{-3}}$ and a velocity of $2 \times 10^4\,\mathrm{ms^{-1}}$. A $4°$ deflection of the jet occurred and increased
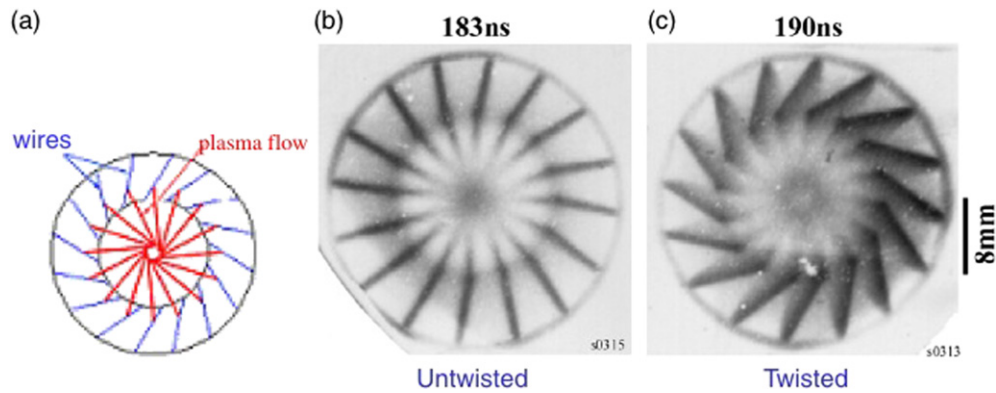
Figure 97. Spinning plasma jets; (*a*) schematic of twisted wire-array configuration illustrating the introduction of angular momentum into converging plasma flow, (*b*) end-on XUV images of untwisted and (*c*) twisted conical wire arrays. The jet in (*c*) is hollow due to rotation [715].

as the foil was placed closer to the jet. It is illustrated in figure 96. Various shock features can be identified including a working surface as found in simulations by Ciardi *et al* [720]. Indeed Hartigan [721] has expressed satisfaction that now laboratory experiments and simulations with *Z*-pinches are able to reveal scaled astrophysical phenomena. In HH objects the eruption of jets from the parent star occurs in pulses, which, as they move in the same direction but at different speeds, different jets create working surfaces where streams of gas collide and generate shock waves.

Astrophysical jets emanate from rotating accretion disks. It follows that the jets could also have angular momentum [722]. In the laboratory by twisting the conical wire array, an azimuthal component of the current is introduced causing axial and radial components of the global magnetic field. In turn the $(J_z B_r - J_r B_z)$ force close to the wire causes rotation of the incoming precursor plasma. The ablated plasma consists of a supersonic, rotating and radially converging flow. Ampleford *et al* [723] have shown that this results in a hollow column on axis. The incoming flow causes an equilibrium radius of the standing shock in which the centrifugal force of the column is balanced by the ρv^2 ram pressure of the flow. End-on XUV images showing the hollow precursor column are shown in figure 97. The axially, emerging, rotating jet is observed to be hollow with a twisting filamentary structure.

The acceleration mechanism for jets in AGNs and YSOs is widely considered to be magnetic [204]. Collimation over large distances is more problematic. Livio [724] wrote that 'there is no direct observation which confirms that jets are hydromagnetically driven.' However in discussing HH flows, Reiparth and Bally [713] quote evidence for magnetic fields from the circular polarization of the radio emission. Appl *et al* [726] have considered the current-driven instabilities in astrophysical jets. Both axial and azimuthal components of magnetic field are assumed to be present as in a tokamak or reversed field pinch (RFP). The pitch of the magnetic field, $r B_z/B_\vartheta$, on axis determines the growth rate of the fastest growing kink instability. Unlike a tokamak it is likely that the two components of the magnetic field are comparable. If the pitch is constant, the jet is unstable, while for variable pitch or magnetic shear the work of Suydam applies [191] and instabilities occur at resonant surfaces where $\underline{k} \cdot \underline{B}$ is zero, $\underline{k}$ being the perturbing wave number. Further away from the source of the jet the azimuthal magnetic field will dominate, and the jet is more like a *Z*-pinch. In modelling the effect of the instability Appl *et al* [726] assume that the jet is bounded by a rigid cylindrical wall, representing the ambient medium, and the return axial current is a skin current in this
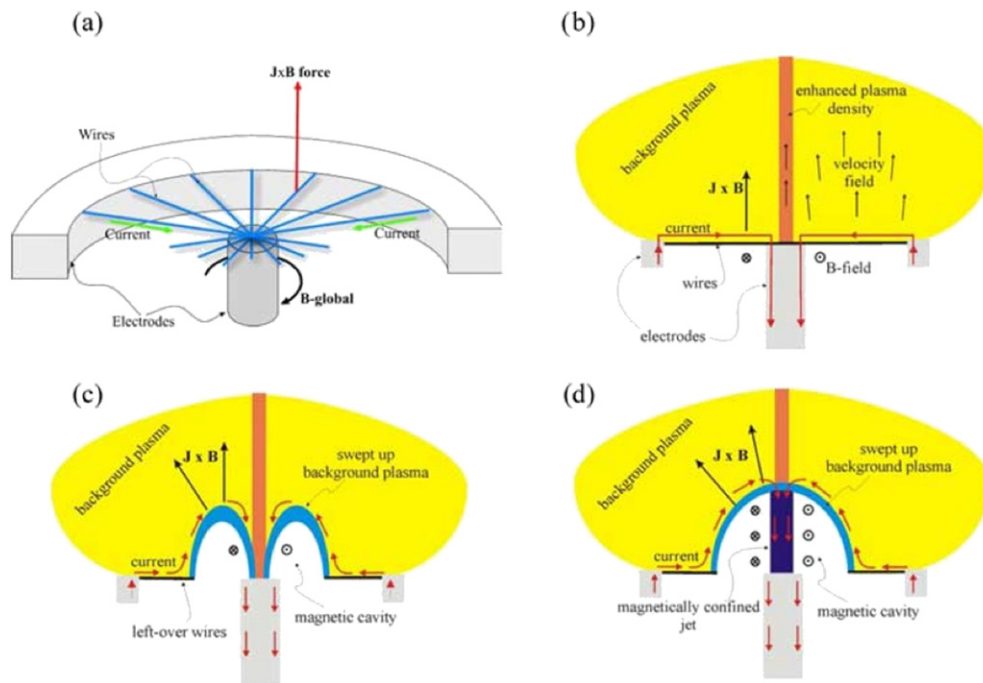
Figure 98. Schematic of a radial wire-array experiment. Currents flow radially through fine metallic wire from an outer ring electrode to a central cylindrical electrode, producing a toroidal magnetic field which lies below the wires. (*b*) The $J \times B$ force acting on the plasma ablated from the wires produces an axially flowing precursor plasma of low magnetic Reynolds' number. (*c*) When gaps form in the wires full acceleration of the plasma with the current begins near the central electrode, leading to the formation of a magnetic cavity, which evolves (*d*) into a magnetic tower jet driven upwards by the azimuthal magnetic field [730, figure 1]. Courtesy of the Royal Astronomical Society.

wall. This is questionable. The argument is that in the frame of the highly supersonic jet the resistive wall will behave as a perfect conductor to magnetic perturbations. (Similar arguments are employed for rotating plasmas in a tokamak, but here there is actually a solid conducting wall). If the kinetic energy of the jet exceeds the magnetic energy, it can be argued that the current driven instability will not destroy the jet, but merely lead to dissipation of the current. Then the gross dynamics will be governed by the KH instability associated with the velocity shear. Lucek and Bell [207] have modelled the 3D MHD evolution of a jet without a rigid wall and find that wild kink instabilities can occur, but [208] can be stabilized by having an axial component of magnetic field.

More needs to be done to resolve the issues. In examining data from an extra galactic radio jet, Kronberg [725] concludes that the energy flow is dominated by the Poynting flux rather than the kinetic energy of the jet. An estimate of the magnetic field from Faraday rotation of 3C 303 gives 3 mG (3×10^{-7} T) at a distance from the jet axis of 400 pc leads to an axial current of $\sim 10^{18}$ A in a low pitch reversed field pinch configuration with β estimated as $\leqslant 10^{-5}$. In the formation of the MHD jet the development of a 'magnetic tower' is postulated [727, 728]. Indeed Hartigan *et al* [729] argue that magnetic fields must be dominant in producing jets, even if they later play only a minor role in bow shocks. The laboratory Z-pinch has been adapted to model the creation of a magnetic tower by Lebedev *et al* [730] and modelled in 2D MHD by Ciardi *et al* [731]. For this radial wire arrays were employed, rather like the spokes off a wheel,
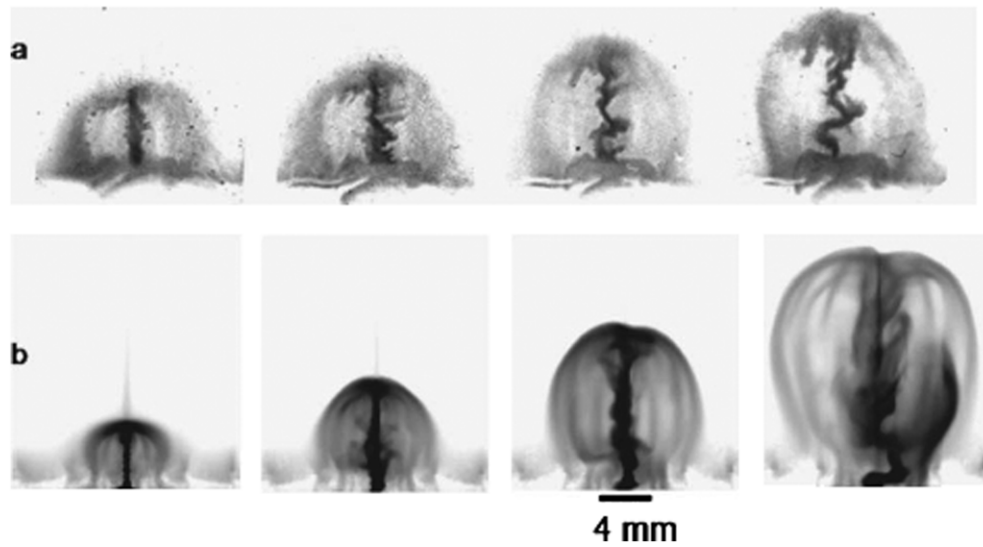
4 mm

Figure 99. The evolution of magnetic tower jets is shown (*a*) in synthetic x-ray emission images from 3D simulations at 210, 220, 230 and 240 ns (from left to right, the intensity being on a logarithmic scale spanning 10^3) and (*b*) experimental, time-resolved extreme UV images at 268, 278, 288 and 298 ns. Reprinted with permission from [706, figure 5]. Copyright 2007, American Institute of Physics.

the axle of which is the cathode. This and the resulting large $J_r B_\vartheta$ upward force, strongest near the cathode, is illustrated in figure 98. In figure 98(*a*) the scheme of the experiment is shown, the MAGPIE generator being able to drive a 1 MA current, rising over 240 ns. The wire ablation phase is illustrated in figure 98(*b*) in which an almost current-free axially moving background plasma is formed. Then because the mass ablation rate increases with the global field [65] which here varies as $1/r$, gaps appear at 220 ns in the wire cores near the cathode and a high R_m plasma carrying the current is driven up axially as shown in figure 98(*c*). A jet-like column develops on the axis in figure 98(*d*). A time sequence of soft x-ray images is shown in figure 99(*b*) showing the magnetic tower together with the central current carrying jet which undergoes $m = 0$ and $m = 1$ instabilities as it moves with Mach $\sim$10 in the z-direction. The magnetic cavity grows axially at 200 km s^{-1} and radially at 50 km s^{-1}. The reason is the large $J_r B_\vartheta$ force at the tip of the toroidal cavity. The instability evolves on the Alfvén transit time scale but the jet is not destroyed and persists for $\sim$20 growth times. Later the magnetic tower and plasma jet get detached from the source. Ciardi *et al* [732] have undertaken a 3D MHD simulation and reproduce in synthetic x-ray emission images in figure 99(*a*) the main features of the experiment. The presence of the initial background plasma is found to be essential for the evolution of the magnetic tower. It supplies some of the mass of the jet through the occurrence of a bow shock ahead of the tower. In this experiment and simulation the ion mean-free path in low density regions however is long $\sim$200 mm, but the ions are strongly magnetized with a Larmor radius of 0.3 mm. This localizes the ion behaviour and permits the use of MHD fluid equations. When a thin foil replaces the radial wires a second magnetic tower is generated through a re-strike of current in the residual mass [733]. This episodic behaviour, similar to that found in astrophysics, was found experimentally [734] and in simulations [735].

In conclusion, the Z-pinch permits scaled astrophysical experiments [736] both in magnetic-free and magnetically dominated phenomena; particularly shocks, jets, magnetic acceleration and magnetic towers.

9. The future

The Z-pinch remains a strong candidate for ICF, though funding of the order required for ignition is only likely to be available if the NIF falls short of expectations. Meanwhile, more compact hohlraum designs, perhaps building on the recent promising results from planar wire arrays, should make Z-pinch driven ICF require a smaller driver and a more manageable yield. The development of a more compact and repetitively pulsed new power source, the LTD, could be the answer.

Some basic physics still requires to be done, for example, clarifying the enhanced radiation power. The author hopes that the discussion in this review will assist in understanding this phenomenon. Six candidate explanations have been put forward; ion-acoustic turbulence (or some generally enhanced collision frequency); ingestion of magnetic energy of $m = 0$ (MHD bubbles; Hall resistance in an inhomogeneous plasma; a 3D MHD with longer current paths (plus numerical heating); drift wave instabilities; and viscous dissipation (both ion and electron viscosity in different regimes) of short wavelength nonlinear $m = 0$ MHD modes.

Related to this, the Z-pinch, using wire arrays or a series of gas puffs at lower line densities, is an impressive K_α source and could be further developed. The deuterium gas-puff Z-pinch gives 3.9×10^{13} neutron yield at 17 MA, and could be further enhanced at higher current, perhaps leading with DT to a useful source of 14 MeV neutrons. At high line density these neutrons are almost certainly thermal rather then beam–target in origin.

The capillary Z-pinch is useful not only in x-ray laser development but also in providing a suitable guide for laser wakefield acceleration.

The application of pulsed power to high energy density physics is impressive. Because of the larger spatial and temporal scales available, compared with laser-driven experiments, more accurate equation of state, transport properties and opacities can be obtained. This was demonstrated at Sandia National Laboratory by using the Z-accelerator to drive flyer-plates on to material samples and examining the shock propagation. For example Knudson *et al* [737], by measuring the principal Hugoniot, the reverberating wave and the mechanical re-shock in liquid deuterium contained by an aluminium drive-plate and a sapphire rear window obtained an equation of state that corrected earlier laser-driven measurements, at pressures up to 400 Gpa. The greater accuracy occurred because of the larger sample and longer times possible with pulsed power.

An exciting development is that of laboratory astrophysics. Scaled experiments have demonstrated Mach 20 jets, with and without magnetic fields, their interaction with other plasma and the development of magnetic towers.

References

[1] Deeney C *et al* 1997 *Phys. Rev.* E **56** 5945
[2] Spielman R B *et al* 1998 *Phys. Plasmas* **5** 2105
[3] Stygar W A *et al* 2004 *Phys. Rev.* E **69** 046403
[4] Baker K L *et al* 1999 *Appl. Phys. Lett* **75** 775
[5] Cuneo M E *et al* 2001 *Phys. Plasmas* **8** 2257
[6] Martin J C 1970 Nanosecond pulse technique *AWE Aldermaston International Report* SSWA JCM/704/49
[7] Mitchell I H *et al* 1996 *Rev. Sci. Instrum.* **67** 1533
[8] Pease R S 1957 *Proc. Phys. Soc. Lond.* **70** 11
[9] Braginskii S I 1957 *Zh. Eksp. Teor. Fiz* **33** 645
    Braginskii S I 1958 *Sov. Phys.—JETP* **6** 494
[10] Haines M G 1982 *Phys. Scr.* **T2/2** 380
[11] Arber T D, Coppins M and Scheffel J 1994 *Phys. Rev. Lett.* **72** 2399
[12] Arber T D *et al* 1995 *Phys. Rev. Lett.* **74** 2698; see also [202]
[13] Russell P G F, Arber T D, Coppins M and Scheffel J 1997 *Phys. Plasmas* **4** 2322
[14] Davies H M, Dangor A E, Coppins M and Haines M G 2001 *Phys. Rev. Lett.* **87** 145004
[15] Chittenden J P and Haines M G 1991 *Phys. Fluids* B **2** 1889
[16] Austin B *et al* 1987 *IEEE Trans. Plasma Phys. Sci.* **15** 226
[17] Rocca J J *et al* 1994 *Phys. Rev. Lett.* **73** 2192
    see also Rocca J J 1999 *Rev. Sci. Instrum.* **70** 3799
[18] Stamper J A *et al* 1971 *Phys. Rev. Lett.* **26** 1012
[19] Tabak M *et al* 1994 *Phys. Plasmas* **1** 1626
[20] Sanford T W L *et al* 1996 *Phys. Rev. Lett.* **77** 5063
[21] Deeney C *et al* 1998 *Phys. Rev. Lett.* **81** 4883
[22] Van Marum M 1790 *Proc. 4th Int. Conf. on Dense Z-Pinches (Vancouver 1997)* (Woodbury, NY: American Institute Physics) (frontispiece) and p ii
[23] Pollock A and Barraclough S 1905 *J. Proc. R. Soc. New South Wales* **39** 131
[24] Pease R S 1985 *J. Proc. R. Soc. New South Wales* **118** 27
[25] Northrup E F 1907 *Phys. Rev.* **24** 474
[26] Bennett W H 1934 *Phys. Rev.* **45** 890
[27] Thomson G P and Blackman M 1946 *British Patent* No 819681
    see also Haines M G 1996 *Plasma Phys. Control. Fusion* **38** 643
[28] Blackman M 1951 *Proc. Phys. Soc. Lond.* B **64** 1039
[29] Cousins S W and Ware A A 1951 *Proc. Phys. Soc. Lond.* B **64** 159
    see also Thonemann P C and Cowhig W T 1951 *Proc. Phys. Soc. Lond.* B **64** 345
[30] Reynolds P and Craggs J D 1952 *Phil. Mag.* **43** 258
[31] Allen J E and Craggs J D 1955 *Br. J. Appl. Phys.* **5** 446
[32] Kurchatov I V 1957 *J. Nucl. Energy* **4** 193
[33] Artsimovich L A *et al* 1957 *J. Nucl. Energy* **4** 203
    Artsimovich L A *et al* 1957 *J. Nucl. Energy* **4** 213
[34] Leontovich M A and Osovets S M 1957 *J. Nucl. Energy* **4** 209
[35] Anderson O A *et al* 1958 *Phys. Rev.* **109** 612
[36] Carruthers R and Davenport P A 1957 *Proc. Phys. Soc. Lond.* B **70** 49
[37] Kruskal M D and Schwarzschild M 1954 *Proc. R. Soc. Lond.* A **223** 348
[38] Tayler R J 1957 *Proc. Phys. Soc. Lond.* B **70** 31
[39] Curzon F L, Folkierski A, Latham R and Nation J A 1960 *Proc. R. Soc. Lond.* A **257** 386; see also [277]
[40] Mather J W 1971 *Methods of Experimental Physics* (New York: Academic) vol 9B, p 187
    See also Mather J W 1965 *Phys. Fluids* **8** 366
[41] Filippov N V, Filippova T I and Vinogradov V P 1962 *Nucl. Fusion Suppl. Pt.2,* 577
[42] Gentilini A, Maisonnier Ch and Rager J P 1979 *Comment. Plasma Phys.* **5** 41
[43] Decker G and Wienecke R 1976 *Physica* C **82** 155
[44] Blumlein A D 1950 *US Patent* 2496979
[45] Haines M G 1978 *J. Phys. D: Appl. Phys.* **11** 1709
[46] Lebedev S V *et al* 1998 *Phys. Plasmas* **5** 3366
[47] Mosher D *et al* 1975 *Ann. NY Acad. Sci.* **251** 632
[48] Shiloh J, Fisher A and Rostoker N 1978 *Phys. Rev. Lett.* **40** 515
[49] Stallings C, Nielson K and Schneider R 1976 *Appl. Phys. Lett.* **29** 404

[50] Young F C *et al* 1986 *J. Appl. Phys.* **48** 3642
[51] Pereira N R and Davis J 1988 *J. Appl. Phys.* **64** R1–27
[52] Haines M G 1998 *Astrophys. Space Sci.* **256** 1
[53] Choi P, Coppins M, Dangor A E and Favre M B 1988 *Nucl. Fusion* **28** 1771
[54] Soto L, Chuaqui H, Favre M and Wyndham E 1994 *Phys. Rev. Lett.* **72** 2891
[55] Lorenz A *et al* 1998 *Phys. Rev. Lett.* **81** 361
    see also Lorenz A and Peacock N J 1999 *Rev. Sci. Instrum.* **70** 1425
[56] Wessel F J *et al* 1992 *Phys. Rev. Lett.* **69** 3181
    see also Chuvatin A *et al* 1996 *Phys. Rev. Lett.* **76** 2282
[57] Arber T D and Howell D F 1996 *Phys. Plasmas* **3** 554
[58] Nash T J *et al* 2004 *Phys. Plasmas* **11** L65
[59] Taylor G I 1950 *Proc. R. Soc. Lond.* A **201** 192
[60] Davis J, Gondarenko N A and Velikovich A L 1997 *Appl. Phys. Lett.* **70** 170
[61] Smirnov V P 1991 *Plasma Phys. Control. Fusion* **33** 1697
[62] Brownell J H *et al* 1998 *Phys. Plasmas* **5** 2071
[63] Nash T J *et al* 1999 *Phys. Plasmas* **6** 2023
[64] Rahman H U, Wessel F J and Rostoker N 1995 *Phys. Rev. Lett.* **74** 714
[65] Lebedev S V *et al* 2001 *Phys. Plasmas* **8** 3734
[66] Kilkenny J D, Dangor A E and Haines M G 1973 *Plasma Phys.* **15** 1197
[67] Chuaqui H, Dangor A E, Haines M G and Kilkenny J D 1981 *Plasma Phys.* **23** 287
[68] Rhodes M, Dawson J M, Leboeuf J N and Luhmann N C 1982 *Phys. Rev. Lett.* **48** 1821
[69] Leboeuf J N, Ratliff S T and Dawson J M 1984 DOE/ET53088-120, IFSR-120 'A study of generalised toroidal
    cusp configurations'
[70] Spalding I 1971 *Adv. Plasma Phys.* **4** 79
[71] Haines M G 1977 *Nucl. Fusion* **17** 811
[72] Kalantar D H and Hammer D A 1993 *Phys. Rev. Lett.* **71** 3806
[73] Skowronek M and Romeas P 1987 *IEEE Trans. Plasma Sci.* **15** 589
[74] Raven A, Willi O and Rumsby P T 1978 *Phys. Rev. Lett.* **41** 554
[75] Craxton R S and Haines M G 1975 *Phys. Rev. Lett.* **35** 1336
[76] Haines M G 1986 *Can. J. Phys.* **64** 912
[77] Tatarakis M *et al* 2002 *Nature* **415** 280
    see also Tatarakis M *et al* 2002 *Phys. Plasmas* **9** 2244
[78] Wagner U *et al* 2004 *Phys. Rev.* E **70** 026401
[79] Wilks S C *et al* 1992 *Phys. Rev. Lett.* **69** 1383
[80] Davies J R, Bell A R, Haines M G and Guérin S M 1997 *Phys. Rev.* E **56** 7193
[81] Haines M G, Wei M S, Beg F N and Stephens R B 2009 *Phys. Rev. Lett.* **102** 045008
[82] Haines M G 2005 *Phys. Lett.* A **347** 143
[83] Kadomtsev B B 1966 *Reviews of Plasma Physics* vol 2 ed M A Leontovich (New York: Consultants Bureau)
    p 153
[84] Haines M G 1981 *Phil. Trans. R. Soc. Lond.* A **300** 649
[85] Dangor A E 1986 *Plasma Phys. Control. Fusion* **28** 1931
[86] Matzen M K 1997 *Phys. Plasmas* **4** 1519
[87] Liberman M A, DeGroot J S, Toor A and Spielman R B 1999 *Physics of High Density Z-Pinch Plasmas*
    (New York: Springer)
[88] Ryutov D D, Derzon M S and Matzen M K 2000 *Rev. Mod. Phys.* **72** 167
[89] International Conference on the Dense Z-Pinch 1984 *1st Conf. (Alexandria, VA, USA) NRL Report*
    International Conference on the Dense Z-Pinch 1989 *2nd Conf. (Laguna Beach, CA, USA) AIP Conf. Proc.*
    195 537
    International Conference on the Dense Z-Pinch 1993 *3rd Conf. (London, UK) AIP Conf. Proc.* **299** 720
    International Conference on the Dense Z-Pinch 1997 *4th Conf. (Vancouver, Canada) AIP Conf. Proc.* **409**
    628
    International Conference on the Dense Z-Pinch 2002 *5th Conf. (Albuquerque, NM, USA) AIP Conf. Proc.* **651**
    459
    International Conference on the Dense Z-Pinch 2005 *6th Conf. (Oxford, UK) AIP Conf. Proc.* **808** 375
    International Conference on the Dense Z-Pinch 2008 *7th Conf. (Alexandria, VA, USA) AIP Conf. Proc.* **1088**
    270
[90] *IEEE Trans. Plasma Sci.* (Special Issue on Z-Pinch Plasmas: August 1998 edited by J Davis and C Deeney;
    April 2002 edited by M R Douglas and R B Baksht)

[91] Spielman R B (ed) 2001 *Laser Part. Beams* **19** 321–595

[92] Folkierski A (ed) 1987 *Proc. Workshops on the Plasma Focus and Z pinch (Toledo, Spain)*
       Etlicher B (ed) 1988 *Proc. Workshops on the Plasma Focus and Z pinch (Nice, France)* (Earlier workshops in
       this series were exclusively concerned with the Plasma Focus)

[93] Haines M G 1965 *Adv. Phys.* **14** 167

[94] Grateau P 1978 *Phys. Fluids* **21** 1302

[95] Alfvén H 1939 *Phys. Rev.* **55** 425
       Lawson J D 1957 *J. Electron. Control* **3** 587

[96] Howell D Private communication

[97] Haines M G 1961 *Proc. Phys. Soc. Lond.* **77** 643
       In a later paper, Moses R W, Gerwin R A and Schoenberg K T 2001 *Phys. Plasmas* **8** 4839 solved a similar
       equation for heat flow to electrodes that supplied helicity to a toroidal plasma through current flow; again
       the voltage required was proportional to the maximum electron temperature, but thermoelectric terms were
       omitted

[98] Braginskii S I 1957 *Zh. Eksp.Teor. Fiz.* **33** 459
       Braginskii S I 1958 *Sov. Phys.—JETP* **6** 358
       Also in Leontovich M A (ed) 1963 *Voprosy Teorii Plasmy* (Moscow: Gosatomizdat)
       Reviews of Plasma Physics (New York: Consultants Bureau1965) vol 1, p 205

[99] Marshall W 1962 *An Introduction to Plasma Physics* (London: Pergamon) pp 227–9 (reported in
       Thompson W B)

[100] Epperlein E M and Haines M G 1986 *Phys. Fluids* **29** 1029

[101] Haines M G 1986 *Plasma Phys. Control. Fusion* **28** 1705

[102] Lawson J D 1957 *Proc. Phys. Soc. Lond.* **870** 6

[103] Haines M G 1960 *Proc. Phys. Soc. Lond.* **76** 250

[104] Hammel J E 1976 LA-6203-MS, Los Alamos Scientific Laboratory

[105] Braginskii S I and Shafranov V D 1959 *Plasma Physics and Problems of Controlled Thermonuclear Reactions*
       (London: Pergamon) vol 2, p 39

[106] Coppins M, Culverwell I D and Haines M G 1988 *Phys. Fluids* **31** 2688

[107] Coppins M, Chittenden J P and Culverwell I D 1992 *J. Phys. D: Appl. Phys.* **25** 178

[108] Fälthammer C G 1961 *Phys. Fluids* **4** 1145

[109] Scudder D W 1983 *Phys. Fluids* **26** 1330

[110] Haines M G 1959 *Proc. Phys. Soc. Lond.* **74** 576

[111] Rosenau P, Nebel R A and Lewis H R 1989 *Phys. Fluids* B **1** 1233

[112] Glasser A H 1989 *J. Comput. Phys.* **85** 159

[113] Chittenden J P and Haines M G 1993 *J. Phys. D: Appl. Phys.* **26** 1048

[114] Dreicer H 1958 *Proc. 2nd Int. Conf. on the Peaceful Uses of Atomic Energy (Geneva, Switzerland)* vol 31
       (Geneva: United Nations) p 57
       see also Dreicer H 1960 *Phys. Rev.* **117** 329

[115] Neff W *et al* 1980 *Phys. Lett.* A **79** 165
       see also Choi P, Deeney C and Wong C S 1988 *Phys. Lett.* **128** 80

[116] Pereira N R 1990 *Phys. Fluids* B **2** 677

[117] Shearer J W 1976 *Phys. Fluids* **19** 1426

[118] Vikhrev V V 1978 *JETP Lett.* **27** 95

[119] Vikhrev V V and Gureev K G 1978 *Sov. Phys.—Tech. Phys.* **23** 1295

[120] Vikhrev V V, Ivanov V V and Prut V V 1986 *Sov. J. Plasma Phys.* **12** 190

[121] Robson A E 1988 *Nucl. Fusion* **28** 2171

[122] Haines M G 1989 *Plasma Phys.Control. Fusion* **31** 759

[123] Chittenden J P, Power A J and Haines M G 1989 *Plasma Phys. Control. Fusion* **31** 1813

[124] Robson A E 1989 *Phys. Fluids* B **1** 1834

[125] Robson A E 1989 *Phys. Rev. Lett.* **63** 2816

[126] Thornhill W, Guiliani J L and Davis J 1989 *J. Appl. Phys.* **66** 4154

[127] Meirovich B E 1982 *Phys. Rep.* **92** 84
       A review of Meirovich's work is given by Stevens C B1985 *Int. J. Fusion Energy* **3** 76

[128] Meirovich B E 1986 *Usp. Fyz. Nauk* **149** 221
       Meirovich B E 1986 *Sov. Phys.—Usp* **29** 506

[129] Chittenden J P and Haines M G 1990 *Phys. Fluids* B **2** 1889

[130] Haines M G *et al* 2006 *Phys. Rev. Lett.* **96** 075003

[131] Bayley J M, Baldock P and Dangor A E 1989 *Dense Z-Pinches, AIP Conf. Proc.* **195** 481

see also Bayley J M 1991 *PhD Thesis* University of London

[132] Struve K W 1980 UCRL-52993 (*Thesis*) Lawrence Livermore Laboratory

[133] Culverwell I D and Coppins M 1990 *Phys. Fluids.* B **2** 129

[134] Cochran F L and Robson A E 1990 *Phys. Fluids* B **2** 123

[135] Shumlak U and Hartman C W 1995 *Phys. Rev. Lett.* **75** 3285

[136] Haines M G and Coppins M 1991 *Phys. Rev. Lett.* **66** 1462

[137] Lehnert B 1952 *Ark. Fys.* **5** 69

[138] Lundqvist S 1952 *Ark. Fys.* **5** 297

[139] Spitzer L and Härm R 1953 *Phys. Rev.* **89** 977

[140] Chew G F, Goldberger M L and Low F E 1956 *Proc. R. Soc. Lond.* **236** 112

[141] Weibel E S 1959 *Phys. Rev. Lett.* **2** 83

[142] Freidberg J P 1982 *Rev. Mod. Phys.* **54** 801

[143] Bernstein I B, Frieman E A, Kruskal M D and Kulsrud R M 1958 *Proc. R. Soc.* A **244** 17

[144] Goedbloed J P 1979 *Lecture Notes on Ideal Magnetohydrodynamics* (Nieuwegeun, The Netherlands: FOM—Instituut voor Plasmafysica)

[145] Hain K and Lüst R 1958 *Z. Naturf.* a **13** 936

[146] Kanellopoulos S, Coppins M and Haines M G 1988 *J. Plasma Phys.* **39** 521

[147] Appert K, Gruber R and Vaclavik J 1974 *Phys. Fluids* **17** 1471

[148] Bateman G 1978 *MHD Instabilities* (Cambridge, MA: MIT Press)

[149] Coppins M 1988 *Plasma Phys. Control. Fusion* **30** 201

[150] Goedbloed J P and Sakanaka P H 1974 *Phys. Fluids* **17** 908

[151] Hammel J E and Scudder D W 1987 *Proc. 14th Eur. Conf. on Controlled Fusion and Plasma Physics* (Petit-Lancy: European Physical Society) part 2, p 450

[152] Sethian J D, Robson A E, Gerber K A and DeSilva A W 1987 *Phys. Rev. Lett.* **59** 892
Sethian J D, Robson A E, Gerber K A and DeSilva A W 1987 *Phys. Rev. Lett.* **59** 1790

[153] Culverwell I D and Coppins M 1989 *Plasma Phys. Control. Fusion* **31** 1443

[154] Cochran F L and Robson A E 1990 *Phys. Fluids* B **2** 2270

[155] Lampe M 1991 *Phys. Fluids* B **3** 1521

[156] Neudachin V V and Sasarov P V 1991 *Nucl. Fusion* **31** 1053
see also Neudachin V V and Sasarov P V 1993 *Nucl. Fusion* **33** 475

[157] Coppins M and Culverwell I D 1997 Dense Z-pinches *AIP Conf. Proc.* **409** 589

[158] Haines M G 1974 *J. Plasma Phys.* **12** 1

[159] Spies G O 1988 *Plasma Phys. Control. Fusion* **30** 1025

[160] Cox P M 1990 *Plasma Phys. Control. Fusion* **32** 553

[161] Cochran F L and Robson A E 1993 *Phys. Fluids* B **5** 2905

[162] Lindemuth I R 1990 *Phys. Rev. Lett.* **65** 179
see also Lindemuth I R 1989 *Phys. Rev. Lett.* **62** 264
Sheehey P 1992 *Phys. Fluids* B **4** 3698

[163] Gomberoff L and Hernández M 1986 *Phys. Rev.* A **27** 1244

[164] Gomberoff L 1983 *Phys. Rev.* A **28** 125

[165] Robinson B B and Bernstein I B 1963 *Ann. Phys.* **18** 110

[166] Velikhov E P 1963 *Atomnaya Energiya* **14** 573
Velikhov E P 1964 *J. Nucl. Energy* C **6** 203

[167] Rosenbluth M N and Simon A 1965 *Phys. Fluids* **8** 1300

[168] Bowers E A and Haines M G 1968 *Phys. Fluids* **11** 2695

[169] Bowers E A and Haines M G 1971 *Phys. Fluids* **14** 165

[170] Akerstedt H O 1990 *J. Plasma Phys.* **44** 507

[171] Coppins M 1989 *Phys. Fluids* B **1** 591

[172] Coppins M, Bond D J and Haines M G 1984 *J. Plasma Phys.* **32** 1

[173] Coppins M and Scheffel J 1992 *Phys. Fluids* B **4** 3251

[174] Scheffel J and Coppins M 1993 *Nucl. Fusion* **33** 101

[175] Tayler R J 1962 *Nucl. Fusion Suppl.* Pt. **3** 887

[176] Schaper U 1983 *J. Plasma Phys.* **29** 1

[177] Schaper U 1983 *J. Plasma Phys.* **30** 169

[178] Coppins M, Bond D J and Haines M G 1984 *Phys. Fluids* **27** 2886

[179] Seyler C E and Freidberg J P 1980 *Phys. Fluids* **23** 331

[180] Freidberg J P 1972 *Phys. Fluids* **15** 1102

[181] Arber T D and Coppins M 1989 *Phys. Fluids* B **1** 2289

[182] Haines M G *et al* 1987 *IAEA Plasma Physics and Controlled Nuclear Fusion Research 1986, Proc. Int. Conf. (Kyoto, Japan, 13–20 November 1986)* (Vienna: IAEA) **2** 573

[183] Haines M G and Kassapakis N G 1998 *IEEE Trans. Plasma Sci.* **26** 1208

[184] Arber T D and Howell D F 1996 *Phys. Rev. Lett.* **76** 2198

[185] Shumlak U and Hartman C W 1996 *Phys. Rev. Lett.* **76** 2199

[186] Zhang Y and Ding N 2006 *IAEA Fusion Energy Ser.* **IF** P5-13

[187] Zhang Y and Ding N 2006 *Phys. Plasmas* **13** 62703

[188] Shumlak U, Colingo R P, Nelson B A and Den-Hartog 2001 *Phys. Rev. Lett.* **87** 205005; see also [523]

[189] Haines M G 2001 *Phys. Rev. Lett.* **87** 135005

[190] Najmudin Z *et al* 2001 *Phys. Rev. Lett.* **87** 215004

[191] Suydam B R 1958 *Proc. 2nd UN Conf. on Peaceful Uses of Atomic Energy (Geneva, Switzerland)* vol 31 (Geneva: United Nations) p 157

[192] Newcomb W A 1960 *Ann. Phys.* **10** 232

[193] Wright R J, Pott D F R and Haines M G 1976 *Plasma Phys.* **18** 1

[194] Delzanno G L *et al* 2007 *Phys. Plasmas* **14** 092901
Delzanno G L and Finn J M 2008 *Phys. Plasmas* **15** 032904
Ryutov D D, Cohen R H and Pearlstein 2004 *Phys. Plasmas* **11** 4740

[195] Artsimovich L A 1964 *Controlled Thermonuclear Reactions* (London: Oliver & Boyd) p 178

[196] Aparicio J, Haines M G, Hastie R J and Wainwright J P 1998 *Phys. Plasmas* **5** 3180
see also Uzdensky D A and Kulsrud R M 1998 *Phys. Plasmas* **5** 3249

[197] Chittenden J P *et al* 1997 *Phys. Plasmas* **4** 4309

[198] Chittenden J P *et al* 1997 *Phys. Plasmas* **4** 2967

[199] Psimopoulos M and Haines M G 1986 *Plasma Phys. Control. Fusion* **28** 917

[200] Coppins M 1993 *Nucl. Fusion* **33** 1715

[201] Taylor J B 1974 *Phys. Rev. Lett.* **33** 1139
see also Taylor J B 1986 *Rev. Mod. Phys.* **58** 741

[202] Arber T D 1996 *Phys. Rev. Lett.* **77** 1766

[203] Zdravkovic D, Coppins M and Bell A R 2001 *Phys. Plasmas* **8** 564
see also Zdravkovic D, Bell A and Coppins M 1997 *Dense Z-Pinches, AIP Conf. Proc.* **409** 265

[204] Begelman M C, Blandford R D and Rees M J 1984 *Rev. Mod. Phys.* **56** 255

[205] Appl S and Camenzind C 1992 *Astron. Astrophys.* **355** 818
Appl S and Camenzind C 1992 *Astron. Astrophys.* **256** 354

[206] Bell A R and Lucek S G 1995 *Mon. Not. R. Astron. Soc.* **277** 1327

[207] Lucek S G and Bell A R 1996 *Mon. Not. R. Astron. Soc.* **281** 245

[208] Lucek S G and Bell A R 1998 *Mon. Not. R. Astron. Soc.* **290** 327

[209] Haines M G 1997 *Dense Z-Pinches, AIP Conf. Proc.* **409** 27

[210] Furth H P, Rosenbluth M N, Rutherford P H and Stodiek W 1970 *Phys. Fluids* **13** 3020

[211] Kerrebrock J 1964 *AIAA J.* **2** 6

[212] Nelson A H and Haines M G 1969 *Plasma Phys.* **11** 811

[213] Dixon R H, Düchs D F and Elton R C 1973 *Phys. Fluids* **16** 1762

[214] Haines M G 1981 *Phys. Rev. Lett.* **47** 917

[215] Kho T M, Bond D J and Haines M G 1983 *Phys. Rev.* A **28** 3156

[216] Willi O and Rumsby P T 1981 *Opt. Commun.* **37** 45

[217] Borghesi M *et al* 2001 *Plasma Phys. Control. Fusion* **43** A267

[218] Lebedev S V *et al* 2000 *Phys. Rev. Lett.* **85** 98

[219] Jones B *et al* 2005 *Phys. Rev. Lett.* **95** 225001

[220] Jones B *et al* 2006 *Phys. Plasmas* **13** 056313

[221] Buneman O 1962 *Plasma Phys.* **4** 111

[222] Ashby D E T F and Paton A 1967 *Plasma Phys.* **9** 359

[223] Krall N A and Liewer P C 1971 *Phys. Rev.* A **4** 2094

[224] Davidson R C and Gladd N T 1975 *Phys. Fluids* **18** 1327

[225] Huba J D and Papadopoulos K 1978 *Phys. Fluids* **21** 121

[226] Winske D and Liewer P C 1978 *Phys. Fluids* **21** 1017

[227] Davidson R C 1978 *Phys. Fluids* **21** 1375

[228] Drake J F *et al* 1984 *Phys. Fluids* **27** 1148

[229] Brackbill J U *et al* 1984 *Phys. Fluids* **27** 2682

[230] Haines M G 2002 *IEEE Trans. Plasma Sci.* **30** 588

[231] Chittenden J P *et al* 1999 *Phys. Rev. Lett.* **83** 100

[232] Chittenden J P 1995 *Phys. Plasmas* **2** 1242
[233] Peterson D L *et al* 1999 *Phys. Plasmas* **6** 2178
[234] Douglas M R *et al* 2000 *Phys. Plasmas* **7** 1935
[235] Rudakov L I *et al* 2000 *Phys. Rev. Lett.* **84** 3326
[236] Sotnikov V I *et al* 2008 *Commun. Comput. Phys.* **4** 611
       see also Sotnikov V I *et al* 2005 *Phys. Plasmas* **12** 092701
[237] Takeda Y and Inuzuka H 2000 *Phys. Lett.* A **265** 282
[238] Barnard A *et al* 1979 *Plasma Physics Controlled Nuclear Fusion Research 1978 (Innsbruch)* vol 2 (Vienna:
       IAEA) p 159
[239] Maisonnier Ch and Rager J P 1979 *3rd Int. Conf. on High Power Electron and Ion Beams and Technology* vol 1
       (Novosibirsk: Institute of Nuclear Physics) p 233
[240] Schmidt H and the Poseidon Team 1983 *Proc. 3rd Int. Workshop on Plasma Focus Research (Stuttgart,
       Germany)* p 107
[241] Trubnikov B A 1986 *Sov. J. Plasma Phys.* **12** 271
[242] Deutch R and Kies W 1988 *Plasma Phys. Control. Fusion* **30** 921
[243] Haines M G 1983 *Nucl. Instrum. Methods* **207** 179
[244] Nardi V 1979 *Plasma Physics and Controlled Nuclear Fusion Research (Innsbruck, 1978)* vol 2 (Vienna:
       IAEA) p 143
[245] Filippov N V 1979 *Sov. Phys.—JETP* **49** 785
[246] Vikhrev V V 1986 *Sov. J. Plasma Phys.* **12** 262
[247] Mitchell I H *et al* 1998 *IEEE Trans. Plasma Sci.* **26** 1267
[248] Kassapakis N 2000 *PhD Thesis* University of London
[249] Yan'kov V V 1991 *Sov. J. Plasma Phys.* **17** 305
[250] Tiseanu I and Mandache N 1994 *Dense Z-Pinches, AIP Conf. Proc.* **299** 356
[251] Lindman E L, Rickard G and Haines M G 1983 *Proc. 11th European Conf. on Controlled Fusion and Plasma
       Physics (Aachen, Germany)* vol 7D pt 2, p 351, paper B-20
[252] Vekshtein G E and Sagdeev R Z 1970 *JETP Lett.* **9** 194
[253] Haines M G 2001 *Laser Part. Beams* **19** 345
[254] Beg F N *et al* 1997 *Plasma Phys. Control. Fusion* **39** 1
[255] Forrest M J, Kirk R E, Muir D G and Peacock N J 1983 *Proc. 11th European Conf. on Controlled Fusion and
       Plasma Physics (Aachen, Germany)* vol 1, p 571
[256] Rosenbluth M, Garwin R and Rosenbluth A 1954 LA-1850 Los Alamos Scientific Laboratory
       see also Miyamoto T 1984 *Nucl. Fusion* **24** 337 who included a plasma temperature in a thin layer to conserve
       energy
[257] Allen J E 1957 *Proc. Phys. Soc. Lond.* B **70** 24
[258] Jukes J D 1958 AERE GP/R 2293, Atomic Energy Research Establishment, Harwell, UK
[259] Von Guderley G 1942 *Luftfahrtforschung* **19** 301
[260] Reynolds J A and Quinn J M P 1961 *J. Nucl. Energy* C **3** 135
[261] Potter D E 1978 *Nucl. Fusion* **18** 813
[262] Kuwabara S 1963 *J. Phys. Soc. Japan* **18** 713
[263] Katzenstein J 1981 *J. Appl. Phys.* **52** 676
[264] Hain K, Hain G, Roberts K V, Roberts S J and Koppendorer W 1960 *Z. Naturf.* a **15** 1039
[265] Roberts K V and Potter D E 1970 *Methods in Computational Physics* vol 9 (New York: Academic) p 339
[266] Potter D E 1971 *Phys. Fluids* **14** 1911
[267] Tayler R J 1960 *Rev. Mod. Phys.* **32** 907
[268] Hopkins D (unpublished report, Imperial College)
[269] Wilkins M L 1980 *J. Comput. Phys.* **36** 281
[270] Harned D S and Kerner N 1985 *J. Comput. Phys.* **60** 62
[271] Culverwell I D *et al* 1989 *Plasma Phys. Control. Fusion* **31** 387
[272] Jones I R *et al* 1980 *Plasma Phys.* **22** 501
[273] Lee K-T, Kim D-E and Kim S-H 2000 *Phys. Rev. Lett.* **85** 3834
[274] Boggasch E P *et al* 1991 *IEEE Trans. Plasma Sci.* **19** 866
[275] Kumpf C *et al* 1996 *Phys. Plasma* **3** 922
[276] Kvartskhava I F *et al* 1971 *Nucl. Fusion* **11** 349
[277] Butov I Ya *et al* 1981 *Sov. Phys.—JETP* **54** 299
[278] Lord Rayleigh 1883 *Proc. Lond. Math. Soc.* **14** 170
[279] Latham R, Nation J A, Curzon F L and Folkierski A 1960 *Nature* **186** 624
[280] Haines M G 1998 *IEEE Trans. Plasma Sci.* **26** 1275

[281] Rosenbluth M and Longmire C L 1957 *Ann. Phys.* **1** 120
[282] Takabe H, Mima K, Montierth L and Morse R L 1985 *Phys. Fluids* **28** 3678
[283] Betti R, Goncharov V N, McCrory R L and Verdon C P 1998 *Phys. Plasmas* **5** 1446
[284] Lobatchev V and Betti R 2000 *Phys. Rev. Lett.* **85** 4522
[285] Shumlak U and Roderick N F 1998 *Phys. Plasmas* **5** 2384
[286] Hammer J H and Ryutov D D 1996 *UCRL-JC-122848* report
[287] Douglas M R, Deeney C and Roderick 1997 *Phys. Rev. Lett.* **78** 4577
[288] Rosenbluth M N, Rostoker N and Krall N A 1962 *Nucl. Fusion Suppl.* **1** 143
[289] Hassam A B and Huba J D 1987 *Geophys. Res. Lett.* **14** 60
[290] Lehnert B and Scheffel J 1988 *Phys. Rev. Lett.* **61** 897
[291] Ryutov D D 1996 *Phys. Plasmas* **3** 4336
[292] Bud'ko A B *et al* 1989 *Phys. Fluids* B **1** 598
[293] Felber F S *et al* 1987 *Megagauss Technology and Pulsed Power Applications* (New York: Plenum) p 117
[294] Felber F S *et al* 1988 *Phys. Fluids* **31** 2053
[295] Hall G N *et al* 2008 *Phys. Rev. Lett.* **100** 065003
[296] Velikovich A L, Cochran F L and Davis J 1996 *Phys. Rev. Lett.* **77** 853
[297] Richtmyer R D 1960 *Commun. Pure Appl. Math* **13** 297
[298] Meshkov E E 1969 *Izv. Akad. Nauk. SSSR Meckh. Zhidk. Gaza* **5** 151
[299] Bud'ko A B and Liberman M A 1992 *Phys. Fluids* B **4** 3499
[300] Folkierski A and Latham R 1963 *Phys. Fluids* **6** 1780
[301] Gol'berg S M and Velikovich A L 1993 *Phys. Fluids* B **5** 1164
[302] Baksht R B, Luchinsky A V and Fedyunin A V 1990 *Sov. Phys.—Tech. Phys.* **37** 1118
[303] Cochran F L, Davis J and Velikovich A L 1995 *Phys. Plasmas* **2** 2765
[304] Sharp D E 1984 *Physica* D **12** 3
[305] Youngs D L 1984 *Physica* D **12** 32
[306] Youngs D L 1989 *Physica* D **37** 270
[307] Read K I 1984 *Physica* D **12** 45
[308] Town R W P and Bell A R 1991 *Phys. Rev. Lett.* **67** 1863
[309] Henshaw M J de C, Pert G J and Youngs D L 1987 *Plasma Phys. Control. Fusion* **29** 405
[310] McCrory R L, Montierth L, Morse R L and Verdon C P 1981 *Phys. Rev. Lett.* **46** 336
[311] Ott E 1972 *Phys. Rev. Lett.* **29** 1429
[312] Basco M M 1994 *Phys. Plasmas* **1** 1270
[313] Infeld E and Rowlands G 1988 *Phys. Rev. Lett.* **60** 2273
[314] Lebedev S V *et al* 1998 *Phys. Rev. Lett.* **81** 4152
[315] Haines M G, Sanford T W L and Smirnov V P 2005 *Plasma Phys. Control. Fusion* **47** B1
[316] Benjamin J *et al* 1981 *Appl. Phys. Lett.* **35** 849
[317] Baksht R B *et al* 1983 *Pis. Zh. Tekh. Fiz.* **9** 1192
[318] Baksht R B *et al* 1983 *Sov. J. Tech. Phys. Lett.* **9** 512
[319] Aivazov I K *et al* 1988 *Sov. J. Plasma Phys.* **14** 110
[320] Balehtev M V *et al* 1989 *Sov. Phys.—JETP* **68** 955
[321] Peterson D L *et al* 1998 *Phys. Plasmas* **5** 3302
[322] Lebedev S V *et al* 2002 *Phys. Plasmas* **9** 2293
[323] Cuneo M E *et al* 2005 *Phys. Rev.* E **71** 046406
[324] Chittenden J P *et al* 2004 *Plasma Phys. Control. Fusion* **46** B457
[325] Lebedev S V *et al* 2000 *Phys. Rev. Lett.* **84** 1708
[326] Cuneo M E *et al* 2005 *Phys. Rev. Lett.* **94** 225003
[327] Chittenden J P *et al* 2001 *Phys. Plasmas* **8** 675
[328] Vikhrev V V, Ivanov V V and Rozanova G A 1993 *Nucl. Fusion* **33** 311
[329] Lovberg R H, Riley R A and Shlachter J S 1993 *AIP Conf. Proc.* **299** 59
[330] Riley R A, Scudder D, Shlachter J and Lovberg R 1996 *Phys. Plasmas* **3** 1314
[331] Rudakov L I and Sudan R N 1997 *Phys. Rep.* **283** 253
[332] Velikovich A L *et al* 2000 *Phys. Plasmas* **7** 3265
[333] Pikuz S A *et al* 1999 *Phys. Rev. Lett.* **83** 4313
[334] Sinars D B *et al* 2001 *Phys. Plasmas* **8** 216
       see also Sinars D B *et al* 2000 *Phys. Plasmas* **7** 1555
[335] Douglass J D *et al* 2007 *Phys. Plasmas* **14** 012704
[336] Chittenden J P *et al* 2000 *Phys. Rev.* E **61** 4370
[337] Shelkovenko T A *et al* 2007 *Phys. Plasmas* **14** 102702

[338] Yu E P *et al* 2007 *Phys. Plasmas* **14** 022705
[339] Alexandrov V V *et al* 2001 *Plasma Phys. Rep.* **27** 89
[340] Desjarlais M P, Kress J D and Collins C A 2002 *Phys. Rev.* E **66** 025401
       see also DeSilva A W and Katsouros J D 1998 *Phys. Rev.* E **57** 5945
[341] Kirkpatrick S 1973 *Rev. Mod. Phys.* **45** 574
[342] Bland S N, Lebedev S V Chittenden J P and Haines M G 2002 *Dense Z-Pinches*, *AIP Conf. Proc.* **651** 75
[343] Nasilowski J 1964 Unduloids and striated disintegration of wires *Exploding Wires* vol 3, ed W G Chase and
       H K Moore (New York: Plenum) p 295
[344] Graneau P 1983 *Phys. Lett.* A **97** 253
       Graneau P 1984 *J. Appl. Phys.* **55** 2598
       Graneau P 1984 *IEEE Trans. Magn.* **20** 444
       Graneau P 1987 *Phys. Lett.* A **120** 77
[345] Molokov S and Allen J E 1997 *J. Phys. D: Appl. Phys.* **30** 3131
[346] Lebedev S V and Savvatimskii A I 1984 *Sov. Phys.—Usp.* **27** 749
[347] Volkov N B, Zubarev N M and Iskol'dskii A M 1996 *JETP* **82** 228
       see also Oreshkin V I 2008 *Phys. Plasmas* **15** 092103
[348] Lebedev S V *et al* 1999 *Phys. Plasmas* **6** 2016
[349] Haines M G *et al* 2000 *Phys. Plasmas* **7** 1672
[350] Benjamin R F, Pearlman J S, Chu E Y and Riordan J C 1981 *Appl. Phys. Lett.* **39** 848
[351] Sherlock M, Chittenden J P, Lebedev S V and Haines M G 2004 *Phys. Plasmas* **11** 1609
[352] Lebedev S V *et al* 2001 *Laser Part. Beams* **19** 355
[353] Ratakhin N A and Baksht R B 2001 *IEEE Trans. Plasma Sci.* **29** 512
[354] Bott S *et al* 2006 *Phys. Rev.* E **74** 046403
[355] Haines M G 2003 *Plasma Phys. Rep.* **29** 586
[356] Resler E L and Sears W R 1958 *ZAMP* **96** 509
       also Resler E L and Sears W R 1958 *J. Aeronaut. Sci* **25** 235
[357] Haines M G and Thompson W B 1963 Optimisation of flowing plasma and external circuit interaction
       Propagation and Instabilities in Plasmas ed W I Futterman (CA: Stanford University Press) p 115
[358] Chittenden J P, Lebedev S V, Oliver B V, Yu E P and Cuneo M E 2004 *Phys. Plasmas* **11** 1118
[359] Chittenden J P *et al* 2001 *Laser Particle Beams* **19** 323
       see also Chittenden J P *et al* 2001 *Phys. Plasmas* **8** 2305
[360] Garasi C J *et al* 2004 *Phys. Plasmas* **11** 2729
[361] Sasorov P V *et al* 2008 *Phys. Plasmas* **15** 022702
[362] Beg F N *et al* 2002 *Phys. Plasmas* **9** 375
[363] Lebedev S V *et al* 2005 *Plasma Phys. Control. Fusion* **47** A91
[364] Sarkisov G S, Rosenthal S E and Struve K W 2008 *Phys. Rev.* E **77** 056406
[365] Coverdale C A *et al* 2002 *Phys. Rev. Lett.* **88** 065001
[366] Mazarakis M G *et al* 2002 *Bull. Am. Phys. Soc.* **47** 4313
       see also Mazarakis M G *et al* 2009 *Phys. Rev.* E **79** 016412
[367] Lemke R W 2009 *Phys. Rev. Lett.* **102** 025005
[368] Beg F N *et al* 2002 *IEEE Trans. Plasma Sci.* **30** 552
[369] Coverdale C A *et al* 2009 *Phys. Rev. Lett.* **102** 155006
[370] Bland S N *et al* 2005 *Phys. Rev. Lett.* **95** 135001
[371] Chittenden J P and Jennings C A 2008 *Phys. Rev. Lett.* **101** 055005
[372] Frese M H *et al* 2002 *IEEE Trans. Plasma. Sci.* **30** 593
[373] Knapp P F *et al* 2010 *Phys. Plasmas* **17** 012704
[374] Hall G N *et al* 2008 *Dense Z-Pinches, AIP Conf. Proc.* **1088** 89
[375] Jones B *et al* 2004 *Rev. Sci. Instrum.* **75** 5030
[376] Lebedev S V *et al* 2004 *Nucl. Fusion* **44** S215
[377] Sanford T W L *et al* 2002 *Phys. Plasmas* **9** 3573
[378] Felber F S and Rostoker N 1981 *Phys. Fluids* **24** 1049
[379] Marder B M, Sanford T W L and Allshouse G O 1998 *Phys. Plasmas* **5** 2997
[380] Hammer J H and Ryutov D D 1999 *Phys. Plasmas* **6** 3302
[381] Ivanov V V *et al* 2006 *Phys. Rev. Lett.* **97** 125001
[382] Terry R E, Davis J, Deeney C and Velikovich A L 1999 *Phys. Rev. Lett.* **83** 4305
[383] Bland S N *et al* 2003 *Phys. Plasmas* **10** 1100
[384] Sanford T W L *et al* 2007 *Phys. Plasmas* **14** 052703
[385] Hall G N *et al* 2006 *Phys. Plasmas* **13** 082701

[386] Deeney C *et al* 1999 *Phys. Plasmas* **6** 3576
[387] Apruzese J P *et al* 2001 *Phys. Plasmas* **8** 3799
[388] Coverdale C A *et al* 2008 *Phys. Plasmas* **15** 023107
[389] Haines M G 2006 *Dense Z-Pinches: 6th Int. Conf. Dense Z-Pinches* ed J Chittenden *AIP Conf. Proc.* **808** 347
[390] Waisman E M *et al* 2004 *Phys. Plasmas* **11** 2009
[391] Atzeni S, Caruso A and Pais V A 1986 *Laser Part. Beams* **4** 393
[392] Lee Y T and More R M 1984 *Phys. Fluids* **27** 1273
[393] Brown S and Haines M G 1997 *J. Plasma Phys.* **58** 577
[394] Brown S and Haines M G 1999 *J. Plasma Phys.* **62** 129
[395] Haines M G 2008 *Dense Z-Pinches*, *AIP Conf. Proc.* **1088** 57
[396] Vikhrev V V, Ivanov V V and Koshelev K N 1982 *Sov. J. Plasma Phys.* **8** 688
[397] Maxon S *et al* 2004 *Phys. Plasmas* **11** 1897
[398] Sotnikov V I *et al* 2006 *IEEE Trans. Plasma Sci.* **34** 2239
[399] Sotnikov V I *et al* 2004 *Phys. Plasmas* **11** 1897
[400] Apruzese J P *et al* 2005 *Phys. Plasmas* **12** 062501
[401] Whitney K G *et al* 2004 *Phys. Plasmas* **11** 3700
[402] Lemke R W 2008 *Lecture at 7th Int. Conf. on Dense Z-Pinches (Alexandria, MD, USA)*
[403] Apruzese J P *et al* 2002 *Phys. Plasmas* **9** 2411
[404] Davis J *et al* 2001 *Laser Part. Beams* **19** 557
[405] Sarkisov G S *et al* 2002 *Phys. Rev.* E **66** 046413
[406] Johnson D J *et al* 2006 *IEEE Trans. Dielectr. Electr. Insul.* **13** 52
[407] Sanford T W L *et al* 2007 *Phys. Rev. Lett.* **98** 065003
[408] Sanford T W L *et al* 2005 *Phys. Plasmas* **12** 022701
[409] Sanford T W L *et al* 2005 *Phys. Plasmas* **12** 122701
[410] Sanford T W L *et al* 2003 *Phys. Plasmas* **10** 1187
[411] Sinars D B *et al* 2000 *Phys. Plasmas* **7** 429
[412] Cuneo M E 1999 *IEEE Trans. Dielectr. Electr. Insul.* **6** 469
[413] Bland S N *et al* 2007 *Phys. Plasmas* **14** 056315
[414] Sinars D B *et al* 2004 *Phys. Rev. Lett.* **93** 145002
[415] Yu E P *et al* 2008 *Phys. Plasmas* **15** 056301
[416] Kantsyrev V L *et al* 2006 *IEEE Trans. Plasma Sci.* **34** 194
[417] Kantsyrev V L *et al* 2006 *IEEE Trans. Plasma Sci.* **34** 2295
[418] Ivanov V V *et al* 2006 *Phys. Plasmas* **13** 012704
[419] Ivanov V V *et al* 2007 *Phys. Plasmas* **14** 032703
[420] Jones B *et al* 2008 *Dense Z-Pinches, AIP Conf. Proc.* **1088** 109
[421] Kantsyrev V L *et al* 2008 *Dense Z-Pinches, AIP Conf. Proc.* **1088** 113
[422] Kantsyrev V L *et al* 2008 *Phys. Plasmas* **15** 030704
[423] Ivanov V V *et al* 2008 *Phys. Rev. Lett.* **100** 025004
[424] Ivanov V V *et al* 2008 *Dense Z-Pinches, AIP Conf. Proc.* **1088** 95
[425] Esaulov A A *et al* 2008 *Phys. Plasmas* **15** 052703
[426] Yadlowsky E J *et al* 1996 *Phys. Plasmas* **3** 1745
[427] Beg F N, Ruiz-Camacho J, Haines M G and Dangor A E 2004 *Plasma Phys. Control. Fusion* **46** 1
[428] Olson C L 2004 *Z-Pinch Inertial Fusion Energy: Landholt–Bornstein Handbook on Energy Technolgies* ed K Heinloth (Berlin: Springer)
[429] Leeper R J *et al* 1999 *Nucl. Fusion* **39** 1283
[430] Melhorn T A *et al* 2003 *Plasma Phys. Control. Fusion* **45** A325
[431] Sanford T W L *et al* 2000 *Phys. Plasmas* **7** 4669
[432] Sanford T W L *et al* 2004 *Plasma Phys. Control. Fusion* **46** B423
[433] Sanford T W L *et al* 2001 *Laser Part. Beams* **19** 541
[434] Slutz S A *et al* 2003 *Phys. Plasmas* **10** 1875
[435] Bailey J E *et al* 2004 *Phys. Rev. Lett.* **92** 085002
[436] Ruiz C L *et al* 2004 *Phys. Rev. Lett.* **93** 015001
[437] Rochau G A *et al* 2007 *Plasma Phys. Control. Fusion* **49** B591
[438] Rochau G A *et al* 2008 *Phys. Rev. Lett.* **100** 125004
[439] Sanford T W L, Lemke R W, Mock R C and Peterson D L 2003 *Phys. Plasmas* **10** 3252
[440] Bailey J E *et al* 2006 *Phys. Plasmas* **13** 056301
[441] Slutz S A *et al* 2006 *Phys. Plasmas* **13** 102701

Slutz S A *et al* 2001 *Phys. Plasmas* **8** 1673

[442] Palmer J B A *et al* 2008 *IEEE Trans. Plasma Sci.* **36** 1272

[443] Lemke R W *et al* 2005 *Phys. Plasmas* **12** 012703

[444] Sanford T W L *et al* 1999 *Phys. Rev. Lett.* **83** 5511

[445] Sanford T W L *et al* 1999 *Phys. Plasmas* **6** 1270

[446] Sanford T W L *et al* 1999 *Phys. Plasmas* **6** 2030

[447] Olsen R E *et al* 1999 *Fusion Technol.* **35** 260

[448] Lemke R W *et al* 2003 *Phys. Plasmas* **10** 1092

[449] Apruzese J P *et al* 2007 *Phys. Plasmas* **14** 042702

[450] Sanford T W L *et al* 2003 *Phys. Plasmas* **10** 4790

[451] Olson R E *et al* 2001 *Rev. Sci. Instrum.* **72** 1214

[452] Sanford T W L *et al* 2008 *IEEE Trans. Plasma Sci.* **36** 22

[453] Hammer J H *et al* 1999 *Phys. Plasmas* **6** 2129

[454] Lemke R W 2008 private communication

[455] Vesey R A *et al* 2007 *Phys. Plasmas* **14** 056302

[456] Cuneo M E *et al* 2002 *Phys. Rev. Lett.* **88** 215004

[457] Hanson D L *et al* 2002 *Phys. Plasmas* **9** 2173

[458] Vesey R A *et al* 2008 *Phys. Plasmas* **15** 042704

[459] Cuneo M E *et al* 2001 *Laser Part. Beams* **19** 481

[460] Stygar W A, Olson R E, Spielman R B and Leeper R J 2001 *Phys. Rev. E* **64** 026410

[461] Slutz S A and Vesey R A 2005 *Phys. Plasmas* **12** 062702

[462] Cuneo M E *et al* 2006 *Plasma Phys. Control. Fusion* **48** R1

[463] Olson C *et al* 2005 *Fusion Sci. Technol.* **47** 633

[464] Rochau G E *et al* 2005 *Fusion Sci. Technol.* **47** 641

[465] Slutz S A, Olson C L and Peterson P 2003 *Phys. Plasmas* **10** 429

[466] Rose D V *et al* 2010 *Phys. Rev. Spec. Top.—Accel. Beams* **13** 010402

[467] Stygar W A *et al* 1997 *Proc. 11th IEEE Int. Pulsed Power Conf. (Baltimore, MD, USA)* p 591

[468] Stygar W A *et al* 2005 *Phys. Rev. E* **72** 026404

[469] Douglas M R *et al* 2000 *Phys. Plasmas* **7** 2945

[470] Calamy H *et al* 2006 *IEEE Trans. Plasma Sci.* **34** 2279

[471] Calamy H *et al* 2008 *Phys. Plasmas* **15** 012701

[472] Welch D R *et al* 2008 *Phys. Rev. Spec. Top.—Accel. Beams* **11** 030401

[473] Stygar W A *et al* 2007 *Phys. Rev. Spec. Top.—Acce. Beams* **10** 030401

[474] Stygar W A *et al* 2006 *Phys. Rev. Spec. Top.—Accel. Beams* **9** 090401

[475] Stygar W A *et al* 2009 *Phys. Rev. Spec. Top.—Accel. Beams* **12** 030402

[476] Mazarakis M G *et al* 2010 *IEEE Trans. Plasma Sci.* **38** 704
see also Mazarakis M G *et al* 2009 *Phys. Rev. Spec. Top.—Accel. Beams* **12** 050401

[477] Bott S C *et al* 2010 *IEEE Trans. Plasma Sci.* **38** 567

[478] Gilgenbach R M 2009 *Dense Z-Pinches, AIP Conf. Proc.* **1088** 259

[479] Chuvatin A V *et al* 2009 *Dense Z-Pinches, AIP Conf. Proc.* **1088** 253

[480] Heflinger L O and Leonard S L 1961 *Phys. Fluids* **4** 406

[481] Folkierski A, Frayne P G and Latham R 1962 *Nucl. Fusion Suppl.* Part 2, 627

[482] Gross R A 1965 *Rev. Mod. Phys.* **37** 724

[483] Kogelschatz U *et al* 1968 *Z. Naturf.* **23** 514

[484] Kleist G *et al* 1969 *Z. Naturf.* **24** 226

[485] Choi P *et al* 1979 *Plasma Physics Controlled Nuclear Fusion Research 1979* vol II (Vienna: IAEA) p 69

[486] Baldock P *et al* 1979 *IOP Plasma Physics Conf. (Oxford)* unpublished paper; results contained in the review [84]

[487] Sze H *et al* 2005 *Phys. Rev. Lett.* **95** 105001

[488] Levine J S *et al* 2006 *Phys. Plasmas* **13** 082702

[489] Sze H *et al* 2007 *Phys. Plasmas* **14** 056307

[490] Shiloh J H 1978 *PhD Dissertation* University of California, Irvine. See also [49]

[491] Spielman R B *et al* 1998 *National Technical Information Service, Document number* SAND 98-0705 (Springfield, VA, 22161)

[492] Coverdale C A *et al* 2007 *Phys. Plasmas* **14** 022706

[493] Coverdale C A *et al* 2007 *Phys. Plasmas* **14** 056309

[494] Velikovich A L *et al* 2007 *Phys. Plasmas* **14** 022701

[495] Welch D R *et al* 2009 *Phys. Rev. Lett.* **103** 255002

[496] Velikovich A L,Whitney K G and Thornhill 2001 *Phys. Plasmas* **8** 4524
[497] Kroupp E *et al* 2007 *Phys. Rev. Lett.* **98** 115001
[498] Wong K L *et al* 1998 *Phys. Rev. Lett.* **80** 2334
[499] Labetsky A U *et al* 2002 *IEEE Trans. Plasma Sci.* **30** 524
[500] Menikoff R *et al* 1977 *Phys. Fluids* **20** 2000
[501] Douglas M R, Deeney C and Roderick N F 1998 *Phys. Plasmas* **5** 4183
[502] McCall G H 1989 *Phys. Rev. Lett.* **62** 1986
[503] Zakaullah M, Akhtar I, Murtaza G and Waheed A 1999 *Phys. Plasmas* **6** 3188
[504] Comisar G G 1969 *Phys. Fluids* **12** 1000
[505] Hirano K *et al* 1985 *Plasma Physics and Controlled Nuclear Fusion Research 1984 (London, UK)* (Vienna: IAEA) p 569
[506] Bostick W H 1963 *Phys. Fluids* **6** 1598
[507] Decker G, Kies W and Pross G 1982 *Phys. Lett.* A **89** 393
[508] Bostick W H *et al* 1966 *Phys. Fluids* **9** 2078
[509] Mather J W and Williams A H 1966 *Phys. Fluids* **9** 2080
[510] Nardi V 1970 *Phys. Rev. Lett.* **25** 718
[511] Bykovskii Yu A and Lagoda V B 1982 *Sov. Phys.—JETP* **56** 61
[512] Imshennik V S and Neudachin S V 1987 *Fiz. Plazmy* **13** 1226
       Imshennik V S and Neudachin S V 1987 *Sov. J. Plasma Phys.* **13** 707
[513] Lee S and Serban A 1996 *IEEE Trans. Plasma Sci.* **24** 1101
       see also Lee S 1985 *Laser and Plasma Technology* ed S Lee (Singapore: World Scientific) pp 37, 64 and 387
       Lee S 1984 *Radiation in Plasmas* ed B Namara (Singapore: World Scientific) vol II, p 978
[514] Zhang T *et al* 2006 *IEEE Trans. Plasma Sci.* **34** 2356
[515] Beg F N *et al* 2000 *J. Appl. Phys.* **88** 3225
[516] Soto L 2005 *Plasma Phys. Control. Fusion* **47** A361
       see also Silva P *et al* 2002 *Rev. Sci. Instrum.* **73** 2583
[517] Soto L *et al* 2009 *Dense Z-Pinches, AIP Conf. Proc.* **1088** 219
[518] Soto L *et al* 2008 *J. Phys. D: Appl. Phys.* **41** 205215
[519] Lebert R, Engel A and Neff W 1995 *J. Appl. Phys.* **78** 6414
[520] Kies W *et al Plasma Sources Sci. Technol.* **7** 21
[521] Choi P *et al* 1993 *Dense Z-Pinches, AIP Conf. Proc.* **299** 288
[522] Koshelev K N *et al* 1988 *J. Phys. D: Appl. Phys.* **21** 1827
[523] Sestero A, Robough B V and Podda A 1980 *Plasma Phys.* **22** 1039
[524] Kukushkin A B, Rantsev-Kartinov V A and Terentiev A R 1997 *Fusion Technol.* **32** 83
[525] Moffat H K 1978 *Magnetic Field Generation in Electrically Conducting Fluids* (Cambridge: Cambridge University Press)
[526] Forrest M J and Peacock N J 1974 *Plasma Phys.* **16** 489
[527] Peacock N J and Norton B A 1975 *Phys. Rev.* A **11** 2142, see also [255]
[528] Bernstein M J 1970 *Phys. Fluids* **13** 2858
[529] Potter D E and Haines M G 1971 *Plasma Physics and Controlled Nuclear Fusion Research (Madison, WI, USA, 1971)* vol 1 (Vienna: IAEA) p 611
[530] Bernstein M J and Comisar G G 1972 *Phys. Fluids* **15** 700
[531] Gary S P and Hohl F 1973 *Phys. Fluids* **16** 997
[532] Gary S P 1974 *Phys. Fluids* **17** 2135
[533] Kondoh Y and Hirano K 1978 *Phys. Fluids* **21** 1617
[534] Hohl F and Gary S P 1977 *Phys. Fluids* **20** 683
[535] Van Paassen H L L, Vandre R H and White R S 1970 *Phys. Fluids* **13** 2606
[536] Lee J H, Loebaka D S and Roos C E 1971 *Plasma Phys.* **13** 347
[537] Johnson D J 1974 *J. Appl. Phys* **45** 1147
[538] Stygar W, Gerdin G, Venneri F and Mandrekas J 1982 *Nucl. Fusion* **22** 1161
[539] Smith J R, Luo C M, Rhee M J and Schneider R F 1985 *Phys. Fluids* **28** 2305
[540] Trubnikov B A and Zhdanov S K 1985 *JETP Lett.* **41** 358
[541] Kondoh Y and Mamada M 1986 *Phys. Fluids* **29** 483
[542] Schmidt H 1987 Inst. für Plasmaforschung, Universitat Stuttgart IPF-87-5
[543] Schmidt H, Kubes P, Sadowski M J and Scholz M 2006 *IEEE Trans. Plasma Sci.* **34** 2363
[544] Rhee M J and Weidman D J 1988 *Phys. Fluids* **31** 703
[545] Hora H, Höptl R and Miley G M 1994 *Plasma Phys. Control. Fusion* **36** 1075
[546] Braginskii S I 1958 *Sov.Phys.—JETP* **34** 1068

[547] Alfvén H and Smårs E 1960 *Nature* **188** 801
[548] Smårs E A 1964 *Ark. Fys.* **29** 97
[549] Skowronek M, Rous J, Goldstein A and Cabannes F 1970 *Phys. Fluids* **13** 378
[550] Skowronek M, Giry L, Gia V T and Roméas P 1980 *Symp. Phys. Ionized Gases* p 278
[551] Benage J Skowronek M and Roméas P 1993 *Dense Z-Pinches, AIP Conf. Proc.* **299** 3
[552] Hartman C W *et al* 1977 *Nucl. Fusion* **17** 909
[553] Morozov A I 1968 *Sov. Phys—Tech.Phys.* **12** 2147
[554] Jones L A *et al* 1981 *Appl. Phys. Lett.* **38** 522
[555] Shlachter J S 1982 The behaviour of a plasma in a high density gas embedded Z-pinch configuration *Thesis* Los Alamos, CA-9333-7
[556] Dangor A E, Favre-Dominquez M B, Lee S and Kahan E 1983 *Phys. Rev.* A **27** 2751
[557] Mather J W and Ahluwalia H S 1988 *IEEE Trans. Plasma Sci.* **16** 56
[558] Veloso F *et al* 2009 *Plasma Sources Sci. Technol.* **18** 045012
[559] Robledo-Martinez A *et al* 1998 *Astrophys. Space Sci.* **256** 491
[560] Tatarakis M, Aliaga-Rossel R, Dangor A E and Haines M G 1998 *Phys. Plasmas* **5** 682
[561] Ruiz-Camacho J *et al* 1999 *Phys. Plasmas* **6** 2599
[562] Mosher D and Colombant D 1992 *Phys. Rev. Lett.* **68** 2600
[563] Aliaga-Rossel R *et al* 1998 *IEEE Trans. Plasma Sci.* **26** 1101
[564] Zakharov S M *et al* 1987 *Sov. J. Plasma Phys.* **13** 115
[565] Kalantar D H *et al* 1991 *J. Appl. Phys.* **23** 8134
[566] Shelkovenko T A *et al* 2001 *Phys. Plasmas* **8** 1305
[567] Shelkovenko T A *et al* 2005 *Phys. Plasmas* **12** 033102
[568] Beg F N *et al* 2006 *IEEE Trans. Plasma Sci.* **34** 2325
[569] Chittenden J P *et al* 2007 *Phys. Rev. Lett.* **98** 025003
[570] Bott S C *et al* 2008 *IEEE Trans. Plasma Sci.* **36** 2759
[571] Green J S *et al* 2006 *Appl. Phys. Lett.* **88** 261501
[572] Shelkovenko T A *et al* 2006 *IEEE Trans. Plasma Sci.* **34** 2336
[573] Shelkovenko T A *et al* 2009 *Phys. Plasmas* **16** 050702
[574] Ivanov V V *et al* 2006 *IEEE Trans. Plasma Sci.* **34** 2247
[575] Pikuz S A *et al* 2001 *Nukleonika* **46** 21
[576] Pikuz S A *et al* 2001 *J. Quant. Spectrosc. Radiat. Transfer* **71** 581
[577] Douglass J D and Hammer D A 2008 *Rev. Sci. Instrum.* **79** 033503
[578] Lebedev S V *et al* 2001 *Rev. Sci. Instrum.* **72** 671
[579] Bott S C *et al* 2004 *Rev. Sci. Instrum.* **75** 3944
[580] Appartaim R K and Maakuu B T 2008 *Phys. Plasmas* **15** 072703
[581] Beg F N *et al* 2003 *Appl. Phys. Lett.* **82** 4602
[582] Shumlak U *et al* 2008 *J. Fusion Energy* **27** 111
[583] Shumlak U *et al* 2009 *Nucl. Fusion* **49** 075039
[584] Beg F N *et al* 2004 *Phys. Rev. Lett.* **92** 095001
[585] Linhart J G 1979 *Nucl. Fusion* **19** 264
[586] Linhart J G 1988 *IEEE Trans. Plasma Sci.* **16** 438
[587] Linhart J G 1988 *Nucl. Instrum. Methods* A **278** 114
[588] Maissonier Ch, Haegi M and Linhart 1965 *Proc. Int. Conf. on Plasma Physics and Controlled Nuclear Fusion Research (Culham, UK)* (IAEA: Vienna)
[589] Turchi P J and Baker W L 1973 *J. Appl. Phys.* **44** 4936
[590] Book D L and Winsor N K 1974 *Phys. Fluids* **17** 662
[591] Bud'ko A B, Liberman M A, Velikovich A L and Felber F S 1990 *Phys. Fluids* B **2** 1159
[592] Hussey T W and Roderick N F 1981 *Phys. Fluids* **24** 1384
[593] Bortolotti A, Linhart J G, Kravãrik J and Kubes P 1993 *Dense Z-Pinches, AIP Conf. Proc.* **299** 372
[594] Cochrane J C *et al* 1993 *Dense Z-Pinches, AIP Conf. Proc.* **299** 381
[595] Peterson D L *et al* 1993 *Dense Z-Pinches, AIP Conf. Proc.* **299** 388
[596] Degnan J H, Baker W L and Turchi P J 1989 *Dense Z-Pinches, AIP Proc.* **195** 34
[597] Degnan J H *et al* 1995 *Fusion Technol.* **27** 115
[598] Degnan J H *et al* 1995 *Phys. Rev. Lett.* **74** 98
[599] Vandevender J P 2009 *Lecture at Wire Array Workshop (UCSD La Jolla, USA)*
[600] Slutz S A *et al* 2009 *Lecture at Wire Array Workshop (UCSD La Jolla, USA)*
[601] Garanin S F, Mamyshev V I and Yakubov V B 2006 *IEEE Trans. Plasma Sci.* **34** 2273
[602] Lindemuth I R and Kirkpatrick R C 1983 *Nucl. Fusion* **23** 263

[603] Dahlin J-E 2001 Reactor potential for magnetized target fusion TRITA-ALF-2001-02, Royal Institute Technology, Stockholm
[604] Rahman H U, Ney R, Wessel F J and Rostoker N 1995 *Comment. Plasma Phys. Control. Fusion* **15** 339
[605] Klir D *et al* 2005 *Plasma Devices Oper.* **13** 39
[606] Hasegawa A *et al* 1986 *Phys. Rev. Lett.* **56** 139
[607] Sheehey P T, Faehl R J, Kirkpatrick R C and Lindemuth I R 1997 *Proc. 7th Int. Conf. Megagauss Magnetic Field Generation 7 Related Topics (Sarov, Russia, 1996)* ed V K Chernyshev *et al* Part I, pp 425–30
[608] Degnan J H *et al* 2008 *IEEE Trans. Plasma. Sci* **36** 80
[609] Anderson O A *et al* 1958 *Phys. Fluids* **1** 489
[610] Colgate S A and Furth H P 1960 *Phys. Fluids.* **3** 982
[611] Vlases G C 1963 *J. Fluid Mech.* **16** 82
     see also Vlases G C 1964 *Phys. Fluids* **7** 1358
[612] Harvey-Thompson A J *et al* 2009 *Phys. Plasma* **16** 022701
[613] Sethian J 1997 *Dense Z-Pinches, AIP Conf. Proc.* **409** 3
[614] Hartman C W *et al* 1997 *Nucl. Fusion* **17** 909
[615] Hartman C W *et al* 1996 *Comment. Plasma Phys. Control. Fusion* **17** 267
[616] Morozov A I 1967 *Zh. Tekh. Fiz.* **37** 2147, see also [553]
[617] Newton A A, Marshall J and Morse R L 1969 *Proc. 3rd Eur. Conf. on Controlled Fusion and Plasma Physics (Utrecht, The Netherlands)* p 119
[618] Cheng D Y and Wang P 1973 *Nucl. Fusion* **13** 458
[619] Winterberg F 1978 *Z. Phys.* A **284** 43
[620] Winterberg F 1983 *Atomkernenerg. Kerntech.* **43** 31
[621] Winterberg F 1998 *Z. Naturf.* a **53** 933
[622] Winterberg F 1998 *Z. Naturf.* a **54** 443
[623] Winterberg F 1998 *Z. Naturf.* a **55** 909
[624] Winterberg F 1998 *Z. Naturf.* a **54** 459
[625] Winterberg F 1981 *Atomkernenerg. Kerntech.* **39** 181
[626] Winterberg F 1981 *Atomkernenerg. Kerntech.* **39** 265
[627] Winterberg F 1999 *Nucl. Fusion* **39** 933
[628] Winterberg F 2000 *Acta Astronaut.* **46** 551
[629] Winterberg F 2003 *Z. Naturf.* a **58** 197
[630] Winterberg F 2003 *Phys. Lett.* A **318** 570
[631] Winterberg F 2003 *Z. Naturf.* a **58** 612
[632] Winterberg F 2004 *Phys. Plasmas* **11** 706
[633] Winterberg F 2006 *Phys. Plasmas* **13** 032501
[634] Hagenson R L *et al* 1981 *Nucl. Fusion* **21** 1351
[635] Robson A E 1984 *Proc. 1st Int. Conf. on Dense Z-Pinches for Fusion* ed J D Sethian and K A Gerber (Naval Research Laboratory) p 2
[636] McCorkle R A 1983 *Nuovo Cimento* B **77** 31
[637] Bolton H R *et al* 1987 *Plasma Physics & Controlled Fusion Research (Kyoto, Japan, 1986)* (IAEA: Vienna) vol 3, p 367
[638] Haines M G 1982 *Unconventional Approaches to Fusion* ed B Brunelli and G A Leotton (New York: Plenum) p 281
[639] Haines M G and Walker S P 1987 *Nucl. Energy* **26** 361
[640] Walker S P, Javadi M and Robson A E 1987 *Fusion Technol. Proc. 14th Symp. on Fusion Technology (Avignon, France, 1986)* (Oxford: Pergamon)
[641] Bolton H R *et al* 1989 *Fusion Eng. Des.* **10** 9
[642] Robson A E 1993 *Dense Z-Pinches, AIP Conf. Proc.* **299** 707
[643] Baronova E O and Vikhrev V V 1997 *Dense Z-Pinches, AIP Conf. Proc.* **409** 67
[644] Degnan J H, Sand R J, Kiuttu G F and Woodall D M 1981 *Low Energy X-ray Diagnostics, AIP Conf. Proc.* **75** 264
[645] Deeney C *et al* 1991 *Phys. Rev.* A **44** 6762
[646] Deeney C *et al* 1995 *Phys. Rev.* E **51** 4823
[647] Deeney C *et al* 1999 *Phys. Plasmas* **6** 2081
[648] Zakharov S V, Smirnov V P and Tsarfin V Ya 1992 *Plasma Physics and Controlled Nuclear Fusion Research (Wuerzburg, Germany, 1992)* (Vienna: IAEA) vol 3, p 481
[649] Branitsky A V *et al* 1997 *Dense Z-Pinches, AIP Conf. Proc.* **299** 580
[650] Whitney K G, Thornhill J W, Apruzese J P and Davis J 1990 *J. Appl. Phys.* **67** 1725

[651] Thornhill J W *et al* 2006 *IEEE Trans. Plasma Sci.* **34** 2377
[652] Jones B *et al* 2006 *IEEE Phys. Plasmas* **15** 122703
[653] Sorokin S A and Chaikovsky 1997 *Dense Z-Pinches, AIP Conf. Proc.* **409** 593
[654] Sze H *et al* 2001 *Phys. Plasmas* **8** 3155
[655] Alikhanov S G *et al* 1984 *Fiz. Plazmy* **10** 0151
       Alikhanov S G *et al* 1984 *Sov. J. Plasma Phys.* **10** 605
[656] Choi P, Dangor A E, Deeney C and Challis C D 1986 *Rev. Sci. Instrum.* **57** 2162
[657] Li C R and Yang T C 1991 *J. Phys. D: Appl. Phys.* **24** 48
[658] Bayley J M *et al* 1991 *J. Appl. Phys.* **69** 613
[659] Chuvatin A S *et al* 2005 *IEEE Trans. Plasma Sci.* **33** 739
[660] Bergman K, Lebert R and Neff W 1997 *J. Phys. D: Appl. Phys.* **30** 990
[661] Bailey J E *et al* 2002 *Phys. Plasmas* **9** 2186
[662] Forsyth E B, Lederman L M and Sunderland J 1965 *IEEE Trans. Nucl. Sci.* **12** 872
[663] Kowalewicz R *et al* 1991 *IEEE Proc. Particle Accelerator Conf. (PAC 91) (San Francisco, CA)* vol 4, p 2631
[664] Kowalewicz R *et al* 1992 *15th Int. Conf. on High Energy Accelerators (Hamburg, Germany, 20–24 July)*
[665] Kowalewicz R *et al* 1992 *Proc. Eur. Particle Accelerator Conf. (EPAC 1992) (Berlin, Germany)* p 1539
[666] Haines M G 1961 *Conf. on Plasma Physics and Controlled Fusion Research (Salzbury)* ed J G Beckerley (Vienna: IAEA) CN10/75
[667] Hess R V 1962 *NASA Publication* sp-25 p 9
[668] Hess R, Brockman P and Grossman W 1963 *Conf. on Ionization Phenomena in Gases (Paris, France)* paper X1,19
[669] Etherington R J and Haines M G 1965 *Phys. Rev. Lett.* **14** 1019
[670] Smirnov A, Ralses Y and Fisch N J 2003 *J. Appl. Phys.* **94** 852
[671] Watkins M L *et al* 1971 *Plasma Physics and Controlled Nuclear Fusion Research (Madison, WI, USA)* vol 1 (Vienna: IAEA) p 611
[672] Lehnert B 1977 *Phys. Scr* **16** 147
       see also Lehnert B 1983 *Nucl. Instrum. Methods* **207** 223
[673] Bonnevier B *et al* 1982 *9th Int. Conf. Plasma Physics and Controlled Nuclear Fusion Research (Baltimore, MD, USA)* (Vienna: IAEA) CN-41/J5
[674] Rahman H U, Amendt P and Rostoker N 1985 *Phys. Fluids* **28** 1528
[675] Chakrabarti N, Fruchtman A, Arad R and Maron Y 2002 *Phys. Lett.* A **297** 92
[676] Osin D *et al* 2004 *IEEE Trans. Plasma Sci.* **32** 1805
[677] Adlam J H and Holmes L S 1963 *Nucl. Fusion* **3** 62
[678] Baker D A *et al* 1971 *Int. Conf. Plasma Physics and Controlled Nuclear Fusion Research (Madison, WI, USA)* (Vienna: IAEA) Cn-28/B2
[679] Velikovich A L, Gol'berg S M, Liberman M A and Felber F S 1985 *Sov. Phys.—JETP* **61** 261
[680] Felber F S, Liberman M A and Velikovich A L 1988 *Phys. Fluids* **31** 3675
[681] Felber F S, Liberman M A and Velikovich A L 1988 *Phys. Fluids* **31** 3683
[682] Appartaim R K and Dangor A E 1988 *J. Appl. Phys.* **84** 4170
[683] Gol'berg S M, Liberman M A and Velikovich A L 1990 *Plasma Phys. Control. Fusion* **32** 319
[684] Wessel F J *et al* 1997 *Dense Z-Pinches, AIP Conf. Proc.* **409** 39
[685] Zehnter P *et al* 1998 *EPS Conf. Plasma Physics (Prague, Czech Republic)* vol 22C (ECA) P.4-082
[686] Leon J F *et al* 1999 12th *IEEE Int. Pulsed Power Conf. (Monterey, CA, USA)* vol 1, p 275
[687] Bland S N *et al* 2004 *Phys. Plasmas* **11** 4911
[688] Zukakishvili G G, Mitrofanov K N, Grabovskii E V and Oleinik G M 2005 *Plasma Phys. Rep.* **31** 652
[689] Illingworth R 1970 *J. Phys. D: Appl. Phys.* **3** 924
[690] Illingworth R 1972 *J. Phys. D: Appl. Phys.* **5** 686
[691] Steden C and Kunze H J 1990 *Phys. Lett.* A **151** 534
[692] Shin H J, Kim D E and Lee T N 1994 *Phys. Rev. E* **50** 1376
[693] Lebert R *et al* 1996 *Opt. Quantum Electron.* **28** 241
[694] Ben-Kish A *et al* 2001 *Phys. Rev. Lett.* **87** 015002
[695] Kwek K H and Tan C A 2009 *Dense Z-Pinches, AIP Conf. Proc.* **1088** 168
[696] Pöckl M *et al* 1996 *J. Phys. D: Appl. Phys.* **29** 2091
[697] Suckewer S and Skinner C H 1995 *Comment. At. Mol. Phys.* **30** 331
[698] Mangles S P D *et al* 2004 *Nature* **431** 535
[699] Geddes C G R *et al* 2004 *Nature* **431** 538
[700] Faure J *et al* 2004 *Nature* **431** 541
[701] Pukhov A and Meyer-ter-Vehn J 2002 *Appl. Phys.* B **74** 355

[702] Tajima T and Dawson J M 1979 *Phys. Rev. Lett.* **43** 267
[703] Leemans W P *et al* 2006 *Nature Phys.* **2** 696
[704] Rowlands-Rees T P *et al* 2008 *Phys. Rev. Lett.* **100** 105005
[705] Ampleford D J *et al* 2007 *Phys. Plasmas* **14** 102704
[706] Ciardi A *et al* 2007 *Phys. Plasmas* **14** 056501
[707] Chittenden J P *et al* 2002 *Phys. Rev. Lett.* **88** 235001
[708] Ryutov D *et al* 1999 *Astrophys. J.* **518** 821
[709] Ryutov D D and Remington B A 2002 *Plasma Phys. Control. Fusion* **44** B407
[710] Bagchi J, Gopal-Krishna, Krause M and Joshi S 2007 *Astrophys. J.* **670** L85
[711] Hardcastle M J *et al* 2007 *Astrophys. J.* **670** L81
[712] Bally J, Morse J and Reipurth B 1996 The birth of stars: Herbig Haro jets, accretion and Boto-planetary disks
          Science with the Hubble Space Telescope II ed P Benvenuti *et al* p 491
[713] Reipurth B and Bally J 2001 *Annu. Rev. Astron. Astrophys.* **39** 403
[714] Hartigan P and Morse J 2007 *Astrophys. J.* **660** 426
[715] Lebedev S V *et al* 2005 *Plasma Phys. Control. Fusion* **47** B465
[716] Ryutov D D and Remington B A 2003 *Phys. Plasmas* **10** 2629
[717] Gardiner T A *et al* 2003 *Astrophys. Space Sci.* **287** 69
[718] Ciardi A *et al* 2007 *Astrophys. Space Sci.* **307** 17
[719] Lebedev S V *et al* 2004 *Astrophys. J.* **616** 988
[720] Ciardi A, Lebedev S V, Chittenden J P and Bland S N 2002 *Laser Part. Beams* **20** 255
[721] Hartigan P 2005 *Astrophys. Space Sci.* **298** 99
[722] Coffey D *et al* 2004 *Astrophys. J.* **604** 758
[723] Ampleford D J *et al* 2008 *Phys. Rev. Lett.* **100** 035001
[724] Livio M 1999 *Phys. Rep.* **311** 225
[725] Kronberg P P 2009 *Proc. IAU Symposium* No. 259, 499
[726] Appl S, Lery T and Baty H 2000 *Astron. Astophys.* **355** 818, see also [205]
[727] Lynden-Bell D 1996 *Mon. Not. R. Astron. Soc.* **279** 389
[728] Lynden-Bell D 2003 *Mon. Not. R. Astron. Soc.* **341** 13
[729] Hartigan P, Frank A, Varniere P and Blackman E G 2007 *Astrophys. J.* **661** 910
[730] Lebedev S V *et al* 2005 *Mon. Not. R. Astron. Soc.* **361** 97
[731] Ciardi A *et al* 2005 *Astrophys. Space Sci.* **298** 277
[732] Ciardi A *et al* 2007 *Phys. Plasmas* **14** 102704
[733] Ampleford D J *et al* 2005 *Astrophys. Space Sci.* **298** 241
[734] Suzuki-Vidal F *et al* 2009 *Astrophys. Space Sci.* **322** 19
[735] Ciardi A *et al* 2009 *Astrophys. J.* **691** L147
[736] Frank A *et al* 2005 *Astrophys. Space Sci.* **298** 107
[737] Knudson *et al* 2004 *Phys. Rev.* B **69** 144209
[738] Oreshkin V I 2008 *Phys. Plasmas* **15** 092103
[739] Jones B, Corerdale C A and Mazarakis M G 2000 *IEEE Trans. Plasma Sci.* **36** 1276